FUNDAMENTAL STUDY OF FRAGMENTATION BEHAVIOR AND ENERGY RELEASE OF REACTIVE MATERIALS

by

Stewart H. Youngblood

Submitted in Partial Fulfillment
of the Requirements for the Degree of
Doctor of Philosophy in Mechanical Engineering
with Dissertation in Intelligent Energetic Systems

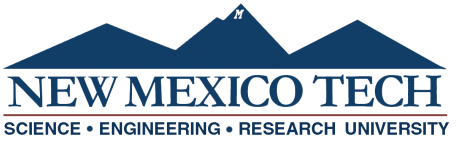

New Mexico Institute of Mining and Technology
Socorro, New Mexico
May, 2022

This dissertation is dedicated to my wife Jenna and my parents Nathan and Anne. The blood, sweat, tears, and diesel that fueled this work were only possible because of your unrelenting support. Without you, none of this would have been possible. I love y'all.

-Stewart

ABSTRACT

Reactive Materials (RMs) are a class of engineered granular composites comprised of metals, metal oxides, and/or polymers. These composites are of interest for defense applications as their fragmentation and energy release characteristics, or thermo-mechanical behavior, can increase the effective energy transfer to a target. Knowledge and predictive capability of the thermo-mechanical behavior of RMs is critical for effective design and application of the materials. In this work, aluminum and Al/PTFE RM specimens were fabricated with varied composition, porosity, and particle size to produce variations in mechanical response and energy release. Quasi-static compression tests, Kolsky bar compression tests, and high velocity impact studies were used to evaluate the mechanical response of the RM specimens at strain rates between 10^{-3} s^{-1} and 10^{5} s^{-1}. A generalized parameterized model was developed and verified for predicting the quasi-static material response of RMs with varying composition, porosity, and particle size of the constituents. Fragment distributions of specimens from the Kolsky bar and high velocity impact studies were used to evaluate existing fragmentation models revealing a generalized RM fragmentation model is still elusive. Application of minimum energy state fragmentation models for predicting characteristic fragment sizes of dynamically fragmenting granular composites was demonstrated and limitations discussed. Bomb calorimetry and vented calorimetry experiments were used to explore the characteristics of RM combustion which is multiphase by nature. A phase-compliant Gibbs minimization of free energy equilibrium solver was developed to improve predictions of energy release and equilibrium product states of RM reactions and verified using bomb calorimetry measurements.

Keywords: Reactive Materials, Aluminum/PTFE Combustion, Granular Composites, Dynamic Fragmentation, Multiphase Equilibrium Modeling, Grady Fragmentation Model

ACKNOWLEDGMENTS

I would like to thank Dr. Michael J. Hargather and Dr. Jamie Kimberley for their unwavering support these past five years. It was a wild ride to say the least and it has been a privilege working alongside you. Your mentorship is truly second to none. I like to think we all have a better understanding of the true meaning of temporal practicality now. And thank you to my committee for all your efforts. I know it was not an easy task given the scope of this work.

To all of my friends and family, thank you for your support and love. And a special thank you to Ben, Paul, and Brad for the late night discussions of multiphase equilibrium, dynamic material behaviors, particle composite engineering, and general head-scratching science. The accomplishments in this work are a testament to the collective knowledge we fostered between us. To my lab mates, thank you for your support and passion. I will forever miss the discussions of ridiculous applications of science, the sunrises and sunsets on days of testing, and conversations alongside the enjoyment of Sophia's burritos and Frito pies. And to be honest, surviving COVID with y'all was a pretty good time too. May Weenie Wednesday live on wherever we are.

This work was supported by Reactive Metals International, Inc.. A special thank you is in order for Bernie Kosowski, Dr. Phil Martellaro, and Steve Thoma for all of their support these past five years. I will forever be grateful.

This dissertation was typeset with LaTeX[1] by the author.

[1]The LaTeX document preparation system was developed by Leslie Lamport as a special version of Donald Knuth's TeX program for computer typesetting. TeX is a trademark of the American Mathematical Society. The LaTeX macro package for the New Mexico Institute of Mining and Technology dissertation format was written by John W. Shipman.

CONTENTS

LIST OF TABLES

LIST OF FIGURES

Figure **Page**

This dissertation is accepted on behalf of the faculty of the Institute by the following committee:

Michael J. Hargather

Academic and Research Advisor

Jamie Kimberley

Research Advisor

Seok Bin Lim

Bhaskar Majumdar

Phil Martellaro

I release this document to the New Mexico Institute of Mining and Technology.

Stewart H. Youngblood February, 2022

CHAPTER 1

INTRODUCTION

1.1 Research motivation

Reactive Materials (RMs) are a class of engineered materials with primary interest as a replacement for inert materials used for structural components[1–3] and high-speed projectiles[4, 5] in munitions systems. RMs of interest consist of pressed metallic and metallic/polymer composites manufactured from micron and nano scale powders. RMs have the ability to enhance the effectiveness of munitions systems through their high energy density[6], improved chemical energy release characteristics compared with bulk metals, and enhancement of the total energy transferred to the target[7]. RMs fracture when subjected to high dynamic loads, resulting in the production of large quantities of fine fragments. These fragments both combust and improve the transfer of kinetic energy on impact, increasing the effective energy transfer to the target. Specific applications include enhancing the effectiveness of kinetic energy weapons and blast and fragmentation effects from warheads[1, 2, 7]. Other interests include applications in defensive structures for protection against high-speed projectile impacts[8].

Knowledge of the fragmentation and energy release behavior of RMs is critical for effective design and application of RM based munition systems. Prior research has focused on understanding the roles that composition, microstructure, and loading have on fragmentation behavior and energy release [8–12]. These efforts support material by design applications, where, through the manufacturing process, the RM material properties, fragmentation behavior, and energy release behavior can be manipulated [9, 13].

Efforts to characterize the thermo-mechanical response of RM generally fall into three groups: empirical fragmentation prediction through high-rate application analogous loading studies, combustion energy release studies, and numerical modeling of the fragmentation process at the mesoscale level. These studies are generally directed by specific interests, and are often limited to the evaluation of a single RM system with fixed compositional or microstructure parameters. While these studies have advanced the knowledge of the physical behavior of RM systems, knowledge gaps continue to persist. These knowledge gaps include a lack of understanding of the direct effects composition, porosity, and particle size have on the bulk material response of RM systems. Many research efforts simply measure parameters needed for applied models, or estimate the material

response using empirical relations that are specific to the system analyzed. Without unifying theories to estimate the bulk material response of a RM system in relation to composition, porosity, and particle size, tunable RM systems cannot be fully realized.

1.2 Manufacturing and observed effects on reactive material systems

RMs may consist of single metal, multi-metal, intermetallic, thermite, or metal polymer compositions generally manufactured through the consolidation of raw precursor powders [6, 12, 14]. Nanometer and/or micrometer sized powders are acquired in the desired particle size range, blended, and consolidated into a bulk composite using a dry powder compaction process [4, 8, 15, 16]. Other manufacturing techniques have been investigated, with interest on decreasing constituent particle size during blending and enhancement of particle contact during consolidation. Investigated techniques include arrested reactive milling using planetary ball mills[14, 17], ultrasonic powder consolidation[18], and layered vapor deposition to create nanofoils[19]. Focus of this work will be on RM systems manufactured using the dry powder compaction process.

Dry powder compaction is a well established industry process for the manufacture of ceramic, metallic, and polymer parts from powders[20, 21]. The process consolidates the constituent powder mix, binding the particles together into a single body[22]. The process lends itself well to automation with high efficiency throughput of pressed parts with tight dimensional tolerances[21]. Dry powder compaction is primarily used in literature to produce RM samples due to the ease of small scale application in a lab environment and likelihood as the primary manufacturing tool for future RM systems.

Two variants of dry powder compaction exist: Uniaxial die pressing and isostatic pressing. Uniaxial die pressing compacts the constitutive powder with loading applied in only one direction, while isostatic pressing compacts the constitutive powder with loading applied uniformly in all directions. Of the isostatic variant, two methods exist: Cold isostatic pressing (CIP) and hot isostatic pressing (HIP). CIP and HIP produce parts with the most uniform density and grain structure when compared to uniaxial pressing[23]. The consolidated powder body produced by these methods is often referred to as a "green body"[20]. However, the term green body is typically used in reference to a consolidated powder body that will be subjected to further processing such as sintering. The samples here are considered finished products after the uniaxial pressing, so they are not referred to as green bodies, but rather as consolidated powder bodies.

The consolidated powder body density is proportional to the applied pressing force, with increasing pressing force decreasing porosity and leading to an increase in the final material strength of the consolidated powder body[21, 24, 25]. The maximum attainable density of the consolidated powder body is limited by the particle shape, size distribution, and particle interaction with surrounding

particles and the die walls [22, 24]. Powder consolidation theory, a description of the applied pressing methods in RM, and observed effects on fragmentation and energy release will be discussed in detail in the subsequent sections.

1.2.1 Powder consolidation theory

Powder consolidation theory describes the compaction of dry powders into a single body. The theory assesses the relative consolidated powder body density obtainable for a given compaction pressure and powder characteristics. Established theories suggest the mechanisms which control the densification of the powder are: particle rearrangement, interparticle friction, plastic and elastic deformation of particle contacts, and fragmentation of particles[21, 22, 24, 26]. Two general classes of compaction behavior are described by powder consolidation theory: compaction of monolithic powders and compaction of granulated powders[21]. Monolithic powders are raw powders which do not stick together or form granulates and generally encompass metallic and some polymer powders[21]. Granulated powders consist of granulates of agglomerated particles as a result of powder cohesion or the use of agglomerating pressing aids and generally encompass ceramics and some polymer powders[21, 24]. In application, it is expected RMs consisting only of metal or metal oxides will exhibit monolithic powder compaction behavior. Some RMs containing polymers may also exhibit monolithic compaction behavior if the polymer does not readily agglomerate. For RMs that are manufactured with polymers that agglomerate, it is expected that granulated powder compaction behavior is more likely to occur.

For monolithic and granulated powders, experimental and numerical results have shown that the size distribution and shape of the particles or granulates strongly influence the packing density of the powders in the die prior to pressing[24]. Lower packing densities decrease the maximum obtainable consolidated powder body density which is undesirable in most applications[21]. Particle shape is also critical in obtainable packing densities. As the relative roundness of mono-sized particles approaches unity, the packing density approaches the limit for spherical particles of 0.64[24]. Higher packing densities can be obtained for particles that are cubes or plates with an aspect ratio of 1:4.4[24]. Typical constituent powders used in manufacturing RM are polygonal to near spherical in shape[3, 12, 15, 27], suggesting maximum packing densities of 0.5 to 0.64 during manufacture. Existing consolidation theory generally assumes spherical particles due to challenges in accounting for particle shape variation[21].

Compaction of monolithic powders can be divided into three primary mechanisms for an ideal pressing process of monosized spheres[21]:

1. Particle rearrangement leading to an increase in density from rearrangement of the loose powder

2. Elastic deformation of the particle bulk with plastic deformation localized to the particle contacts, leading to collapse of the voids which surround the particles. This void reduction allows the density to reach 80-90% of the theoretical maximum density (TMD)

3. Plastic deformation of the particle bulk leading to isolation and sealing off of voids. Bulk plastic behavior is similar to a solid with isolated voids. Further compaction is obtained through plastic deformation or fracturing of particles in accommodating neighboring particles.

Obtaining 100% TMD with monosize powders requires pressing pressures on the order of four times the yield strength of the powder particles[21]. These high pressures are not practically obtainable for many materials due to mechanical limits of pressing equipment. Monosize powders consist of a single size particle, whereas binary or ternary powders have two and three different primary particle sizes, respectively. Typical monolithic pressing utilizes powders with varied particle size to improve initial packing density and reduce the required pressing pressure to obtain a given consolidated powder body density[21].

Using powders with multiple particles sizes permits higher consolidated powder body densities due to smaller particles occupying voids between larger particles, decreasing the total void inclusion in the consolidated powder body[21]. For significant increases in consolidated powder body density with bimodel spherical powders, experimental and numerical simulations have shown diameter ratios between the large and small particle size groups must be greater than seven[21]. Improvement in void reduction and high consolidated powder body density leads to an increase in contact area between particles as a result of increased particle deformation and interlocking[25, 28]. As a result, the cohesive force between the compacted particles increases, leading to an enhancement in material strength of the consolidated powder body[28, 29].

1.2.2 Dry powder compaction techniques

Uniaxial compression utilizes a die and punch to compress the loose powder, where a force axially aligned to the punch is applied to compress the powder into the die. Pressing pressures can be on the order of 10^3 MPa. Uniaxial pressing can either be a single action or double action process. In single action, a single punch is used to compress the powder into the die with a fixed base. In double action, two punches are used to compact the powder from both ends in the die. Uniaxial pressing is a common industry method for manufacturing green bodies, but does suffer from density gradients in the compacted powder body. These gradients are a result of decreased compaction pressure inside the bulk powder resulting from interparticle friction and friction between particles and the die wall[21]. It has been shown that a decrease in P_{ax} is directly related to an increase in the length to diameter ratio[21], implying that density gradients will be more prevalent in

long pressed parts. A double action process is clearly preferred as the magnitude of the P_{ax} decrement is reduced by half. The double action process also isolates the lowest pressure, and thus density, region to the center of the consolidated powder body[21].

Cold isostatic pressing (CIP) utilizes an elastomeric mold with the constituent powder sealed inside. The sealed mold is pressurized hydrostatically, often with water or hydraulic fluid[20]. Two methods of CIP are employed: wet bag pressing and dry pressing. Wet bag pressing uses a flexible rubber mold that is filled with powder, submerged into a pressure vessel, and then pressurized to compact the powder. Dry bag pressing utilizes a mold fixed in the pressure vessel that is not removed. The mold is filled with powder, sealed with a steel mandrel, and pressurized. In both methods, the pressure is released slowly to control mold rebound and prevent damage to the consolidated powder body surface finish[24]. This hydrostatic pressure applied in this process is generally on the order of 400 MPa for industrial applications [21].

The main advantage of the CIP process is that the uniform application of pressure mitigates the negative effects of die wall friction on compaction pressure as seen with uniaxial pressing. The result is near uniform density of the consolidated powder body and a uniform grain structure. A downside to this method is geometric tolerances can be lower than uniaxial pressing and the change in volume of the powder during the pressing process must be accounted for to ensure proper geometry of the consolidated powder body is obtained[24].

Similar to the CIP process, hot isostatic pressing (HIP) relies on the uniform pressurization of a powder containing mold. This mold is often made of a high-melting-point metal and is pressurized using an inert gas[24, 30]. The pressing process is conducted under high temperature, which depending on the powder pressed, can range from hundreds to thousands of degrees Celsius for pressures up to 200 MPa[24]. The heating process drives lattice diffusion, grain boundary diffusion, plastic deformation by dislocation motion, viscous flow rearrangement, and grain boundary sliding [24]. These effects improve the consolidation process of particles, particle cohesion, and the microstructure of the body. This leads to improvements in material properties such as ductility and tensile strength. These mechanisms are similar to what occurs in the sintering process[24, 31], however the high pressure compaction of the HIP process amplifies these mechanisms and permits near 100% TMD of the consolidated powder body to be obtained[20, 24]. Unfortunately, HIP is complex, expensive, and often presents challenges in obtaining acceptable dimensional accuracy[24]. HIP is therefore generally used in specialty applications, the aerospace industry, and on occasion the manufacturing of RMs[32].

1.2.3 Effects of manufacturing methods on RM mechanical response and fragmentation behavior

In literature, RM specimens are most often consolidated using the CIP process [3, 4, 8, 16]. Uniaxial pressing has been used in the literature, though it is less prevalent than the CIP process[15, 33]. HIP has been used in the consolidation of aluminum based RMs[1, 34], but is the least prevalent of the three methods. Minimal research has looked at direct comparison of consolidation methods to ascertain the effects on the material response and fragmentation behavior. However, some insights have been reported on the effects CIP and HIP have on the RM fragmentation process and the importance of particle cohesion[16, 32, 34]. The authors and RM systems studied are summarized in Table 1.1.

Table 1.1: Summary of RM compositions, particle size, and dry compaction consolidation methods of discussed studies on manufacturing effects on RM mechanical response and fragmentation

Authors	RM Composition	Constituent Powders	Consolidation Method	Sintering
Chiu et al.[34]	Al/W	Al: 9 um and 20 um mean W: 200 µmx4 mm rods	CIP at 345 MPa HIP at 100 MPa,500 °C	None
Olney et al.[32]	Al/W	Al: 20 µm mean W: 200 µmx4 mm rods	CIP at 345'MPa HIP at 200 MPa,500 °C	None
Nesterenko et al.[16]	Al/W	Al: 9 µm mean W: 200 µmx4 mm rods	CIP and HIP No Specifications	None

Work by Chiu et al.[34] is the best comparison of the CIP and HIP processes on fragmentation behavior. Chiu et al.[34] looked at the effects of particle size and consolidation method on expanding ring experiments of aluminum (Al) and tungsten rings driven to failure using explosives at strain rates on the order of 10^4 s^{-1}. Two Al/W systems were evaluated: coarse Al powder (70 µm maximum particle size and 20 µm mean particle size) consolidated with 200 µmx4 mm-long W rods and fine Al powder (20 µm maximum particle size and 9 µm mean particle size) consolidated with 200 µmx4 mm-long tungsten rods. Both systems were 24% Al and 76% tungsten by mass, equivalent to a volume fraction of 69% Al and 31% tungsten, and had a measured porosity of 8-15% for the evaluated specimens. These two systems are referred to by Chiu et al. as coarse and fine, respectively. Both systems were manufactured using either CIP or CIP and then HIP (CIP+HIP).

Fragmentation differences between CIP and HIP of the systems were most discernible for the coarse consolidated system[34]. Analysis of the collected coarse system fragments revealed a similar mean fragment size of 20 µm for both consolidation methods which aligns with the mean particle size of 20 µm of the constituent Al powder. However, the CIP+HIP coarse system exhibited a lower distribution peak and the production of finer and larger fragments than

the CIP material[34]. Fragments of the fine system yielded similar fragment size distributions for both consolidation methods, with a mean fragment size of nominally 20μm. However, this is more than twice the constituent Al mean particle size of 9μm, in contrast to the coarse system behavior. The CIP+HIP fine system also exhibited a slightly higher production of fine particles and lower peak in mean particle size relative to the CIP system[34].

Olney et al.[32] and Nesterenko et al.[16] built on the work by Chiu et al.[34] by attempting to identify differences in the compaction process between the consolidation methods and identify the influence on the failure mechanisms of the tested RM. Olney et al.[32] looked at the coarse Al/W RM system and Nesterenko et al.[16] looked at the fine Al/W RM system studied by Chiu et al.[34]. Both sets of authors observed that for CIP, the particles only undergo rearrangement and do not fuse during consolidation. Images of the CIP+HIP specimen microstructure obtained using scanning electron microscopy (SEM) showed that CIP followed by HIP improved particle bonding and led to fusing of the Al particles.

Olney et al.[32] provided insight to the change in fracture mechanisms through numerical analysis of drop weight tests. Specimens were crushed to failure using a DYNATUP model 9250HV impact test machine to obtain strain rates on the order of 10^3 s^{-1}. Computational modeling of particle interaction under this impact loading scenario was performed using Raven, a 2D Eularian hydrocode, with Mie-Gruneisen equation of states and Johnson-cook material and failure models for the the Al and tungsten particles [16, 32]. In these simulations, particle cohesion was varied with the Al particles of the CIP RM systems stated as unbonded and the CIP+HIP systems stated as bonded. Quantitative explanation of the unbonded and bonded simulation conditions was not directly stated, but it is implied that the unbonded condition allows the Al particles to freely move and the bonded Al particles to behave as a bulk material.

Olney et al.[32] found that the CIP+HIP course material initially compressed under loading, reducing in porosity from 8.3% to 3.2% at which point shear instability started. The improved particle cohesion in the CIP+HIP coarse material reduced particle dislocations, allowing shear localization and the formation of zones of intense shear strain (shear bands)[32]. These shear bands create high intensity stress zones which lead to transgranular fracture[35, 36]. Developed stress in the bulk is relieved by these fractures, preventing further fracturing of the bulk and the formation of larger fragments. The transgranular fracture also leads to production of fragments smaller than the primary constituent particle size[16, 32]. Alternatively, Olney et al.[32] found that the coarse CIP material did not reduce in porosity under loading, and failure occurred through particle separation predominately driven by intergranular fracturing (fracture path between particles). The result was the formation of a large number of fragments on the scale of the primary constituent powders[16, 32, 34]. These observations of the difference in fragment size production in these simulations align with the qualitative differences identified in fragment size distributions of the CIP and CIP+HIP course systems[32, 34].

The results by Chiu et al.[34], Olney et al.[32], and Nesterenko et al.[16]

strongly suggests that particle cohesion is a major factor in controlling the failure mechanism of an RM system consolidated using a dry powder compaction process. The application of heat to the material through HIP or sintering can increase particle cohesion[21, 31], which can lead to shear band development and transgranular fracture of the compacted particles for the Al/W RM systems discussed[16, 32, 34]. In contrast, decreased particle cohesion associated with CIP can lead to failure of the discussed RM systems through intergranular fracture and separation of constituent particles[16, 32, 34, 35].

1.2.4 Effects of manufacturing methods on RM combustion energy release behavior

Minimal research has looked at direct comparison of consolidation methods to ascertain the effects on combustion energy release behavior of RMs. Work by Ding et al.[33] evaluated the effects of particle size and sintering on the combustion energy release rates of aluminum/copper oxide/PTFE (Al/CuO/PTFE) RM, providing some insight on influencing factors on combustion energy release of RM systems. Table 1.2 summarizes the manufacturing of the Al/CuO/PTFE RM evalauted by Ding et al.[33].

Table 1.2: Summary of RM composition, particle size, and dry compaction consolidation method of discussed study on manufacturing effects on RM energy release

Author	RM Composition	Constituent Powders	Consolidation Method	Sintering
Ding et al.[33]	Al/CuO/PTFE	Al: 50 nm and 5 µm/ CuO: 50 nm and 10 µm PTFE: 350 nm and 350 µm	Uniaxial at 60-100 MPa	360 - 380 ° 60°/hr

Using a drop weight impact ignition device, cylinders 10 mm in diameter and 10 mm long were initiated in a closed bomb, and pressure measurements used to infer the energy releases from combustion. Ding et al.[33] observed that both decreasing particle size and application of sintering increased the energy release rate of the Al/CuO/PTFE RM formulation[33]. For the nano-scale powder RMs evaluated, the increase in energy release rate associated with sintering was on the order of three times the rate of unsintered nano-scale powders. For micron-scale powder RMs, the increase in energy release rate associated with sintering was on the order of twice the rate of unsintered micron-scale powders[33], indicating sintering has a pronounced influence on energy release, but an underlying particle size influence exists. Because of the similarities between HIP and sintering[24, 30], it is expected a similar increase in energy release would be observed for a HIP RM system compared to CIP or uniaxialy pressed RM system.

This work by Ding et al.[33] suggests that the contact area between particles may be a factor in controlling the energy release rate of an RM system. Considering powder consolidation theory, where small particles of various sizes, and separately application of heat through a HIP or sintering process, lead to an increase in particle contact, the improved intermolecular contact between the fuel and oxidizer reduces the required diffusion distance of the reactants. It is possible that this effect is permitting the reaction process to occur at a significantly higher rate. However, this could also be related to differences in fragment size production between the sintered and unsintered materials. Prior work has demonstrated a higher production of fine fragments is possible when heat is applied in the consolidation process as compared to materials not heated during manufacturing[34]. Because fine fragments are known to burn more rapidly[7, 14], it is possible observations by Ding et al.[33] are associated with differences in fragment size production rather than differences in particle contact. It is expected both mechanisms are contributing factors to the increase in energy release rates observed by Ding et al[33], but without further study the exact influence of the mechanisms on the energy release rate cannot be ascertained.

1.3 Reactive material application and fragmentation behavior

The fragmentation characteristics of RM are of high interest for enhancing the efficiency and effectiveness of conventional munition systems[14, 16]. RM applications include ballistic based systems utilizing single or clusters of projectiles and warhead casings driven to failure through explosive loading. The fragmentation characteristics of RM systems improve the efficiency of kinetic energy transfer to the target as the RM projectile can penetrate the target, but the production of smaller fragments minimizes over-penetration, improving conversion of kinetic energy into the target. The production of small fragments also support the combustion of the RM[1, 16], further increasing energy input into the target, as discussed later in this chapter

Applications of interest vary widely in loading conditions and rate. Strain rates between 10^3 s^{-1} and 10^5 s^{-1} can be expected for ballistic systems[12], and 10^4 s^{-1} for explosively driven warheads where preshocking of the material during launch is known to change the microstructure [1, 15, 16]. In order to effectively utilize RMs in application, the material response and fragmentation behavior must not only be understood, but constitutive models must be developed to support engineering design and computational modeling efforts.

1.3.1 Quasi-static and dynamic mechanical response of RM

Studying the mechanical response of RM systems under quasi-static and dynamic loading is a critical step in understanding the failure mechanisms and fragmentation behavior of RMs[11, 15, 37, 38]. The quasi-static response is generally

studied using a universal testing machine (UTM) to compress the specimen to failure at strain rates of 10^{-3} s^{-1}. Compressive loading is chosen as the granular nature of RMs tends to result in poor strength characteristics under tensile loading[11, 37]. The dynamic response of RM systems is most often studied using a Kolsky bar, also referred to in literature as the split Hopkinson pressure bar. The Kolsky bar technique provides the means to measure the stress-strain response of a material specimen subjected to strain rates of typically 10^3 s^{-1}[39], and up to 10^4 s^{-1} using specimens with specific gauge section geometries[37]. Drop hammer tests have also been used in literature, but are less common and do not provide the same measurement fidelity as Kolsky bar testing[37]. These tools provide a quantitative means to assess the influence of compositional and mesoscale characteristics on material response[11, 38, 40], develop constitutive models of the material response[9, 41], and a means to study fragmentation under well characterized loading[13, 15, 42].

Work by Cai[37] demonstrated the manipulation of mesoscale structures present in RM through particle size variation. Using quasi-static and Kolsky bar experiments at strain rates of 10^{-3} s^{-1} and 10^2 s^{-1}, respectively, Cai assessed the material response of three RM systems: tin/PTFE (Sn/PTFE), aluminum/PTFE (Al/PTFE), and aluminum/tungsten/PTFE (Al/W/PTFE). These compositions were consolidated using the CIP process into cylinders that were 10 mm in diameter and 10 mm in length. Unfortunately, little comparative discussion was made of particle size effects for the Sn/PTFE and Al/PTFE systems beyond qualitative observations. Detailed discussion was presented on the Al/W/PTFE system, which was mixed at the following mass percentages: 5.5%Al/77%W/17.5%PTFE. The volume fraction of this composition is: 14.6%Al/28.5%W/56.9%PTFE. Cai fixed the Al and PTFE particle sizes at 2 µm and 100 nm, respectively. Two tungsten particle sizes were evaluated: less than 44 µm (coarse system) and less than 1 µm(fine system). The coarse system was evaluated at 14.3% and 1.6% porosity and the fine system was evaluated at 14.3% porosity[37].

Cai[37] used a UTM to measure the quasi-static compressive strength of the specimens, and observed an increase in quasi-static compressive strength from 6 MPa for the porous coarse system to 16.5 MPa for the dense-coarse system, a 175% increase. This aligns with general observations of porosity effects on material strength of granular compacts[43]. Decreasing the particle size led to an increase in strength from 16.5MPa for the dense-coarse system to 27.5MPa for the porous-fine system, a 66% increase. Similar trends were observed for the dynamic strength of the system, with a 33% increase (18 MPa to 24 MPa) in dynamic compressive strength between the porous and dense coarse systems and 83% increase (24 MPa to 44 MPa) between the dense-coarse and porous-fine systems[37].

The increase in strength as a result of decreasing particle size aligns with similar observations of particle size effects on material strength of granular ceramics[44, 45]. However, Cai[37] noted that this result was unexpected given the higher porosity of the fine system relative to the coarse system. Based upon

these results, and observations of reduced packing density with the fine tungsten system, Cai proposed that the fine tungsten particles occupied a larger volume than the coarse particles. This led to an enhanced spatial distribution of tungsten particles allowing the fine particles to interact early during loading and create a load bearing structure reinforced by the PTFE matrix. This structure improved the load carrying capacity of the material, overcoming the decrease in strength due to porosity. Cai referred to this process as force chain development[37].

The proposed force chain hypothesis by Cai[37] has found support from work by other authors. Herbold et al.[38] modeled the same Al/W/PTFE systems as studied by Cai[37], and the numerical results supported the force chain hypothesis. Similar particle size effects and force chains were observed by Chiu and Nesterenko[40] in their assessment of Al/W systems using quasi-static and Kolsky bar testing. The results of Cai[37], Herbold[38], and Chiu and Nesterenko[40] suggest that for some systems, changes in particle size can lead to structural formation at the mesoscale, indicating spatial dependencies that must be accounted for. Herbold et al.[38] proposed that understanding the distribution of particles at the mesoscale and the particle shape could be used to identify criteria for force chain development, though no specific methodology was given for making this determination[38].

Numerical simulations play an important role in developing an understanding of the mesoscale behavior of RM systems as previously discussed[16, 38, 40]. Equally important is modeling the bulk material response in support of a broad spectrum of engineering and material development efforts using constitutive models, which are lacking for many RM compositions[9]. Of particular interest is the Johnson-Cook constitutive model[46], which finds regular use in numerical simulations[9, 47]. The Johnson-Cook model describes the strain, strain rate, and temperature dependencies of the von Mises flow stress, σ_{vm}, of a material as[46]:

$$\sigma_{vm} = \left[A + B\epsilon_p^{n_{JC}}\right]\left[1 + C\ln\left(\dot{\epsilon}/\dot{\epsilon}_{JC}\right)\right]\left[1 - T^{*m_{JC}}\right] \tag{1.1}$$

Where ϵ_p is the equivalent plastic strain, $\dot{\epsilon}$ is the strain rate, $\dot{\epsilon}_{JC} = 1.0\ \mathrm{s}^{-}1$, and T^* the homologous temperature. The five material constants, A, B, C, n_{JC}, and m_{JC}, must be determined experimentally[46]. The first bracketed expression represents the stress state as a function of strain for $\dot{\epsilon}/\dot{\epsilon}_{JC} = 1$ and $T^* = 0$. The second bracketed expression represents the effects of strain rate. The third bracketed expression represents the effects of temperature. RM systems have been shown to have the potential for strain and strain rate dependencies[9, 37] as well as temperature dependencies[9]. Research efforts have shown the Johnson-Cook model is generally well suited for both the nature of loading, load rate dependence, and composite nature of RM[9, 41, 48].

The use of quasi-static and Kolsky bar tests are valuable tools in determining the parameters of the Johnson-Cook model[47]. Based on a lack of constitutive models for the Al/W/PTFE system, Zhang et al.[9] conducted a large parametric study of four different mixture variations of the system to determine the Johnson-Cook parameters for each variation. Using quasi-static testing and Kolsky bar

tests, Johnson-Cook parameters were determined for strain rates of 10^{-3} s^{-1} up to $7{\cdot}10^{3}$ s^{-1} and temperatures between 20 °C and 200 °C. Zhang et al. could not identify a direct correlation between the evaluated Al/W/PTFE composition variations and measured material moduli and strengths, but did concede that without understanding the influence of the mesoscale characteristics and porosity it would not be possible to assess a correlation to composition[9].

Work by X. Zhang et al.[49] studied the effects of tungsten content on the Al/W/PTFE system, providing insight into compositional effects. Using quasi-static testing and Kolsky bar tests, three Al/W/PTFE composition variations were evaluated[49]. X. Zhang et al. found that the addition of tungsten improved the compressive strength of the specimens up to 62% for specimens that were 10% tungsten by volume compared to specimens that contained no tungsten[49]. A decrease of 22% in compressive strength of the specimens was observed when the tungsten content was increased to 28.5% by volume compared to the specimens that were 10% tungsten by volume. The additional tungsten was found to transition the material behavior from a ductile response to a brittle response. Similar trends were observed for Kolsky bar tests performed by X. Zhang et al.[49]. These results suggest that compositional effects may include interactions at the mesoscale that simple relations may not capture.

Observations of residual stresses in the compacted powder grains of an RM system, imparted through the compaction process during manufacture, have been found to have a considerable impact on material response[11]. Kline and Hooper[11] found that the annealing process improved the compressive strength, compressive ductility, tensile strength, and fracture toughness of pure Al RM. Kline and Hooper consolidated 3.5 µm Al powder using the CIP process into 10 mm cylindrical specimens with a porosity of 6.3%. Two separate annealing treatments of 15 minutes and 30 minutes at 200 $^{\circ}C$ were applied and the material response of the annealed specimens was compared to the response of the non-annealed specimens.

Kline and Hooper observed non-annealed specimens failing at nominally 210 MPa at 2.5% strain and the annealed specimens failing at nominally 230 MPa at up to 12% strain, a significant increase in ductility under compressive dynamic loading[11]. No detectable difference was reported in compressive strength or work hardening between the 15 and 30 minute annealing times. Dynamic Brazilian disk tests were also performed using the Kolsky bar, and the annealing treatment was found to increase the tensile strength under dynamic loading of the specimens from 25 MPa for the unannealed condition to 60 MPa for the 30 minute annealed condition. Fracture toughness measurements were made in accordance with the ASTME 399 standard using three-point bend tests. A fracture toughness of 0.5 $MPa{\cdot}m^{1/2}$ was measured for the unannealed specimen, and annealing for 30 minutes increased the fracture toughness of the material to 1.75 $MPa{\cdot}m^{1/2}$, a 250% increase in toughness[11]. For comparison, the fracture toughness of 6061 Al is reported to be between 18 $MPa{\cdot}m^{1/2}$[50] and 33 $MPa{\cdot}m^{1/2}$[16]. Values of fracture toughness measured by Kline andHooper[11] are more typically asso-

ciated with brittle materials such as ceramics, and similar values have been observed with other RM systems[12, 27].

Kline and Hooper[11] studied the microstructure of the specimens and did not observe sintering or discernible change in grain structure of the Al compacts due to the annealing process. Kline and Hooper proposed that the differences in material response were a result of dislocation recovery reducing the residual stress within existing grains imparted by the CIP process, thus enhancing the materials ductility[11]. These results suggest that the residual stress state may be a strong influencing factor on the final material response of RMs consolidated through dry powder compaction processes.

Efforts in literature predominately utilize Kolsky bar tests for measurements of the material response of RM systems. However, Kolsky bar testing is also well suited to the study of the fracture process of materials[42, 51]. Recently, the application of Kolsky bar tests has been extended to the study of the fragmentation of RM through quantitative measurements of the size distributions of fragments[13, 15].

Hargather et al.[15] studied the Al/W RM system comprised of constituents powders less than 44 μm in size. The composition was pressed uniaxially into 6.35mm cylinders with a length to diameter ratio (L/D) of unity. Porosity was not reported. Three different compositions were evaluated with the following mass ratios: 4.5%Al/95.5%W, 12.5%Al/87.5%W, and 30%Al/70%W. The volume fractions of the compositions are: 25.3%Al/74.7%W, 50.5%Al/49.5%W, and 75.6%Al/24.4%W. Specimens were subjected to a strain rate of nominally 2000 s^{-1}, and improved ductility with increasing Al content was observed. At a volume fraction of 75.6% Al, the specimen was found to resist failure and remain intact. For the two compositions that fragmented, size distributions of the fragments were measured. A decrease in fine fragment production was observed for the 12.5%Al/87.5%W by mass (50.5%Al/49.5%W by volume) system, the more ductile of the two compositions that fragmented. This methodology introduced by Hargather et al.[15] provides a means to quantitatively characterize the fragmentation of RM systems subjected to a well characterized loading rate. This reduces error associated with assumptions of loading, as is the case with high velocity impact and explosively driven experiments[13].

1.3.2 Dynamic response and fragmentation of RMs under impact conditions

Use of RMs in ballistic type applications necessitates the validation of anticipated performance. This is accomplished by simulating the impact environment and associated loading conditions through high velocity impact of RM specimens launched from gas guns[5, 11, 12] or powder driven guns[4, 13, 27]. In these studies, specimens may be fired at thin metal plates to trigger the fragmentation of the specimen, or fired directly into an anvil. Varying the thickness and density of thin

metal plates, commonly steel or Al, provides an additional means to tune the applied strain rate separately from varying impact velocity[12]. Impact velocities in these studies are typically between 0.3 km/s and 2 km/s.

High velocity impact studies are predominately led by Hooper and coworkers[11, 12, 27], with contributions by Thuot et al.[5]. These efforts have focused on measuring the distributions of fragments as a result of dynamic failure of RM projectiles. Published work by both groups has been limited to single constituent consolidated powder RMs. Hooper[4, 27] investigated the fragmentation of Al projectiles manufactured by CIP of 3.2 µm Al powder into cylinders from which 25.1 mm diameter spheres were cut. Final porosity of the Al specimens was 15%. These specimens were launched using a 42 mm smooth-bore powder gun through three thicknesses of steel plates: 0.912 mm, 1.52 mm, and 3.04 mm. Fragmentation under the following impact velocities was investigated: 610 m/s, 1220 m/s, and 1829 m/s. Fragments produced from the impact were caught using a tube filled with low density shaving cream and fragment size distributions measured. Hooper reported that at least 90% of the collected fragment mass consisted of particles 44 µm in size or larger.

Kline and Hooper[11] extended previous work by Hooper[4, 27] by investigating the effects of annealing on the fragmentation behavior of Al RM. Instead of spheres, Kline and Hooper[11] investigated cylinders manufactured by CIP of 3.5 µm Al powder into 10 mm diameter by 10 mm long cylindrical specimens with a porosity of 6.3%. Annealing treatments were the same as those applied for their Kolsky experiments discussed previously: 15 and 30 minutes at 200 $^{\circ}C$. The cylindrical specimens were launched through a 1.62 mm thick 2024 Al plate at a velocity of 607 m/s and separately launched directly into an anvil at 585 m/s[11]. Produced fragments were caught using a tube filled with artificial snow and fragment size distributions measured.

Tang and Hooper[12] studied zinc RM using a similar experimental methodology. Tang and Hooper manufactured 10 mm diameter by 10 mm long cylinders from $<$10 µm zinc powder with a porosity of 4.75% using the CIP process. These specimens were then annealed for four hours at 336$^{\circ}C$ to improve ductility, and negligible sintering or mass diffusion between particles was observed. The cylindrical specimens were launched through a 1.62 mm thick 7075 Al plate at six velocities: 386 m/s, 459 m/s, 545 m/s, 600 m/s, 680 m/s, and 763 m/s[12]. Produced fragments were caught using a tube filled with artificial snow and fragment size distributions measured.

Thuot et al.[5] studied the fragmentation of Al 25.25 mm spheres manufactured by CIP of 6.8 µm Al powder with a porosity of 15.5%. The projectiles were launched using a 41.2 mm powder driven gas gun through a 1.59 mm thick steel impact plate at three velocities: 610 m/s, 1220 m/s, 1830 m/s. The generated fragments from impact and perforation of the steel plate were caught using a tube filled with low density shaving cream and fragment size distributions measured.

The fragmentation behavior of RM in these studies[5, 11, 12, 27] is measured quantitatively through size distributions of the fragments. The statistics of these

distributions provide information on the bulk material response that is useful for design and application purposes[13], and indirect understanding of the actual mechanism of fracture[27]. Dynamic fracture events of ductile materials, such as metals, typically generate fragment distributions that are best characterized by an exponential function with a characteristic length or mass scale[27]. Exponential forms of these distributions are generally considered to be governed by Poisson statistics associated with the uncorrelated nucleation of cracks or failure points[27, 52, 53]. The exponential distribution derived by Mott and Linfoot[54] is widely used in literature[4], and takes the following general form[54, 55]:

$$N_d(m_f) = \frac{1}{3m_f}\left(\frac{m_f}{\mu_c}\right)^{\frac{1}{3}} \exp\left(-\left(\frac{m_f}{\mu_c}\right)^{\frac{1}{3}}\right) \tag{1.2}$$

Here the general Mott form represents the number of fragments distributed by mass, $N_d(m)$, as a function of fragment mass, m_f, and the characteristic length scale, μ_c, associated with the primary crack nucleation. Other distribution forms are discussed in detail by Grady[52, 53] and Elek and Jaramaz[56].

RMs manufactured through the consolidation of powder constituents have been found to regularly behave as a brittle material under high-rate dynamic loading[11, 12, 27, 40]. Dynamic fracture events of brittle materials typically generate fragment distributions that are best characterized by a power-law relation[12, 27, 57]. Recently, the general power law form proposed by Astrom et al.[57] has found use in RM research efforts, and takes the form[27, 57]:

$$N_d(\forall) \propto \forall^{-k_s} f(\beta\forall) \tag{1.3}$$

Here the general form by Astrom et al.[57] represents the number of fragments distributed by volume, $N_d(\forall)$, as a function of the volume raised to a scaling exponent, k_s. A damping function, $f(\beta\forall)$ is included to cut off the power-law behavior beyond a length scale governed by β. The scaling exponent of the power law distribution has been found to exhibit certain aspects of scale-invariance[58], and is often treated as a fractal with a particular dimensionality[27]. Observations in literature have found the scaling exponent to be insensitive to the material or directionality of loading, and strongly dependent on the dimensionality of the object loaded to failure[57, 58]. Work by Astrom et al.[57] and Oddershede et al.[58] suggests universality of the scaling exponent may exist.

Hooper[27] proposed that the fragmentation process of RM under high-velocity impact loading can be well described using a combined exponential and power-law form. This was based on observations from mass-size probability distributions measured for varied impact velocities against 1.52 mm and 0.912 mm thick target plates. Hooper found that the distribution behavior was similar for impacts against both plate thickness[4, 27]. Hooper observed for the lowest velocity impact that a distinct maximum in the fragment distribution existed and demonstrated both exponential and power-law type behavior[27]. With increasing impact velocity, the distribution became dominated by power-law behavior.

Hooper[27] proposed a theoretical fit for the distribution of small fragments using the general form of the power-law presented by Astrom et al. (Equation 1.3)[57] . Hooper chose an exponential damping function for $f(\beta\Psi)$, which is consistent with work by Oddershede et al.[58], assumed a size-independent aspect ratio of unity, and recast the equation into a distribution of the number of fragments over linear fragment size, s. The restructured power-law equation is[27]:

$$N_d(s) \propto s^{\Psi-(\Psi k_s+1)} exp(-(\beta s)^{\Psi}) \tag{1.4}$$

Here, Ψ is the dimensionality of the fragmenting object. Hooper[27] used $\Psi = 3$ as proposed by Astrom et al.[57] for experimental results.

Experimental challenges exist in measuring the distribution of fragments over a linear size when a large number of small fragments are present. For the two highest velocity impacts, the majority of the fragment mass measured was well below 1 mm and Hooper did not find counting fragments in this size range to be experimentally viable[27]. Instead, Hooper converted the fragment distribution to mass distributed over s, to form[27]:

$$m_d(s) = \frac{1}{s_o}\left(\frac{s}{s_o}\right)^{-\Lambda} \frac{exp(-(\beta s)^{\Psi})}{f_{exp}(\beta s_o)} \tag{1.5}$$

$$where: \Lambda = (2\Psi - (\Psi k_s + 1)) \tag{1.6}$$

This conversion introduces a dependency on the minimum fragment size, s_o, and the generalized exponential integral function, $f_{exp}(x)$[27]. As before, the power-law behavior is controlled by the constant β. Here s_o is equal to 44 um, the smallest sieve size used by Hooper[27].

Hooper[27] describes the distribution of large fragments using the general exponential form proposed by Mott and Linfoot[54] and given by Equation 1.2. Again, Hooper[27] restructured Equation 1.2 to represent a mass distribution over a linear length scale assuming a three-dimensional (3D) fragmentation event, which takes the form[27]:

$$m_d(s) = \frac{1}{6\mu_c}\left(\frac{s}{\mu_c}\right)^3 exp(-s/\mu_c) \tag{1.7}$$

Equations 1.5 and 1.7 are combined with a weighting factor, Π, that controls the influence of each distribution form. It is expected that Π is velocity and thus strain rate dependent[12, 27]. In order to account for the affects of microbranching and damage regions near the crack surface that are suspected of driving fine fragment production, Hooper reduced the size of the fragments in the exponential distribution by $2/\beta$[27]. The final general form of the distribution proposed by Hooper is:

$$m_d(s) = \Pi \frac{1}{s_o} \left(\frac{s}{s_o} \right)^{-\Lambda} \frac{exp(-(\beta s)^{\Psi})}{f_{exp}(\beta s_o)} + (1-\Pi) \frac{1}{6\mu_c} \left(\frac{s+2/\beta}{\mu_c} \right)^3 exp\left[- \left(\frac{s+2/\beta}{\mu_c} \right) \right] \quad (1.8)$$

Hooper[27] proposed that a universal value of $k_s = 5/3$ used in literature should apply[57, 58], and evaluated this for the lowest speed impact of 610 m/s where both power-law and exponential behavior was observed. This leads to $\Lambda = 0$, and the general form of the distribution for the low speed case reduces to:

$$m_d(s) = \Pi \beta exp(-\beta(s - s_o)) + (1-\Pi) \frac{1}{6\mu_c} \left(\frac{s+2/\beta}{\mu_c} \right)^3 exp\left[- \left(\frac{s+2/\beta}{\mu_c} \right) \right] \quad (1.9)$$

Hooper[27] fit the proposed distribution forms to the raw fragment size data using a standard least-squares fit governed by the Levenberg-Marquardt algorithm. Fitted parameters are: the scaling parameter k_s, the power-law length scale, β, the weighting parameter, Π, and the exponential characteristic length, μ_c. For the high velocity impacts, Π takes a value of unity as the distribution adheres purely to a power-law behavior. Hooper[27] found that for the high speed cases $k_s \approx 5/3$, affirming the potential for a universal scaling parameter and the choice by Hooper to reduce the distribution form for the low speed case. The invariance in the power law scaling parameter aligns with observations by Oddershede et al. and Astrom et al.[57, 58]. This further reinforces the possibility of universality of the scaling parameter for a given spatial scale.

Fragment size distribution forms by Hooper[27] have been extended to other RM systems[11, 12]. Using a similar methodology, Kline and Hooper[11] applied the reduced distribution proposed by Hooper[27] to thin plate and anvil impact tests with Al RM. Equation 1.9 was found to fit the measured fragment distributions for both test scenarios and all annealing conditions[11]. Tang and Hooper observed a bi-model exponential distribution of their zinc fragments[12], aligning with observations by Hooper for low speed impacts[27]. To fit the data, a bi-model form of the Mott exponential distribution used by Hooper[27] was proposed[12], and is:

$$m_d(s) = \Pi \frac{1}{6\mu_{c,1}} \left(\frac{s}{\mu_{c,1}} \right)^3 exp\left[- \left(\frac{s}{\mu_{c,1}} \right) \right] + (1-\Pi) \frac{1}{6\mu_{c,2}} \left(\frac{s}{\mu_{c,2}} \right)^3 exp\left[- \left(\frac{s}{\mu_{c,2}} \right) \right] \quad (1.10)$$

Here, $m_f(s)$, is a function of s, the two size scales of the distribution, $\mu_{c,1}$ and $\mu_{c,2}$, and Π, that is expected to be velocity/strain-rate dependent as observed in earlier work by Hooper[4, 27]. Comparison of the bi-model fit to the measured fragment sizes with the largest fragment removed showed reasonable agreement[59].

Thuot et al.[5] observed an exponential/power-law distribution of fragment sizes, similar to the low velocity distributions observed by Hooper[27], for Al spheres launched through a 1.59 mm thick steel impact plates at three velocities: 610 m/s, 1220 m/s, 1830 m/s [5]. These results suggests the specimen behaved more ductile during failure, in contrast to the pure power-law behavior associated with brittle materials observed by Hooper at similar velocities for Al RM[27]. Before drawing conclusions between these results, it will be noted, that Thuot et al.[5] and Hooper and coworkers[11, 12, 27] report data for single test cases, and did not consider statistical significance or reproducibility of results. Observed difference may be associated with statistical variation inherent with experimental testing. However, the trends reported by the authors are consistent for multiple testing conditions. Therefore, it will be assumed that the reported material behavior, and therefore behavior difference, is valid for both authors. The only significant difference between Thuot et al.[5] and Hooper[27] is particle size of the Al powder, with Thuot et al. and Hooper using 6.8 µm and 3.2 µm Al powder, respectively. The difference in results suggests particle size may be the influencing factor. This aligns with observations in literature using Kolsky bar tests[16, 37, 38, 40], and suggests observations made using Kolsky bar tests are potentially extendable to higher strain rate applications.

Work by Hooper and coworkers[2, 12, 27] affirm that the distribution of fragments for a variety of RM may be represented by exponential forms, power-law forms, or combination of the two. Their work defined mathematical forms representing these distributions based on material response and applied loading[11, 12, 27]. These distributions are important tools in developing the predictive capability of RM fragmentation, and while the distributions were formulated for single component RM, it is expected the developed theory should apply to multi-component RM and validation of this is needed. Unfortunately, determination of the fit parameters have largely been an empirical process[4, 11, 27], restricting predictive capability of RM fragmentation.

Several strides in predicting parameters of the proposed distributions have been made. Tang and Hooper[12] have developed analytical models for estimating strain rate during impact and velocity dependent weighting factors for the distribution fits. They have also shown an energy-balance model of fragmentation can be used to predict the characteristic length scale for both exponential and power-law forms (μ_c and β, respectively). Their work applied the traditional Grady model of fragmentation[60–62].

The equilibrium energy balance approach to fragmentation first proposed by Grady[60] assumes the fracture process of a material is driven by the forces associated with the local kinetic energy in the material imparted by the high-strain rate loading process, representative of the intensity of expansion of the body, and resisted by the surface energy of the material[60]. An estimate of the characteristic

fragment size was initially found through the determination of the equilibrium state associated with the material surface energy, generated fracture surface area, and the kinetic energy imparted to the material by the high-strain rate loading process[60]. Glenn and Chudnovsky[63] suggested the stored elastic (strain) energy in this process cannot be neglected and proposed a modified form of the Grady equation[63, 64]. Later forms of the model proposed by Grady claim to account for the energy stored elastically in the material during loading[61, 62]. However, the assumptions and methods applied in accounting for the elastic strain energy are highly suspect. Hooper and coworkers[11, 12] have found the later form of the Grady model to provide good agreement, which will be the form discussed in this section for consistency with prior literature. The later form of the Grady model takes the form[55, 61]:

$$\lambda = \left(\frac{\sqrt{24} K_f}{\rho C \dot{\varepsilon}} \right)^{\frac{2}{3}} \tag{1.11}$$

This model provides the means to estimate the nominal fragment size, λ, as a $2/3$ power-law function of the applied strain rate, $\dot{\varepsilon}$ and measurable material properties to include the dynamic initiation fracture toughness of the material, K_f, the density of the material, ρ, and wave speed of the material, C. Grady has stated, based on observations of a wide range of materials, that agreement of the model should be within 25% of experimental results[61]. It is recommended to approximate the dynamic initiation fracture toughness, K_f using the Mode-I static fracture toughness, K_{IC}, of the material[27, 60, 61]. Measurements of static and dynamic initiation fracture toughness of zinc RM by Tang and Hooper[12] support this approximation for RM. The bulk wave speed, C_b, is regularly used in literature for C[11, 12, 27, 61]. However, in the initial derivation of the model[60], C is the bar wave speed of the material, C_o, based on the assumption of one-dimensional (1D) elastic behavior[60]. The use of both wave speeds are common in literature, with Grady finding good agreement using both[60, 61]. A detailed discussion of the derivation, application, and suspected errors of the energy balance model proposed by Grady is presented in Chapter 2.

The Grady model has been shown to be appropriate for a wide range of materials, including heterogeneous and granular materials[60]. A comparison of theoretical predictions using the Grady model to experimentally determined characteristic fragment sizes of different heterogeneous, granular materials studied by three different authors are presented in Figure 1.1.

It is evident from Figure 1.1 that the application of the Grady model is reasonably well suited to heterogeneous, granular materials such as RM. Grady observed good agreement with fragmentation experiments of oil shale using the dilatational wave speed and other appropriate parameters of the material[60]. Thuot et al.[5] also observed good agreement of the Grady model with fragmentation results of Al spheres using the dilatational wave speed. Tang and Hooper[12] utilized the bulk wave speed of their zinc materials, and found good agreement

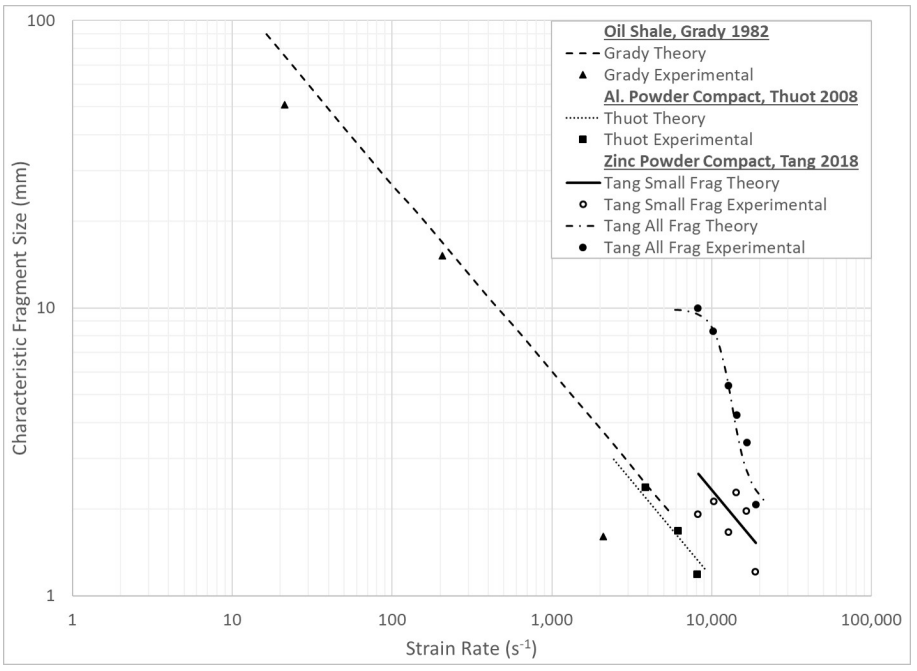

Figure 1.1: Log-Log plot of experimentally determined characteristic fragment size from literature[5, 12, 60] in relation to applied strain rate. Theoretical predictions of characteristic fragment size calculated using the Grady model are represented by lines.

of the Grady model to their fragmentation results when calculating the characteristic fragment size as a weighted function of size peaks in the distribution.

For fragment distributions with multiple characteristic features, it is important to appropriately weight the features of the distribution in determining the characteristic fragment size. For Tang and Hooper[12], three characteristic features were observed in their distribution: two fragment size peaks in the mass size distribution of small fragments and one large fragment. Direct comparison of the Grady model to the average of the two characteristic peaks of the distributions showed acceptable agreement within $\sim$25%. The experimental results are denoted as "Small Frag" and Grady model results as "Small Frag Theory" in Figure 1.1. However, significant improvement was obtained when the experimental characteristic fragment size was calculated by mass weighting the contributions of the two fragment size peaks and large fragment[12]. The theoretical characteristic fragment size was calculated in a similar manner, using the Grady model to represent the small fragments produced and determination of weighting based on developed analytical models[12]. These experimental results are denoted as "All Frag" and theoretical results as "All Frag Theory" in Figure 1.1.

Efforts by Hooper and coworkers have provided distribution forms that can be used to quantify the fragment distributions of RMs subjected to high velocity impacts[11, 12, 27]. Efforts have shown how to estimate variables required by the

distributions using measurable material properties, providing the first steps in developing the means to predict RM fragmentation. Characteristic length scales have been found to be well approximated using the Grady energy-balance model of fragmentation[5, 12], and a number of distribution variables determined to be near constant[4, 27], aligning with well established literature values[57, 58]. If the required material properties are known, the distribution methodology proposed by Hooper[27] appears to be capable of predicting the fragment distribution of RM systems[12]. Therefore, to obtain a unifying theory to fully predict RM fragmentation, it is necessary to first be able to predict the bulk material properties used in these distributions and supporting analytical models.

1.3.3 Dynamic response and fragmentation of RMs under explosive loading conditions

Application interest for RM systems in warheads is as an alternative casing material designed to enhance blast effects through immediate combustion post-detonation[1, 65], or enhance energy on target through the impact and combustion of generated fragments[2, 3, 65]. It is common in literature efforts studying RM systems for warhead casings to refer to the materials as structural reactive materials (SRM)[2]. These materials are studied using expanding ring experiments[16, 34], small scale warhead tests[1, 2], or the explosive launching of individual fragments[13, 15].

Expanding ring experiments, also called expanding ring tests (ERT), are an established experimental tool for studying the dynamic constitutive and failure behavior of materials at strain rates of 10^4 s^{-1}[66]. In these experiments, a thin ring of material is driven, generally by an explosive charge at its center, into a state of uniform radial expansion[16, 66]. The radial expansion velocity is typically measured using a Velocity Interferometer System for Any Reflector (VISAR)[59, 66] or Photon Doppler Velocimetry (PDV)[16] system. From the velocity measurement with respect to time, the deceleration can be calculated and through the equations of motion the magnitude of stress, strain, and strain rate can be determined[59, 66]. The shock wave effects on the accuracy of measured properties have been found to be minimal for homogeneous materials[66]. In addition to measurements of stress and strain, fragments can be collected for fragment size distribution analysis[59].

Nesterenko et al.[16] studied the fragmentation behavior of Al/W RM and investigated the mesoscale effects due to explosive loading using expanding ring experiments. The evaluated RM system consisted of Al particles between 4.5 µm and 7 µm and tungsten particles less than 44 µm in size. This composition was consolidated using the CIP process into rings with an outer diameter of 19.15 mm, inner diameter of 12.19 mm, and porosity of 10.3%. The RM ring was driven to failure using an explosive charge and measurements of the expansion velocity were made using a PDV system. Resultant strain rate was measured to be

$2 \cdot 10^4$ s^{-1}, and characteristic fragment size was on the order of 100 µm. SEM analysis of the fragments revealed fusing of of the Al particles, which was consistent with observations made through numerical analysis of the Al/W RM response to shock loading[16].

Interestingly, the characteristic fragment size measured was reported to be an order of magnitude smaller than calculated using the Grady fragmentation model (Equation 1.11), and the conclusion was the particle spacing was driving the fragmentation behavior instead of the bulk response[16]. However, Nesterenko et al.[16] acknowledged that the material properties associated with homogeneous 6061 Al alloy were used to approximate the fracture toughness of the Al/W RM, calling into question the validity of their conclusion. As previously discussed, granular RM regularly have fracture toughnesses that can be one to two orders of magnitude less than those of their constituent particles[11, 12, 27]. Thus the order of magnitude difference in characteristic fragment size observed by Nesterenko et al.[16] could solely be related to difference in the fracture toughnesses used and the actual fracture toughness of the RM material. The erroneous use of the fracture toughness of a homogoenous material to approximate those of the Al/W RM for use in the Grady fragmentation model reinforces the importance of using experimentally determined or correctly approximated material properties in existing models.

Small-scale warhead tests are similar in process to expanding ring experiments, but are designed to study blast effects[1, 3] and fragment production[1, 2]. Unsurprisingly, published experimental work is limited in the testing of small-scale RM warheads, and this work does not measure the strain rate applied to the case during the explosive loading event. Wilson et al.[1] studied the blast effects of two RM systems (composition not reported) in comparison to pure Al RM and Zhang et al.[3] studied the blast effects of aluminum and molybdenum oxide (Al/MoO_3) RM in comparison to pure Al RM. Both authors used the HIP process to consolidate their respective RM systems into cylindrical cases 43.6 mm in diameter with an inner diameter of 33.5 mm. 100 g of C-4 explosive was used to drive the case to failure inside a blast chamber instrumented with pressure transducers and high speed cameras. Wilson et al.[1] caught the fragments produced from the case for some tests using a snow soft catch and measured the fragment size distributions.

When compared to the results of the Al only RM casing, Wilson et al.[1] found a significant increase in the pressure of the primary blast front as a result of the combustion of fine fragments produced from the initial case failure. Subsequently, an increase in the reflected blast front pressure was observed, associated with the impact of larger fragments with the chamber walls that led to production of additional fine fragments and combustion. Wilson et al. noted that the final overpressure was similar for all three systems, suggesting that the total energy contribution of the RM casing to the system was small compared to that of the C-4 explosive, but the production of fine fragments due to the initial case failure and later impact with the chamber walls could enhance local blast front pressures[1]. Zhang et al.[3] noted similar results for the two systems evaluated,

but found that the smaller production of fragments decreased the enhancement effect. Results by Wilson et al.[1] and Zhang et al.[3] suggests fragment size is a limiting factor in the final energy release of the material, such that only fragments below a minimum size combust and contribute to the total energy release.

Kotei[2] used small-scale warhead case tests and high velocity impact tests to study the difference in fragmentation of Al only RM systems. Using a blast chamber and snow soft catch similar to Wilson et al.[1], Kotei drove RM cases of 44.45mm in outer diameter, with inner diameter of 38.1 mm, to failure using 95% nitromethane sensitized with 5% ethylenediamine as the explosive charge. Separately, Kotei fired 10 mm diameter RM cylinders, 10 mm in length, at 550 m/s and 620 m/s through Al plates of unspecified thickness. All RM specimens had 5% porosity and were consolidated using the CIP process.

Kotei observed a higher production of fine fragments from the explosive driving of the SRM case to failure compared to fragment production by high velocity impact. For explosive loading of the casing to failure, 80% of the total mass of fragments was less than 2 mm in diameter, and 60% of the total mass of fragments was less than 1 mm in diameter. For failure driven by high velocity impact at 620 m/s, the highest strain rate impact case, 40% of the total mass of fragments were less than 2 mm and 25% less than 1 mm[2]. No strain rate for the high velocity impact testing was reported by Kotei, but based on similar work by Tang and Hooper[12], it is expected the projectiles were subjected to strain rates on the order of $10^4 s^{-1}$, similar to those expected for the explosive loading of a warhead case[16, 66]. The results by Kotei[2] suggest the differences in the application of loading between the explosive (tensile loading) and high velocity impact (compressive loading) events are influencing the fragmentation behavior, with possible influence from changes in the mesoscale structure of the bulk material due to shock loading as observed by Nesterenko et al.[16].

More recently, a new test methodology for studying the effects of explosive loading has been introduced by Hargather et al.[15]. Instead of driving a RM warhead casing to failure to study the fragmentation behavior, Hargather et al. "launched" and fragmented specimens using a small explosive charge inside a shock tube[15]. The subsequent fragments travel down the axis of the shock tube which has optical access ports for high speed schlieren imaging systems. Fragment size distributions are measured from the fragment area projected onto calibrated image sensors[13, 15], similar to methods used by Grady and Kipp[62] in analyzing data from radiographic images of fragmentation events.

Hargather et al.[15] applied their explosive launch methodology to three Al/W composition variations previously evaluated using Kolsky bar tests. The specimen geometry was the same as used in Kolsky testing for continuity. The fragmentation behavior observed under explosive loading was found to be qualitatively similar[15]. The more brittle of the compositions (4.5%Al/95.5%W by mass, 25.2%Al/74.7%W by volume) failed into a large number of small fragments. Conversely, the more ductile of the compositions failed into a small number of large fragments, with the 12.5%Al/87.5%W by mass system (50.5%Al/49.5%W by volume) failing into two primary fragments, and the

30%Al/70%W by mass system (75.6%Al/24.4%W by volume) failing into one fragment. Unfortunately, discussion of results were limited to qualitative observations and no fragment size distributions of the explosive tests were reported.

1.4 Reactive material energy release behavior and theory

The energy release characteristics of RM systems are critical aspects of designing RM systemsn[14, 67]. When RMs ignite, the combustion process releases stored chemical energy. Understanding the theoretical and actual energy release capability[6, 67–70], mechanisms that govern this combustion process[7, 71, 72], mesoscale influences on the combustion process[7, 10, 33, 73], and mechanisms that initiate the combustion process[8, 65] are primary areas of research. Research efforts describe evaluated compositions differently, and may use terms such as RM systems, thermites, and energetic materials. For discussions here, these terms will be treated as synonymous as all can be classified as RMs.

Knowledge of energy output from the combustion of an RM system is one of the fundamental components of application design of RM systems, and is studied under ideal conditions and with application-analogous experiments. Combustion under ideal conditions provides an understanding of maximum energy release potential of an RM system, and is studied theoretically[6, 67, 69] and experimentally[10, 69, 73, 74]. However, review of prior research and comparison of results between research efforts reveals persistent issues of disagreement between theoretical predictions and experimental measurements of adiabatic flame temperature (product species temperature), energy release, and product species.

Application-analogous experiments aim to develop an understanding of the energy release of RM systems against different targets and under varied loading conditions[1, 68, 70, 75]. Unfortunately, without a clear understanding of the maximum energy release potential of a RM system, it is impossible to assess the efficiency of RM combustion under application-analogous conditions. As a result, definite identification of combustion inefficiencies cannot be made. Combustion of RM systems is known to be limited by the quantity of fine particles produced[1, 7], and research efforts continue to work towards the relationship total energy release has to the size distribution of fragments produced[1, 16]. Unfortunately, a unifying theory has yet to be published. An understanding of the maximum energy release of an RM system under ideal conditions is a critical component of understanding the energy release behavior of an RM system in application and the role fragmentation behavior has on energy release behavior.

1.4.1 Experimental methods for measuring energy release of RMs

The combustion process of RM is primarily characterized by experimental measurements of energy release[68, 69, 73, 76], temperature of the combustion

event (temperature of products)[75, 77], and product species[71, 78]. Energy release is studied under ideal conditions using variations of bomb calorimetry[10, 73, 74, 79] and digital scanning calorimetry[76], and in application using vented calorimeters[68, 69]. Temperatures of RM combustion under impact conditions using high speed imaging pyrometers have been demonstrated by Densmore et al.[75, 77] as a viable technique, but the technique has not found adoption elsewhere in published RM literature. Product species of combustion under ideal conditions are measured in real time using using mass spectrometry[71, 78]. Condensed product species from these reactions are typically analyzed after combustion using X-ray diffraction techniques[71, 76, 78, 80].

Bomb calorimetry measures the total energy released by a combustion process under constant volume conditions[81, 82]. This is a closed process as mass exchange between the environment and the sealed container, generally called a combustion bomb, does not occur. In traditional bomb calorimetry, energy output is determined by measurements of the temperature rise of the bomb and a working fluid surrounding the bomb, such as water[10]. If the combined specific heat of the bomb and working fluid are known, the temperature differential induced by the combustion event can be used to determine the change in internal energy of the bomb, and thus the total energy input into the bomb from the combustion process. The measured energy output is often referred to as the heat of combustion or heat of reaction of the material, and unless stated otherwise the terms energy release and heat of combustion are treated as synonymous here. Parameters under which combustion takes place can be well controlled and characterized, allowing ideal combustion conditions and near complete combustion of samples to be obtained[82].

Typically, bomb calorimetry is used to measure the energy release of a fuel in an oxidizing environment[81, 82], most commonly oxygen, air, and in limited cases flourine gas[79, 83]. The material of interest is placed in the bomb under the chosen gas environment and ignited using a nichrome wire. The gas environment is held at high pressure to minimize the pressure rise from product gases of the reaction and heating of the gas, approximating a constant pressure environment, and also to drive the reaction fully to completion[10, 81, 82]. For RM systems that contain constituents that act as oxidizers in the reaction (e.g. MoO_3, PTFE, etc), assessment of the energy release from only the composition is best performed using an inert atmosphere[84]. Argon is most prevalent in literature[72, 73], though in some instances nitrogen at low pressure has been used[85]. Tests using pure oxygen environments have been performed and are appropriate for RM systems that rely on atmospheric oxygen for combustion[10]. Traditional bomb calorimetry techniques have been used by several authors to study the energy release of RM systems, to include aluminum/iron oxide (Al/Fe_2O_3)[73], aluminum/titanium dioxide/iron oxide ($Al/TiO_2/Fe_2O_3$)[85], and Al/PTFE[79].

Alternatively, energy output can be determined by pressure measurements of the interior of the combustion bomb[69]. The pressure rise inside the bomb corresponds to the energy transfer from the combustion process to the gas environment inside. This method requires several assumptions of the gas properties

inside the bomb, low pressure gas environment at the start of the combustion process, and does not account for the heat loss to the bomb itself. Uncertainty analysis by Perry et al.[69] showed errors are typically less then 5% using the method, largely due to rate differences between the energy flow to the gas and the bomb body and pressure data acquisition on timescales on the order of the combustion event[69]. This methodology has been used with varying degrees of success in studying RM energy release, to include aluminum/tungsten oxide (Al/WO_3)[69], aluminum/hydrated tungsten oxide (Al/WO_3H_2O)[69], boron/titanium/tungsten (B/Ti/W)[80], and aluminum/copper oxide/PTFE (Al/CuO/PTFE)[33].

Application specific energy release of RM systems is typically studied under impact loading using a vented calorimeter, first reported on by Ames[68]. In using the vented calorimeter, an RM specimen is launched using a gas or powder gun system through a thin plate sealing a port on the calorimeter chamber and into an anvil inside the chamber to trigger ignition of the bulk material and fragments. The pressure inside the chamber is measured, and from the total change in the quasistatic pressure the energy release of the specimen can be calculated[68], similar to pressure based methods for bomb calorimetry[69]. Uncertainty analysis by Ames[68] showed that effects of mass loss through the hole in the perforated plate were negligible as a result of choked flow at the hole and the short duration of the combustion event.

Vented calorimetry is often adopted to permit optical diagnostics to be used to study the combustion event, and has been used in the attempted assessment of combustion efficiency[86], initiation criteria[70], and combustion behavior[68, 75] of RM systems. Zhang et al.[86] used vented calorimetry to study the energy release variation with impact velocity of tungsten zirconium (W/Zr) and Al/PTFE RM. Estimates of combustion efficiency were presented based on theoretical predictions, and ranged from 13% at an impact velocity of 750 m/s to 42% at an impact velocities of 1335 m/s for the W/Zr system. For the Al/PTFE system, reported combustion efficiencies ranged from 7% for an impact velocity of 850m/s to 86% for an impact velocity of 1200 m/s. Zhang et al. observed increasing energy release with increasing impact velocity, supporting the concept of increasing combustion efficiency and extent of reaction with increasing impact velocity[86]. Luo et al.[70] also studied the W/Zr system using a vented calorimeter. Similar to Zhang et al.[86], Luo et al.[70] observed increasing energy release with increasing impact velocity and identified critical limits for combustion to occur.

Densmore et al.[75, 77] studied the Al/PTFE and nickel/aluminum (Ni/Al) systems using vented calorimetry and high speed pyrometry. Peak combustion temperatures were found to be 3300 K for Al/PTFE impacted at 1675 m/s and and 3600 K for Ni/Al impacted at 1725 m/s, with the duration of combustion events on the order of tens of milliseconds. Similar to Zhang et al.[86], Densmore et al.[75] observed low combustion efficiencies for high velocity impact, with measured energy release 58% of that predicted for Ni/Al and 52% of that predicted for Al/PTFE by the thermo equilibrium solver CHEETAH[87].

Interestingly, Densmore et al.[75] and Zhang et al.[86] both evaluated similar

Al/PTFE compositions, but observed different combustion efficiencies. Densmore et al.[75] reported a 52% combustion efficiency for 26%Al/74%PTFE by mass at 1725m/s, while Zhang et al.[86] reported 86% combustion efficiency of 24%Al/76%PTFE by mass at 1200m/s. Results by Zhang et al[86] and Luo et al.[70] both showed increasing impact velocity should increase combustion efficiency, and as such it would be expected that Densmore et al.[75] would report a higher efficiency. These results suggest error exists in either measurement or theoretical predication of one or both of the authors. No discussion of the validity of theoretical predictions was provided by either of the authors, and thus the quantitative efficiencies reported are suspect. It is likely the noted differences are primarily related to the methods used to produce the theoretical predictions, as discussed in the subsequent section.

1.4.2 Theoretical methods for predicting the energy release of RMs

Modeling of the energy release of RM systems is generally approached in two conventional methods: Analytical solutions of idealized reactions with limited products [6, 69, 88] and thermochemical equilibrium solvers using a minimization of the Gibbs free energy of the mixture approach[67, 75, 89, 90]. The combustion process of RM systems is complex and characterized by high temperatures, leading to dissociated species[78, 91] and multiphase products[71, 76, 92]. Typically, complex reactions of this nature are best solved with thermochemical equilibrium solvers [67, 90, 92].

Work by Fischer and Grubelich[6] has been the fundamental baseline for the potential available energy release of stochiometric RM mixtures at STP conditions of 298 K and 0.1 MPa. Fischer and Grubelich assessed the theoretical reaction, adiabatic flame temperature, and energy release of metals with metal oxides (thermites), gaseous oxygen, and other metals (intermetallic reactions). Many of the investigated thermite and intermetallic reactions are of interest for potential RM applications. Fischer and Grubelich compared two analytical approaches of calculating energy release for stoichiometric compositions of thermite and intermetallic reactions[6]. The first approach (traditional) assumed only solid phase products formed, aligning with past analytical methodologies[88, 93]. The second approach (improved) considered the phase transition temperatures of the product species. Only two product species were considered for the thermite reactions, and only one product species was considered for the intermetallic reactions.

Fischer and Grubelich[6] identified erroneously high adiabatic flame temperatures, which corresponds to the theoretical product species temperature, when using the traditional analytical methodology of assuming solid phase products. Significant improvement of adiabatic flame temperature predictions where observed when phase transitions of the product species were considered[6]. The stoichiometric thermite reaction of Al/Fe_2O_3 ($2Al+Fe_2O_3$) demonstrates this improvement well. Here, the product species of the reaction are aluminum oxide

(Al_2O_3) and iron (Fe). Assuming the products exist only in a solid phase using the traditional method, the adiabatic flame temperature was calculated to be 4382 K. This answer is over 1000 K higher than the nominal 3000 K observed in literature for this composition[73]. In addition, the calculated temperature is over 1000 K higher than the boiling temperature of elemental iron, reported as 3139 K[94]. Using the traditional approach, the calculated adiabatic flame temperature not only deviates significantly from measured values as discussed by Fischer and Grubelich[6], it is a non-physical answer as solid phase iron cannot exist at the calculated temperature.

Alternatively, by considering phase transitions using the improved method, Fischer and Grubelich[6] report a temperature of 3135 K with liquid phase Al_2O_3 and liquid and gas phase iron present. This result is a significant improvement in alignment with experimental values of nominally 3000 K. It is noted that gas phase iron is present below the boiling temperature of 3139 K reported for iron[94], but the calculated result is accepted as physically possible and "phase compliant" as the difference of single degrees in temperature are attributed to differences in thermodynamic data sources or rounding errors.

Fischer and Grubelich[6] showed a significant improvement in adiabatic temperature predictions and demonstrated the concept of phase compliancy, but did not attempt to validate their calculated energy release results. This is likely due to lack of appropriate experimental data. Energy release measurements obtained through bomb calorimetry are good candidates for comparison to theoretical predictions. Unfortunately, caution must be exercised when utilizing existing published results as efforts in literature often react compositions in pure oxygen[74] or nitrogen[85] environments following traditional procedures[81, 82]. The high pressure oxygen environment can have a significant impact on the reaction paths and thermochemistry of the reaction, preventing a direct comparison to theoretical results by Fischer and Grubelich[6]. Similar effects can be expected for a nitrogen environment as at high temperatures, similar to those associated with RM reactions, reactions can take place with nitrogen.

Recent work allows comparison of analytical predictions to energy release predictions for two compositions: Al/Fe_2O_3[73] and Al/WO_3[69]. Sahoo et al.[73] studied the stochiometric composition of Al/Fe_2O_3 using a bomb calorimeter filled with argon at 0.5MPa[73]. Perry et al.[69] studied a range of Al/WO_3 compositions, including stochiometric, using a bomb calorimeter filled with air at atmospheric pressure (0.1 MPa)[69]. Analysis by Perry et al.[69] indicated the impact of air on the reaction at this low pressure was negligible for the experiments. Comparison of results by Sahoo et al.[73] and Perry et al.[69] to predictions by Fischer and Grubelich[6] are presented in Table 1.3.

Significant error is observed, with an over prediction in energy release of 42% for the Al/Fe_2O_3 composition and 153% for the Al/WO_3[69] composition by the improved phase compliant method used by Fischer and Grubelich[6]. Reported experimental results were consistent across multiple tests and varying mixture ratios for the respective compositions. Furthermore, measurement uncertainty

Table 1.3: Comparison of measured energy release of the stoichiometric mixtures of aluminum and iron oxide (Al/Fe_2O_3) and aluminum/tungsten oxide (Al/WO_3) to analytical predictions. Energy release is reported by total mass of composition

Composition	Measured Energy Release	Predicted Energy Release	Error
Units:	kJ/g	kJ/g	%
$2Al+Fe_2O_3$	2.78[73]	3.95[6]	42
$2Al+WO_3$	1.15[69]	2.91[6]	153

was reported as $\pm$ 17% by Perry et al.[69], but unreported by Sahoo et al.[73]. Considering the reported experimental error of Perry et al.[69], results by the authors suggests that the deviation between experimental and theory cannot be explained by experimental error alone. In addition, the observed error aligns with similar error observed by Perry et al.[69] using the thermochemical equilibrium solver CHEETAH[69]. The work by Fischer and Grubelich[6] demonstrates the critical nature of considering the phase state of product species in improving approximations, especially of adiabatic flame temperature, but deviations from experimental energy release results indicate additional improvement is warranted.

A limitation of work by Fischer and Grubelich[6] was the assumption of only two product species. This was necessary for simplification to permit analytical solutions to be find with out computational methods. However, experimental studies have shown that dissociated species are present in the reaction products of RM combustion[71, 78]. In order to consider these additional species from a theoretical stand point, it is necessary to use thermochemical equilibrium solvers.

Thermochemical equilibrium solvers primarily used in RM literature use a minimization of Gibbs free energy methodology[67, 69, 76]. The Gibbs free energy is a thermodynamic potential function derived through the second law of thermodynamics, and provides a measure of the useful work that can be obtained from a system at constant temperature and pressure. Chemical equilibrium of a system exists at the global minimum associated with the Gibbs function[95, 96]. Using thermodynamic data of considered product species, a computational routine finds the optimal set of product species that minimize the Gibbs free energy of the system for a prescribed state of the system. Thus, the quality of the solution is dependent upon the accuracy of the thermodynamic data used and proper consideration of potential product species.

Equilibrium solvers utilize three thermodynamic properties measured at

constant pressure for calculations: The specific heat capacity, C_P°, enthalpy, H°, and entropy, S°[97, 98]. The temperature dependencies of these properties are captured using polynomial parameterizations of experimental and theoretical data, most commonly in a power-law series of the form $\sum_{j=0}^{n} a_j T^j$[97]. Experimental and theoretical thermodynamic data generally originates from JANAF, NIST, and Russian thermochemical tables[97, 99]. Polynomials of condensed phase species (liquid or solid) are typically generated using fits to experimental data, with temperature bounds of the polynomials generally dictated by phase change temperatures of the species[99]. Polynomials of gas phase species are typically generated using fits to theoretical data generated using ideal gas law calculations[99]. Temperature bounds of gas phase polynomials are generally 300 K to 5000 K, an arbitrary choice of practicality for gas phase combustion calculations[97]. This is highly problematic as the ideal gas law calculations used to generate the gas phase thermodynamic data do not consider phase transition limitations. Unfortunately, the accuracy of utilized thermodynamic data is an enduring question, as no systematic investigation has been carried out to verify available data[97].

Due to available gas phase thermodynamic data failing to consider phase transition temperatures, it is possible for equilibrium solvers to calculate solutions that are not phase compliant, and thus non-real. Equilibrium solvers typically rely upon the temperature bounds of the polynomial forms of data for assessing if a species may be present in the products[98, 100]. Thus, if the temperature bounds of polynomial data used by equilibrium solvers are not verified to align with phase transitions temperatures, phase compliancy can not be guaranteed in solutions by the solvers. As shown by Fischer and Grubelich[6], phase compliancy of solutions is a critical requirement of predicting the combustion process of RM systems.

Efforts by Koch and coworkers[67, 89] are the most prolific work on multiphase combustion modeling of RM systems. Koch et al.[89] reviewed seven different equilibrium solvers for application in modeling solid phase reactions, all of which used minimization of Gibbs free energy routines. These seven solvers were: CERV, CHEETAH, EKVI, ICT, NASA CEA, REAL, and TANAKA. Of these codes, CHEETAH and NASA CEA[98] find wide-spread use in RM research[67, 69, 78]. Koch et al.[89] compared the predicted adiabatic flame temperature and product species from the evaluated solvers for six compositions with solid phase reactants at pressures from 0.01MPa to 10 MPa. Of interest to this work are the comparisons of predictions for aluminum and molybdenum oxide thermite (Al/MoO_3). For the Al/MoO_3 composition, adiabatic flame temperature predictions were within 10% for all pressure conditions for four of the solvers: CERV, EKVI, NASA CEA, and REAL. Significant deviation was observed for predicted product species, with best agreement obtained only at atmospheric pressure (0.1 MPa) where product species were found to agree within nominally 10% for NASA CEA and REAL solvers. Koch et al. did not address observed differences in predictions and did not verify thermodynamic data used by the solvers. Given all solvers used minimization of Gibbs free

energy routines, it is suspected variances or errors in thermodynamic data are the source of the deviations in results.

Subsequent work by Koch[67] used NASA CEA to evaluate a range of metal-fluorocarbon RM compositions. Koch provided adiabatic flame temperature and equilibrium compositions for the combustion of fourteen elemental metals with PTFE and discussed potential chemical reaction mechanisms. Unfortunately, Koch provided limited discussion of the validity of the results obtained by CEA. Koch did compare the adiabatic flame temperature of various magnesium compounds with PTFE at 0.1 MPa, and observed between 20% and 50% over-prediction by CEA[67], indicating significant deviation from experimental results were still present. Koch provided no discussion of verification of the polynomial data utilized by CEA for the evaluated composition.

Reviewing CEA predictions by Koch[67] of the adiabatic flame temperature and product compositions for the reaction of Al/PTFE thermite reveal deviations from experimental observations and non-physical product states. Comparison of the product species for the Al/PTFE composition consisting of 49% by mass of Al and 51% PTFE to experimental measurements by Zhang et al.[71] reveal several discrepancies. Zhang et al. used real time mass spectroscopy coupled to a differential scanning calorimeter with thermogravimetric analysis to study the reaction products of Al/PTFE at temperatures between 750 K and 1300 K. These temperatures are lower than the adiabatic flame temperature by design, as Zhang et al. purposefully cooled the product gases from the reaction to assess the species state change with temperature. For temperatures above 870 K, no free carbon was detected and the primary product species consisted of Al, AlF_3, and Al_4C_3[71]. In contrast, CEA predictions by Koch[67] showed Al_4C_3 did not form and primary products were AlF, AlF_2, AlF_3, and free carbon as graphite. Of the total moles of product species, graphite was reported as representing 25%[67]. Results by Koch are representative of the instantaneous products after reaction at the calculated adiabatic flame temperature of approximately 1900 K. Zhang et al.[71] measured the product species at 1300 K, and it is possible the dissociated species AlF and AlF_2 recombined into AlF_3 due to the lower temperatures. However, Al_4C_3 missing from the predictions, in contrast to the experimental results by Zhang et al., is cause for concern. Condensed Al_4C_3 is stable up to 2400 K[101] and therefore should be a viable reaction product at 1900 K.

The Al/PTFE results by Koch[67] also lack phase compliancy. The presence of gas phase Al was predicted for multiple Al/PTFE composition mixtures with product temperatures below the boiling point of Al of nominally 2800 K[94]. The temperature of the products is only above 2800 K for mixtures between 20% and 42% Al by mass. For mixtures with approximately 45% to 47% Al by mass, gas phase Al was predicted in the products by Koch[67]. This is a non-real possibility as the temperature of the products is below the boiling temperature of Al. This discrepancy was not addressed by Koch[67] and would indicate he did not review the thermodynamic data used by CEA to ensure phase compliancy.

Consideration of multiphase products[6, 90], phase compliancy[6], and multiple product species[67, 71, 76] are necessary to improve theoretical predictions.

Unfortunately, analytical methods that readily handle multiphase products and phase compliancy are not well suited to more than two product species. Thermochemical equilibrium solvers that readily handle multiphase products and multiple product species are not currently built to enforce phase compliancy due to limitations of existing polynomial forms of thermodynamic data[97, 99]. This problem is further compounded by the challenge of ensuring the use of proper thermodynamic data and species. It is evident from existing theoretical efforts that significant improvement is warranted in methodologies for predicting the energy release of RM systems and experimental validation is a requirement to assess quality of predictions. Only then can a true evaluation of combustion efficiency and combustion limitations of RM in application be made.

1.5 Objectives of present research

It is evident from the existing body of research that unifying theories for predicting fragmentation and energy release behavior of RMs are still absent from the field of research. The RM fragmentation process has been well characterized by fragment size distributions, but validated theories predicting the effects of composition, porosity, and particle size on bulk material properties used by these distributions are non-existent. The study of the energy release of RM systems is significantly hindered by varied theoretical methods that yield predictions of product temperature, energy release, and product species that deviate significantly from experimental results and often are non-realistic solutions. Lastly, the association between energy release and fragment production still remains elusive in published literature.

A systematic, fundamental approach is warranted to characterize the macroscale mechanical, fragmentation, and combustion behavior of RM systems with the goal of forming unifying theories that allow prediction of performance. This approach will incorporate and build upon existing theories that show promise for universal application to RM. The theories and methodologies developed in this work to predict fragmentation and energy release behavior will be demonstrated across multiple RM systems with statistical significance considered. Lastly, relations governing the association between energy release and fragment production will be explored. The following specific objectives will govern this research:

- Develop and experimentally validate predictive theories for bulk material properties in relation to composition, porosity, and particle size. Considered bulk material properties will be density, elastic modulus, fracture toughness, dilatational and shear wave speed, and yield and compressive strength.
- Develop and experimentally validate a methodology for predicting fragment size distributions of multiple RM systems utilizing developed theories for bulk material properties.

- Develop and experimentally validate a methodology for predicting RM energy release under ideal conditions that considers both dissociated species and phase compliancy of product species.
- Validate experimentally the predictive capability of the effective energy release of multiple RM systems in application utilizing combined theories developed in this work for fragment size distributions and ideal energy release.

CHAPTER 2

DEVELOPMENT OF ANALYTICAL FRAGMENTATION THEORY FOR REACTIVE MATERIAL SYSTEMS

High-rate dynamic loading leading to fracture and production of fragments is central to RM applications. Brittle failure is often observed in RM systems made through dry powder compaction methods and reported fracture toughness measurements align with these observations[11, 12, 27]. Measured fracture toughnesses of RM systems approach those of ceramics and typically are an order of magnitude less than the constituent materials[11, 12, 27]. These literature observations lead to the tentative conclusion that the fracture of RM systems can be primarily characterized by brittle material models.

The failure of brittle materials is regularly viewed from the perspective of linear elastic fracture mechanics (LEFM)[42, 51, 60, 102, 103]. Brittle materials are often associated with research efforts in geological materials[104–106], ceramics[42, 51], armor and projectile applications[51, 60, 62], and amorphous solids such as glass[103, 107, 108]. An extensive review of mechanisms and models for the failure, strength, and fragmentation of brittle materials under dynamic loading is given by Ramesh et al.[42]. In this work, dynamic fracture of brittle materials is characterized by the formation of cracks (nucleation), growth of cracks, and coalescence of cracks. These three characteristics are directly influenced by the heterogeneity characteristics of the material, such as porosity and pore size distributions[42].

Efforts reported in literature have demonstrated that LEFM and considerations of heterogeneity characteristics of a material generally approximate the failure of materials near quasi-static conditions to a reasonable degree[42, 102, 107]. However, these techniques often fail to adequately represent the failure of materials subjected to high-rate dynamic loading[60, 109]. To resolve the discrepancies for dynamic loading scenarios, early work by Grady[60] built on the equilibrium energy balance theory of fracture by Griffith[107] and applied a minimum energy density state approach to develop analytical approximations of characteristic fragment sizes. This minimum energy based approach accounted for inertial (kinetic energy) contributions brought on by the dynamic loading conditions[60]. Subsequent work by Glenn and Chudnovsky [63] also used a minimum energy approach as well as accounting for elastic strain energy contributions. Later work by Grady[61, 110] applied a simple energy balance to account for the kinetic energy and elastic strain energy contributions. These models were derived assuming homogeneity of the materials, but have shown good agreement

when compared to characteristic fragment sizes measurements of heterogeneous materials[5, 60].

More recently, work by Zhou et al.[109, 111] accounted for strength heterogeneity of the material and energy contributions in modeling the dynamic fracture of rings and rods of model ceramic materials using a numerical solution methodology. However, this model does not consider other material heterogeneity. The model developed by Zhou et al.[109, 111], referred to as the ZMR model[42], provided improved agreement to experimental and simulated measurements of characteristic fragment sizes, but unfortunately a path to an analytical solution was identified as non-feasible[109].

The field of RM research has regularly relied upon the energy-based fragmentation model for materials that undergo brittle fracture developed by Grady[60, 61]. The selection of the Grady fragmentation model (henceforth referred to as the Grady model) by the RM community[5, 11, 12, 27] is likely the result of the simplicity of the analytical model, which depend on readily measurable material properties[60], and observations of good agreement with experimental results[5, 12, 60]. The use of the Grady model is also wide-spread in the defense community[112]. Interestingly, good agreement has regularly been obtained for heterogeneous, granular materials such as RMs in application, despite the lack of consideration of heterogeneity characteristics of the materials. This suggests that these dependencies may be partly captured by the measured material parameters utilized by the Grady model. Therefore, analytical predictions of material parameters utilized by the Grady models are expected to capture the heterogeneity dependencies.

This work recognizes that application of improved models to RM systems, such as the ZMR model, is a worthy endeavor to consider for future efforts. However, this work will focus on improvements to the models and methodologies associated with work by Grady[60, 61] to maximize the scientific contribution to the RM and defense communities. In order to understand the application of the Grady models to granular composites such as RM systems and the material parameters which may capture the heterogeneity dependencies, it is necessary to understand the derivation of the fragmentation model proposed by Grady[60].

2.1 Energy conservation of fragmentation under dynamic loading

In response to insignificant characterization of the dynamic fracture process, Grady[60] proposed an equilibrium energy balance approach to resolve discrepancies and provide quantitative means to determine a nominal fragment size that characterizes the fragmentation of a material. An equilibrium energy balance approach is not novel to the field of fracture mechanics, and aligns with the fundamental approach by Griffith[107] in applying the first and second law of thermodynamics to explain the formation and growth of cracks in solids as an equilibrium process[102]. However, Grady[60] accounted for kinetic energy of

the expanding material, suspecting it was the driving force of fragmentation of materials subjected to high-rate loading.

Grady[60] first approached dynamic fragmentation of brittle materials from the perspective of a body expanding from an initially compressed state. This compressed state was assumed to occur from the application of a dynamic compressive load. Upon removal of the dynamic compressive load, the considered body transitions to a state of rapid expansion in an attempt to return to a state of equilibrium. This expansion is treated as perfectly elastic, and it is implicitly assumed the rate of expansion is equal to the rate of compression from loading. This process is further idealized by assuming an adiabatic process and that compressibillity effects are negligible[60, 63]. This expansion process leads to kinetic energy associated with the body. The kinematic and thermodynamic state of the bulk material of the bulk body is described by the density, ρ, the rate of density change, $\dot{\rho}$, and temperature, T. For consistency with prior works[60, 61] the original nomenclature used by Grady is retained here.

In the expansion process, Grady[60] initially assumed the kinetic energy resulting from the outward motion of the expanding body is primarily responsible for initiating and driving the fragmentation process. The sole mechanism resisting the fracturing forces driven by the expansion process of the body was assumed to be the surface energy of the material. Grady intuitively recognized that the total kinetic energy of the body cannot be available for fragmentation[60, 63]. This is based on the observation that after the fragmentation process, fragments continue to travel away from the body at high speed, and thus a considerable portion of the kinetic energy contained by the bulk body is distributed across the kinetic energy of the individual fragments in free flight.

Grady[60] surmised that the local kinetic energy must be responsible for driving fragmentation. In this consideration, Grady considered a spherical mass element of radius a within the expanding bulk body immediately prior to fragmentation. The considered bulk body and relative location of the mass fragment element are illustrated in Figure 2.1. This mass element constitutes the mass of an average fragment after fragmentation. The fragment element exhibits a kinetic energy relative to a global reference frame that applies to the bulk body motion, E_{KE}, but also a local kinetic energy relative to a reference frame at the center of mass of the element, E'_{KE}, which is associated with the local expansion process of the element. Grady assumed that due to symmetry of the idealized fragmentation process, the mass element experiences no net impulse during the fragmentation process such that E_{KE} remains unchanged. Thus, during fragmentation, E_{KE} does not contribute to the fragmentation process and is conserved. It is the local kinetic energy relative to the center of mass of the element, E'_{KE}, that drives the fragmentation process.

The considered spherical fragment element of radius, a, is is illustrated in Figure 2.2. The element is assumed to expand uniformly from the center of the element at a rate defined by $\dot{\rho}$. This is equivalent to the rate of change in volume of the element with constant mass. The total kinetic energy associated with this

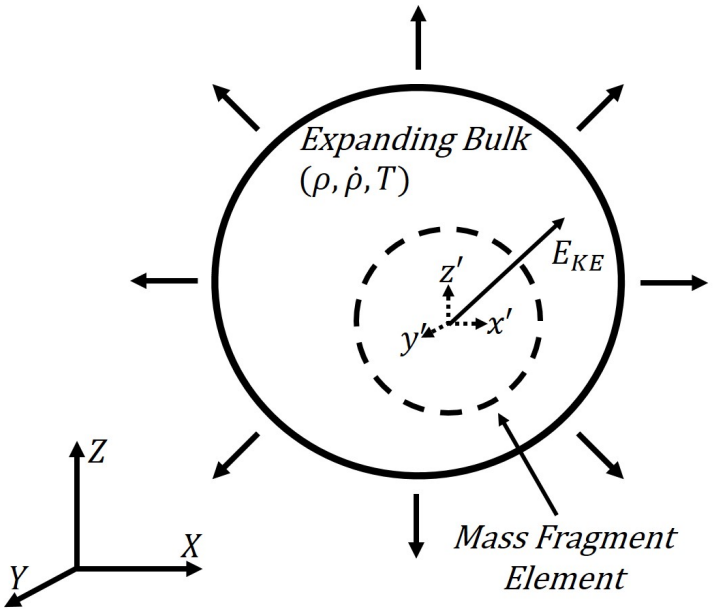

Figure 2.1: Schematic of expanding bulk with spherical fragment element denoted by dashed line. Solid arrows represent motion or variables relative to global reference frame.

expansion of the element is found by the summation of the kinetic energy, $dE_{KE,l}$, of a finite number of spherical shells of mass dm within the element.

The mass of the shells are a function of the radius of the element, r, described by:

$$dm = 4\pi\rho r^2 dr \tag{2.1}$$

Each shell has a unique radial expansion velocity that is a function of r and the uniform 1D strain rate, $\dot{\varepsilon}$:

$$\dot{r} = -\dot{\varepsilon} r \tag{2.2}$$

For a uniform expansion of a spherical element the strain rates in the X direction, $\dot{\varepsilon}_{xx}$, the Y direction, $\dot{\varepsilon}_{yy}$, and Z direction, $\dot{\varepsilon}_{zz}$ are equivalent such that $\dot{\varepsilon}_{xx} = \dot{\varepsilon}_{yy} = \dot{\varepsilon}_{zz} = \dot{\varepsilon}$. Recognizing $\dot{\rho}/\rho$ is equivalent to the 3D volumetric strain rate, $\dot{\varepsilon}$ is related to $\dot{\rho}$ by:

$$3\dot{\varepsilon} = \frac{\dot{\rho}}{\rho} \tag{2.3}$$

Therefore, the kinetic energy of each shell can be described as:

$$dE'_{KE} = \frac{1}{2}\dot{r}^2 dm = \frac{4\pi}{18}\left(\frac{\dot{\rho}^2}{\rho}\right) r^4 dr \tag{2.4}$$

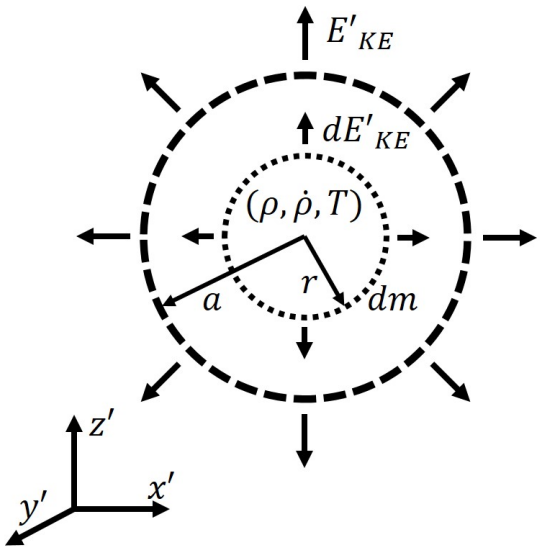

Figure 2.2: Schematic of spherical fragment element of radius a. Spherical shell of mass dm considered for integration indicated by dotted boundary. Coordinate system resides at the center of mass of the element, but is offset for clarity.

The local kinetic energy of the element is then given through the integration of Equation 2.4 from the center of the element to outer radius yielding:

$$E'_{KE} = \int_0^a dE'_{KE} = \frac{2\pi}{45}\left(\frac{\dot{\rho}^2}{\rho}\right)a^5 \tag{2.5}$$

The local kinetic energy of the element is the total energy available for fragmentation. Distributing this energy across the volume of the element yields a local kinetic energy density, κ:

$$\kappa = \frac{E'_{KE}}{\frac{4}{3}\pi a^3} = \frac{1}{30}\frac{\dot{\rho}^2}{\rho}a^2 \tag{2.6}$$

A relation between κ and the fracture surface area created is found by recognizing that the considered element is representative of an average fragment size produced by fragmentation of the bulk[60]. Thus, κ is related to the fracture surface area, which corresponds to the surface area of the fragment element, A_{FE}, by the ratio of the surface area to volume, $\forall_{FE}$, of the spherical element, ν_r. This ratio is described by Equation 2.7, and the local kinetic energy density takes the new form in Equation 2.8:

$$\nu_r = \frac{A_{FE}}{\forall_{FE}} = \frac{4\pi a^2}{\frac{4}{3}\pi a^3} = \frac{3}{a} \tag{2.7}$$

$$\kappa = \frac{3}{10}\frac{\dot{\rho}^2}{\rho v_r^2} \tag{2.8}$$

It is typical to define a dynamic process by the strain rate the material is subjected to. Using Equation 2.3, κ is rewritten as a function of strain rate as given by:

$$\kappa = \frac{27}{10}\frac{\rho\dot{\varepsilon}^2}{v_r^2} \tag{2.9}$$

Energy is expended in the form of work in the creation of new fracture surface area[102, 107]. For the spherical fragment element, the surface area of the element corresponds to the fracture surface area. Thus, the energy associated with the generation of fracture surface area corresponds to the surface energy distributed across the element surface. This distributed surface energy, or fragment surface energy as referred to by Grady[60], is a function of the surface energy of the material, ζ, and A_{FE}. Applying LEFM, ζ is related to the energy release rate associated with crack growth, G_{IC}, as $G_{IC} = 2\zeta$[102]. G_{IC} is related to the elastic modulus, E, and the static Mode-I fracture toughness as $K_{IC} = \sqrt{EG_{IC}}$. Using 1D elastic theory, E can be represented as a function of density and the bar wave speed by $E = \rho C_o^2$. Thus, ζ can be approximated using readily measurable material properties as:

$$\zeta = \frac{K_{IC}^2}{2E} = \frac{K_{IC}^2}{2\rho C_o^2} \tag{2.10}$$

The total surface energy density of the element, Γ, is then given by:

$$\Gamma = \frac{\zeta A_{FE}}{\forall_{FE}} = \frac{K_{IC}^2}{2\rho C_o^2} v_r \tag{2.11}$$

Grady[60, 61] derived the surface energy contribution as a function of the static fracture toughness. Later work by Grady[62] recognized that the fracture toughness may vary with the loading rate, and subsequently replaced K_{IC} with K_f. It is generally accepted that a good first approximation of K_f is K_{IC}. For consistency with the original derivation, the form K_{IC} is retained here.

The initial model derivation by Grady[60] did not include the potential energy that corresponds to the elastic strain energy stored in the element through work from the deformation process[60, 63]. The elastic strain energy was excluded on the assumption that the contribution would be small in brittle materials undergoing dynamic loading. Comparison to experimental fragment sizes of brittle oil shale and high-strength, brittle steel cylinders showed the Grady model correctly predicted trends, but over-predicted characteristic fragment sizes by 10% to 35%. This indicated that the kinetic energy was likely the primary contributor to driving the fracture process of these brittle materials, but other mechanisms, such as elastic strain energy, may play a role.

Subsequent work by Grady[61] considered the elastic energy stored in the fragment element and assumed all of the stored energy was consumed by the fragmentation process. Grady[61] took the elastic strain energy density, v, to be a function of the average tensile stress, σ_b, and average strain, ϵ_b, of the bulk (and thus element) immediately before fragmentation, given by $v = U/\forall_{FE} = \frac{1}{2}\sigma_b\varepsilon_b$. Grady further assumed that the bulk modulus, K_b, described the stress and strain relationship by $K_b = \sigma_b/\epsilon_b$ and that $K_b = \rho C_b^2$. Applying these assumptions permitted v to be recast as a function of σ_b, ρ, and C_b:

$$v = \frac{1}{2}\frac{\sigma_b^2}{\rho C_b^2} \tag{2.12}$$

Grady[61] proposed that σ_b was a function of time, t, as a result of the expansion process of the body:

$$\sigma_b = \rho C_b^2 \dot{\varepsilon} t \tag{2.13}$$

Treating the expansion of the body as a linear process, instantaneous failure of the bulk occurs at a critical stress state, σ_{cr}, occurring at time t_{cr}. For this failure to occur, Grady[61] assumed every fragment element in the bulk fails independently through the coalescence of cracks. Grady[61] further assumed the radius of the fragment element corresponds to the propagation distance of a crack at coalescence. This propagation distance is assumed to be governed by the "communication horizon" of the material, $L_{pd} = C_b t$, and limited by the bulk speed of sound[61]. Thus, the radius of the fragment element is given as $a = C_b t_c$. Using Equation 2.7, Equation 2.13, and $a = C_b t_c$, Equation 2.12 is recast as:

$$v = \frac{9}{2}\frac{\rho\dot{\varepsilon}^2}{\nu_r^2} \tag{2.14}$$

The total energy density of the fragment element as a function of ν_r is then given by:

$$E_{FE}(\nu_r) = \kappa(\nu_r) + v(\nu_r) + \Gamma(\nu_r) \tag{2.15}$$

Where κ (Equation 2.9), v (Equation 2.14), and Γ(Equation 2.11), of the fragment element are:

$$\kappa = \frac{27}{10}\frac{\rho\dot{\varepsilon}^2}{\nu_r^2}$$

$$v = \frac{9}{2}\frac{\rho\dot{\varepsilon}^2}{\nu_r^2}$$

$$\Gamma = \frac{K_{IC}^2}{2\rho C_o^2}\nu_r$$

Important insight can be gained by plotting the behavioral trends of the total energy density of the fragment element given by Equation 2.15 and component

energy densities of the fragment element given by Equations 2.9, 2.14, and 2.11. To visualize these trends, an idealized material is considered in which all material properties are equal to unity and the body is subjected to a strain rate of unity. This approach creates an opportunity for the direct observation of the functional trends of the energy density functions relative to the surface area to volume ratio and surface area of the fragment element. The energy densities, surface area to volume ratio, and surface area parameters are further normalized by the largest values of the parameters considered for the theoretical case. The normalized energy densities of a fragment element of the idealized material are plotted as a function of the normalized surface area to volume ratio and the normalized fragment surface area in Figure 2.3.

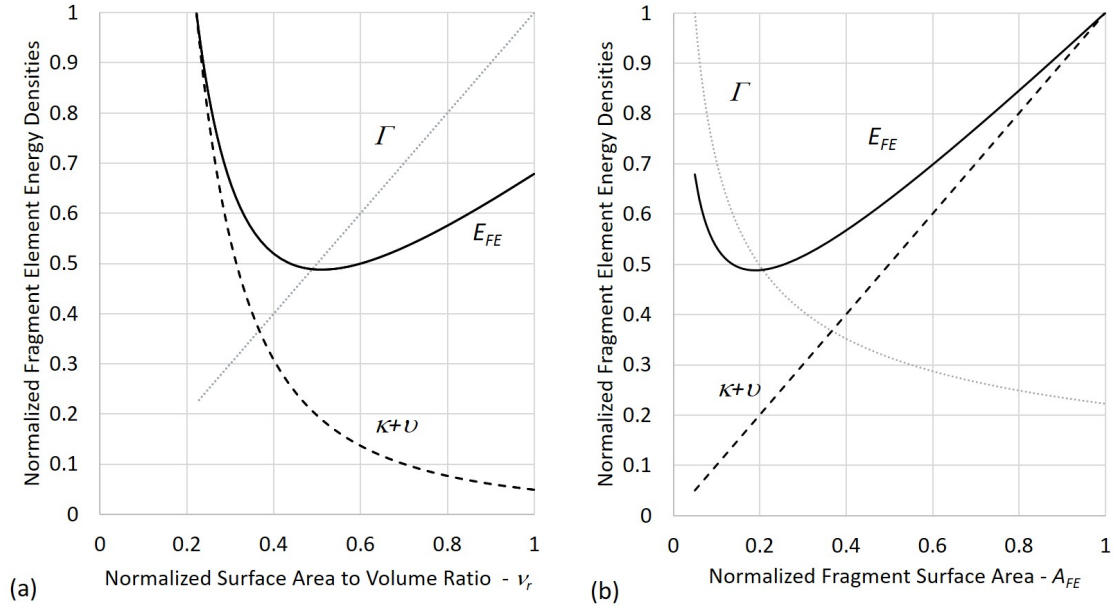

Figure 2.3: Normalized energy densities of a fragment element of an idealized material as a function of (a) normalized surface area to volume ratio ν_r and (b) normalized fragment surface area A_{FE}. The total energy density of the element, E_{FE}, is shown as a solid black line in both figures. The sum of the kinetic energy density and elastic strain energy density, $\kappa+\upsilon$, is shown as a dashed line. The surface energy density, Γ, is shown as a dotted line.

Figures 2.3(a) and 2.3(b) clearly indicate that E_{FE} does not reach a zero-state. Instead a local minimum exists, corresponding to $dE_{FE}/d\nu_r = 0$ or alternatively $dE_{FE}/dA_{FE} = 0$. In considering the formation of a crack, Griffith[107] applied the first and second law of thermodynamics when considering fragmentation as a thermodynamic process in which equilibrium is sought. Therefore, the fracture area formed corresponds to the minimization of free-energy of the material. Grady[60] applied the equilibrium approach used by Griffith[107], and considered the E_{FE} derived here as the free-energy density of the fragment element[60,

63]. Grady[60] minimized this free-energy density with respect to the fragment surface area to volume ratio, which corresponds to the local minimum in Figure 2.3(a). Grady[60] initially considered only the local kinetic energy density, κ, in this equilibrium process. In this initial effort, Equation 2.15 takes the form of Equation 2.16 and the minimum energy state in relation to ν_r takes the form in Equation 2.17:

$$E_{FE}(\nu_r) = \frac{27}{10}\frac{\rho\dot{\varepsilon}^2}{\nu_r^2} + 0 + \frac{K_{IC}^2}{2\rho C_o^2}\nu_r \tag{2.16}$$

$$dE_{FE}/d\nu_r = 0 = -\frac{27}{5}\frac{\rho\dot{\varepsilon}^2}{\nu_r^3} + \frac{K_{IC}^2}{2\rho C_o^2} \tag{2.17}$$

As discussed previously, literature typically reports the nominal, or characteristic, fragment size, λ. Acknowledging that the nominal fragment size is equivalent to the diameter of the fragment, such that $\lambda = 2a$, then for a spherical element $\nu_r = 3/a = 6/\lambda$. Thus, the nominal fragment size that corresponds to the minimum energy state can be found by rearranging Equation 2.17 which yields the original form of the Grady model for brittle materials[60]:

$$\lambda = \left(\frac{\sqrt{20}K_{IC}}{\rho C_o \dot{\varepsilon}}\right)^{2/3} \tag{2.18}$$

In looking at the spalling of brittle materials Grady proposed a revised form of Equation 2.18 that claimed to include elastic strain energy:

$$\lambda = \left(\frac{\sqrt{24}K_{IC}}{\rho C_o \dot{\varepsilon}}\right)^{2/3} \tag{2.19}$$

Equation 2.19 is regularly applied in RM literature[5, 11, 12] and subsequent work by Grady and coworkers[62, 62, 113] report it as the preferred form for spalling and impact fragmentation of both ductile and brittle materials. Unfortunately, this work's careful review of the derivation of Equation 2.19 reveals two fundamental flaws.

The first flaw is associated with an error in the kinetic energy density. In determining Equation 2.19, Grady[61] made an error when reforming the kinetic energy density. Grady[60] previously defined the kinetic energy density as a function of surface area to volume ratio, ν_r, and then later changed it to be a function of the nominal fragment size for his derivation of Equation 2.19. Performing this change resulted in an arithmetic error which is detailed in Appendix A. The reformed kinetic energy density equation originally proposed by Grady[61] is presented as Equation 2.20 and the correctly reformed equation is presented as Equation 2.21:

$$\kappa = \frac{1}{120}\rho\dot{\varepsilon}^2\lambda^2 \tag{2.20}$$

$$\kappa = \frac{9}{120}\rho\dot{\varepsilon}^2\lambda^2 \tag{2.21}$$

The form reported by Grady[61] is ninefold smaller than the correct form. This error led Grady[61, 110] to falsely conclude that the kinetic energy comprised only 15% of the total energy density and thus elastic strain energy was the dominant contributor. Correctly reforming the kinetic energy reveals that the kinetic energy contribution to the energy density is in fact 37%; a non-negligible contribution. This erroneous conclusion is still found in recent works by Grady[110]. By concluding the kinetic energy was small, and thus negligible, subsequent derivations by Grady[61, 110] ignored kinetic energy on the assumption that elastic strain energy drove the fracture process. Oddly, this conclusion is in complete contradiction to earlier work by Grady[60] and Glenn and Chudnovsky[63, 64] that found kinetic energy was the driving force of fracture of materials under high-rate dynamic loading conditions; a conclusion justified at the time by comparison to experimental results of brittle materials.

The second flaw is associated with the methodology used by Grady[61] in determining the nominal fragment size in this later work. In determining Equation 2.19, Grady[61] took a simple energy balance of the local fragment element energy densities assuming the kinetic energy contribution was negligible ($\kappa \approx 0$) and assigning a negative sign to the surface energy density term:

$$E_{FE}(\nu_r) = 0 = 0 + \frac{9}{2}\frac{\rho\dot{\varepsilon}^2}{\nu_r^2} - \frac{K_{IC}^2}{2\rho C_o^2}\nu_r \tag{2.22}$$

The negative sign assigned to the surface energy density is likely based on the assumption that energy is consumed in the creation of new fracture surfaces following Griffith's work[107]. Grady[61] subsequently solved for ν_r, and thus λ, using:

$$\frac{9}{2}\frac{\rho\dot{\varepsilon}^2}{\nu_r^3} = \frac{K_{IC}^2}{2\rho C_o^2} \tag{2.23}$$

This simple energy balance proposed by Grady[61] ignores the concept of thermodynamic equilibrium through fracture, the governing fundamental principle in the guiding work by Griffith[107], Grady's initial theory[60], and subsequent theory by Glenn and Chudnovsky[63, 64]. Consideration of the energy balance of the fragment element as described by Equation 2.22 implies all of the stored energy is consumed by the production of fragments and resultant fragment surface area. However, the simple observation that fragments eject from a dynamically fragmenting body indicates only a portion of the stored energy is consumed in the formation of fragments. This was recognized in the foundational work by Grady[60] and Glenn and Chudnovsky[63] who correctly rejected a simple energy balance approach. Thus, this later work by Grady[61] is in further contradiction to prior theory without explanation.

Approaching fracture as an equilibrium process is simply seeking the fragment surface area that corresponds to the collective minimum of the characteristic

free energies of the system: kinetic energy, potential energy, and surface energy. Fundamentally, the indication of an equilibrium state of this system corresponds to $dE_{FE}/d\nu_r$[96]. This approach does not consider how energy is transferred during the formation of fragment surface area nor is it necessary. This is intuitively shown by manipulating the signage of the surface energy density term in Equation 2.15. With a positive surface energy term, the characteristic fragment size that minimizes Equation 2.15 is given by Equation 2.18. With a negative surface energy term, which follows the argument that energy is consumed in the formation of new fracture surfaces, the characteristic fragment size that minimizes Equation 2.15 is again given by Equation 2.18. This demonstrates that regardless of the signage applied to the surface energy term, the same characteristic fragment size is obtained. This confirms that the minimum energy state shown in Figure 2.3 does exist, reinforcing that the simple energy balance approach used by Grady[60] is fundamentally flawed.

Recent work by Grady[110] continues to perpetuate the simple energy balance approach in the formulation of a characteristic fragment size model for rings of ductile materials. Equation 2.18 from early work by Grady[60] is the only correctly derived form of the Grady fragmentation models for brittle fracture. All subsequent efforts in general dynamic fracture studies[42, 62, 109, 110, 113, 114] and RM literature[5, 11, 12] that utilize Equation 2.19 or the pure energy balance methodology from which it was derived are in error.

Grady's[61] model incorporating elastic strain energy is correctly derived here using the minimum energy state equilibrium approach. The energy density of the fragment element is given by Equation 2.24, and the minimum energy state given by Equation 2.25:

$$E_{FE}(\nu_r) = \frac{27}{10}\frac{\rho\dot{\varepsilon}^2}{\nu_r^2} + \frac{9}{2}\frac{\rho\dot{\varepsilon}^2}{\nu_r^2} + \frac{K_{IC}^2}{2\rho C_o^2}\nu_r \tag{2.24}$$

$$dE_{FE}/d\nu_r = 0 = -\frac{27}{5}\frac{\rho\dot{\varepsilon}^2}{\nu_r^3} - 9\frac{\rho\dot{\varepsilon}^2}{\nu_r^3} + \frac{K_{IC}^2}{2\rho C_o^2} \tag{2.25}$$

Thus, the nominal fragment size, λ, that corresponds to the minimum energy state can be found by rearranging Equation 2.25 yielding:

$$\lambda = \left(\sqrt{\frac{5}{4}}\frac{K_{IC}}{\rho C_o \dot{\varepsilon}}\right)^{2/3} \tag{2.26}$$

Comparison of the newly derived Equation 2.26 to the original equation derived by Grady[60] (Equation 2.18) reveals the manner in which elastic strain energy is considered leads to a 60% reduction in the nominal fragment size predicted. Plotting the kinetic energy only and kinetic energy and elastic strain energy Grady theories alongside experimental data of nominal fragment sizes of fractured brittle granular materials reveals severe deviation from experimental

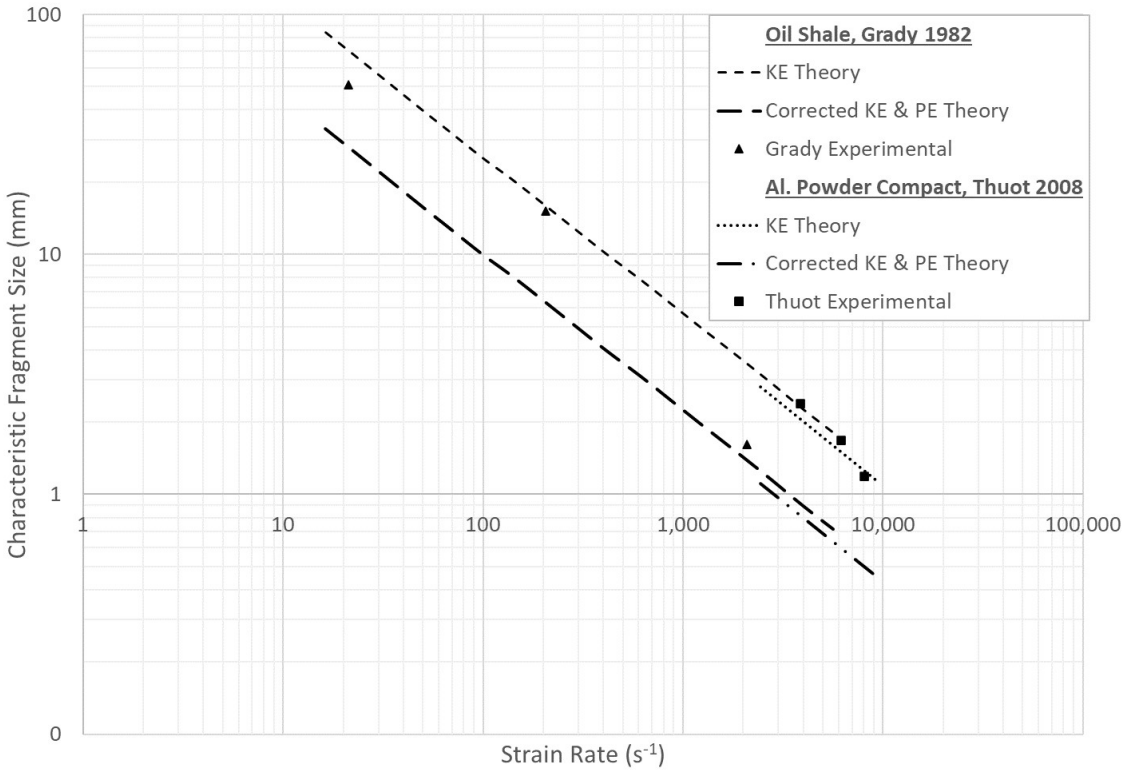

Figure 2.4: Comparison of the early Grady model that only accounted for kinetic energy (KE) and the corrected Grady model that accounts for elastic strain energy kinetic energy (PE & KE) to experimentally determined nominal fragment sizes of brittle, granular materials discussed previously in this work. Poor agreement is observed for the Grady model that considers elastic strain energy.

measurements of nominal fragment sizes of brittle granular materials, as seen in Figure 2.4.

The deviation of the later Grady model from experimental results is suspected to be tied to the calculation of the elastic strain energy density associated with the fragment element. Grady[61] assumed the elastic strain energy was primarily a function of the stress state of the bulk prior to fracture. Grady reported that the calculated stress state prior to fragmentation using Equation 2.13 generally aligned well with experimental measurements[61], suggesting that it is the functional form of Equation 2.14 or the chosen stress and strain state that is in error. Grady did not consider the possibility that the bulk stress at fracture likely exceeds the yield strength of the material. When the yield strength of the material is exceeded, the body undergoes plastic strain preventing additional energy from being stored elastically. Over estimating the elastic strain energy for fracture could explain why Equation 2.26 severely under predicts nominal fragment

sizes when compared to experimental measurements.

Work by Glenn and Chudnovsky[63] approached the problem of fragmentation from the same foundational principles as Grady[60]. However, Glenn and Chudnovsky minimized the total energy in the bulk material, while Grady[60, 61] minimized the energy density of a single fragment. Like Grady[61], Glenn and Chudnovsky[63] assumed that the stress state of the bulk prior to fracture governed the elastic strain energy. However, they recognized there must be a limit to the strain energy available, which they surmised was dictated by the yield stress of the material. As such, they assumed that the yield stress was a reasonable estimate of the stress state prior to fracture, especially given that brittle materials tend to fail shortly after yielding. Therefore the total stored elastic energy in the dilating body that is available for fragmentation, $E_{PE,db}$, was taken to be[63]:

$$E_{PE,db} = \frac{4}{3}\pi R_{db}^3 \left(\frac{\sigma_{Y,db}^2}{2K_{db}}\right) \tag{2.27}$$

Where R_{db} is the radius of the dilating body, $\sigma_{Y,db}$ is the yield stress of the dilating body, and K_{db} is the bulk modulus of the dilating body. Glenn and Chudnovsky took the total kinetic energy in the dilating body that is available for fragmentation, $E_{KE,db}$, to be[63]:

$$E_{KE,db} = \frac{2}{5}\pi N_{db}\rho\dot{\varepsilon}^2 a^5 \tag{2.28}$$

Where N_f is the total number of fragments that can be volumetrically contained by the dilating body, given by $N_f = (R_{db}/a)^3$. Inspection of Equation 2.28 reveals it to be Equation 2.5 derived by Grady[60], but recast to be a function of $\dot{\varepsilon}$ and scaled by N_f. Finally, Glenn and Chudnovsky considered the total fragment surface energy in the dilating body that is available to resist fragmentation, $E_{SE,db}$, to be[63]:

$$E_{SE,db} = N4\pi a^2\gamma \tag{2.29}$$

Combining equations 2.27, 2.28, and 2.29 and assigning a negative sign to the surface energy density in line with Griffith's work[107] yields the total energy of the dilating body as a function of fragment radius given by Equation 2.30, and the minimum energy state as reformed by Glenn and Chudnovsky[63] given by Equation 2.31:

$$E_{db}(a) = E_{PE,db} + E_{KE,db} - E_{SE,db} \tag{2.30}$$

$$dE_{TE,db}/da = 0 = a^3 + \alpha^\star a - 2\beta^\star \tag{2.31}$$

Where:

$$\alpha^\star = \frac{2\beta^\star}{R} + \frac{5}{3}\left(\frac{\sigma_y}{\rho C_b \dot{\varepsilon}}\right)^2 \tag{2.32}$$

$$\beta^\star = \frac{5}{2}\left(\frac{K_{IC}}{\rho C_b \dot{\varepsilon}}\right)^2 \tag{2.33}$$

Inspection of Equation 2.31 reveals it to be a depressed cubic equation, which can be solved using numerical methods or the general solution given by Glenn and Chudnovsky[63]:

$$a = 2(\alpha^\star/3)^{1/2}\sinh(\phi^\star/3) \tag{2.34}$$

Where:

$$\phi^\star = \sinh^{-1}\beta^\star(3/\alpha^\star)^{3/2} \tag{2.35}$$

Glenn and Chudnovsky[63] compared their model given by Equation 2.31 to experimental fragment sizes of high-strength, brittle steel cylinders from Weimer and Rogers[115], which is the same data that Grady[60] compared his initial model to. Poor agreement of Equation 2.31 to the experimental data was reported. By separating out the kinetic energy and elastic strain energy contributions and comparing predicted fragment sizes to the steel cylindrical data, Glenn and Chudnovsky found that poor agreement was observed only when elastic strain energy was considered, and that good agreement over the data range was obtained when only the local kinetic energy was considered. This led Glenn and Chudnovsky to propose the possibility that a dynamic fragmentation process is uncoupled from the stored elastic strain energy when the local kinetic energy is sufficient to initiate fragmentation.

2.2 The elastic strain energy contribution to dynamic fragmentation

To evaluate the observation that a dynamic fragmentation event is uncoupled from the stored elastic strain energy in the material, this work will combine the approaches by Grady[60] and Glenn and Chudnovsky[63] by minimizing the total energy of a fragment element. This allows the elastic strain energy to be included in a form that utilizes the yield stress while holding true to the original derivation assumptions that governed Grady[60]. More importantly, this permits an assessment of whether the dynamic fragmentation process is uncoupled from the stored elastic strain energy in general or whether Glenn and Chudnovsky's[63] observation was unique to their approach and assumptions.

Following Grady's[60] approach describing the energy of a fragment element, Equation 2.6 is recast to be a function $\dot{\varepsilon}$, such that the local kinetic energy of the fragment element is:

$$E'_{KE} = \frac{2\pi}{5}\rho\dot{\varepsilon}^2 a^5 \tag{2.36}$$

Assuming the elastic strain energy density of the fragment element is described by $\nu_r = (1/2)\sigma_Y^2/E$, the total elastic strain energy contained within the fragment element is:

$$E'_{PE} = \nu_r \mathcal{V}_{FE} = \frac{2\pi}{3}\frac{\sigma_Y^2 a^3}{E} \tag{2.37}$$

Lastly, the total surface energy of the fragment element is found by recasting Equation 2.10 to be a function of E, removing the 1D elastic theory relation, and multiplying by the fragment element volume, yielding:

$$E'_{SE} = \Gamma \forbidden{V}_{FE} = \frac{2\pi K_{IC}^2 a^2}{E} \tag{2.38}$$

Following the term signs of Griffith's work[107], the total energy of the fragment element is given by Equation 2.39, with the minimum energy state given by Equation 2.40:

$$E'_{FE}(a) = E'_{KE} + E'_{PE} - E'_{SE} \tag{2.39}$$

$$dE'_{FE}(a)/da = 0 = a^3 + \frac{\sigma_y^2}{\rho \dot{\varepsilon}^2 E} a - \frac{2K_{IC}^2}{\rho \dot{\varepsilon}^2 E} \tag{2.40}$$

Inspection of Equation 2.40 reveals a depressed cubic equation which is the same functional form as obtained by Glenn and Chudnovsky[63]. However, the coefficients differ which is expected given Equation 2.40 was arrived at by minimizing the energy of the fragment element and not the energy of the dilating body as performed by Glenn and Chudnovsky[63]. This work will use Weimer and Rogers'[115] steel case fragmentation data to evaluate the model derived here (Equation 2.40), Glenn and Chudnovsky's[63] model (Equation 2.31), Grady's[60] early model that considers only local kinetic energy (Equation 2.18), and the corrected version of Grady's[61] later model that includes elastic strain energy (Equation 2.26). Weimer and Rogers'[115] data is vital for this evaluation as there are few experimental studies which have both fragmentation data and the necessary material property information utilized by the discussed models.

Weimer and Rogers[115] reported fragment sizes of high-strength, brittle steel cylinders driven to failure using Composition B explosive at strain rates $\dot{\varepsilon} \approx 4 \cdot 10^4$ s^{-1}[60]. Fragmentation data was reported for two types of steel: FS-01 steel which is a fine grained, oil hardened tool steel; and HF-1 steel which is a large grained silicomanganese steel. The strength and fracture toughness of the steels were manipulated using heat treating, and the recovered fragments fitted to the cumulative distribution model by Mott[54]. The measured material properties of relevance to the models discussed here, the measured Mott size parameters (half the average fragment mass), and the Mott parameters transformed to a spatial scale are summarized in Table 2.1. Transformation of the Mott parameter, μ_m, is performed assuming two separate geometric models: spherical fragments, where $\lambda_{m,sp} = (6/4\pi\rho * \mu_m)^{1/3}$, and cubic fragments where $\lambda_{m,cu} = (2\mu_m/\rho)^{1/3}$. Measurements of density, wave speeds, and elastic modulus were not reported by Weimer and Rogers[115]. However, Grady[60] and Glenn and Chudnovsky[63] both assumed typical values for steel to be $\rho = 7840$ kg/m^3 and $C_o = C_b = 5000$m/s. This work will assume the same, in addition to $E = 200$ GPa based on Medved and Bryukhanov's[116] observations of small variations in elastic moduli of high-strength steels subjected to varying heat treatments.

Table 2.1: Fragmentation data and material properties from Weimer and Rogers[115]

Sample	K_{IC}	σ_y	μ_m	$\lambda_{m,sp}$	$\lambda_{m,cu}$
Units:	MPa*m$^{1/2}$	MPa	mg	mm	mm
FS-01 (A)	21.7	2570	19	2.1	1.7
FS-01 (B)	24.2	2036	24.1	2.3	1.8
FS-01 (C)	31.4	1777	34.1	2.6	2.0
FS-01 (D)	57.3	1520	97.4	3.6	2.9
HF-1 (A)	32.5	1233	23.3	2.2	1.8
HF-1 (B)	37.5	949	70.7	3.3	2.6
HF-1 (C)	40.3	760	42.2	2.7	2.2

The four models are compared to Weimer and Rogers'[115] FS-01 Steel fragmentation data in Figure 2.5 and Weimer and Rogers' HF-1 Steel fragmentation data in Figure 2.6. For the models described by Equation 2.40 and Equation 2.31 that take a depressed cubic form, a is solved for using a standard least-squares fit governed by the generalized reduced gradient algorithm. Poor agreement of the models is observed when elastic strain energy is considered. By separating the kinetic energy and elastic strain energy contributions and comparing predicted fragment sizes to the steel cylindrical data, good agreement over the data range is obtained when only the local kinetic energy is considered.

In this work, three separate models looking at different reference frames of a fragmenting body, all based on the same foundational principles of thermodynamic equilibrium through fracture, demonstrate good alignment to the experimental data only when local kinetic energy is considered. This behavior is demonstrated in two distinctly different experimental fragmentation data sets of high-strength, brittle steels of varying strength and ductility. This suggests a strong potential for this behavior to be representative of general dynamic fragmentation events at strain rates on the order of or greater than 10^3 s^{-1} (based on comparisons in Figure 2.4). The comparisons of the models to experimental data in Figure 2.5 and 2.6 indicate that even when appropriate limits of the yield strength are applied, poor alignment of nominal fragment size predictions can be expected when elastic strain energy is assumed to contribute to the dynamic fragmentation event. This implies that the energy assumed to participate in the fragmentation event is incorrectly estimated when elastic strain energy is considered. This observation carries significant weight as this behavior has been alluded to by other works[63, 64], but has never been rigorously verified against experimental data. While it is recognized that the verification efforts in this work are not exhaustive, based on the above results it is reasonable to conclude that the elastic strain energy of a material is indeed uncoupled from the dynamic fragmentation process under high strain rate conditions (typically strain rates greater than 10^2). This conclusion reaffirms both Glenn and Chudnovsky's[63] observa-

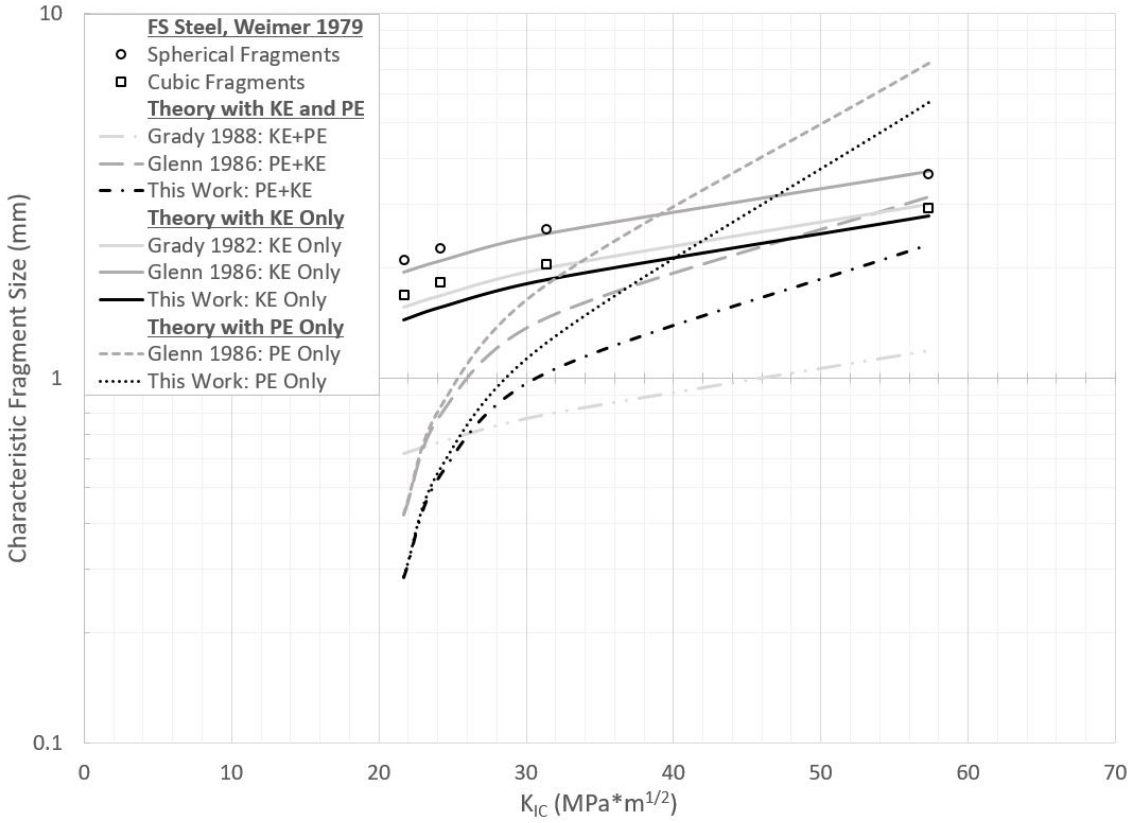

Figure 2.5: The corrected Grady model[61], Glenn and Chudnovsky's model[63], and the model derived in this work that account for elastic strain energy (PE) and kinetic energy (KE) as well as the early Grady model[60] which considers kinetic energy only compared to experimentally determined nominal fragment sizes of high strength, brittle FS-01 steel. Poor agreement of the models is observed when elastic strain energy is considered.

tions and the fundamental error in the later work by Grady[55, 61] that assumed elastic strain energy to be the sole contributor to dynamic fracture.

It is unclear why the elastic strain energy appears to be uncoupled from the dynamic fragmentation process at the strain rates discussed here. One possibility is that the dynamically loaded body fails through the coalescing of cracks driven by the dynamic event faster than the body can respond elastically. This concept was explored theoretically by Glenn et al.[64] in later work. Observations from their theoretical approach indicated that kinetic energy would dominate at high loading rates as observed here and elastic strain energy would dominate under quasi-static conditions. These observations align with those made by other research efforts[103, 109, 111] and traditional predictions by Griffith[107]. It was proposed that there is likely a transitional regime where both the elastic strain energy and kinetic energy contribute, but limits bounding this regime were not

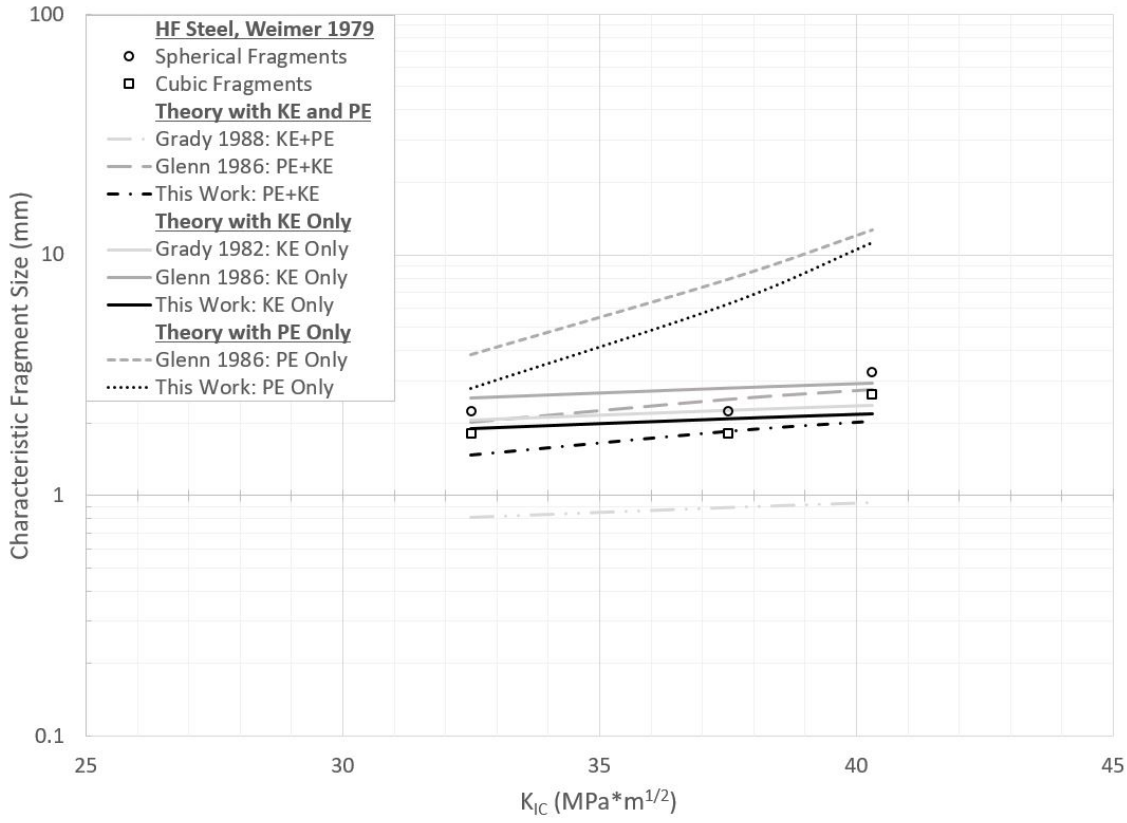

Figure 2.6: The corrected Grady model[61], Glenn and Chudnovsky's model[63], and the model derived in this work that account for elastic strain energy (PE) and kinetic energy (KE) as well as the early Grady model[60] which considers kinetic energy only compared to experimentally determined nominal fragment sizes of high strength, brittle HF-1 steel. Best agreement appears to be for the models that only consider kinetic energy.

established. Unfortunately, the lack of comparison to experimental data leaves the theory unvalidated. More recent works have explored the contributions of strain energy on fracture using phase field fracture models[117], but these theoretical endeavors only explored fracture at strains rates of 10^2 s^{-1} or less and lacked experimental verification. It would be a worth while endeavor for future works to explore why the elastic strain energy appears to be uncoupled from a dynamic fragmentation process at high strain rates and establish regimes that describe which energy of the system is the primary contributor to fracture.

For the case when only the local kinetic energy is considered, the model derived by this work generally underpredicts with an average magnitude of error of 28% for spherical fragments and 11% for cubic fragments; Glenn and Chudnovsky's[63] model generally underpredicts for spherical fragments and overpredicts for cubic fragments, with an average magnitude of error of 5% for

spherical fragments and 20% for cubic fragments; and Grady's[60] early model generally underpredicts, with an average magnitude of error of 22% for spherical fragments and 5% for cubic fragments. When comparing to the HF-1 steel fragmentation data from Weimer and Rogers[115], good agreement of the models is again observed only when kinetic energy is considered. When only the local kinetic energy is considered, the model derived by this work generally underpredicts with an average magnitude of error of 24% for spherical fragments and 9% for cubic fragments; Glenn and Chudnovsky's[63] model generally overpredicts, with an average magnitude of error of 11% for spherical fragments and 26% for cubic fragments; and Grady's[60] early model generally underpredicts, with an average magnitude of error of 18% for spherical fragments and 11% for cubic fragments.

It is interesting that despite the spherical fragment assumption employed by the models, Grady's[60] early model and the model derived by this work align best when a cubic geometrical transform is applied to the Mott parameter while the Glenn and Chudnovsky's[63] model best aligns when a spherical geometrical transform is used. It is tempting to let this observation suggest there is a relationship between the observed alignment to the experimental data and the reference frame employed by the models, where Grady[60] and this work look at the energy of the fragments themselves and Glenn and Chudnovsky[63] look at the energy of the dilating body. However, this very well could be a reflection of the challenges in transforming experimental fragment mass distributions from literature into spatial scale distributions. Without the ability to look at Weimer and Rogers'[115] fragments, a firm conclusion of the existence of a particular relationship cannot be drawn.

In light of the above, an argument of which model is optimal is limited by comparisons to Weimer and Rogers' data [115]. A better approach may be to identify the set of models that best bound the nominal fragment size produced from a dynamically fragmenting body. As shown, model alignment strongly depends on the assumed shape of the fragments, and fragments are rarely purely spherical or cubic in shape. As such, it is reasonable to take Glenn and Chudnovsky's[63] model as the upper bound of nominal fragment sizes and Grady's[60] model or the model derived by this work as the lower bound. While the early form of the Grady model[60] is of primary interest given its widespread use in the field of RM and defense, all three models will be assessed against the fragmentation data generated by this work to ascertain the best approach for RM systems. Henceforth, the term Grady model directly refers to Equation 2.18 and the associated assumptions and is repeated for convenience here as Equation 2.41. Assuming only kinetic energy contributes to the dynamic fragmentation process, and reforming to predict nominal fragment size, Glenn and Chudnovsky's fragmentation model[63] minimizing the energy of the bulk (MEB) takes the form given by Equation 2.42 and the fragmentation model minimizing the energy of the fragment (MEF) derived in this work takes the form given by Equation 2.43:

$$\lambda = \left(\frac{\sqrt{20} K_{IC}}{\rho C_o \dot{\varepsilon}} \right)^{2/3} \tag{2.41}$$

$$\lambda_{MEB}^3 + 40 \left(\frac{K_{IC}}{\rho C_b \dot{\varepsilon}} \right)^2 \left(\frac{\lambda_{MEB}}{2R_{db}} - 1 \right) = 0 \tag{2.42}$$

$$\lambda_{MEF} = \left(\frac{4K_{IC}}{\sqrt{\rho E} \dot{\varepsilon}} \right)^{2/3} \tag{2.43}$$

2.3 Heterogeneity effects on energy based fragmentation models

Recent works have highlighted the critical importance of considering heterogeneity characteristics of the material in predicting both the dynamic strength and fracture of materials[42, 51, 109, 111]. The early Grady model does not directly account for these characteristics, but as has been shown, good agreement is often obtained for brittle, granular materials. This interesting observation suggests that the Grady model indirectly accounts for the bulk average impact of material heterogeneity through the measured material properties used by the model. Recognizing that the Grady model is a function of the material properties ρ, C_o, and K_{IC}, it is suspected that the combined heterogeneity effects on these properties permit the model to reasonably approximate the fragmentation process of brittle, granular materials despite the simplistic theory applied.

Prior works have shown that density and wave speeds are primarily functions of the porosity and composition of the material[43, 118, 119]. The fracture toughness is a mechanical property that represents the energy required to fracture a material that contains cracks, and prior works suggest it should be dependent on porosity, particle size, composition, and the specific characteristics of the microstructure[106, 120, 121]. Grady[62] and Glenn et al.[64] suggested the fracture toughness also increases under dynamic loading, similar to how material strengths are known to increase under dynamic load[42, 51]. Tang and Hooper[12] observed a negligible difference in fracture toughness measurements between strain rates of 10^{-2} and 10^{1}, and reported that the use of the static Mode-I fracture toughness at higher strain rates may be appropriate for brittle RMs. From a perspective of fracture mechanics, this is a negligible difference in strain rate from which Tang and Hooper[12] drew their conclusion[102]. However, good agreement of the Grady fragmentation model[60] with experimental results of brittle RM materials at high strain rates suggests loading rate dependence of the fracture toughness of RM systems is small compared to the heterogeneity dependencies. This is not unexpected for brittle materials[102].

In light of the above observations, it is hypothesized that the effects of heterogeneity of the material on the fracture behavior are primarily captured by the

fracture toughness in the Grady model. This aligns with literature observations where the measured K_{IC} of RM systems is regularly an order of magnitude lower than the K_{IC} of the constituent homogenous materials[11, 12], and good agreement of the Grady model is only observed when the K_{IC} is known through experimental measurements[5, 12]. To confirm this hypothesis, this work will consider heterogeneity effects on all parameters used by the Grady model and assess the magnitude of impact.

2.4 Prediction of bulk material properties

For heterogeneous, granular materials, prediction of bulk properties is of interest to multiple fields of research including ceramics[43–45, 122, 123], pharmaceuticals[124, 125], powder metallurgy[43, 126], metallic foams[127–129], geology[130], and RM systems[86, 131]. Composition[86, 124, 125, 130, 131] and porosity[43, 127–129] dependencies are the typical focus of research efforts. However, efforts in literature have also focused on heterogeneity effects such as those associated with grain/particle size, particle shape, and size distributions[44, 45, 126, 132].

Bulk properties are typically calculated using exact methods[133–136], self-consistent methods[130, 137–140], or statistical methods[43, 122, 130, 132, 141]. Exact methods can provide the most accurate solutions[130], but require complete knowledge of the flaw structure, geometry, orientation, interface characteristics, and spatial distribution of all constituent components at all locations within the bulk[130, 132]. As a result, solutions are material specific[130] where numerical simulations are usually the only path to finding solutions[134] and analytical solutions are not obtainable except for special cases[130, 133].

Self-consistent methods estimate the elastic response of a heterogeneous composite to a distribution of inclusions in the material by estimating the response of a uniform matrix that has the same, but yet-to-be determined, elastic properties as the composite to an isolated inclusion[130, 137]. Analytical solutions exist for specific geometries or limiting cases (such as porous solids), but it is often necessary to solve multiple equations simultaneously to obtain predictions[130, 137]. Typically, inclusions and/or particles are assumed to be ellipsoidal or spherical in shape in deriving analytical solutions[130, 137]. In cases where the geometrical characteristics of the composite microstructure correspond to the assumed characteristics in the theoretical solutions, good agreement between predictions and experimental results is observed[130].

Statistical approaches are better suited to general material theory applications[130, 132, 142], and assume the bulk property of interest does not depend on a particular sample and large sub-regions of the material are statistically identical across the bulk[43, 130, 132, 142]. Statistical approaches find application in modeling[16, 38, 134] and often provide a path to analytical approximations of material properties[43, 45, 106, 122, 132]. Arguably,

the most commonly used statistical approach is the generalized rule of mixtures (GRM)[43, 130, 132], which is often referred to as the general rule of mixtures. The GRM has been shown to approximate many material properties of heterogeneous, granular composite materials well, to include elastic moduli[43, 132], material strengths[43, 132], hardness[132], thermodynamic properties[131, 132, 143], and mass densities[131, 132]. The GRM is typically applied when determining composition or porosity effects, but is not designed to account for specific heterogeneity effects associated with grain/particle size, particle shape, and size distributions, for which empirical or semi-empirical analytical models are typically applied[44, 45, 132].

For material and mechanical properties, the GRM takes the general power-law form[43]:

$$M_c^J = \sum_{i=1}^{N} (\forall_{f,i} M_i^J) \tag{2.44}$$

Here, the GRM approximates the bulk material property (e.g. density, elastic modulus, etc.) of a composite material, M_c, as a volume fraction weighting of individual component properties. The individual component property of the ith component, M_i, is multiplied by the respective volume fraction, $\forall_{f,i}$, and the product summed over all N components. The material property that is weighted by the volume fraction is scaled by a fractal parameter, J, to account for effects of microstructure. For cases where J is not equal to unity, J must be determined experimentally for the specific material property of interest[43]. Inspection of Equation 2.44 shows it to be a continuous, monotonic function for the range of fractal parameters between $-\infty > J > +\infty$. Typical values of J for material parameters such as moduli, strengths, and wave speeds are less than or equal to unity[43, 122].

Equation 2.44 can be used to describe both the composition and porosity dependence of materials. For systems comprised of constituents with similitude in the order of magnitude of moduli and material strengths, the linear form of Equation 2.44 approximates the composition dependencies well[144]. This implies composition dependencies for systems comprised of similar materials are independent of the microstructure as $J = 1$ [132, 143]. Porosity dependencies are generally strongly influenced by microstructure characteristics[43, 132, 143], and therefore $J \neq 1$. For estimating the effects of porosity, it is generally assumed that the material phase which comprises the pores provides negligible additive contribution to the bulk material response[43, 132]. This is based on the simple observations that the material property of the pore material phase, M_p, is often an order, and in some cases orders of magnitude, less than the material properties of the surrounding materials, such that $M_p << M_1, M_2, ...M_N$. Application of the GRM has been demonstrated for materials with porosities ranging from less than 10% to greater than 90% as seen with metal foams[127, 128]. One observation that is rarely discussed in literature is that the J parameter is not constant, and varies over different ranges of porosity as a result of different microstructure effects dominating the material behavior[127, 128, 132]. Kovacik[122, 145] identified a

general porosity limit of 20% for a constant value of J, after which microstructure effects begin to vary as porosity increases, thus changing the value of J. It is noted that alternative models have been proposed that provide more accurate treatment of materials[132, 141, 143], but these models are semi-empirical and require additional parameters that must be determined through experiments or modeling that limit their general application to materials[132, 143].

For thermodynamic properties of the bulk material, composition dependencies dominate, and the GRM takes the general linear mass fraction form[132]:

$$E_{TP,c} = \sum_{i=1}^{N} (Y_i E_{TP,i}) \tag{2.45}$$

Here, the GRM approximates the bulk thermodynamic property (e.g. specific heat, internal energy, etc) of a composite material, $E_{TP,c}$, as a mass fraction weighting of the individual component properties, $E_{TP,i}$. The individual component property of the ith component is multiplied by the respective mass fraction, Y_i, and the product summed of all N components. This form of the GRM assumes the components are uniformly connected, and generally provides good agreement for compositional dependencies[131, 132]. However, for some properties such as specific heat, the mass fraction based GRM may underestimate the bulk thermodynamic behavior by up to 10% due to connectivity effects associated with the microstructure[132]. To account for microstructure effects, empirical relations are used and are specific to the material studied[132].

Particle size effects on bulk material properties are generally qualitatively understood, but quantitatively described using empirical or semi-empirical models. Literature efforts have shown that the elastic modulus of a wide range of granular composite materials can be assumed to be independent of particle size and shape in most applications[44, 122, 132]. However, pore geometry is known to strongly influence the elastic modulus at high porosity, which is partially dependent on the particle size and shape of the constituents[45]. Reviews of existing literature by Spriggs et al.[44], Kovacik[122], Ji et al.[43], and Choren et al.[141] suggest that pore geometry effects, and therefore particle size and shape effects, can be ignored when approximating the elastic modulus for materials with porosities of 20% or less.

It has been shown that the strength of heterogeneous granular composites is inversely proportional to the average size of the constituent particles[44, 45, 126, 132]. In studying the strength of sintered Al_2O_3 with average particle sizes between 1 and 250 µm, Spriggs et al.[44] proposed that the transverse bending strength, σ_{TB}, can be described as:

$$\sigma_{TB} = C \cdot S_c^{-1/3} \tag{2.46}$$

where C is an empirical constant and S_c the average constituent particle or grain size in µm. Assuming σ_{TB} has units of MPa, inspection of Equation 2.46 indicates the empirical constant C must have units of MPa·µm$^{1/3}$. This implies a physical

meaning of C, equivalent to the transverse bending strength of the bulk material with an average constituent particle or grain size of 1 µm.

Carniglia[45] reported an inverse square-root dependence on particle size for the uniaxial compressive strength of ceramics at or near room temperature. However, based on review of available literature, German[132] reported that viable general strength models for granular composites are not available. German did recommended the semi-empirical Hall-Petch relation[146] as a first-order approximation of composite material strengths (e.g. compressive, shear, or tensile strength) in relation to average particle size:

$$\sigma_c = \sigma_{o,d} + K_g \cdot S_c^{-1/2} \tag{2.47}$$

In the context of a granular composite, the material strength of the composite material, σ_c, is a function of an experimentally determined material constant that is equivalent to the stress required for particle dislocation, $\sigma_{o,d}$, average constituent particle or grain size, and a experimentally determined sensitivity parameter, K_g[146]. Similar to the form proposed by Carniglia[45], material strength varies with the inverse square-root of the microstructure scale. However, the Hall-Petch relation is known to deviate from real material behavior when particle or grain sizes approach the nano-scale[147] and is intended for use in capturing the effects of grain dislocation and grain boundary interactions of ductile materials[147] which may preclude its application to brittle materials.

Recent research has challenged the uniqueness and theoretical validity of the inverse square-root form of the Hall-Petch relation [148]. In Li et al.'s[148] review paper, Bayseian Meta-Analysis was used to evaluate the fit quality of the Hall-Petch relation to 61 data sets, many of which prior authors used to justify the theoretical validity of the Hall-Petch relation and its inverse square-root form. Also evaluated were generalized power law, exponential, and logarithmic based models alongside the Hall-Petch relation. Li et al. found that these alternative models provided equal or better fitment to the data when compared to the Hall-Petch relation, and that the exponent in the Hall-Petch relation can vary from $-1/2$ and still provide good results because of the number of free-fitting parameters in the model. This aligns with work by other authors in literature who chose different exponent values applied to the grain size term or model forms and reported good agreement[44, 148]. Li et al.[148] suggests the Hall-Petch relation is a valid empirical relation, making it useful for prediction, interpolation, and extrapolation for specific materials, but there is likely little physical meaning to the inverse-square root form of the equation as well as the specific values of the parameters.

Parameterization models are generally applied to account for the cumulative effects that composition and microstructure have on bulk material properties[45, 126, 132, 149]. These parameterization models provide simple representation of the cumulative effect as the product of the individual effects associated with the composition and microstructure, and have shown good agreement with experimental results in literature[45, 126, 132]. Accounting for the effects due to composition, porosity, and particle size on a heterogenous, granular composite material

yields a general parameterization form comprised of three functions:

$$M_c = F_{M,1}(C) \cdot F_{M,2}(p) \cdot F_{M,3}(S_c) \tag{2.48}$$

Where the bulk material property of the composite material is the resultant product of the dependency functions of composition, $F_{M,1}(C)$, porosity, $F_{M,2}(p)$, and particle size, $F_{M,3}(S_c)$, of the material property of interest. Equation 2.48 is a generalized expression, and it is important to recognize that in application the functional dependencies for each material may best be incorporated as a unique function within another dependency function.

The prediction of the density of a heterogeneous composite material is well defined in literature[132]. However, the prediction of the wave speeds and Mode-I fracture toughness are enduring challenges[123, 132, 150]. For the Mode-I fracture toughness, qualitative relations to composition and heterogenity characteristics of the microstructure have been reported[106, 132], but definitive models which are reasonably accurate remain elusive[132]. For wave speed, work in literature either applies Equation 2.44 by experimentally determining the fractal parameter, J[43], or by employing analytical approximations that relate wave speeds to the moduli of the material[123, 150]. These relations allow the knowledge of the composition and microstructure dependencies of the elastic modulus, which is often better understood[43, 122], to inform the prediction of wave speeds. To reduce error by stacking of approximations, and because extensive research exists on predicting the elastic modulus of heterogenous, granular composite materials, the Grady model is reformed here to be a function of elastic modulus, E, rather than the bar wave speed. This is accomplished by reversing the 1D elastic theory relation of $C_o = \sqrt{E/\rho}$ applied by Grady[60] in representing C_o as a function of ρ and E. This reversal yields:

$$\lambda = \left(\frac{\sqrt{20} K_{IC}}{\sqrt{E\rho}\dot{\varepsilon}} \right)^{2/3} \tag{2.49}$$

The recasting of the Grady equation to be a function of elastic modulus removes the 1D elastic theory relation originally applied by Grady[60], a relation with questionable integrity for heterogeneous, granular materials[43] as a result of wave scattering and attenuation by the microstructure[123, 135, 136, 150]. Comparisons of nominal fragment size predictions by Equation 2.49 and the unreformed Equation 2.18 to Weimer and Rogers'[115] fragmentation data of high-strength steel reveals less than a 1% change in predicted nominal fragment size. This supports that the removal of the relation should have a negligible impact on predictions for homogeneous, isotropic materials.

2.5 Developed material property models

The engineering and application design of RM systems requires knowledge of the material's elastic properties and strengths in addition to the fragmentation

behavior. Knowledge of material strengths, such as yield strength or ultimate compressive strength, is important for constitutive model development[9, 49] and structural applications[1, 7, 8]. In order to provide a predictive means of a characteristic, or nominal, fragment size for an RM system that does not rely solely on experimental values of material properties, it will be necessary to establish predictive tools for the density, elastic modulus, and Mode-I fracture toughness. As discussed in Section 1.5, this work will focus on predictive theories for addressing the dependence these bulk material properties have on composition, porosity, and particle size.

The density of a material is dependent on the composition and porosity, but not the particle size of the material[132], such that the particle size dependency function in Equation 2.48 is $F_{\rho,3}(S_c) = 1$. The composition dependence, $F_{\rho,1}(C)$, and porosity dependence, $F_{\rho,2}(p)$, of the composite material density are readily described using linear ($J = 1$) GRMs[132]. Accordingly, the density of an RM system will be approximated in this work by the parameterized form:

$$\rho_c = F_{\rho,1}(C) \cdot F_{\rho,2}(p) \cdot (1) = \sum_{i=1}^{N} (\forth_{f,i} \rho_i)(1 - p) \tag{2.50}$$

Where ρ_c is the density of the bulk material, p is the porosity of the material, $\forth_{f,i}$ the volume fraction of the ith component, and ρ_i the density of the ith component.

The composition dependence of the elastic modulus of a composite material can generally be described using the linear form of the GRM[132]. Two models are typically applied in determining the elastic modulus dependence on composition: isostrain and isostress. The isostrain model is often referred to as the Voigt average, and the components of the composite material are assumed to carry the same strain, but vary in stress[130]. The isostress model is often referred to as the Reuss average, and the components of the composite material are assumed to care carry the same stress, but vary in strain[130]. The Voigt average is presented as Equation 2.51, and takes the traditional form of the linear GRM ($J = 1$)[130]. The Reuss average is presented as Equation 2.52, and takes the inverse form of the linear GRM ($J = -1$)[130]:

$$E_{c,v} = \sum_{i=1}^{N} (\forth_{f,i} E_i) \tag{2.51}$$

$$E_{c,r} = \left[\sum_{i=1}^{N} (\forth_{f,i} / E_i) \right]^{-1} \tag{2.52}$$

Where E_i is the elastic modulus of the ith component.

These models assume isotropic behavior of the individual components and of the bulk composite material, an assumption which may not always hold true for heterogeneous, granular composite materials. However, literature efforts have shown that the elastic modulus of most heterogenous, granular composite

materials are bounded by these two models[130, 132, 144]. A common first approximation of the elastic modulus of a heterogeneous, granular composite material based on the composition proportions is the mean of the two models, where errors within 3% can be obtained[132]. The average of the two models takes the form:

$$E_{c,r} = \frac{\sum_{i=1}^{N}(\forall_{f,i}E_i) + \left[\sum_{i=1}^{N}(\forall_{f,i}/E_i)\right]^{-1}}{2} \tag{2.53}$$

Recently, Luo[144] proposed a revised form of Equation 2.53. To better estimate elastic properties of particulate composites, Luo isotropized the Voigt and Reuss models in a volume element based on the equivalence of normal and shear strain energy. Validation of the model showed good agreement to particulate composites with similitude moduli, such as tungsten carbide and cobalt composites, and particulate composites with moduli that differed by orders of magnitude, such as glass and epoxy composites. Given the demonstrated wide applicability and validation for particle composites, this work will apply Luo's Isotropic V/R model[144]. The composition dependence of the elastic modulus, $F_{E,1}(C)$, of an RM system will be approximated using:

$$F_{E,1}(C) = \frac{2}{\left[\sum_{i=1}^{N}(\forall_{f,i}E_i)\right]^{-1} + \sum_{i=1}^{N}(\forall_{f,i}/E_i)} \tag{2.54}$$

The porosity dependence of the elastic modulus of a composite material is best described using the power-law form of the GRM[43, 122, 132, 141]. Assuming that the material phase which comprises the pores provides negligible additive contribution to the bulk material response, the porosity dependence of the elastic modulus of a porous material is approximated using[132]:

$$E_p = E_o(1-p)^{1/J_E} \tag{2.55}$$

Here, the elastic modulus of the porous material, E_p, is the product of E_o that corresponds to the full density material, and the material volume fraction determined using the porosity scaled by one over the the elastic modulus fractal scaling parameter, J_E. For a multi-component material, E is the elastic modulus of the material with composition dependence considered at full density, and thus is equivalent to $F_{E,1}(C)$. Therefore, the porosity dependence of the elastic modulus, $F_{E,2}(p)$, of an RM system will initially be approximated in this work using:

$$F_{E,2}(p) = (1-p)^{1/J_E} \tag{2.56}$$

The fractal parameter must be determined experimentally for each RM system if exact values are to be obtained. However, boundaries can be identified for the parameter to guide this work. German[132] reported values of J_E between

0.25 and 0.33 for heterogeneous, granular materials. Ji et al.[43] reported J_E values for brittle metal oxide compacts of between 0.241 and 0.284. Good agreement using these values of J_E were shown for porosities less than 20% for all materials considered[43], aligning with expectations reported by German[132] and the porosity limit for a single J value proposed by Kovacik[122, 145].

In literature, reported porosities of RM systems are typically less than 10%[2, 11, 12] and no more than 20%[4, 5, 16, 37]. The limited range of porosity studied in RM systems is likely associated with minimum material strength requirements for potential applications, as up to a 60% reduction in material strength can be expected for materials with porosities of 20%, with further reductions in strength with increasing porosity[43, 126]. This is the result of increasing flaws in the material with increasing porosity, leading to easier fracture and failure of the material at lower loads[132]. Recognizing that RM systems commonly display brittle behavior in literature, are comprised of metallic and metallic oxide components, and are less than 20% porosity for application reasons, it is expected that values of J_E will be between 0.24 and 0.29 for metallic RM systems. This expectation will be evaluated in this work, in addition to the effects polymers have on J_E for metallic/polymer RM systems. As discussed previously, the elastic modulus of heterogenous, granular materials is generally assumed to be independent of particle size for porosities of 20% or less[44, 122, 132]. Given that RM systems are generally less than 20% porosity in application, based on prior works[44, 122, 132] it is expected that the particle size dependence function of the elastic modulus will be equal to unity, such that $F_{E,3}(S_c) = 1$. Therefore, the elastic modulus of an RM system will be approximated in this work by the following parameterized form:

$$E_c = F_{E,1}(C) \cdot F_{E,2}(p) \cdot (1) = \frac{2}{\left[\sum_{i=1}^{N}(\forall_{f,i}E_i)\right]^{-1} + \sum_{i=1}^{N}(\forall_{f,i}/E_i)}(1-p)^{1/J_E} \quad (2.57)$$

Determining the compositional dependence of material strengths of a heterogeneous, granular composite material is reported to be unpredictable in practice[132]. This is the result of microstructure influences, which include interface between constituent particles, phase connectivity, particle size and shape, and the relative magnitude between material strengths and moduli of the constituent phases. Prior works have typically focused on predicting tensile strength[43, 126, 132] and little discussion of predictive methods for yield or compressive strengths have been made in relation to composition[43]. Regardless, reliable constituent strength models are lacking for predicting the composition dependencies of material strength[132].

This work will assume that the compositional dependence of material strengths is similar to the dependence of the elastic modulus. This is based on the observation that in the elastic loading regime of a material, the developed stress is proportional to the applied strain as given by the elastic modulus. As such, it is expected the material strength will exhibit a similar proportional

response to composition. This work will approximate the composition dependence function for the yield and compressive failure strengths, $F_{\sigma,1}(C)$, using the Isotropic V/R model[144], taking the form:

$$F_{\sigma,1}(C) = \frac{2}{\left[\sum_{i=1}^{N}(\not{V}_{f,i}\sigma_i)\right]^{-1} + \sum_{i=1}^{N}(\not{V}_{f,i}/\sigma_i)} \tag{2.58}$$

Where σ_i is the material strength of interest of the ith component.

The porosity dependence of the strength of heterogenous, granular composite materials is generally better understood, but predictive analytical models are semi-empirical. The porosity dependence of the yield or compressive strength of a heterogenous, granular composite material is generally best described using the power-law form of the GRM[43, 45, 132]. Assuming that the material phase which comprises the pores provides negligible additive contribution to the bulk material response, the porosity dependence of the material strength of a porous material is approximated using[43]:

$$\sigma_p = \sigma_o(1-p)^{1/J_\sigma} \tag{2.59}$$

Here, the material strength (yield or compressive) of the material, σ_p, is the product of the full density material strength, σ_o, and the material volume fraction determined using the porosity scaled by one over the material strength fractal scaling parameter, J_σ. For a multi-component material, σ_o is the strength of the material with composition dependence considered at full density, and thus is equivalent to $F_{\sigma,1}(C)$. Therefore, the porosity dependence of the material strength, $F_{\sigma,2}(p)$, of an RM system will be approximated in this work using:

$$F_{\sigma,2}(p) = (1-p)^{1/J_\sigma} \tag{2.60}$$

The fractal parameter, J_σ, must be determined experimentally for each RM system if exact values are to be obtained. Ji et al.[43] reported $J_\sigma = 0.14$ for the compressive strength of a copper/copper(I) oxide (Cu/Cu_2O) granular composite material, with good agreement of the power-law GRM observed for porosities less than 20%. Ji et al.[43] also reported a potential universal value of $J_\sigma = 0.25$ for the tensile strengths of sintered and un-sintered metal compacts of a variety of compositions. Good agreement using these values of J_σ were shown for porosities less than 20% for all materials considered[43], suggesting the potential for universal fractal parameters for different material strengths.

Material strength is known to have a strong particle size dependency[44, 132]. For approximating the particle size dependency, German[132] recommends the semi-empirical Hall-Petch relation given as Equation 2.47. However, this relation does not lend itself to application in a parameterized model as the functional form is for predicting the total bulk behavior, including composition effects, by experimental fitting of two parameters: $\sigma_{o,d}$ and K_g. To incorporate particle size effects, this work will generalize the Spriggs equation[44] using Li's[148] work to

inform the process. This generalized form of the Spriggs equation, which is an inverse power-law relation, is given by:

$$\sigma(S_c) = \sigma_{1\mu m} \cdot (S_c/1\mu m)^{-n_\sigma} \tag{2.61}$$

Where $\sigma_{1\mu m}$ is an empirical constant that represents the material strength of interest when the bulk is comprised of an average constituent particle or grain size of 1 µm and n_σ is effectively a sensitivity parameter describing the bulk material strength relationship to particle or grain size. To maintain consistency of units, S_c has units of µm and is normalized by 1 µm. The generalized form of the Spriggs equation requires two parameters to be determined, both of which have clearly defined physical meaning.

To incorporate Equation 2.61 into the parameterized model form used in this work, it is necessary to apply the model to the individual constituents only. This approach permits the particle size dependency of the constituents to be determined without the interference of compositional influences, and then weighted by the compositional dependency described by Equation 2.58 and porosity dependency described by Equation 2.60 to estimate the material strength of a composite of the constituents. This assumes that the particle size dependencies are minimally affected by interaction of the constituent particles. The validity of this assumption is likely questionable, but the extent of the impact of interactions on the model predictions is unknown and warrants evaluation. Combining the dependency functions given by Equations 2.58 and 2.60 and applying Equation 2.61 to the constituents, the yield and compressive strength of an RM system is approximated in this work by the following parameterized form:

$$\sigma_c = F_{\sigma,1}(C) \cdot F_{\sigma,2}(p) \cdot F_{\sigma,3}(S_c) = \frac{2}{\left[\sum_{i=1}^{N}(\Psi_{f,i}\sigma_i)\right]^{-1} + \sum_{i=1}^{N}(\Psi_{f,i}/\sigma_i)}(1-p)^{1/J_\sigma} \tag{2.62}$$

$$\text{where: } \sigma_i = (\sigma_{1\mu m,i} \cdot (S_{c,i}/1\mu m)^{-n_{\sigma,i}}) \tag{2.63}$$

Analytical theories for predicting the Mode-I fracture toughness of heterogenous, granular composite materials with a reasonable degree of accuracy are currently an enduring field of research[29, 106, 120, 132]. The fracture strength of a heterogenous, granular composite material primarily depends on composition and the characteristics of the microstructure. Specific microstructure characteristics that are suspected to have strong influence on K_{IC} include the interface strengths between constituent particles, the size and shape of constituent particles, and porosity[29, 106, 120, 132]. Indirect approaches have found use in providing insight to potential fracture toughness behavior, where properties such as strength, ductility, and hardness provide a basis for predicting fracture toughness[106, 132]. However, microstructure influences tend to limit these indirect approaches to qualitative assessments[132].

The composition dependence of K_{IC} has been shown experimentally to be linearly proportional for some granular composites such as tungsten carbide/-cobalt (WC/Co) composite materials[132] and glass-epoxy materials[106]. However, other materials demonstrate a defined peak in fracture toughness that does not align with linearly increasing content of one or more constituents. This is suspected to be the result of uncharacterized microstructure effects[132]. For example, aluminum oxide/zirconium dioxide (Al_2O_3/ZrO_2) materials with a nominal particle size less than 2 µm have a distinct peak in fracture toughness at a ZrO_2 content volume fraction of 0.15 [132].

Particle size and porosity effects are less understood, but typically have the highest impact on fracture toughness. Prior works have shown these mesoscale characteristics of a composite material harbor other sub-dependencies such as the interface strength between particles and the distribution of particle contact areas[29, 106, 120]. Porosity generally has the most detrimental impact on the fracture toughness of a material, with one study observing a 50% decrease in K_{IC} with 1% porosity, and 90% decrease in K_{IC} with 10% porosity[132]. Experimental efforts have shown that the porosity dependence of metal powder composites may take the form of an inverse power-law[151]. Alternatively, other experimental efforts have shown that the porosity dependence of sintered ceramic composites may take a linear form[121]. Strengths of a material are generally observed to increase with decreasing particle size[44, 45, 132]. However, this behavior is not always observed with K_{IC}. For boron carbide/titanium carbide (B_4C/TiC) material, K_{IC} increases when the particle size is increased from 1 µm and peaks at 10 µm. Further increase in particle size beyond 10 µm decreases K_{IC} for the B_4C/TiC material[132].

This work recognizes that the fracture toughness should exhibit composition, porosity, and particle size dependencies, of which knowledge of other microstructure characteristics may be needed to resolve. Careful review of available literature[29, 44, 45, 106, 120, 132, 151] has provided no clear approach to predicting K_{IC} in relation to composition, porosity, and particle size. This work will approach estimating K_{IC} in a similar manner as the material strengths, where the compositional dependency is given by the Isotropic V/R model, porosity dependence given by the power law GRM, and the particle size dependence given by the generalized form of the Spriggs equation applied to the constituents. The parameterized form of the K_{IC} model therefore takes the form:

$$K_{IC,c} = F_{K_{IC},1}(C) \cdot F_{K_{IC},2}(p) \cdot F_{K_{IC},3}(S_c)) = \frac{2}{\left[\sum_{i=1}^{N}(\forall_{f,i} K_{IC,i})\right]^{-1} + \sum_{i=1}^{N}(\forall_{f,i}/K_{IC,i})}(1-p)^{1/J_K} \quad (2.64)$$

$$\text{where: } K_{IC,i} = (K_{1\mu m,i} \cdot (S_c, i/1\mu m)^{-n_{K,i}}) \quad (2.65)$$

Where J_K is the fractal parameter, $K_{1\mu m,i}$ is an empirical constant that represents the K_{IC} of the ith constituent when the bulk is comprised of an average con-

stituent particle or grain size of 1 μm, and $n_{K,i}$ is a sensitivity parameter describing the bulk K_{IC} relationship to particle or grain size.

The majority of the current research on predictive methods for dilatational and shear wave speed is focused on the application of numerical methods for modeling the microstructure influence on these properties[136, 152]. Limited discussion of compositional dependence[153] or particle size[154] dependence is available in literature with no definitive conclusions presented. Porosity dependence relations vary widely and are typically described using power-law relations[43, 123, 145] with varying degrees of agreement, typically between 5% and 30% of measured values for porosities less than 30%. In light of a lack of definitive analytical models for the dilatational and shear wave speeds, this work will propose a simple analytical model and address its validity. Following the parameterized form of the elastic modulus, the dilatational and shear wave speeds are assumed to be functions of composition and porosity with no particle size dependency for porosities less than 20%. Applying guidance by German[132] for cases where analytical approximations are not well defined, these dependency functions will take the form of a linear GRM. The dilatational wave speed will initially be approximated in this work by the parameterized form given as Equation 2.66. The shear wave speed will initially be approximated in this work by the parameterized form given as Equation 2.67:

$$C_{d,c} = F_{C_d,1}(C) \cdot F_{C_d,2}(p) \cdot (1) = \sum_{i=1}^{N} V_{f,i} C_{d,i}(1-p) \tag{2.66}$$

$$C_{s,c} = F_{C_s,1}(C) \cdot F_{C_s,2}(p) \cdot (1) = \sum_{i=1}^{N} V_{f,i} C_{s,i}(1-p) \tag{2.67}$$

2.6 Developed fragmentation theory

This work will apply and assess the general fragment mass-size distribution, $m_d(s)$, proposed by Hooper[27] for RM systems, which captures both power-law and exponential fragmentation behavior, presented as Equation 2.68:

$$m_d(s) = \Pi \frac{1}{s_o} \left(\frac{s}{s_o}\right)^{-\Lambda} \frac{\exp(-(\beta s)^{\Psi})}{f_{exp}(\beta s_o)} + (1-\Pi)\frac{1}{6\mu_c}\left(\frac{s+2/\beta}{\mu_c}\right)^3 \exp\left[-\left(\frac{s+2/\beta}{\mu_c}\right)\right] \tag{2.68}$$

$$where: \Lambda = (2\Psi - (\Psi k_s + 1)) \tag{2.69}$$

Using a standard least-squares fit governed by the Levenberg-Marquardt algorithm, Hooper[27] fitted the following parameters (previously defined in Chapter 1) to experimental data: k_s, β, Π, and μ_c. The s_o parameter is dependent on the experimental measurement technique and the dimensionality of the fragmenting specimen is $\Psi = 3$ as proposed by Astrom et al.[57] and Hooper[27]. This work will follow the same methodology for fitment to experimental data, and will also investigate analytical or semi-empirical methods in which the parameters can be estimated based on experimental observations in this work. Based on the observations of Hooper and peers[11, 12, 27], it is expected that β, Π, and μ_c are strain-rate dependent functions, with μ_c described reasonably well by the Grady model[27]. As shown by Hooper[27], k_s is expected to take the universal value of $k_s = 5/3$. However, k_s will be determined for all experimentally measured fragment size distributions in this work to assess the validity of the universal value for RM systems. Furthermore, this work will use a standard least-squares fit governed by the generalized reduced gradient algorithm to determine k_s, β, Π, and μ_c.

The proposed analytical models for nominal fragment size are summarized in Table 2.2. Proposed analytical models for density, elastic modulus, wave speeds, Mode-I fracture toughness, and yield and compressive strengths are summarized in Table 2.3. These models were formed assuming porosities of 20% or less of the RM material, which is the general upper porosity bound of RM systems due to application intent. The proposed analytical models are designed to describe the variation of material properties of composite mixtures when knowledge of the behavior of the individual constituents is known. It is important to recognize the models do not provide a predictive means of material response fully independent of experimental testing. However, based on careful review of the literature the models are built from, the proposed models have the potential to permit the mapping of the material response of single component granular materials and multi-component granular composites in relation to composition, porosity, and particle size with a significant reduction in experimental testing. Evaluation of the models against the experimental data generated by this work will assess the validity of the approach and guide further refinements.

Table 2.2: Summary of analytical models for predicting the nominal (characteristic) fragment size of an RM system

Approach	Proposed Model	Notes
Minimizing Energy of Dilating Bulk	$\lambda_{MEB}^3 + 40\left(\frac{K_{IC}}{\rho C_b \dot{\varepsilon}}\right)^2\left(\frac{\lambda_{MEB}}{2R_{db}} - 1\right) = 0$	Potential upper size bound
Minimizing Energy Density of Fragment	$\lambda = \left(\frac{\sqrt{20}K_{IC}}{\sqrt{E\rho\dot{\varepsilon}}}\right)^{2/3}$	Potential lower size bound
Minimizing Energy of Fragment	$\lambda_{MEF} = \left(\frac{4K_{IC}}{\sqrt{\rho E\dot{\varepsilon}}}\right)^{2/3}$	Potential lower size bound

Table 2.3: Summary of analytical models for predicting material properties of an RM system

Property	Proposed Model
Density ρ_c	$\rho_c = (1-p)\sum_{i=1}^{N}(\forall_i \rho_i)$
Elastic Modulus E_c	$E_c = \frac{2}{\left[\sum_{i=1}^{N}(\forall_{f,i} E_i)\right]^{-1} + \sum_{i=1}^{N}(\forall_{f,i}/E_i)}(1-p)^{1/J_E}$
Dilatational Wave Speed $C_{d,c}$	$C_{d,c} = \sum_{i=1}^{N} \forall_i C_{d,i}(1-p)$
Shear Wave Speed $C_{s,c}$	$C_{s,c} = \sum_{i=1}^{N} \forall_i C_{s,i}(1-p)$
Fracture Toughness σ_c	$K_{IC,c} = \frac{2}{\left[\sum_{i=1}^{N}(\forall_{f,i} K_{IC,i})\right]^{-1} + \sum_{i=1}^{N}(\forall_{f,i}/K_{IC,i})}(1-p)^{1/J_K}$ $where: K_{IC,i} = (K_{1\mu m,i} * (S_c, i/1\mu m)^{-n_{K,i}})$
Material Strength σ_c	$\sigma_c = \frac{2}{\left[\sum_{i=1}^{N}(\forall_{f,i} \sigma_i)\right]^{-1} + \sum_{i=1}^{N}(\forall_{f,i}/\sigma_i)}(1-p)^{1/J_\sigma}$ $where: \sigma_i = (\sigma_{1\mu m,i} * (S_c, i/1\mu m)^{-n_{\sigma,i}})$

CHAPTER 3

EXPERIMENTAL METHODS FOR STUDY OF REACTIVE MATERIAL FRAGMENTATION

Assessment and validation of the analytical material property and fragmentation models for RM systems proposed by this work will be performed using five experimental techniques: quasi-static compression tests, quasi-static fracture toughness tests, wave speed measurements, Kolsky bar compression tests, and high-velocity impact tests. Quasi-static compression and fracture toughness tests will be used to determine material properties for assessment of the analytical material property models. Kolsky and high-velocity impact tests will be used to drive specimens to failure at varied strain rates. For Kolsky testing, strain rates on the order of 10^3 s^{-1} will be evaluated. For high-velocity impact, strain rates between 10^4 s^{-1} and 10^5 s^{-1} will be evaluated. Fragments from these tests will be collected and analyzed to determine fragment size distributions for assessment of the analytical fragmentation models.

3.1 Quasi-static compression testing

For verification of analytical predictions, it is necessary to measure the elastic (Young's) modulus of the RM systems in this work. Quasi-static compression testing is the preferred method for this measurement instead of tensile testing as granular RM systems are generally very weak in tension[11, 37]. This leads to differences in the material response for compressive and tensile loading, as specimens may yield in compression, but fail before yield in tension. As such, this weakness under tensile loading can lead to non-representative strength or elastic modulus measurements[155]. Quasi-static compression testing also permits yield strength and ultimate compressive strength to be determined, two important structural engineering parameters.

RM specimens in this work are loaded under unaxial stress to failure at room temperature using a UTM in accordance to the methods outlined by the American Society for Testing of Materials (ASTM) E9 Standard: Standard Test Methods of Compression Testing of Metallic Materials at Room Temperature[155]. The ASTM E9 standard has been demonstrated to provide consistent, reproducible yield strength, compressive strength, and elastic modulus measurements for

materials[156]. While this standard is specific to metallic specimens, it is applicable to both ductile and brittle materials[155]. Therefore, it is expected to be suitable for both metallic and metallic/polymer RM systems. The ASTM E9 experimental testing methodology applicable to RM testing is shown schematically in Figure 3.1 and summarized as follows[155]:

- Material specimens are to be cylindrical in shape, with a length to diameter ratio (L_o/D_s) between 0.8 and 3 for diameters less than 30 mm.
- Ends of the material specimen in contact with the top and bottom anvil of the UTM should be lubricated to reduce friction.
- Load will be applied to specimens under displacement controlled conditions at a constant strain rate of 0.002 mm/mm·s^{-1}.
- Specimens will be loaded to failure.

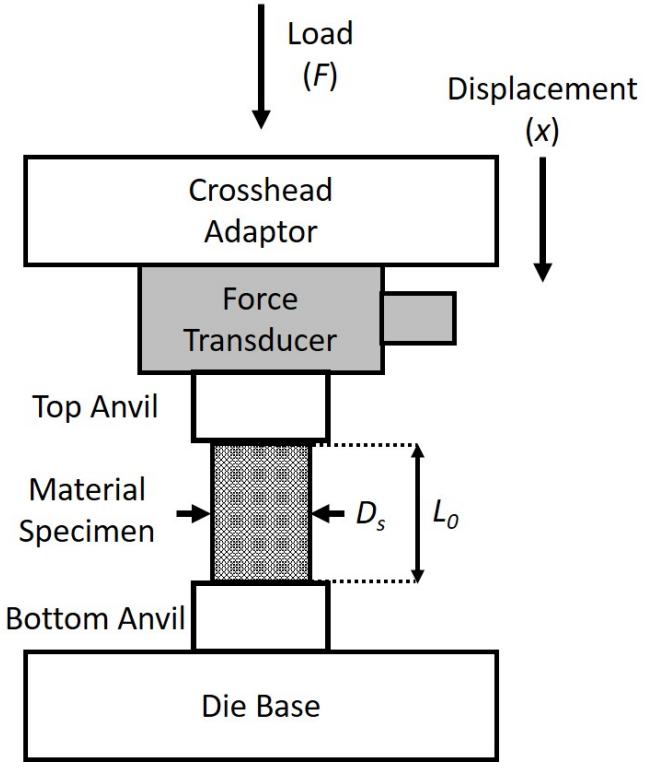

Figure 3.1: Schematic of quasi-static uni-axial compression testing. Primary components and measured properties labeled.

UTMs typically measure applied force, F, using a force transducer and cumulative displacement, x, based on the travel of the loading head. Due to limitations in structural rigidity of UTMs, a compliance correction to the cumulative

displacement is necessary to ensure the measurement accurately represents the specimen response. The compliance of a machine is determined by performing a compression test with the UTM anvils in direct contact. The measured force and displacement data then gives the compliance of the UTM as a function of applied force. The correction is performed by incrementally subtracting the compliance of the machine from the measured displacement data based on the force associated with the displacement measurement. This yields the true displacement associated with the specimen, x_{cor}. This work will use an ESM 1500 UTM equipped with a 6670 N (1500 lbf) load cell and an ATS 905 UTM equipped with a 4450 N (1000 lbf) load cell to conduct quasi-static tests. The force and corrected displacement data is converted to engineering stress and engineering strain data for a cylindrical material specimen with known diameter and length as:

$$\sigma_{comp} = \frac{F}{A_s} = \frac{F}{\pi/4 D_s^2} \tag{3.1}$$

$$\varepsilon = \frac{L_o - x_{cor}}{L_o} \tag{3.2}$$

An engineering stress-strain curve of a granular RM is presented in Figure 3.2, and is typical of the quasi-static response of an RM system. In this work the stress and strain are taken as positive for specimens in compression.

It is typical for specimens to exhibit what appears to be non-linear stress-strain behavior at the early quasi-static compression loading conditions. As seen in Figure 3.2, this is also the case with RM specimens. The non-linearity typically results from backlash in UTM components[157] and from developing contact between the specimen and bearing surfaces of the anvils at low forces[158]. This behavior is strongly influenced by the friction between the specimen and anvil surface. Friction can also affect the linear stress-strain behavior, and has been shown to impact the measured values of strength and elastic modulus when friction is high, as is the case when lubrication is not used[156, 158]. However, when friction is low, as is the case when lubrication is used, friction effects do not directly impact the measurement of the ultimate compressive strength, yield strength, or elastic modulus, and are ignored when making these measurements[157, 158].

Lubrication is highly important for ensuring the measured elastic modulus through compression experiments is comparable to that measured through tension experiments[157–159]. When friction between specimen and anvil is high, the elastic modulus becomes strongly dependent on the L_o/D_s ratio. Work by Chau[159] and Williams & Gamonpilas[158] showed corrections can be applied to align elastic modulus measurements from compression tests with measurements from tensile tests. These methods are applicable to measurements from compression tests where strain is calculated using the measured crosshead displacement, as will be done in this work. For specimens with $L_o/D_s = 1$ and Poisson's ratios less than or equal to 0.3, a no-slip end condition (high-friction) between specimen and anvil leads to a difference in elastic modulus between the two test methods of less than 4%, and increases with decreasing L_o/D_s ratio and

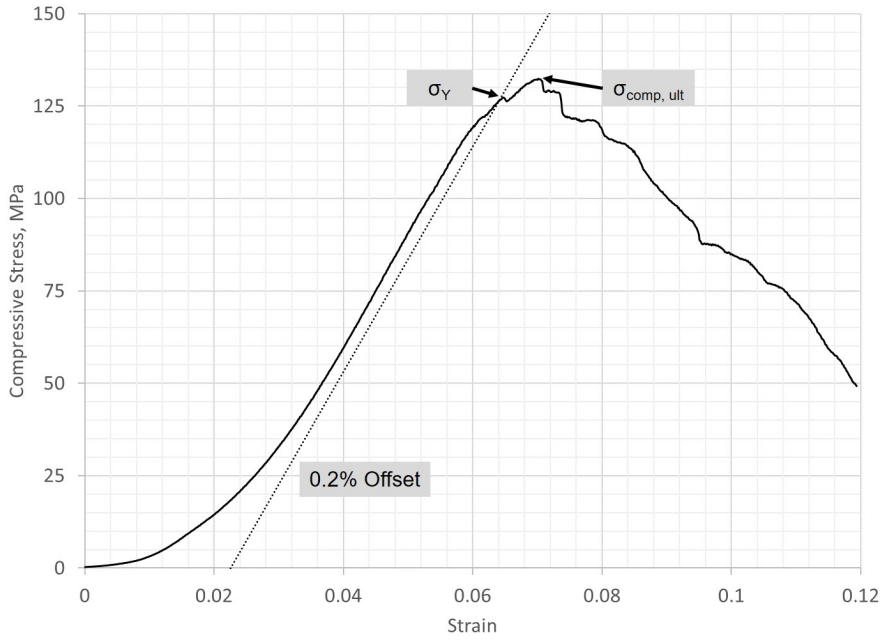

Figure 3.2: The stress-strain history typical of a granular RM composite uniaxially compressed to failure.The stress data is normalized by the ultimate compressive strength of the specimen. The 0.2% offset is plotted of the linear response portion of the curve for determining the elastic modulus and yield strength.

increasing Poisson's ratio of the material[159]. Alternatively, for the zero friction end condition, this difference is 0%[159]. Some friction between specimen and anvil is always present, even when lubrication is applied. Therefore, this work will utilize specimens with an $L_o/D_s = 1$ and lubrication to minimize this error.

From the stress and strain data, the ultimate compressive strength, yield strength, and elastic modulus can be determined. This work utilizes the MATLAB computational environment to apply processing routines to determine the strengths and elastic modulus of the material specimen from the raw force-displacement data. This is done to reduce time in bulk processing data and to minimize human error. Material property values are determined, with corresponding governing ASTM standards noted, as follows:

- Ultimate compressive strength, $\sigma_{comp,ult}$, is determined as the maximum stress obtained before failure (ASTM E9)[155].
- Elastic modulus is determined as the slope of a straight line fitted to the linear elastic region of the stress-strain curve (ASTM E111)[157]. This linear elastic region is selected manually in this work.
- Yield strength is calculated using the standard 0.2% offset method[155]. A line is plotted parallel to the linear elastic portion of the stress-strain curve

with a 0.2% strain offset, as shown in Figure 3.2. The yield strength corresponds to the intersection of the 0.2% offset line with the stress-strain curve (ASTM E9)[155].

Material property values obtained from quasi-static compression tests have an uncertainty associated with the direct measurements (e.g. force, displacement, specimen parameters) and the propagated uncertainty into calculated parameters (e.g. stresses and strains). The methodologies detailed by Taylor[160] are used here in determining these uncertainties. The uncertainties associated with direct measurements are summarized in Table 3.1. Propagated uncertainties of calculated parameters are summarized in Table 3.2.

Table 3.1: Summary of measurement uncertainties associated with the quasi-static compression tests

Measurement	Notation	Reported Uncertainty	Method of Determination
Specimen Length	δL_o	$\pm$0.02 mm	Digital Mitutoyo caliper resolution
Specimen Diameter	δD_s	$\pm$0.02 mm	Digital Mitutoyo caliper resolution
ESM 1500 Load Cell Force	δF_{ESM}	$\pm$4.5 N	ESM 1500 data sheet
ESM 1500 Displacement	δx_{ESM}	$\pm$0.01 mm	ESM 1500 data sheet
ATS 905 Load Cell Force	δF_{ATS}	$\pm$4.5 N	ATS 905 data sheet
ATS 905 Displacement	δx_{ATS}	$\pm$0.003 mm	ATS 905 data sheet

Table 3.2: Summary of propagated uncertainties associated with the quasi-static compression tests

Calculated Parameter	Reported Uncertainty	Uncertainty Equation
Specimen Stress	Test Specific	$\frac{\delta\sigma}{\sigma} = \sqrt{\left(\frac{\delta F}{F}\right)^2 + \left(\frac{2\delta D_s}{D_s}\right)^2}$
Specimen Strain	Test Specific	$\frac{\delta\epsilon}{\epsilon} = \sqrt{\left(\frac{\delta x}{x}\right)^2 + \left(\frac{\delta L_o}{L_o}\right)^2}$
Elastic Modulus	Test Specific	$\frac{\delta E}{E} \approx \sqrt{\left(\frac{\delta\sigma_y}{\sigma_y}\right)^2 + \left(\frac{\delta\epsilon_{\sigma_y}}{\epsilon_{\sigma_y}}\right)^2}$

3.2 Fracture toughness testing

Fracture toughness, K_c, is a measurable material property that quantifies a material's ability to resist fracture. The fracture toughness is proportional to the square-root of the critical energy release rate during fracture, G_{cr}. The energy release rate, G, represents the change in the total potential energy of the body per unit area of fracture surface formed, and crack growth is initiated when G overcomes the critical value G_{cr} which is nominally a material constant[102]. Fracture toughness is characterized for three modes of loading: opening, in-plane shear, and out-of-plane shear[102]. Grady[60] and Glenn and Chudnovsky[63, 64] assumed that the dynamic fragmentation of a material is predominately driven by the opening mode, or Mode-I. Agreement with experimental results supports this assumption. Thus, the fracture toughness measurement of interest for their works was K_{IC}, as it is in this work.

The Mode-I fracture toughness is generally measured using three different techniques: Crack tip opening displacement (CTOD), J-integral, and critical stress intensity factor. The CTOD and J-integral methods are well suited for materials that undergo both elastic and plastic deformation, where appreciable plastic deformation before fracture is observed[102], and are well described by the ASTM E1820 standard[161]. These methods require specific specimen geometries that can be challenging to manufacture for testing of brittle materials or granular compacts[162–165]. As such, these methods will not be considered for Mode-I fracture toughness measurements of RM systems in this work.

The critical stress intensity factor method is applicable to materials that are

nominally linear-elastic, such as brittle materials[102]. In the method, specifically designed test specimens with a predefined crack geometry are loaded to failure. For a "sharp" crack tip, the stress intensity, K, at the crack tip is:

$$K = Y_k \sigma \sqrt{\pi c_{cr}} \tag{3.3}$$

where σ is the applied stress, c_{cr} the characteristic crack dimension, and Y_K a dimensionless constant that depends on geometry and mode of loading. Equation 3.3 is valid for any σ, and at the point of initiation of crack tip advancement, the value of K corresponds to the critical stress intensity, K_C.

Determination of K_{IC} using the critical stress intensity factor method is generally governed by the ASTM E399 standard[166] which describes testing for multiple specimen geometries. Of these tests, the ASTM E399 three-point bend test is most readily used in RM research[11, 12, 27]. However, three-point bend test are generally poorly suited for measuring the fracture toughness of brittle materials[162, 163] or granular compacts[164, 165] due to challenges in manufacturing specimens. Typically for brittle materials or granular compacts, diametrical compression testing techniques (DCTTs) are preferred[151, 164, 165, 167–169]. In literature, DCTTs are often referred to as "Brazillian Disc" tests[162, 170, 171] in regards to one of the earliest forms of DCTTs originating from Brazil[172]. However, the DCTT term is a classification of experiments that encompasses the general method of diametrically compressing circular disks to failure, and will be used here to describe these types of experiments.

The diametrical compression induces tensile stresses at the center of the specimen, normal to the vertical diameter. Experimental and numerical efforts have shown compressive stresses develop near the contact regions along the circumference of the specimen, but transition to tensile stress that is found to be nominally constant over the center region of the specimen[121, 162, 167, 168, 170]. DCTTs are typically used for indirect tensile testing measurements of brittle materials and powder compacts[167], for which the ASTM D3967 standard[173] governs. The tensile stress is calculated assuming failure occurs at the point of maximum tensile stress located at the center of the specimen[170, 173]. The DCTT review paper by Li and Wong[170] and a comparative methods study by Zhang and Yu[163] showed that the tensile strengths determined using DCTT methods for heterogeneous, granular materials compare well to results from direct tensile tests. DCTT specimens for fracture toughness measurements have a machined notch, which varies in geometry[121, 151, 164, 165], located at the specimen center.

Research efforts studying the fracture toughness of granular metal and metal oxide powder compacts have utilized single-edge V-notch diametrical compression test (SVDCT) specimens with good success[121, 164]. A schematic of the specimen and applied loading is shown in Figure 3.3. A thorough description and verification of the technique is given by Clobes and Green[121] who applied the technique to porous Al_2O_3 compacts. The single edge V-notch method is preferred for granular compacts as the manufacturing of specimens for testing is significantly simplified[164]. A single V-notch is machined using a 0.3 mm thick circular diamond saw blade into one face of the cylindrical specimen[121, 164, 174].

The notch is then "sharpened" to ensure a sharp crack is present. This is typically performed using a razor blade with diamond paste on the blade tip[121]. A sharpened V-notch is required to simulate a "sharp" crack, and the root radius of the notch must be on the order of the relevant microstructural defects, such as pore or particle size, to produce accurate toughness measurements[121]. Clobes and Green report that notch radii should be less than $\leq$50 µm to provide accurate results and demonstrated this radius is readily obtainable using a razor blade with diamond paste on the blade tip[121].

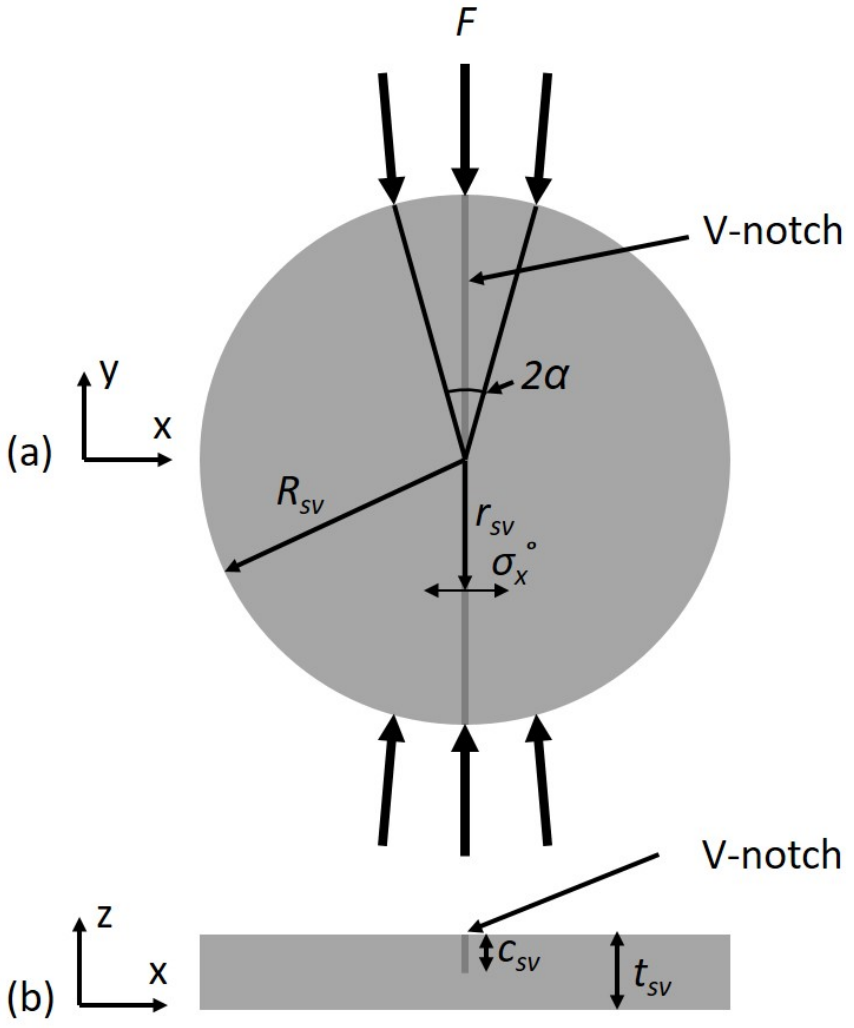

Figure 3.3: Schematic of single-edge V-notch diametrical compression (SCVDT) specimen.(a) Axial view showing V-notch extending across the surface of the disk and (b) side view showing depth of V-notch. Specimen dimensions, force, and stress parameters labeled for calculating Mode-I fracture toughness.

Crushing and plastic deformation at the contact interface of the UTM platens and specimen can negatively impact tests due to premature failure of the specimen. To mitigate this, bearing strips are used to distribute the load over the specimen circumference with an arc length with an half-angle of α. This reduces the contact pressure and helps ensures failure of the specimen along the V-notch[121]. When using bearing strips, the horizontal stress, σ_x°, along the center-line plane indicated in Figure 3.3 is[121]:

$$\sigma_x^\circ = \frac{-2F}{\pi D_{sv} t_{sv} \alpha} \left\{ \frac{[1-\bar{r}^2] sin2\alpha}{1 - 2\bar{r}^2 cos2\alpha + \bar{r}^4} + tan^{-1} \left[\frac{1+\bar{r}^2}{1-\bar{r}^2} tan\alpha \right] \right\} \tag{3.4}$$

Where $\bar{r}$ is the ratio of radial position over the total radius ($\bar{r} = r_{sv}/R_{sv}$), D_{sv} is the specimen diameter, and t_{sv} is the specimen thickness.

The peak horizontal tensile stress, $\sigma_{t,max}$, occurs at the center of the disk, where $r = 0$. The peak tensile stress is obtained by reducing Equation 3.4 to[121]:

$$\sigma_{t,max} = \frac{2F}{\pi D_{sv} t_{sv}} \frac{sin2\alpha - \alpha}{\alpha} \tag{3.5}$$

The Mode-I critical stress intensity factor of the single V-notch specimen is described by Equation 3.3 for a semi-infinite plate with an edge crack subjected to tension as[102, 121]:

$$K_{IC} = 1.12\sigma_f \sqrt{\pi c_{sv}} \tag{3.6}$$

Where σ_f is the stress at crack initiation. Combining Equation 3.5 with Equation 3.6 yields the K_{IC} for the SVDCT specimen:

$$K_{IC} = \frac{2.24 F_{ci} \sqrt{c_{sv}}}{\sqrt{\pi} D_{sv} t_{sv}} \frac{sin2\alpha - \alpha}{\alpha} \tag{3.7}$$

Where F_{ci} is the vertical load at crack initiation, and c_{sv} is the notch depth.

Fracture toughness measurements of brittle materials obtained using the SVDCT method have shown good agreement to fracture toughness measurements using traditional methods[121]. Fracture toughness measurements using SVDCT specimens have been shown to be independent of notch depth and specimen thickness[121, 174]. However, it is recommended that the notch depth, c_{sv}, should be at least $1/4$ of the specimen thickness[121]. Typical specimen diameters are 12.7 mm[121].

Based on the demonstrated successes in literature[121, 164, 174], this work will apply the SVDCT method to measure the Mode-I fracture toughness of the RM systems studied in this work. The work by Clobes and Green[121] is used to guide the specimen manufacturing and testing procedures. Referring to Figure 3.3, the SVDCT specimens are manufactured with the dimensions specified in Table 3.3. A 0.397 mm (0.015 in) diameter ball end mill is used to machine a notch into the specimens. A ball end mill is chosen over a square end mill to mitigate

the presence of any sharp machined edges which could introduce stress risers. To prevent damage to the specimen during machining, a custom clamping jig is used to axially and radially retain the specimen during the machining process. To prevent binding and breaking of the end mill in the notch during machining a constant flow of compressed air is used to clear the notch of chips. The notch is sharpened using a 0.23 mm (0.009 in) thick razor blade (American line 66-0089) coated with 4000 grit (2-4 µ m) diamond paste. This sharpening produces notches with radii less than $\leq$50 µm in line with requirements imposed by Clobes and Green's work[121]. The machining setup is shown in Figure 3.4(a).

Specimens are loaded to failure using either an ADMET eXpert 4200 UTM equipped with a 110 N (25 lbf) load cell or an ATS 905 UTM equipped with a 1100 N (250 lbf) load cell. Loading is applied at a nominal displacement rate of 0.012 mm/s. The initiation of the crack is indicated by a sharp drop in applied load and visual observation of the SVDCT specimen. Cardstock is used as bearing strips per literature[121] with lubrication applied between the cardstock and UTM platens. The thickness of this cardstock is 0.15 mm thick. The width of the impressions in the cardstock is measured to determine α. Permanent marker is applied to the contact faces of the specimen for improved identification of the impressions in the cardstock. The typical UTM setup is shown in Figure 3.4(b).

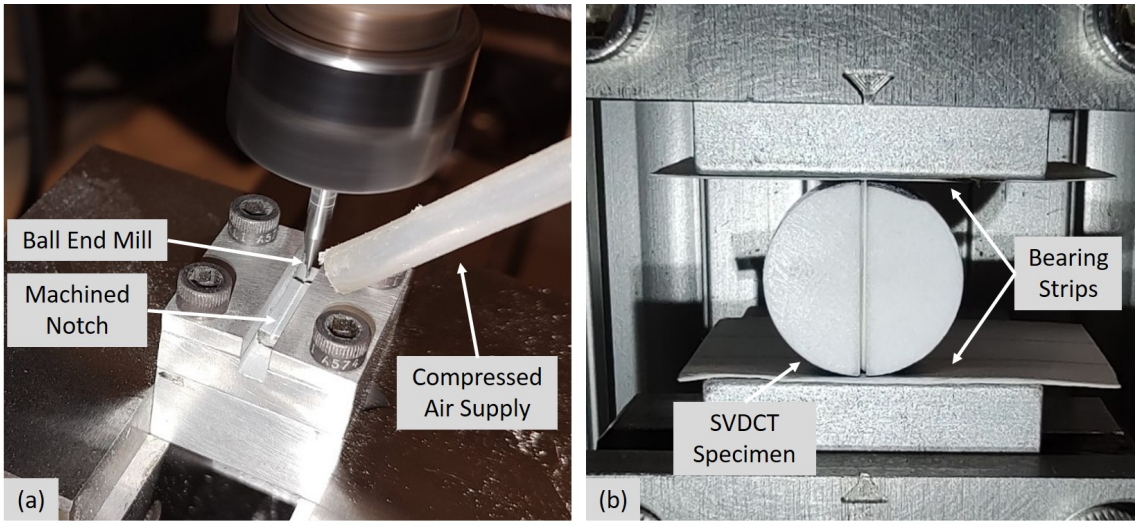

Figure 3.4: Overview of specimen machining and UTM setup with critical components labeled. (a) Machining of specimen using clamping jig and (b) typical UTM setup for testing specimens.

Table 3.3: Summary of the SVDCT specimen dimensions utilized in measuring the Mode-I fracture toughness of RM systems in this work.

System Parameter	Value	Units
Specimen Diameter D_{sv}	12.7	mm
Specimen Thickness t_{sv}	4	mm
V-Notch Depth c_{sv}	1	mm
V-Notch Root Radius	$\leq$50	µm

Fracture toughness values obtained from the SVDCT method have an uncertainty associated with the direct measurements (e.g. force, specimen parameters) and propagated uncertainty associated with the calculated parameters (e.g. half-angle and fracture toughness). The methodologies detailed by Taylor[160] are used here in determining these uncertainties. The uncertainties associated with direct measurements are summarized in Table 3.4. Propagated uncertainties of calculated parameters are summarized in Table 3.5.

Table 3.4: Summary of measurement uncertainties associated with the SVDCT method

Measurement	Notation	Reported Uncertainty	Method of Determination
eXpert 4200 Load Cell Force	δF_{WMC}	$\pm$0.17 N	WMC 25N load cell data sheet
ATS 905 Load Cell Force	δF_{ATS}	$\pm$1.1 N	ATS 905 data sheet
Arc length	δL_{arc}	$\pm$0.02 mm	Digital Mitutoyo caliper resolution
SVDCT Specimen Diameter	δD_{sv}	$\pm$0.02 mm	Digital Mitutoyo caliper resolution
SVDCT Specimen Thickness	δt_{sv}	$\pm$0.02 mm	Digital Mitutoyo caliper resolution
Notch Depth	δc_{sv}	$\pm$0.02 mm	CNC travel resolution

Table 3.5: Summary of propagated uncertainties associated with the SVDCT method

Calculated Parameter	Reported Uncertainty	Uncertainty Equation
Half-angle	Test Specific	$\frac{\delta\alpha}{\alpha} = \sqrt{\left(\frac{\delta L_{arc}}{L_{arc}}\right)^2 + \left(\frac{\delta D_{sv}}{D_{sv}}\right)^2}$
Fracture Toughness	Test Specific	$\frac{\delta K_{IC}}{K_{IC}} = \left[\left(\frac{\delta F}{F}\right)^2 + \left(\frac{\delta D_{sv}}{D_{sv}}\right)^2 + \left(\frac{\delta t_{sv}}{t_{sv}}\right)^2 + \left(\frac{\delta c_{sv}}{2c_{sv}}\right)^2 + \left(\frac{2\alpha cos(2\alpha) - sin(2\alpha)}{\alpha(sin(2\alpha) - \alpha)}\delta\alpha\right)^2\right]^{\frac{1}{2}}$

3.3 Wave speed measurements

Ultrasonic time-of-flight (TOF) measurements are typically used to measure the dilatational and shear wave speeds of materials[65], and are regularly applied to heterogeneous, granular compacts[11, 12, 152, 154]. TOF techniques determine the wave speed of a material by measuring the time it takes a particular wave type to travel a known distance in the material[65], and are typically applied to specimens that are millimeters to centimeters in size [11, 12, 65, 175]. This calculation is described simply[175]:

$$C_w = \frac{L_w}{t_t} \tag{3.8}$$

where the wave speed of interest, C_w, is a function of the distance traveled by the wave, L_w, divided by the transit time, t_t, it takes for the wave to traverse L_w.

TOF measurements may be conducted with one or two ultrasonic transducers. For a single transducer system, the transducer acts as both the wave emitter and wave receiver. The emitted wave travels the length of the specimen, reflects off the free end of the specimen, and returns back to the transducer. The transit time is the time between the emission and the receiving of the wave pulse by the transducer, and the distance traveled is therefore twice the length of the specimen such that $L_w = 2L_o$. For a two transducer set up, where one transducer is the wave emitter and the second transducer the wave receiver, the distance between the transducers is the distance traveled, such that $L_w = L_o$. TOF wave speed measurements of heterogeneous, granular materials are known to vary with wave frequency due to dispersion and wave interaction with the microstructure[152, 176]. Measurement variation with frequency is most pronounced at frequencies below 2 MHz, and above 2 MHz the variation is typically less than 5%[152, 176].

An Olympus 45MG TOF thickness gauge is used by this work to determine the dilatational and shear wave speeds of the studied RM systems. The Olympus 45MG is a single transducer system and returns the transit time of the wave type of interest. The wave speed of interest is then calculated using Equation 3.8 and the length of the specimen. Dilatational wave speeds are measured using a 10 MHz ultrasonic dilatational wave transducer with a 6.35 mm element tip. Shear wave speeds are measured using a 5 MHz ultrasonic shear wave transducer with a 6.35 mm diameter element tip. The measurement uncertainty of the wave speeds are determined used methodologies detailed by Taylor[160] and are summarized in Table 3.6.

Table 3.6: Summary of measurement and propagated uncertainties associated with the wave speed measurements

Measurement	Notation	Reported Uncertainty	Method of Determination
Wave Travel Distance	δL_w	± 0.02 mm	Digital Mitutoyo caliper resolution
Transit Time	δt_t	± 0.01 µs	Olympus 45MG temporal resolution
Calculated Wave speed	$\delta C_w / C_w$	Specimen Specific	$\frac{\delta C_w}{C_w} = \sqrt{\left(\frac{\delta L_w}{L_w}\right)^2 + \left(\frac{\delta t_t}{t_t}\right)^2}$

3.4 Kolsky bar compression testing for dynamic response and fragmentation

The use of Kolsky bar experiments in RM research is well established[9, 11, 13, 15, 37, 38, 40, 49]. Traditionally, the method is used to study the dynamic stress-strain response of materials, to include metals, ceramics, and polymers at strain rates of 10^2 s^{-1} to 10^4 s^{-1}[177]. Similarly, RM research efforts have used Kolsky bar experiments to measure the dynamic stress-strain response for quantitative assessment of the influence of compositional and meso-scale characteristics on material response[37, 38, 40]. Kolsky bar experiments are also used to determine parameters for the Johnson-Cook constitutive model[46] in conjunction with quasi-static tests[9, 49]. Recently, Kolsky bar experiments have found application in studying fragmentation of RM systems under well characterized loading[13, 15]. The use of Kolsky bar experiments in this manner permits improved assessment of strain-rate dependent fragmentation models as the strain rate is directly measured.

A schematic of the Kolsky bar system used in this work is shown in Figure 3.5, and can be considered representative of a typical Kolsky bar system. The system consists of two long cylindrical bars, called the incident and transmitted bars. These bars are designed, both dimensionally and through material selection, so that the bars behave elastically throughout the duration of a test[177]. Bar material selection is dependent on the specimen material to be tested, with demonstrated bar materials include maraging steel, 7075-T6 aluminum, and magnesium alloys for general use, PMMA for very soft materials, and tungsten carbide for ceramics[177]. A specimen is positioned between the incident and transmitted bars, usually with platens at the interface if bar damage of concern. These platens are generally made of the same material as the bars and protect the bar ends from damage. Typically, the length to diameter ratio of the bars (L_b / D_b) is on the or-

der of 100, the bar diameter to specimen diameter ratio (D_b/D_s) is on the order of 2 to 4, and the length to diameter ratio of the specimen (L_o/D_s) is between 0.6 to 1[177]. Subscripts I, R, and T refer to incident, reflected, and transmitted, respectively.

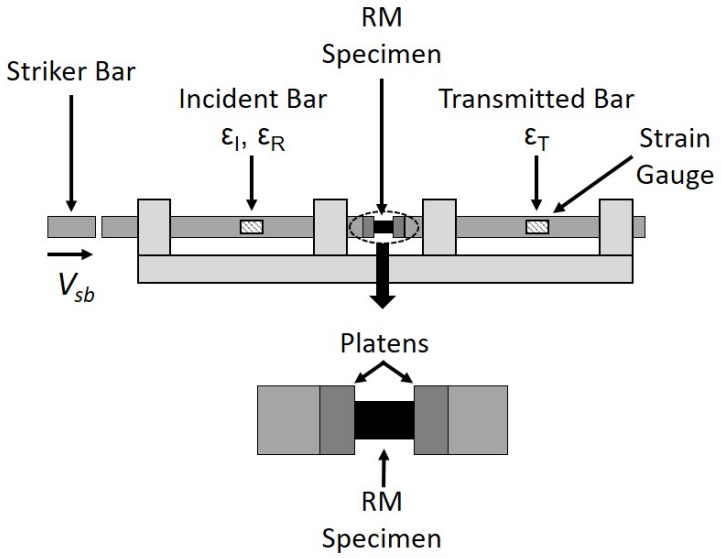

Figure 3.5: Schematic of Kolsky bar testing. Primary components and measured strains are labeled.

To apply loading to a specimen, a striker bar, typically made of the same material as the incident bar, impacts the incident bar at the end opposite the specimen. This induces a compressive elastic wave which propagates down the incident bar to the specimen. The strain of this incident wave can be calculated using[177]:

$$\varepsilon_I = \frac{V_{sb}}{2C_{o,I}} \tag{3.9}$$

Where V_{sb} is the projectile velocity and $C_{o,I}$ the bar wave speed of the incident bar, where $C_o = \sqrt{E_b/\rho_b}$. Striker bars are typically launched using a compressed gas gun[178]. A buffer material is placed between the impacting striker and incident bar to manipulate the incident pulse. This "pulse-shaper" is typically copper, and is used to create a longer rise time of the pulse, decreasing wave dispersion and promoting stress homogeneity in the specimen[177]. In this work, Equation 3.9 is not used as ε_I is measured directly using strain gauges.

When the incident pulse reaches the specimen/incident bar interface, a reflected wave travels back into the incident bar. A transmitted wave travels into the transmitted bar once the compressive wave moves through the specimen and reaches the specimen/transmitted bar interface. Strain gauges are fixed to each

bar and measure the strain of these waves, with the locations selected so the incident and reflected waves in the bars do not overlap[177]. For a half-bridge strain gauge arrangement the measured strain of a bar, ε_b, is determined from the measured bridge voltage, $V_{m,k}$, using [179]:

$$\varepsilon_b(t) = \frac{2}{k_g}\frac{V_{m,k}(t)}{V_{ex}} \tag{3.10}$$

Where k_g is the gauge factor of the strain gauges and V_{ex} is the excitation voltage of the bridge. The measured strain in the bar from the incident wave, $\varepsilon_I(t)$, the reflected wave, $\varepsilon_R(t)$, and the transmitted wave, $\varepsilon_T(t)$, are used to calculate the strain rate, stress, and strain of the specimen using one dimensional elastic wave propagation theory, as discussed below.

Determination of the mean axial engineering strain rate in the specimen, $\dot{\varepsilon}_s$, at any time is a function of the initial specimen length, L_o, and the difference in particle velocity between the specimen/incident bar interface, $v_{p,I}(t)$, and specimen/transmitted bar interface, $v_T(t)$. Using the known bar wave speed, $C_o = \sqrt{E_b/\rho_b}$, $\dot{\varepsilon}_{s,e}$ can alternatively be determined using the measured strain of the three waves of interest[177]:

$$\dot{\varepsilon}_{s,e}(t) = \frac{v_{p,I}(t) - v_{p,T}(t)}{L_o} = \frac{C_{o,I}(\varepsilon_I(t) - \varepsilon_R(t)) - C_{o,T}\varepsilon_T(t)}{L_o} \tag{3.11}$$

The mean axial compressive stress, $\bar{\sigma}_s(t)$, in the specimen at t is calculated using the normal forces at the two specimen/bar interfaces determined using the measured bar strains. For cases when the specimen and bar interfaces are lubricated, this calculated stress is uniaxial. The normal force at the specimen/incident bar interface is:

$$F_{s,I}(t) = E_{b,I}(\varepsilon_I(t) + \varepsilon_R(t))A_{b,I} \tag{3.12}$$

And the normal force at the specimen/transmitted bar interface is:

$$F_{s,T}(t) = E_{b,T}(\varepsilon_T(t))A_{b,T} \tag{3.13}$$

Where the normal forces are a function of the elastic modulus of the bars and the bar cross-sectional areas, A_b. Knowing the normal forces applied to the specimen and the initial cross-sectional area of the specimen before loading, $\bar{\sigma}_s$ is then given by Equation 3.14:

$$\bar{\sigma}_s(t) = \frac{F_{s,I}(t) + F_{s,T}(t)}{2}\frac{1}{A_s} \tag{3.14}$$

Inspection of Equations 3.12, 3.13, and 3.14 shows a force imbalance is possible, implying a non-uniform stress state can exist in the specimen. This is known to be the case at early loading times. However, as wave reflections continue in the specimen and the specimen begins to flow plastically at a later loading time,

the stress state of the specimen essentially becomes uniform[177]. This implies force equilibrium is obtained, such that $F_{s,I} \approx F_{s,T}$. For bars of the same material, force equilibrium corresponds to $\varepsilon_I + \varepsilon_R \approx \varepsilon_T$. Force equilibrium is a time dependent process, and typically multiple reverberations of the elastic wave inside the specimen are required to reach equilibrium. A pulse-shaper can be used to create a controlled rise time of the incident pulse, which decreases the time for force equilibrium to be obtained[177]. This is important in brittle materials which fail shortly after the elastic regime of the material response. Ramesh[177] reported a rule of thumb for when force equilibrium is obtained to be three reverberations for most materials, and five reverberations for ceramics.

Assuming a uniform stress state ($F_{s,I} \approx F_{s,T}$), uniaxial stress conditions, and 1D elastic wave propagation, the values of engineering strain rate, $\dot{\varepsilon}_{s,e}$, engineering strain, $\varepsilon_{s,e}$, and engineering stress, $\sigma_{s,e}$, in the specimen are[177]:

$$\dot{\varepsilon}_{s,e}(t) = \frac{C_{o,I}(\varepsilon_I(t) - \varepsilon_R(t)) - C_{o,T}\varepsilon_T(t)}{L_o} \tag{3.15}$$

$$\varepsilon_{s,e}(t) = \int_0^t \dot{\varepsilon}_{s,e}(t)dt \tag{3.16}$$

$$\sigma_{s,e}(t) = \frac{E_{b,T}A_{b,T}}{A_s}\varepsilon_T(t) = \frac{E_{b,I}A_{b,I}}{A_s}(\varepsilon_I(t) + \varepsilon_R(t)) \tag{3.17}$$

In this work, the strain rate, strain, and stress are considered positive for specimens in compression. The above equations are derived assuming constant cross-sectional area of the specimen, which gives the engineering values of strain rate, strain, and stress. These equations also represent a two wave analysis methodology. The true strain rate, strain, $\dot{\varepsilon}_{s,t}$, true strain, $\varepsilon_{s,t}$, and true stress, $\sigma_{s,t}$, in the specimen are[177]:

$$\dot{\varepsilon}_{s,t}(t) = \frac{\dot{\varepsilon}_{s,e}(t)}{1 - \varepsilon_{s,e}(t)} \tag{3.18}$$

$$\varepsilon_{s,t}(t) = -\ln[1 - \varepsilon_{s,e}(t)] \tag{3.19}$$

$$\sigma_{s,t}(t) = \sigma_{s,e}(t)[1 - \varepsilon_{s,e}(t)] \tag{3.20}$$

It is noted that Equation 3.20 is derived assuming plastic incompressibility.

This work will use a Kolsky bar system as described by the schematic shown in Figure 3.5. This system uses bars and platens made from maraging steel with the system characteristics summarized in Table 3.7. For the intended specimen geometry of $D_s = 6.35$ mm and $L_o = 6.35$ mm, realizable peak strain rate has been demonstrated to be on the order of 3×10^3 s^{-1}. Per the standard recommended by Ramesh[177], the measured stress-strain curve is reported at the average strain rate taken over the strain rate history. For engineering stress-strain curves, this is the engineering strain rate given by Equation 3.15. For true stress-strain curves, this is the true strain rate given by Equation 3.18.

Table 3.7: Summary of the applied Kolsky bar system parameters, to include bar and platen maragin steel properties

System Parameter	Value	Units
Elastic Modulus $E_{b,I}, E_{b,T}$	200	GPa
Poisson's Ratio $\nu_{b,I}, \nu_{b,T}$	0.30	
Wave speed $C_{bar,I}, C_{bar,T}$	4790	m/s
Density $\rho_{b,I}, \rho_{b,T}$	8100	kg/m^3
Bar Diameter $D_{b,I}, D_{b,T}$	12.70	mm
Cross-sectional Area $A_{b,I}, A_{b,T}$	126.66	mm^2

The loading event and fragmentation of a specimen is observed using a Shimadzu HPV-X2 high-speed camera operating at 500,000 fps with a flash lamp for illumination. A clear enclosure surrounds the specimen and contains the specimen fragments which can be ejected at high velocities while permitting free movement of the bars. Fragments are recovered by manual cleaning of the enclosure and any remnants of lubricant or non-specimen debris are removed manually during visual inspection. Recovered fragments are processed according to the size analysis methods discussed later in this section. The experimental setup with the imaging system and fragment enclosure installed on the Kolsky bar system is shown in Figure 3.6.

Reported Kolsky bar measurements of RM specimens typically do not include a discussion of measurement uncertainty[11–13, 15, 180]. This is not unique to the field of RM research as uncertainties of Kolsky bar measurements are rarely discussed in works from other fields[51, 179]. Recently Brizard et al.[179] explored in detail the sources of uncertainty in Kolsky bar measurements. Their analysis assumed negligible temporal jitter in sampling by the data recording device and bars of the same material. Brizard et al. reported the uncertainty of calculated strain in the bars to be reasonably described by[179]:

$$\frac{\delta\varepsilon(t)}{\varepsilon(t)} = \sqrt{\left(\frac{\delta k_g}{k_g}\right)^2 + \left(\frac{\delta \nu_b}{\nu_b}\right)^2 + \left(\frac{\delta V_{ex}}{V_{ex}}\right)^2 + \left(\frac{\delta V_{m,k}}{V_{m,k}}\right)^2} \tag{3.21}$$

Where the uncertainty in bar strain propagates into two wave analysis calculations of engineering strain rate, engineering strain, and engineering stress with

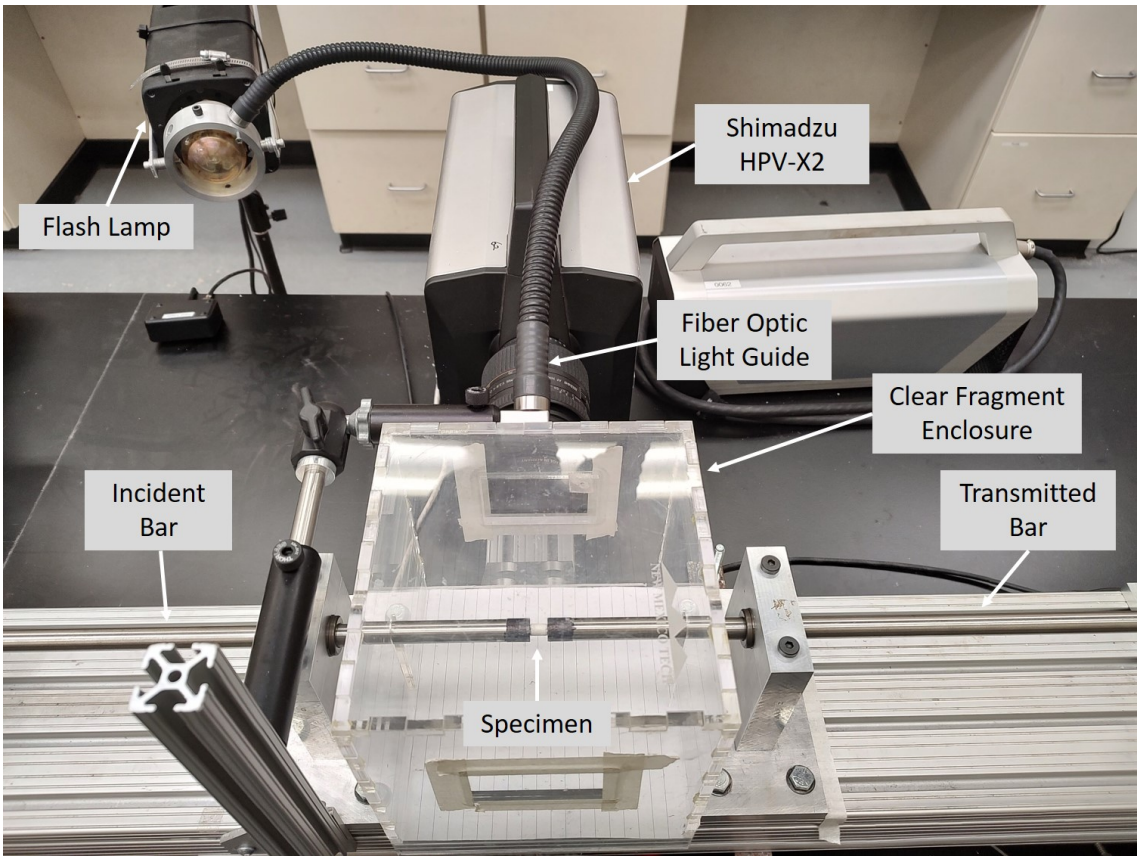

Figure 3.6: Overview of experimental Kolsky bar system with high-speed imaging system and fragment enclosure installed.

the uncertainties approximated by:

$$\frac{\delta\dot{\varepsilon}_{s,e}(t)}{\dot{\varepsilon}_{s,e}(t)} = \sqrt{\left(\frac{\delta C_o}{C_o}\right)^2 + \left(\frac{\delta L_o}{L_o}\right)^2 + \left(\frac{\delta\varepsilon_r(t)}{\varepsilon_r(t)}\right)^2} \tag{3.22}$$

$$\frac{\delta\varepsilon_{s,e}(t)}{\varepsilon_{s,e}(t)} \approx \frac{\delta\dot{\varepsilon}_{s,e}(t)}{\dot{\varepsilon}_{s,e}(t)} \tag{3.23}$$

$$\frac{\delta\sigma_{s,e}(t)}{\sigma_{s,e}(t)} = \sqrt{\left(2\frac{\delta D_b}{D_b}\right)^2 + \left(2\frac{\delta D_s}{D_s}\right)^2 + \left(\frac{\delta E_b}{E_b}\right)^2 + \left(\frac{\delta\varepsilon_T(t)}{\varepsilon_T(t)}\right)^2} \tag{3.24}$$

Once a uniform stress state in the specimen was nominally obtained, Brizard et al.[179] reported the average uncertainty in stress and strain became reasonably constant. For the data discussed in their work, the average uncertainty in stress and strain was $\pm 4\%$.

Brizard et al.[179] used a signal conditioner which had an uncertainty proportional to the amplitude of the input voltage from the strain gauges. As such the uncertainty of $V_{m,k}$ had a temporal variation which increased with the amplitude of the voltage signal. Because a signal conditioner is not used in this work the uncertainty in $V_{m,k}$ is not a function of time and is simply the measurement uncertainty associated with the HBM Gen2i DAQ used here. The measurement uncertainties associated with the Kolsky bar system used in this work are summarized in Table 3.8. In cases where exact uncertainties are not known, this work will use those suggested by Brizard et al.[179]. The measurement uncertainties are summarized in Table 3.8 and propagated uncertainties are summarized in Table 3.9. Here the uncertainty in the measurements are $\approx\pm$ 2.5%, inline with reported values by Brizard et al.[179]. As expected, using a high-resolution DAQ and foregoing a signal conditioner significantly reduces the measurement uncertainty in comparison to the system used by Brizard et al.[179].

Table 3.8: Summary of measurement uncertainties associated with the Kolsky bar tests

Measurement	Notation	Reported Uncertainty	Method of Determination
Gauge Factor	$\frac{\delta k_g}{k_g}$	$\pm$0.5%	Micro-measurements data sheet
Poisson's Ratio	$\delta \nu_b$	$\pm$0.005	General uncertainty theory by Taylor[160]
Excitation Voltage	δV_{ex}	$\pm$0.01% + 3 mv	Tenma 72-6610 data sheet
Measured Bridge Voltage	$\delta V_{m,k}$	$\pm$0.05 mv	HBM Gen2i DAQ calibration report
Bar Wave Speed	$\frac{\delta C_o}{C_o}$	$\pm$0.1%	Brizard et al. [179] reported
Elastic Modulus	$\frac{\delta E_b}{E_b}$	$\pm$0.1%	Brizard et al. [179] reported
Specimen Length	δL_o	$\pm$0.02 mm	Digital Mitutoyo caliper resolution
Specimen Diameter	δD_s	$\pm$0.02 mm	Digital Mitutoyo caliper resolution

Table 3.9: Propagated uncertainty of measurements of bar strain, engineering stress, engineering strain, and engineering strain rate using the Kolsky bar system

Calculated Parameter	Notation	Reported Uncertainty	Uncertainty Equation
Bar Strain	$\frac{\delta\varepsilon_{b,e}(t)}{\varepsilon_{b,e}(t)}$	$\pm$2.4%	Equation 3.21
Specimen Strain Rate	$\frac{\delta\dot{\varepsilon}_{s,e}(t)}{\dot{\varepsilon}_{s,e}(t)}$	$\pm$2.4%	Equation 3.22
Specimen Strain	$\frac{\delta\varepsilon_{s,e}(t)}{\varepsilon_{s,e}(t)}$	$\pm$2.4%	Equation 3.23
Specimen Stress	$\frac{\delta\sigma_{s,e}(t)}{\sigma_{s,e}(t)}$	$\pm$2.5%	Equation 3.24

3.5 High velocity impact testing

High velocity impact tests are a well defined experimental method for studying the fragmentation of RM systems at strain rates beyond 10^3 s^{-1}[5, 11, 12, 27]. These types of tests also simulate the impact environment and loading conditions associated with ballistic type applications. In these studies, specimens may be fired at thin metal plates or fired directly into a rigid anvil to trigger the fragmentation of the specimen. This work will focus on the thin metal plate methodology as fragments can readily be studied after impact using high-speed imaging and soft catch systems[5, 11, 12, 12].

Thin metal plate impact tests allow the applied strain rate to be controlled by varying the impact velocity and the thickness and density of the plates[12]. The thin plates are typically steel or aluminum and vary between sub-millimeter and single-millimeters in thickness. Tang and Hooper[12] proposed an estimate of the average bulk strain rate applied to a cylindrical RM specimen at impact with a thin plate:

$$\bar{\dot{\epsilon}} = \frac{V_{Im} - V_{res}}{r_s} \tag{3.25}$$

Where the average strain rate, $\bar{\dot{\epsilon}}$, is a function of the velocity of the specimen at impact, V_{Im}, the residual velocity of the specimen/fragment bulk after impact, V_{res}, and the radius of the cylindrical specimen, r_s.

This relation was derived by Tang and Hooper[12] assuming that the bulk fragmentation behavior is minimally influenced by the transient compressive and tensile stresses at early times immediately after impact, and instead implied the average bulk behavior can be described by looking at a longer time scale. However, Tang and Hooper do not provide a direct explanation of the formulation of Equation 3.25, obscuring the underlying physics. Equation 3.25 has not been directly validated experimentally or through modeling, but good agreement of fragmentation predictions to experimental results using this approximation suggests it appropriately captures the bulk behavior for the conditions and RM system evaluated by Tang and Hooper[12]. However, good agreement could also be the result of similarities in magnitude of the chosen velocities and specimen dimension to other speeds and length scales that control the specimen response under impact conditions.

Inspection of the relation and the underlying work of Tang and Hooper[12] permits an intuitive analysis to be made of the governing physical principles of Equation 3.25. Tang and Hooper observed that cylindrical zinc RM specimens failed due to radial expansion during penetration of target plates. Thus, the radial strain due to the outward expansion of the projectile during impact was the driving force of crack development. Assuming a linear elastic, isotropic material, the radial strain rate, $\dot{\epsilon}_{rad}$, can be related to the longitudinal strain rate, $\dot{\epsilon}_{long}$ by:

$$\dot{\epsilon}_{rad} = -\nu_{RM}\dot{\epsilon}_{long} \tag{3.26}$$

Where ν_{RM} is the Poisson's ratio of the RM specimen. The longitudinal strain rate is related to the change in velocity of the specimen during the perforation process by:

$$\dot{\epsilon}_{long} = \frac{V_{res} - V_{Im}}{L_o} \tag{3.27}$$

A generalized radial strain rate relation for the impact of cylindrical specimens is then obtained by combining Equations 3.26 and 3.27 to form:

$$\dot{\epsilon}_{rad} = -\nu_{RM}\frac{V_{res} - V_{Im}}{L_o} \tag{3.28}$$

From Equation 3.28 there is not a clear path to obtaining Equation 3.25 based on physical principles. Therefore, Equation 3.28 is considered the more appropriate relationship as it is based on physical principles.

The residual velocity after impact is measured using high-speed imaging. Typically, the spatial translation of the center of mass of the fragment bulk is manually tracked across multiple frames and the bulk velocity calculated[12]. This method can prove challenging as it is typical for fragments of the specimen to ignite after impact, especially in the presence of air, obscuring fragments at early times after impact. Measurements of the fragment bulk at a later time, and some distance, after impact can improve the identification of the center of mass of the fragment cloud, but the effects of drag must be accounted for to calculate the original residual velocity. This is a non-trivial task as the fragments that comprise the cloud vary in shape and size and therefore do not experience a uniform deceleration.

In studying the fragmentation of heat treated zinc RM impacting thin aluminum plates, Tang and Hooper[12] used an energy balance approach to derive an analytical approximation of the residual velocity of the fragment bulk after impact with a thin plate, aligning with validated theory proposed in literature[181]. Based on observations of plugging of the thin plate a portion of the kinetic energy of the specimen was assumed to be consumed as plastic work in driving a cylindrical plug from the impact plate and as dynamic work in accelerating the plug, and that the mass loss of the specimen at the initial impact is negligible, Tang and Hooper proposed that the residual velocity, V_{res}, can be calculated as[12]:

$$V_{res}^2 = \left(\frac{m_s}{m_s + \rho_{IP}\pi r_s^2\ t_{IP}}\right) V_{Im}^2 - \frac{2\pi\ t_{IP} r_s}{m_s + \rho_t \pi r_s^2\ t_{IP}}\left[\frac{\sigma_{Y,IP} t_{IP}}{\sqrt{3}} + \frac{\rho_{IP} r_s V_{Im}^2}{2}\right] \tag{3.29}$$

Where m_s is the initial mass of the specimen before impact, ρ_{IP} is the density of the impact plate, t_{IP} is the thickness of the impact plate, and $\sigma_{Y,IP}$ is the yield strength of the impact plate material. This analytical approximation was shown to provide good agreement to experimental measurements of residual velocity[12]. However, this relationship is likely specific to the the tests conducted by Tang and Hooper[12] as other penetration behaviors have been observed for thin plate[181].

High-speed imaging is commonly used in RM fragmentation research efforts to determine the residual velocity of fragments after impact[11, 12]. High-speed imaging techniques can also be used to measure fragment sizes for determining fragment size distributions. Grady and Kipp[62, 114] demonstrated the technique in characterizing the fragmentation of bulk metals driven to failure by high velocity impact. In their works, high-speed x-ray imaging was used to obtain 2D area projections of fragments in flight. From the 2D projections, the equivalent spherical diameters of fragments were determined from the measured area, similar in manner to methods used by computerized particle size analyzers in determining fragment sizes. This work will apply high-speed imaging techniques and traditional soft catch methods in studying the fragmentation of RM systems using the analysis techniques discussed in Section 3.6.

High velocity impact testing will be conducted here using a smooth-bore powder gun with a 14 mm diameter (0.55 in) bore. This gun is connected to a stainless steel chamber with optical access ports, and RM specimens are launched using one-piece sabots manufactured from Onyx material, a chopped carbon fiber impregnated nylon, printed using a Markforged 3D printer[13]. After the sabots are stripped from the specimens they impact a thin target plate, triggering fragmentation of the specimens. The experimental setup is built specifically for this work, and is shown in Figure 3.7. An example of an additively manufactured sabot with a cylindrical RM specimen is shown in Figure 3.8.

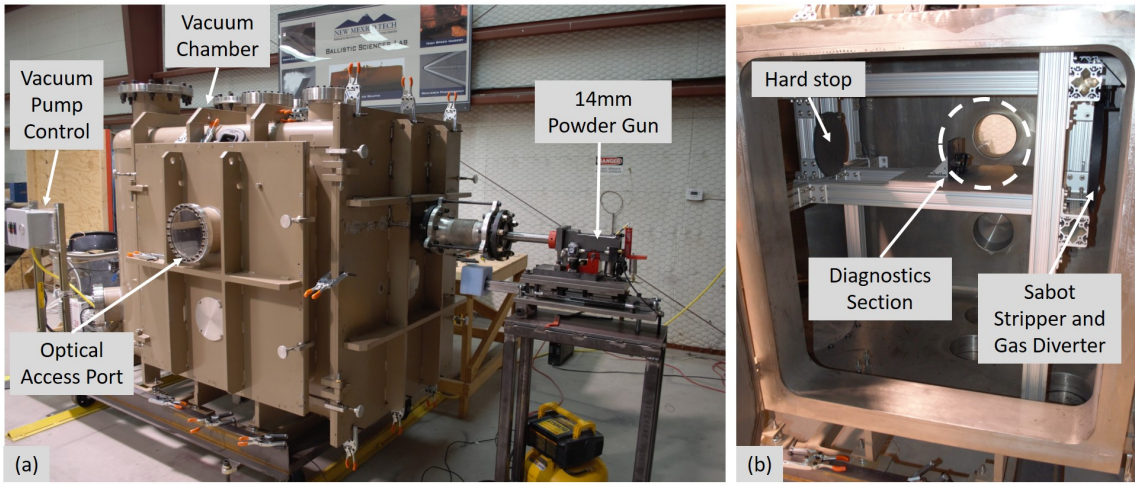

Figure 3.7: Experimental setup for high velocity impact testing of RM systems. (a) Exterior view of 14 mm powder gun and chamber with primary components labeled. (b) Interior of chamber with primary components labeled. Diagnostics section is indicated, with primary hardstop installed.

The propellant gases from the gun are diverted by the gas diverter to minimize interference with imaging in the diagnostics section. A secondary hard stop is used to protect the rear of the chamber in the event the specimen or fragments

Figure 3.8: Example of additively manufactured sabots with RM cylindrical specimens. At left is a sabot with RM specimen installed in preparation for launch in the 14 mm powder gun. At right is the sabot and specimen separated prior to assembly. The ruler scale is marked in millimeters on the bottom and inches on the top.

over-shoot the primary rubber hard stop in the diagnostics section. The gun system can launch these saboted RM specimens at velocities between 0.5 km/s and 1.8 km/s, providing a wide range of available strain rates. Commercial smokeless powder is used to launch saboted RM specimens from the gun. 50 caliber Browning machine gun (BMG) brass casings are modified for use in the gun and are hand loaded onsite. Muzzle velocity of the saboted RM specimens is controlled by varying the mass of smokeless powder. Smokeless powder mass for a desired muzzle velocity with a given saboted RM specimen mass is estimated using the Interior Ballistics of High Velocity Guns, Version 2 (IBHVG2) interior ballistics computer code[182]. IBHVG2 powder combustion models have been developed for use in this work specific to the gun system and smokeless powder used, providing the means to predict muzzle velocity to within 5%.

Due to spatial limitations between the gas diverter and the muzzle of the gun, aerodynamic stripping of sabots is not feasible. Instead a traditional mechanical stripping methodology is employed[183, 184]. A tool steel sabot stripping assembly is attached to the muzzle of the gun system inside the chamber and restrained by the gas diverter. A diagram of the assembly is shown in Figure 3.9.

Inside the tool steel housing is 8 mm of Buna-N rubber positioned approximately 63 mm from the muzzle to initiate the separation of the sabot from the specimen. Behind the rubber separator is a 63.5 mm long machined nylon arrestor that collapses under impact to stop the sabot. This process restricts the axial flow of propellant gas exiting the muzzle of the gun. These gases are redirected radially through the gas dump.

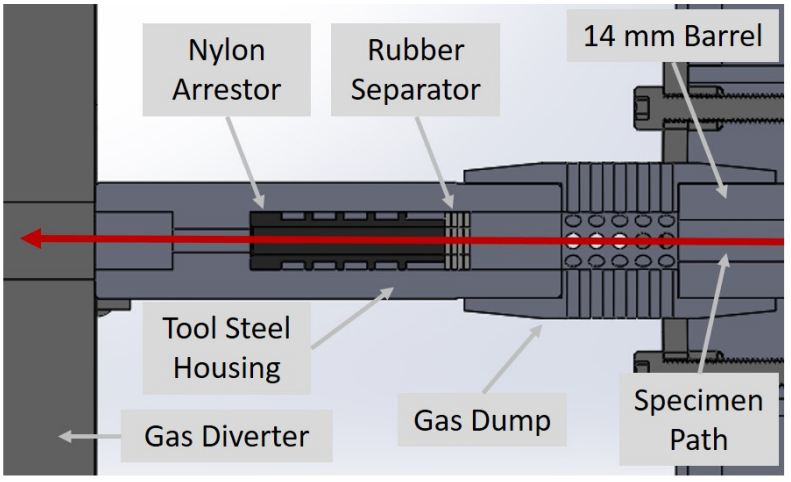

Figure 3.9: Overview of sabot stripping assembly. The specimen flight path and primary components are labeled.

RM specimens are secured to the printed sabots using paraffin wax. The paraffin wax provides adequate holding strength to retain the specimen on the sabot during launch by the gun, but minimal resistance to the mechanical stripping of the sabot from the specimen. This method has been shown to reliably provide clean separation of non-granular projectiles, such as 7 mm steel ball bearings. However, when applied to RM specimens some damage is not uncommon due to the fragility of RM specimens and the nature of the mechanical interactions during the stripping process. This damage is typically superficial as the specimen bulk remains intact, but small fragments and powder tend to precede and travel alongside RM specimens. While not ideal, these issues are not unusual when mechanically stripping sabots from specimens[183–185] and have negligible effect on the experimental outcomes.

The stainless steel chamber provides the means to launch RM specimens into either vacuum, inert gas, or air environments. The use of vacuum and inert environments improve optical diagnostics, as the combustion of fragments in flight is minimized. Conducting tests at vacuum levels >99% mitigates drag forces, permitting residual velocity measurements to be made downstream of the impact plate with negligible difference between measurements made directly behind the impact plate. Mitigation of drag forces also improves measurements of radial expansion velocity of the fragment cloud post-penetration of a target. This work will conduct impact fragmentation tests at vacuum levels of >99.6% ($\leq$3 Torr).

To avoid undesirable interaction of the specimen with a diaphragm material at the muzzle, the chamber is sealed at the breach of the gun using a thin coating of vacuum grease on the modified 50 caliber BMG case.

The resulting fragments from impact with the target plate are imaged in the diagnostics section. The approximate imaging field of view relative to the target plate is shown in Figure 3.10. A soft catch system is used to catch fragments after they pass through the diagnostics section. As with prior research efforts[1, 2, 11, 12, 186], artificial snow is used as the catch medium and contained inside open ended PVC tubes. The use of artificial snow simplifies the fragment extraction process, as the snow containing fragments is melted and water filtered to recover the fragments. Residual water is then evaporated before the fragments are analyzed to determine size distributions. The artificial snow catch systems also have the potential to quench RM fragment reactions and prevent particles from combusting after impact. Typically, 90% to 98% of the original fragment mass can be recovered using these techniques[12, 27].

In order to utilize a snow soft catch system in a vacuum environment, it is necessary to prevent sublimation of the snow. This is accomplished by temperature conditioning the snow filled tubes using a commercial walk-in freezer capable of reaching 265 K. For temperatures of $\leq$265 K, ice will not sublimate into gas phase water for pressures $>$2 Torr[187], which is below the vacuum level of $\sim$3 Torr utilized in this work. PVC tubes of 160 mm diameter and 410 mm length are filled with artificial snow produced using a Fujimarca MC-709SE shaved ice machine and ice made from reverse osmosis water. The PVC snow tubes are placed downstream of the diagnostic section of the stainless steel chamber as shown in Figure 3.10. A rubber hard stop is used to ensure fragments do not exit the PVC tube. Fragments are recovered by melting the snow and passing the water through analytical filter paper. Fragments of 5 µm and greater in size are readily recovered using this system. Recovered fragments are processed according to the size analysis methods discussed in the follow section.

A high-speed focused-shadowgraph system[188] is used to observe the RM fragments in flight. Focused-shadowgraph systems provide collimated (parallel) light through the diagnostic section. The use of collimated light yields a true projection of fragment sizes onto the imaging sensor of the high-speed cameras. Calibration of the sensors to an object of known size before testing permits fragment sizes to be determined. A SI-LUX 640 nm spoiled coherence laser provides short pulse durations of illumination of the diagnostic section on the order of a hundred nanoseconds, reducing streaking of the imaged fragments. A Specialised Imaging SIM-X high resolution framing camera is paired with the focused-shadowgraph system to observe the specimen impact with the target plate and subsequent fragmentation. Fifteen frames are obtained at a typical frame rate of 70,033 fps with an image resolution of 1360x1024 pixels. This provides a spatial imaging resolution of 0.06 mm/pixel. A Shimadzu HPV-X2 is paired to the auxiliary optical port on the SIM-X camera to also observe the impact event. 128 frames are obtained at a typical frame rate of 500,000fps with an image resolution of 400x250 pixels. This provides a spatial imaging resolution of

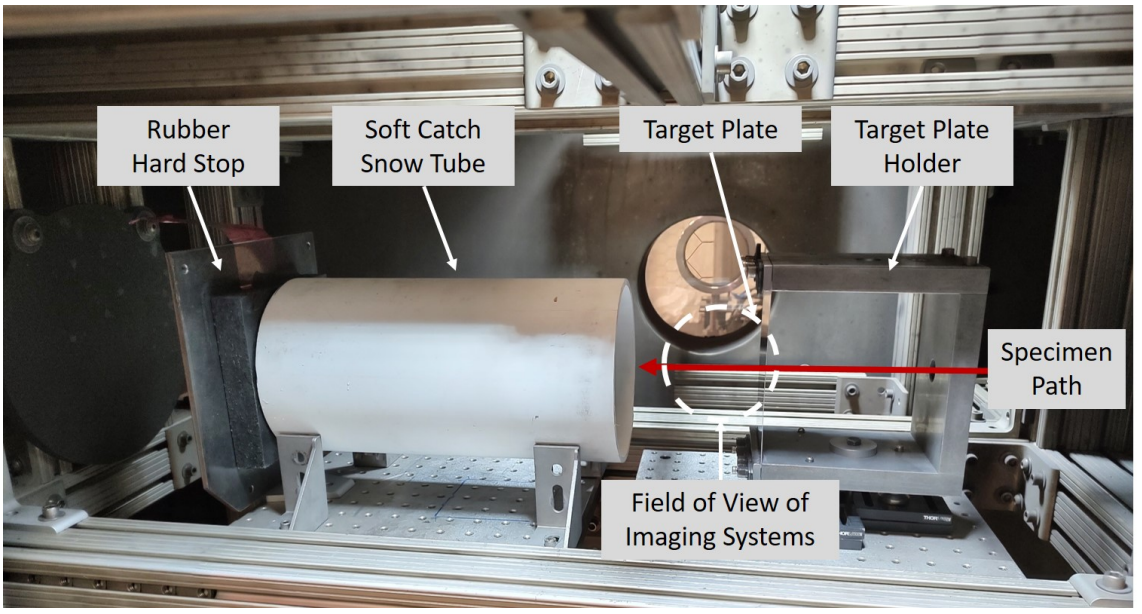

Figure 3.10: Experimental set up for impact fragment experiments inside the vacuum chamber. The specimen flight path and primary components are labeled. The approximate field of view of the high-speed imaging system is also indicated.

0.11 mm/pixel. An overview of the optical setup relative to the vacuum chamber is shown in Figure 3.11.

This work will use Equation 3.28, Equation 3.29, and experimental measurements of residual and radial expansion velocity for determining applied strain rate during impact. Assessment of the validity and experimental evaluation of Equation 3.28 will also be considered by this work. Velocity measurements in this work are extracted from the high-speed footage taken by both the SIM-X and HPV-X2 cameras. Image correlation routines are applied to determine the directional translations of the fragment bulk in the horizontal and vertical directions for calculating residual and radial velocities. This information can also be used to stitch images from the high-speed footage to form single composite images. This yields a composite image representing a visual timeline of all fragments which pass through the field of view of the high-speed imaging system[186]. Images acquired by the high-speed imaging system contain a large number of fragments which vary in shape and size and have pronounced edge features. Early efforts in this work found that spatial feature correlation algorithms[186, 189] are not well-suited to the stitching of these types of images because features of one fragment may be assigned to another fragment, leading to correlation failure. The use of phase correlation routines have been found to provide robust stitching of images containing large numbers of fragments, and is the preferred method used in this work.

The applied phase correlation routine follows the mathematical procedures

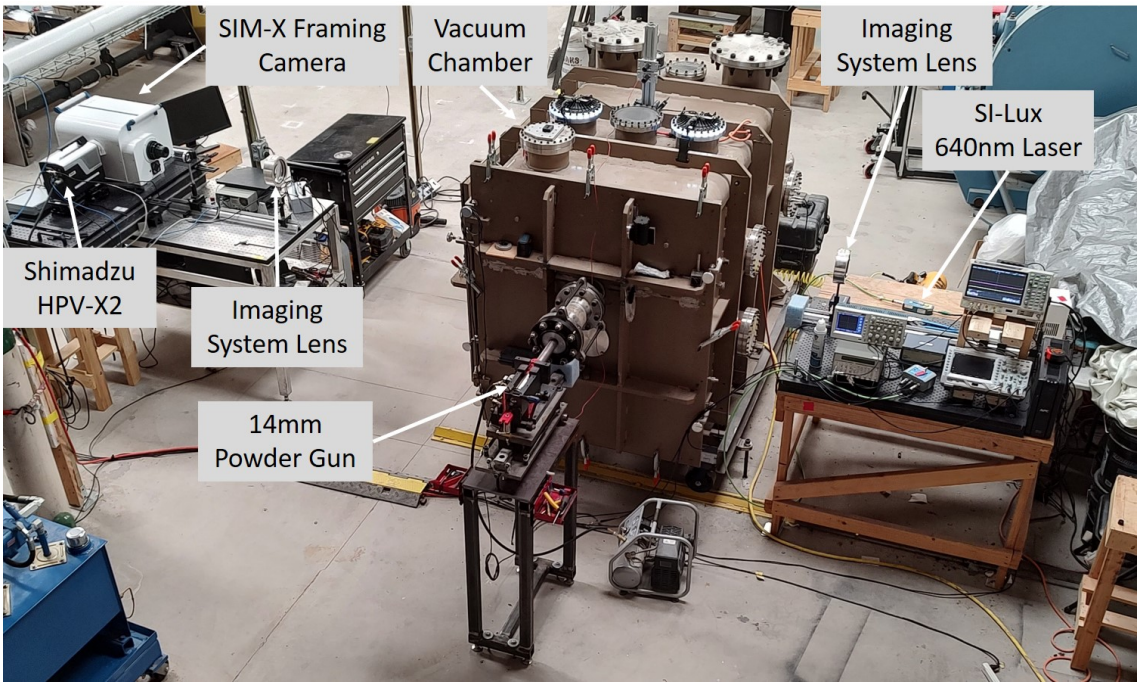

Figure 3.11: Overview of the focused-shadowgraph imaging system used for the high velocity impact studies.

outlined by Szeliski[189]. In this routine, two considered images are transformed into the Fourier domain and the cross-power spectrum calculated. An inverse Fourier transform is taken of the cross-power spectrum matrix and the location of the maximum value or "peak" determined in the transformed matrix. The spatial location of the peak corresponds to the magnitude of the image shift in 2D space, but does not provide directional translation information[189]. Subsequent processing routines assess directional shifts of the determined magnitude to identify the direction of translation of the image that provides the optimal correlation. This routine is repeated until all images are stitched forming the final composite image. The calculated translation information is then used to estimate the bulk velocity of the fragments[186, 190] supporting residual and radial velocity measurements. An example of a visual timeline of high-speed ($>$300 m/s) RM fragments passing through the field of view of a high-speed imaging system is shown in Figure 3.12, which was created using 80 frames from the high-speed footage of a test. The black border in Figure 3.12 is an artifact of the stitching process and does not impact the velocity measurements. The black border is slanted at an angle as a result of particles travelling downward due to a slant in trajectory relative to the horizontal axis of the field of view.

Uncertainty of these measurements have been discussed in detail elsewhere[190, 191]. The general uncertainty of the velocity measurements, V_G, is dominated by the spatial uncertainty of the x-axis travel, L_x, the y-axis travel, L_y, and the temporal resolution of the laser, t_L[190]. The uncertainty of L_x

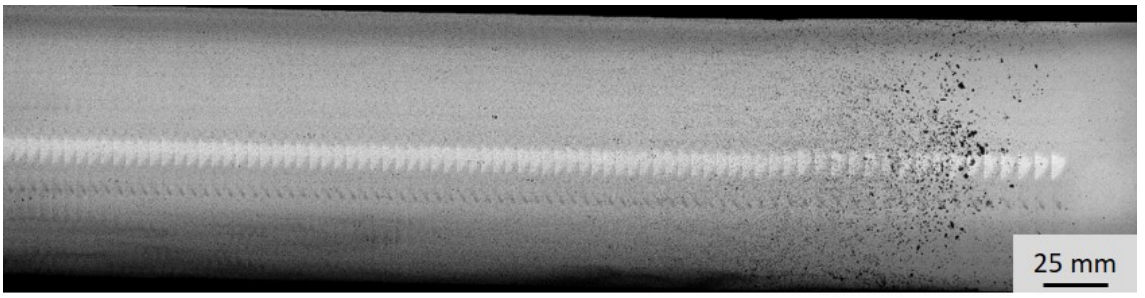

Figure 3.12: Example visual timeline of fragments passing through the field of view of high-speed imaging system using 80 frames from the high-speed footage of a test[186].

and L_y is given by the discretization uncertainty of the images. Treating the pixels on the imaging sensor as linear scale graduations, the discretization uncertainty is taken as half the graduation spacing or half a pixel[190]. The measurement uncertainties and propagated uncertainty of the velocities measured from the SIM-X and HPV-X2 images are summarized in Table 3.10 and, 3.11 respectively. Note that the propagated uncertainties of the strain rate calculations are not considered here given the lack of certainty in actual representation of strain rates experienced during penetration event.

Table 3.10: Summary of measurement and propagated uncertainties associated with the velocity measurements from the SIM-X high-speed footage

Measurement	Notation	Reported Uncertainty	Method of Determination
Travel in x-axis	δL_x	± 0.03 mm/pixel	Discretization uncertainty
Travel in y-axis	δL_y	± 0.03 mm/pixel	Discretization uncertainty
Laser Temporal Resolution	δt_L	± 0.05 µs	SI-LUX data sheet
General Velocity Uncertainty	$\frac{\delta V_G}{V_G}$	Measurement Specific	$\frac{\delta V_G}{V_G} = \sqrt{\left(\frac{\delta L_x}{L_x}\right)^2 + \left(\frac{\delta L_y}{L_y}\right)^2 + \left(\frac{\delta t_L}{t_L}\right)^2}$
Impact Velocity	$\frac{\delta V_{Im}}{V_{Im}}$	$\pm 0.5\%$	Peak impact velocity of 1000 m/s

Table 3.11: Summary of measurement and propagated uncertainties associated with the velocity measurements from the HPV-X2 high-speed footage

Measurement	Notation	Reported Uncertainty	Method of Determination
Travel in x-axis	δL_x	$\pm$0.06 mm/pixel	Discretization uncertainty
Travel in y-axis	δL_y	$\pm$0.06 mm/pixel	Discretization uncertainty
Laser Temporal Resolution	δt_L	$\pm$0.05 µs	SI-LUX data sheet
General Velocity Uncertainty	$\frac{\delta V_G}{V_G}$	Measurement Specific	$\frac{\delta V_G}{V_G} = \sqrt{\left(\frac{\delta L_x}{L_x}\right)^2 + \left(\frac{\delta L_y}{L_y}\right)^2 + \left(\frac{\delta t_L}{t_L}\right)^2}$
Impact Velocity	$\frac{\delta V_{Im}}{V_{Im}}$	$\pm$2%	Peak impact velocity of 1000 m/s
Residual Velocity	$\frac{\delta V_{res}}{V_{res}}$	$\pm$5%	Max observed velocity of 375 m/s
Radial Velocity	$\frac{\delta V_{rad}}{V_{rad}}$	$\pm$8%	Max observed velocity of 240 m/s

3.6 Fragment size analysis

The size distributions of recovered RM fragments are typically analyzed using manual sieving[27] or computerized particle size analyzers[11, 12]. Manual sieving is the traditional method for particle size analysis[192, 193] and yields a mass-size distribution which is the basis of existing RM distribution models[11, 12]. Manual sieving is recommended as the preferred size analysis method by NIST[192] as it mitigates errors associated with transforming from one physical basis to another (e.g. spatial basis to mass basis). Computerized particle size analyzers provide high-fidelity characterization of fragments, as particles on the order of 10 µm can be characterized[11, 12] and fragment morphology can be measured. Computerized particle size analyzers applied in RM research typically measure the area of a 2D projection of a fragment onto a calibrated imaging sensor. The size of a fragment is determined from the measured area of the 2D projection as an equivalent spherical diameter[61, 62] or as the minimum Feret distance[11]. Fragment size data is then binned to form size distributions, and subsequently transformed into mass-size distributions for analysis and fitting of distribution models[11, 12].

This work will apply both manual sieving and optical analysis methods in analyzing fragments. Manual sieving of recovered fragments is conducted using a sieving protocol developed specifically for this work. Prior RM research efforts have not detailed a specific sieving methodology[5, 27], so the protocol used in this work is informed by prior standardizing efforts[192–194]. Fragments are separated using a sieve stack comprised of US Standard sieve sizes meeting the ASTM E-11 standard[195]: 3.35 mm, 2.80 mm, 2.36 mm, 2.00 mm, 1.70 mm, 1.40 mm, 1.00 mm, 0.600 mm, 0.425 mm, 0.250 mm, 0.150 mm, and 0.045 mm. Uncertainty in sieve sizes is given by the reported significant figures on the sieves[160], which is conservatively taken here as $\pm 1\%$. Fragments are sieved by agitation of the sieve stack using a vibrating table in five minute intervals. This agitation duration was found to be the minimum that yields a change in sieve mass below 1 mg indicating adequate separation of the fragments[193]. Sieved fragments are weighed and binned by size to generate mass-size distributions. For fragments recovered from Kolsky bar tests, the sieve stack is agitated for five minutes once before weighing. For fragments recovered from impacts tests, the sieve stack is agitated for five minutes and then sabot or sabot stripper debris are manually removed. The separated RM fragments are then agitated for an additional five minutes before weighing.

Optical size analysis of fragments recovered from the soft catch and Kolsky bar tests is conducted using a scanning optical microscope built for this work, shown in Figure 3.13. The system consists of a metallurgical microscope equipped with a transmitted illumination source and 5 megapixel (MP) camera with a 5X objective lens. The system provides a 2.28 mm x 1.7 mm imaging field of view with a discretization uncertainty of the images of 0.4 µm/pixel. Due to diffraction limitations, the system cannot reliably image particles below 2.6 µm in size. To overcome the limited field of view, a precision microcontroller X-Y stage is used to translate a sample holder containing recovered fragments

through the field of view of the system and to trigger the camera. This sample holder is 76 mm x 64 mm in size to provide enough area to adequately disperse the fragments. Typically, 2400 5 MP images are collected which are then stitched based on the programmed spatial translation of the microcontroller. This yields a single composite image containing all fragments imaged on the sample holder. An example composite image from the scanning optical microscope is shown in Figure 3.14. The composite image represents a total field of view of 7.78 mm x 1.7 mm, and was created from 12 images with a field of view 2.28 mm x 1.7 mm and horizontal spatial difference between images of 0.5 mm. For stitched images it is necessary to reduce resolution to maintain manageable file sizes. As a result the discretization uncertainty of the stitched images increases to 1.65 µm/pixel. The black border in Figure 3.14 is an artifact of the stitching process, and does not impact the final fragment size analysis of the images.

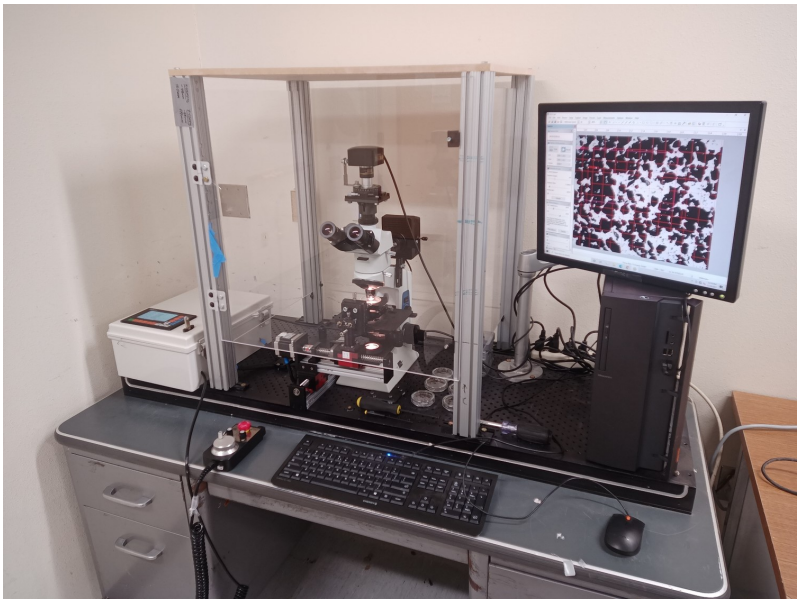

Figure 3.13: Scanning optical microscope used for analyzing recovered fragments from experimental tests. Camera view of a portion of the fragments on the sample holder can be seen on the system monitor.

Automated image processing routines are applied to the composite images from the microscope to identify, isolate, and calculate the fragment areas projected onto the imaging sensor. These routines are implemented in the MATLAB computational environment and utilize a number of functions from the MATLAB image processing toolbox. These processing routines and application to fragment size measurements have been explored by other works[186, 190, 191] and provide a robust means for analyzing fragments. A visual representation of the process is shown in Figure 3.15.

The unprocessed images are first converted to a binary image using the *im-*

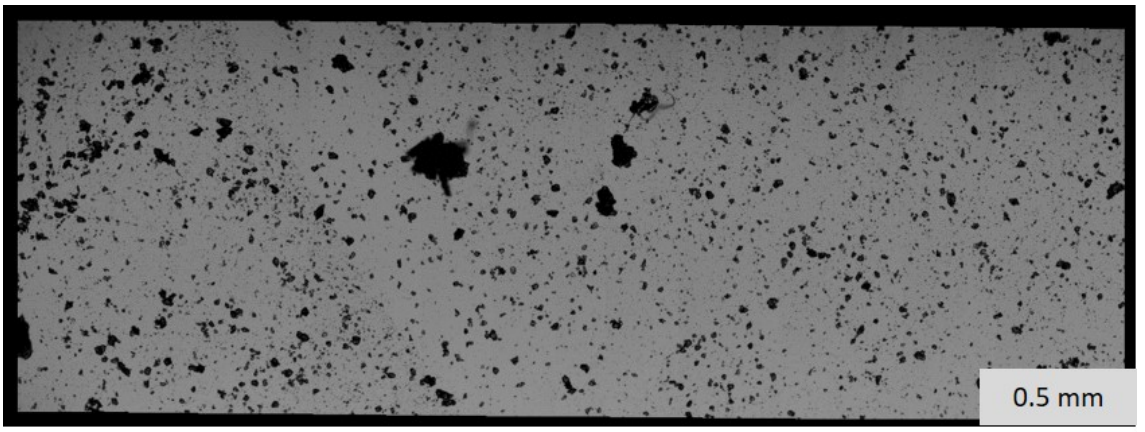

Figure 3.14: Example composite image of 12 images from the scanning optical microscope[186].

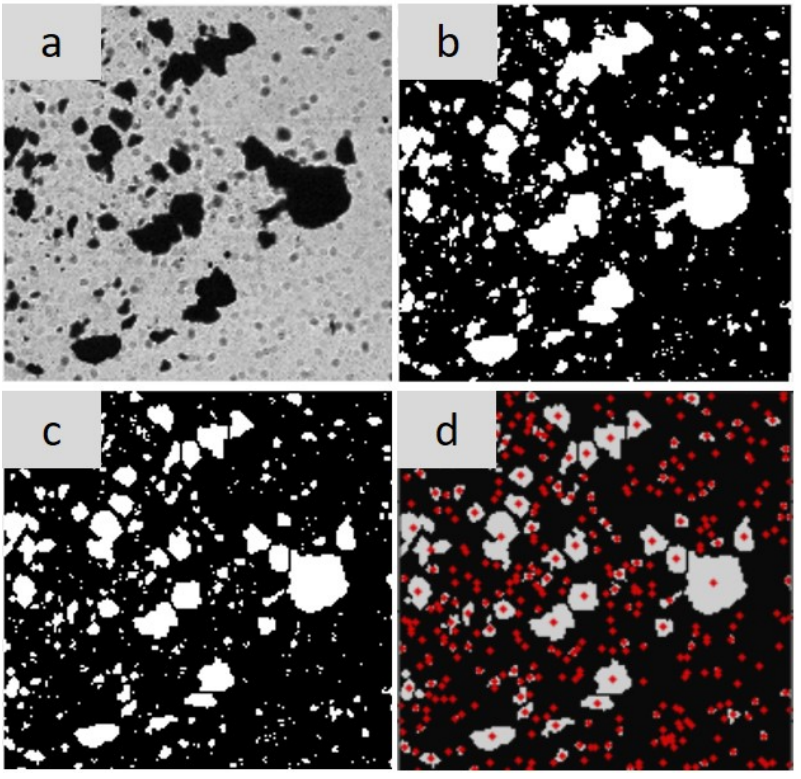

Figure 3.15: Overview of fragment size analysis of an image. (a) the unprocessed image is (b) binarized, then (c) segmented to identify fragments, from which (d) the centroids are identified in red[186]

binarize function in MATLAB. The binary image is then inverted to obtain an image with a black background and white fragments, as shown in Figure 5b.

Next, fragments of one square pixel in area are removed and the remaining fragments are then binned into small (bottom 25% in area), medium (25% to 75% in area), and large (top 25% in area) groupings. Each group is individually processed to segment fragment clusters by removal of the connecting pixels between individual fragments. This segmentation utilizes either the watershed function, which applies the watershed transform using the Fernand-Meyer algorithm as described by Meyer[196], or an opening morphological process as described by Gonzalez[197]. The segmentation method is chosen for each individual test based on which process yields optimal segmentation of the fragment clusters. An segmenting process is considered optimal when it provides the smallest decrease in total projected fragment area in the image. The final image containing isolated fragments is shown in Figure 5c. The *bwboundaries* function is then applied to identify individual fragments, calculating the pixel area of each fragment, and determining the fragment centroids. The centroids of identified fragments are shown in Figure 5d. Using a calibration image taken prior to testing, a spatial scale per pixel is used to convert the pixel areas to a spatial measurement. Using an equivalent spherical particle assumption[186], the equivalent diameter d_{eq} of the fragments is calculated from the determined fragment areas A_{frag} using $D_{eq} = \sqrt{A_{frag} * 4/\pi}$. The uncertainty of these equivalent spherical fragment size measurements is dominated by the systematic error resulting from the discretization of the digital images[186].

Challenges can arise in segmenting fragments due to the fragment number density of the clusters and the morphology of the fragments. Clusters with a high number density of fragments cannot be adequately segmented using a morphological opening process. This is a result of excessive bridging between fragments due to the close contact of fragments for which the watershed algorithm is better suited to segmenting these types of clusters. However, when fragments have rough and jagged edges, false identification of fragment interfaces can occur resulting in over segmentation by the watershed algorithm. This results in a significant reduction in the total projected fragment area in the image. In these cases, where the size analysis routines cannot separate fragment clusters without over segmentation, the processed fragment cluster is excluded from the size analysis.

One of the challenges of imaging fragments is the potential for overlap of the projected fragment areas in dense fragment clusters. Grady and Kipp[62] proposed a statistical approach to correct for the error associated with overlap of projected fragment areas[62, 114] based on the statistical work for randomly positioned areas proposed by Johnson and Mehl[198]:

$$A_{act} = A_{obs} \ln \left(1 - A_{obs}/A_{reg}\right)^{-1/(A_{obs}/A_{reg})} \tag{3.30}$$

Where the actual projected area of the fragments, A_{act}, is a function of the observed projected area of the fragments, A_{obs}, corrected by a logarithmic, power-law function dependent on the ratio of A_{obs} to the area of a region that fully contains the fragment cloud, A_{reg}. It has been observed through a Taylor expansion that A_{act} approaches A_{obs} as $A_{obs} << A_{reg}$, but is always greater than

A_{obs}[62, 114]. This approach has not been verified experimentally, but recent works[186, 191] would suggest that the extrapolation of dense, two dimensional projected fragment areas into three dimensions is a dubious endeavor. In cases where fragments are densely clustered in either the high-speed or microscope images, this work will rely on the manual sieving data as the primary representation of the size distribution of fragments.

This work will utilize the general fragment mass-size distribution form proposed by Hooper[27] for RM systems. This form captures both power-law and exponential fragmentation behavior and Equation 2.68 is repeated here for convenience:

$$m_d(s) = \Pi \frac{1}{s_o} \left(\frac{s}{s_o} \right)^{-\Lambda} \frac{\exp(-(\beta s)^{\Psi})}{f_{exp}(\beta s_o)} + (1-\Pi) \frac{1}{6\mu_c} \left(\frac{s+2/\beta}{\mu_c} \right)^3 \exp\left[- \left(\frac{s+2/\beta}{\mu_c} \right) \right] \quad (3.31)$$

$$where: \Lambda = (2\Psi - (\Psi k_s + 1)) \quad (3.32)$$

To determine the parameters of Equation 7.22 for a fragment size distribution, it is necessary to work with mass-size distributions. The sieve data inherently provides mass-size, but the size distributions from the images must be transformed into normalized mass-size distribution, $m_d(s)$. This transform has been discussed in detail by Youngblood et al.[186] for the case when an equivalent spherical particle assumption is employed. Because the size distributions are comprised of discrete bin sizes, the transformed mass–size distribution is defined by discrete points associated with the mean equivalent spherical particle size of the bin[186]:

$$m_d(s_m) = \frac{d_m^3 N_{bin}}{\sum_{i=1}^{n} d_{m,i}^3 N_{bin,i}} \quad (3.33)$$

Where s_m is the mean equivalent diameter of the bin size in the fragment size distribution, N_{bin} is the number of fragments observed for the bin size. Note that $m_d(s_m)$ is independent of the density of the material and is equivalent to the volume-size distribution of the fragments. For a given $m_d(s_m)$, a standard least-squares fit governed by the generalized reduced gradient algorithm is used to determine the following parameters: k_s, β, Π, and the exponential characteristic length, μ_c. The measurement uncertainties associated with this fragment size analysis have been discussed elsewhere in detail[186, 190, 191]. Following these prior works, the uncertainties associated with the size analysis here are summarized in Table 3.12.

Table 3.12: Summary of measurement uncertainties associated with the fragment size analysis

Measurement	Notation	Reported Uncertainty	Method of Determination
Sieved Bin Mean diameter	$\frac{\delta d_{m,sieved}}{d_{m,sieved}}$	$\pm$1 %	Significant figures of sieves[160]
Sieved Bin Mass	$\delta m_{d,sieved}$	$\pm$0.001 g	Digital milligram scale resolution
Spatial Resolution of Microscope Images		$\pm$0.4 µm/pixel	Discretization uncertainty
Spatial Resolution of Composite Microscope Images		$\pm$1.65 µm/pixel	Discretization uncertainty
Mean Equivalent Spherical Particle	$\delta d_{m,image}$	Image Specific	2x Discretization uncertainty[186]

CHAPTER 4

PREDICTING THE ENERGY RELEASE OF REACTIVE MATERIAL COMPOSITIONS

The combustion process of RM systems is complex and characterized by high temperatures, leading to dissociated species[78, 91, 199] and multiphase products[71, 76, 92]. As discussed in Section 1.4.2, prior research efforts have approached the prediction of the energy release of RM systems using either analytical methods of idealized reactions that enforce the proper phases of species[6, 69, 88] or thermochemical equilibrium solvers[67, 75, 89, 90] that are better suited to handle the complexity of dissociated species, but do not currently properly account for phases of species. Unfortunately, both methods still have limitations in their ability to predict the energy release of RM systems.

This work improves the predictive capability of the energy release of RM systems by accounting for both the dissociation of product species and enforcing phase constraints of species, referred to here as phase compliancy. Phase compliancy is implemented here into an equilibrium solver to determine the validity of product species based on phase transition temperatures from thermodynamic datasets. Existing equilibrium solvers used in RM literature (e.g. CEA and CHEETAH)[67, 69, 78, 200] are not suited to modification due to the closed-source nature of the source code and thermodynamic data sets used. Therefore, this work uses Cantera[100], an open-source thermodynamic and equilibrium solver tool suite that interfaces with the MATLAB computational environment. Cantera is an established thermochemical equilibrium solver for modeling both gas and condensed phase reactions[201–203], and readily permits the incorporation of computational routines for assessing phase compliancy of equilibrium solutions and the use of user specified thermodynamic data sets with phase transition temperatures of species.

In order to develop the means to ensure phase compliancy with Cantera, it is first necessary to understand the general theory of the minimization of Gibbs free energy methodology applied by the solver. The subsequent sections will discuss the underlying function of the equilibrium solver routines, the application of phase compliancy checks, and verification of thermodynamic data to be used with Cantera. This work will only consider thermochemical equilibrium and will not investigate reaction kinetics.

4.1 Phase compliancy with Gibbs minimization of free energy solvers

The chemical equilibrium of a multiphase mixture is calculated using a minimization of Gibbs free energy methodology by Cantera[100]. This is the same methodology applied by CEA[98] and CHEETAH[87]. Gibbs free energy is a thermodynamic potential function, found through the second law of thermodynamics, that provides a measure of the useful work that can be obtained from a system at constant temperature and pressure[199]. Chemical equilibrium of a system, in this case the mixture of gas and condensed phase species, exists at the global minimum associated with the Gibbs function[95, 96]. The change in Gibbs free energy of a multiphase mixture dG_{mix} in a system can be represented as a function of the change in pressure dP, temperature dT, and molar composition dN_i of the mixture [96]:

$$dG_{mix} = VdP - SdT + \sum_{i=1}^{k} \mu_i dN_i \tag{4.1}$$

For a system at constant temperature and pressure, integration of Equation 4.1 yields Equation 4.2 which describes the total Gibbs free energy of the mixture G_{mix} as a function of the sum of chemical potential, μ_i, and number of moles, N_i, of i constituent species:

$$G_{mix} = \sum_{i=1}^{k} \mu_i N_i \tag{4.2}$$

Treating the multiphase mixture as a non-ideal solution, the chemical potential, μ_i, takes the general form[95]:

$$\mu_i = \mu_i^{\circ}(T) + RT \ln \lambda_i \tag{4.3}$$

Where μ_i is a function of the chemical potential at the standard state, μ_i°, the ideal gas constant, R, and the activity, λ_i, of the species i of interest.

The chemical potential at the standard state, for a species i of interest, is[98]:

$$\frac{\mu_i^{\circ}(T)}{RT} = \frac{s_i^{\circ}(T)}{R} + \frac{h_i^{\circ}(T)}{RT} - \frac{h_{298,i}^{\circ}}{RT} + \frac{\Delta_f h_i^{\circ}}{RT} \tag{4.4}$$

Where μ_i° of species i is a function of the temperature of the mixture, the standard state molar entropy at T, $s_i^{\circ}(T)$, the standard state molar enthalpy at T, $h_i^{\circ}(T)$, the standard state molar enthalpy at $T = 298.15$ K, $h_{298,i}^{\circ}$, and the molar enthalpy of formation at $T = 298.15$ K, $\Delta_f h_i^{\circ}$[204]. For the assumption of a reference state at $T_{ref} = 298.15$ K used by most equilibrium solvers including Cantera[87, 98, 205], $h_{298,i}^{\circ} = \Delta_f h_i^{\circ}$ and Equation 4.4 reduces to:

$$\frac{\mu_i^{\circ}(T)}{RT} = \frac{s_i^{\circ}(T)}{R} + \frac{h_i^{\circ}(T)}{RT} \tag{4.5}$$

Incorporating Equation 4.3 and 4.5 into Equation 4.2 and rearranging to a unitless form yields Equation 4.6 that defines the Gibbs free energy of a multiphase mixture:

$$\frac{G_{mix}}{RT} = \sum_{i=1}^{k} \left(\frac{s_i^{\circ}(T)}{R} + \frac{h_i^{\circ}(T)}{RT} + \ln \lambda_i \right) N_i \tag{4.6}$$

The activity of a condensed phase species is equal to unity ($\lambda_{co} = 1$)[95, 98]. The activity of a gas phase species is equal to the partial pressure, $P_{g,i}$, of the species in the mixture[206]. A mixture of gas phases is described as a Dalton mixture of ideal gases by Cantera[100], and the thermodynamic state of this ideal gas mixture is defined as a function of pressure, temperature, number of moles of gas in the mixture, n, the volume of the gas mixture, $\cancel{V}_g$, and the ideal gas constant using $P\cancel{V}_g = nR_uT$. The activity of a single gas phase species, $\lambda_{g,i}$, in an ideal Dalton mixture can therefore be described as a function of the total pressure of the gas mixture, P_{mix}, the number of moles of species i, $n_{g,i}$, and the total number of moles of the gas phases in the mixture, $n_{g,mix}$[95]:

$$\lambda_{g,i} = P_{g,i} = P\frac{n_{g,i}}{n_{g,mix}} \tag{4.7}$$

Equilibrium is obtained for the thermodynamic and compositional state which minimizes the Gibbs free energy of the mixture ($dG_{mix} \approx 0$) as defined by Equation 4.6. For experimental measurements of RM energy release using bomb and vented calorimeters, the system can be assumed to be closed (negligible mass exchange with the environment) for finding the equilibrium state. The minimization of the Gibbs free energy is therefore constrained by conservation of mass as a result of the closed system assumption. Mass in the system is tracked on an elemental basis using:

$$\sum_{i=1}^{k} \left(\alpha_{s,ji} N_i \right) - \beta_{m,j} = 0 \tag{4.8}$$

Where the stoichiometric coefficient, α_{ji}, represents the number of atoms of element j in species i, and the total number of moles of element j originally present in the mixture is represented by $\beta_{m,j}$[95]. Equation 4.8 is applied j times to ensure all elements originally present are conserved.

Minimization of the Gibbs free energy, as given by Equation 4.6, is accomplished in Cantera using the Villars-Cruise-Smith (VCS) stoichiometric optimization algorithm[95, 98, 100]. Details of the exact implementation of the VCS optimization routine can be found in the methodology review of equilibrium algorithms by Smith[95]. By inspection of Equation 4.6, for a fixed temperature and pressure (TP) condition, the optimal set of species and molar quantities, N_i, that minimizes the Gibbs free energy of the mixture, G_{mix}, is found while adhering to the constraint given by Equation 4.8. For other state conditions, such as a fixed

enthalpy and pressure (HP) or fixed internal energy and volume (UV) conditions, iterative routines must be applied. In the case of HP equilibrium, temperature is iterated while pressure is kept constant, with TP equilibrium found for each new temperature state. This iteration continues until the enthalpy of the product mixture is equal to the initial enthalpy of the reactant mixture. In the case of UV equilibrium, temperature and pressure are both iterated, with TP equilibrium found for each new state. This iteration continues until the internal energy and specific volume of the product mixture is equal to the initial values of the reactant mixture[100].

Given that the minimization of Equation 4.6 is an optimization problem, the boundaries that govern the optimization process and define the allowable solution space are critical. By Equation 4.6, the boundaries for an applied optimization routine are given only by the mixture state (temperature and pressure), conservation of mass given by Equation 4.8, the potential product species, and the valid temperature ranges of the thermodynamic data. Careful review of the Cantera source code found that phase compliancy enforcement is not applied by the VCS routine. Specifically, the VCS routine as applied extends thermodynamic data beyond temperature bounds for phase transitions established in the dataset. This is reported to improve the robustness of the VCS routine in finding an equilibrium solution for reactions containing only gas phase species, where extending thermodynamic data generally introduces only a small amount of error[100]. However, for high temperature reactions with multiphase products, the extension of thermodynamic data becomes highly problematic as temperature bounds generally dictate phase change temperatures of condensed and gas phase species.

To enforce phase compliancy using Cantera, computational routines outside the Cantera VCS optimization routine are applied in this work. For each predicted equilibrium state, the routines determine the phase transition temperatures of each of the predicted product species. If any species are found outside their respective phase as dictated by the polynomial bounds in the thermodynamic data set, the species are removed from consideration as a viable product species in the solution. To maintain mass conservation of the system the total elemental molar amounts of the removed species are redistributed to the appropriate phase for the elemental species in the mixture. If any unconsidered species in the thermodynamic data set are permitted elementally and are phase compliant the routines will add the species back to the mixture for consideration in the solution. This aspect is important as finding the equilibrium state of the mixture is an iterative process in which the predicted temperature of the mixture varies during the process. Cases can arise when a product species was rightfully excluded for phase compliancy for one iteration of the solution product state but subsequently permissible for a later iteration due to the change in the predicted mixture temperature. Once all potential product species have been verified, the equilibrium state of the mixture is redetermined. This process continues until a phase compliant equilibrium state is determined.

Review of work by Gordon and McBride[98] indicates CEA should also have phase compliancy enforcement capability, where the phase transitions are indi-

cated by the temperature bounds of the thermodynamic data. However, careful review of the thermodynamic data used by CEA found systemic errors in temperature bounds of species when compared to data in the CRC Handbook[94], the NIST Standard Database Number 69[207], and the NIST-JANAF Thermochemical tables[208]. One of the most significant errors is in the temperature bounds of the thermodynamic data for gases, which are generally 300 K to 5000 K, an arbitrary choice of practicality for gas phase equilibrium calculations[97] that was made without consideration for multiphase reactions. This prevents the successful implementation of intended phase compliancy routines in CEA. The temperature bounds of thermodynamic data with phase change temperatures are verified in this work to ensure Cantera will provide phase compliant results with the applied phase verification routines.

4.2 Verification of thermodynamic data

A thermodynamic data set was constructed here for use with Cantera with species specific to the RM systems considered in this work. Constructing a new thermodynamic data set from existing data was necessary to permit verification of thermodynamic data and phase temperature bounds and to maintain a source history of the data. The molar thermodynamic properties of individual species of a mixture can be calculated by Cantera using the 7-coefficient NASA polynomial or 7-coefficient Shomate polynomial parameterization forms of constant pressure specific heat, enthalpy, and entropy at the standard state pressure of 0.101MPa (14.7psi)[99, 100]. Thermodynamic data in these polynomial forms was sourced by this work primarily from the NIST Standard Database Number 69[207]. The thermodynamic data used to generate these polynomials was verified against the derivative source which is the NIST-JANAF Thermochemical tables[208] before incorporation into the data set used by Cantera. For any species lacking complete data in the NIST database, thermodynamic data was sourced from literature.

Temperature bounds are included with these polynomials that dictate the valid temperature range. These temperature bounds should coincide with phase change temperatures of the respective species. Phase change temperatures of species considered in this work were sourced from the NIST-JANAF Thermochemical tables[208], the CRC Handbook[94], and NIST Standard Database Number 69[207]. For species not in these sources or lacking complete data, phase change information was sourced from literature.

Both polynomial forms of molar thermodynamic data are used in this work as the NIST Standard Database Number 69 provides coefficients for Shomate polynomials while the data in literature is often of the NASA polynomial form. The seven-coefficient Shomate polynomial form represents the thermodynamic functions given by Equation 4.9, 4.10, and 4.11 with five coefficients defining the specific heat, C_p°, enthalpy, h°, and entropy, s°, with the addition of an integration

constant to the enthalpy and entropy forms denoted by F and G respectively:

$$C_p^\circ = A + B\tau + C\tau^2 + D\tau^3 + \frac{E}{\tau^2} \tag{4.9}$$

$$h^\circ = A\tau + B\frac{\tau^2}{2} + C\frac{\tau^3}{3} + D\frac{\tau^4}{4} - \frac{E}{\tau} + F \tag{4.10}$$

$$s^\circ = A\ln\tau + B\tau + C\frac{\tau^2}{2} + D\frac{\tau^3}{3} - \frac{E}{2\tau^2} + G \tag{4.11}$$

Where $\tau = T/1000\ K$, T is in Kelvin, and A, B, C, D, E, F, and G are the polynomial coefficients sourced from the NIST Standard Database Number 69[209].

The seven-coefficient NASA polynomial form represents the molar thermodynamic functions given by Equation 4.12, 4.13, and 4.14 with five coefficients defining the standard state specific heat, enthalpy, and entropy, with the addition of an integration constant to the enthalpy and entropy forms:

$$\frac{C_p^\circ}{R_u} = a_1 + a_2T + a_3T^2 + a_4T^3 + a_5T^4 \tag{4.12}$$

$$\frac{h^\circ}{R_uT} = a_1 + a_2\frac{T}{2} + a_3\frac{T^2}{3} + a_4\frac{T^3}{4} + a_5\frac{T^4}{5} + a_6T^{-1} \tag{4.13}$$

$$\frac{s^\circ}{R_u} = a_1\ln T + a_2T + a_3\frac{T^2}{2} + a_4\frac{T^3}{3} + a_5\frac{T^4}{4} + a_7 \tag{4.14}$$

Where a_1 through a_7 are the polynomial coefficients sourced from the database or determined through fitment to thermodynamic data.

Thermodynamic databases[207, 208] lack complete thermodynamic data for PTFE with chemical formula of $(C_2F_4)_n$, the primary fluorocarbon compound used in metal-polymer RM system[67]. The NASA Glenn thermodynamic database[210], which is the source of the thermodynamic data used by CEA, does not include data for PTFE. Thermodynamic data for PTFE in the NIST Standard Database Number 69[207] is incomplete and inconsistent. Data is regularly available for tetrafluro-ethylene (C_2F_4), the highly reactive and unstable gas phase monomer that is polymerized to form PTFE[211]. C_2F_4 data is in both the NASA and NIST database[207, 210] as well as CEA[210]. Available data for the monomer has temperature bounds in the range of 300 to 6000 K[210], suggesting the data was generated using ideal gas law calculations for an arbitrary temperature range[97, 99]. C_2F_4 does exist at room temperature conditions[211], but the instability of C_2F_4 makes it highly unlikely that the species would exist at high temperatures at or near ambient pressure. As such, the upper temperature bound of the thermodynamic data for C_2F_4 is non-representative of the peak temperature the species can exist at. It is suspected that C_2F_4 thermodynamic data has been misunderstood to be representative of PTFE by researchers, as evident by the number of publications that report reaction characteristics of RM

systems that contain PTFE using CEA[67, 200]. These works do not report an alternative thermodynamic data source for PTFE which would be necessary for applicable results.

The complete thermodynamic dataset for PTFE reported by Lau et al.[212] is used here. Lau et al. used digital scanning calorimetry (DSC) to characterize the thermodynamic state of PTFE samples with various crystallinities from 220 K to 700 K at the standard state pressure of 0.101MPa (14.7psi). Lau et al. also carefully reviewed and aggregated existing PTFE thermodynamic data in literature for temperatures between 0.3 K and 220 K at the standard state pressure of 0.101MPa (14.7psi). The upper temperature bound of 700K adequately captures the thermodynamic state of PTFE needed for equilibrium calculations, as beyond 782 K, at the standard state pressure of 0.101MPa (14.7psi), PTFE begins to endothermically decompose to the gas phase monomer C_2F_4[71]. Lau et al.[212] reported variation of heat capacity between amorphous and 100% crystalline samples, which is not unexpected. The granules that comprise PTFE powders are typically 100% crystalline[212] unless otherwise specified. Therefore, thermodynamic data for 100% crystalline PTFE from Lau et al.[212] is used here. This data is reported to have a standard deviation of less than 0.3% for the temperature range between 220 K and 700 K.

Another notable observation is that complete thermodynamic datasets of elemental carbon typically originate from graphite experiments. While graphite is considered a viable product species by other researchers[67, 200], typical timescales of RM reactions are on the order of tens of milliseconds[72, 77, 78] which impose temporal limitations that preclude formation of the organized structure of graphite[213]. Similar combustion time scales in hydrocarbon combustion suggest soot is more likely to form which consist of amorphous, loose chain, and graphitic molecule conglomerates[214, 215]. Differences in thermodynamic properties between graphite[216] and amorphous carbon formations[217] do exist due to the differences in the molecular structure. However, accurate thermodynamic data and thermodynamic models of soot are lacking due to the complexities and temperature dependencies of the conglomerate formations[214, 218]. Therefore, thermodynamic data for graphite is used here to approximate elemental carbon recognizing that this may not be the best representation of the carbon formations in combustion processes involving PTFE.

The selection of species for the thermodynamic dataset used by Cantera is governed by the reactants. Reactant species are determined by the considered RM system, and the potential product species are selected based on the elemental availability dictated by the reactants. Thermodynamic data availability and justification of the viable physical existence as a product species also guides the selection process. As an example, for the combustion of Al/PTFE, available thermodynamic data for all species containing a combination of Al, C, and/or F elements, and the elemental species themselves would be included. The thermodynamic dataset assembled in this work, sources of data, and assumptions are detailed in Appendix D.

4.3 Energy release predictions and equilibrium states

The heat of combustion of a reaction is defined as the energy released as heat by the reaction[199]. This release of thermal energy is calculated as the difference in the sums of the heats of formations of the reactants and product species[199, 219] and is applicable for any equilibrium state:

$$Q_{comb} = \sum_{prod} N_p \Delta_f h_p - \sum_{react} N_r \Delta_f h_r \tag{4.15}$$

The reaction event of an RM system consists of an evolving equilibrium state associated with the changing temperatures and pressures of the reaction products. These changes in temperature and pressure of the reaction products are due to energy exchange with the environment. Initially, the energy released by the reaction is distributed to the reaction products in heating them to a high temperature. As time passes, energy from the hot reaction products transfers to the surrounding environment and the reaction products cool. Consequently, the chemical equilibrium state, and thus product species, will change due to the changing thermodynamic state. It is clear from Equation 4.15 that the product species of the state have significant impact on the calculated energy release. This implies that the calculated heat of combustion will vary depending on the considered equilibrium state of the reaction. Because it is possible to consider the thermal energy release for different equilibrium states of a reaction, discussions and comparisons of energy release of a reaction must also consider the thermodynamic state for which the energy release is calculated for or measured at.

The total energy release of a reaction corresponds to an equilibrium state characterized by thermal equilibrium of the reaction products with the surrounding global environment[199]. This state can be approximated as the product species returning to the initial temperature of the reactants through transfer of energy to the environment. Because this is effectively the lowest energy state that is obtainable for the reaction, the heat of combustion is maximized for the system[199]. This state is referred to here as the global equilibrium state. The typical experimental measurement that represents this condition is bomb calorimetry where the temperature change of the system is monitored post-initiation until thermal equilibrium of the system is established. The chemical composition for RM systems at global equilibrium is characterized by a limited number of product species of which the majority are condensed solid phase[6].

Another equilibrium state that is typically of interest is associated with the adiabatic flame temperature [6, 67]. This is considered a local equilibrium state here as the reaction products have achieved chemical and thermodynamic equilibrium, but by definition have not come to thermal equilibrium with the surrounding global environment. At this equilibrium state a large number of dissociated species are present due to the high temperature, which directly impacts calculations made using Equation 4.15. Because the condition does not represent the lowest energy state of the system, the energy release calculated for the condition must be less than the total energy release of the reaction. This has been

indirectly shown by Fischer and Grubelich[6] who demonstrated that using total energy release in calculating led to significant over prediction of temperatures and non-physical results[6].

The concept of local and global equilibrium states has significant implications for comparisons of theoretical predictions to experimental results or experimental results between different methods. Comparisons of energy release calculated for the condition to measurements from bomb calorimetry is not appropriate as the condition represents a local equilibrium state and bomb calorimetry measures at a global equilibrium state. Alternatively, direct comparisons of long timescale measurements from bomb calorimetry to short timescale measurements in vented chamber calorimetry may present challenges due to the potential differences in the equilibrium state of the systems. The error associated with these comparisons will strongly depend on the rate at which the reactions approach the global equilibrium condition both in composition of product species and temperature. These nuances in comparing energy release have not been discussed in other works studying RM energy release[49, 67–69, 75, 77, 84, 85], but will guide the analysis efforts here.

CHAPTER 5

EXPERIMENTAL METHODS FOR STUDY OF REACTIVE MATERIAL ENERGY RELEASE

The energy release of RM systems studied in this work will be measured using the two primary experimental methods applied in RM literature: bomb calorimetry[10, 73, 74, 79] and vented calorimetry[68, 69, 75, 86]. Measurements of the energy released from the combustion of RM specimens under ideal conditions will be performed using bomb calorimetry, where measurements of both the energy release and internal pressure of the bomb will be taken. Measurements of the energy released from the combustion of RM specimens under impact conditions analogous to application will be performed using a vented calorimeter, where measurements of both the energy release and size distributions of fragments will be taken.

Results from bomb calorimetry are used to validate the energy release predictions by the Cantera equilibrium solver for the global equilibrium state of the evaluated RM systems. Subsequently, results from vented calorimetry are compared to energy release measurements from the bomb calorimeter and energy release predictions for the local equilibrium state associated with the measurement conditions to ascertain combustion efficiency. This supports the developing understanding of the association between fragment production and energy release.

5.1 Bomb calorimetry

Bomb calorimetry measures the total energy released by the chemical reaction (combustion) of a material sample under constant volume conditions [81, 82]. A schematic representative of a conventional bomb calorimeter system, with a pressure tap, is shown in Figure 5.1. A material sample (solid, liquid, or powder) is placed in a ceramic crucible inside a sealed container, traditionally called a combustion bomb, filled with a gas. The bomb gas may be an oxidizing agent such as air or oxygen, as is typical with studies of solid and liquid fuels[79, 81–83]. Alternatively, the bomb gas may be inert, such as argon, to insure the sample is the only component of the reaction as is typical with thermites or RMs[73, 84]. The combustion bomb is surrounded by a working fluid, typically water or oil[10, 82], and a stirrer moves the working fluid around the bomb to promote thermal

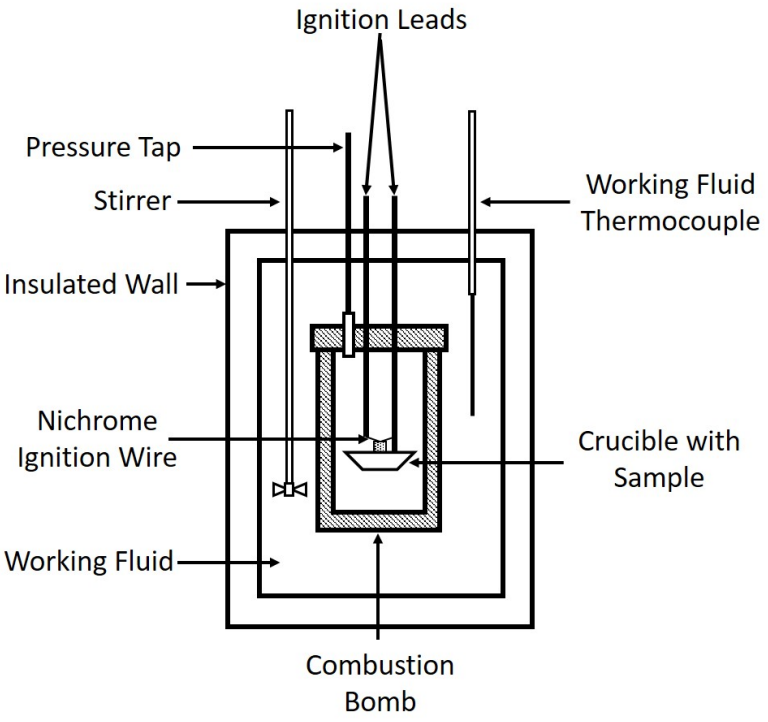

Figure 5.1: Schematic of a typical bomb calorimeter system. Primary components are labeled. Specific to this work is a pressure tap for measuring the interior pressure of the combustion bomb.

equilibrium of the system. A nichrome wire in contact with the sample is heated to initiate the reaction.

In bomb calorimetry, the change in internal energy of the system, comprised of the combustion bomb, gas in the bomb, and working fluid, is measured to infer the total net heat into the system[81, 82]. The combustion bomb and working fluid remain constant in volume, and therefore no work is done by these system components. Because the combustion event inside the bomb is a constant volume process, no work is done by the gas in the bomb. This corresponds to $(Pd\forall)_{cb} = 0$, where the subscript cb indicates the gas internal to the combustion bomb. From the first law of thermodynamics, the change in internal energy, ΔU, of this system, assuming no change in the kinetic energy or potential energy, is:

$$\Delta U = Q \tag{5.1}$$

Where Q is the total net heat into and out of the system. To mitigate energy out of the system, insulation or an air gap surrounds the working fluid. Thus, the change in internal energy of the system is assumed to be solely a result of the heat into the system which is taken as the energy released from the reaction of the sample[81, 82]. Because the heat released by the reaction takes time to propagate

through the system, it can takes tens of minutes for thermal equilibrium to be obtained after reaction of the sample.

The reported energy released from a chemical reaction, typically called the heat of combustion, corresponds to the change in enthalpy at constant pressure[199, 219]. The enthalpy change of a constant pressure, constant volume system is[96]:

$$\begin{aligned} \Delta H &= \Delta U + \forall dP + Pd\forall \\ \Delta H &= \Delta U + 0 + 0 \\ \Delta H &= \Delta U = Q \end{aligned} \tag{5.2}$$

Therefore, bomb calorimetry approximates the change in enthalpy of the system, ΔH, corresponding to the energy release from the reaction of the sample, as the change in internal energy of the system, ΔU. For this approximation to hold, a near constant pressure condition must be maintained inside the combustion bomb, permitting $\Delta H = Q$ via Equation 5.2. This simplifies the energy release measurements, as only the constant pressure specific heat must be known and temperature change of the system measured to determine the change in enthalpy and thus energy release from the chemical reaction of the sample. The change in enthalpy, ΔH, of this system is[82]:

$$\Delta H = m_{sys} \sum_{i=1}^{k} \frac{m_i}{m_{sys}} C_i \Delta T = m_{sys} C_{sys} \Delta T \tag{5.3}$$

Where ΔH is a function of the mass weighted sum of the constant pressure specific heats of the system components (combustion bomb, working fluid, gas in combustion bomb) and the change in temperature of the system, ΔT. The specific heat contribution by the sample is negligible for small sample mass sizes ($<$1 g)[81, 82]. Because ΔT is generally small for bomb calorimetry measurements, constant specific heat is assumed[81]. The specific heat of the system, C_{sys}, which is the summation of the mass weighted specific heat contributions of the system components, is determined by the temperature rise, ΔT, of the system for a known energy release. Typically, C_{sys} of the system is determined from the temperature rise resulting from the energy released by the combustion of benzoic acid[82] or thermal energy from a resistive heating element[85].

The majority of combustion reactions, including RM systems[220–222], release gaseous species[199]. For the constant pressure approximation to hold, it is necessary to minimize the change in internal pressure of the bomb due to the additional moles of product gas. This is traditionally accomplished using a high initial pressure of the gas in the bomb[81, 82]. A high initial pressure increases the number of initial moles of gas, minimizing the pressure increase from the additional moles of gas product species. Typical initial gas pressures in the combustion bomb are 3 MPa (30 atm) to minimize the pressure change from the reaction of the sample[81, 82]. For properly sized carbon, nitrogen, and hydrogen

based samples (≤ 1 g), such as hydrocarbon fuels, the high pressure environment typically minimizes the measurement error associated with the constant pressure assumption to <0.1%[81]. As a result, the $(\forbar dP)_{cb}$ correction is typically ignored by works using high initial pressure in the combustion bomb[82]. For RM systems, application is typically at or below 101 kPa (1 atm), and the multiphase nature of the species introduces pressure dependencies of the reaction[221–223]. Therefore, combustion of RM samples at high pressure is not desirable.

For reactions of samples under pressure conditions near 101 kPa, the energy release measurement must be corrected for the pressure increase due to the additional moles of gas product species to ensure the correct change in enthalpy is measured[81]. For carbon, nitrogen, and hydrogen based samples, such as hydrocarbon fuels, the correction can be made analytically by calculating the pressure rise based on the mole change of gas species in the bomb, assuming the product species of the reaction based on stoichiometry[81]. Analytical corrections are not viable for RM systems due to the complexity of the reaction. Wang et al.[221] observed equilibrium pressures on the order of 1 MPa for nano Al/BiO_3 in Parr 1108 combustion bombs with an initial pressure of 101 kPa and samples sizes below 1 g. For cases where the constant pressure approximation cannot be maintained, the change in enthalpy of the system, ΔH, corresponding to the energy release from the reaction of the sample, is[81, 96]:

$$\Delta H = \Delta U + (\forbar dP)_{cb} = m_{sys} C_{sys} \Delta T + (\forbar dP)_{cb} \tag{5.4}$$

This work uses direct pressure measurements of the internal pressure of the combustion bomb to calculate the $(\forbar dP)_{cb}$ term. Initially a 102B04 PCB Piezotronics pressure transducer was used for pressure measurements, but was found not to be suitable for the long time scales associated with bomb calorimeter pressure measurements, which are on the order of minutes. This is due to the discharge behavior of piezoelectric transducers leading to artificial decrease in the voltage and thus pressure signal with time. Instead, an Endevco 8530C-100 absolute piezoresistive transducer was utilized for internal pressure measurements as it provides a true pressure measurement regardless of the measurement duration. The Endevco transducer provides microsecond resolution for pressures less than 0.69 MPa. The measurement uncertainty of the Endevco 8530C is reported by the manufacture as ± 4 KPa. These pressure measurements also provide the potential to infer phase transitions of species, as demonstrated by Baijot et al[222], Wang et al.[221], and Williams et al.[220].

A Parr 6200 bomb calorimeter is used to measure the energy release of RM systems studied in this work. The measurement uncertainty of the machine is conservatively taken as 0.1% which is the reported precision of the measurement. The Parr 6200 uses Parr 1108 series combustion bombs, with an interior volume of 0.342 L, and 2 L of water as the working fluid that surrounds the bomb. For measurements of non-oxidizing RM systems, bombs are filled with air at 101 kPa. For measurements of self-oxidizing RM systems, the Parr 1108 bombs are filled with argon at 101 kPa. Argon is chosen for two reasons: the constant pressure specific

heat of argon has negligible variation with temperature[207] reducing measurement error, and argon does not react with the RM sample ensuring the measured energy release corresponds only to the reaction of the sample[84]. To mitigate residual air in the 1108 bombs after self-oxidizing samples have been loaded, loaded bombs are subjected to vacuum for seven minutes followed by a dry argon purge. This process is performed in an antechamber of an argon purged glove box. Two purges are performed in the antechamber before the bombs are moved inside the glove box, sealed, and then removed from the glove box for testing. Because argon is used, the traditional use of benzoic acid to determine the constant pressure specific heat of the system is not possible, as the benzoic acid requires oxygen to sustain a reaction. Therefore, an electric resistive heater is used to determine the specific heat capacity of the system in a manner similar to the method applied by Kobyakov et al.[85].

Wang et al.[221] and Williams et al.[220] showed that for Al based RM systems, particle size effects on the energy release measurement can be minimized by using constituent powders with single micron particle sizes. Therefore, the mean constituent particle size for energy release measurements of RM systems studied in this work is $\sim$10 µm to minimize particle size effects. To minimize the total and peak pressure rise in the Parr 1108 bomb resulting from combustion of the sample[221], RM powder samples do not exceed 1 g.

5.2 Vented calorimetry

Vented calorimetry measures the energy released from the chemical reaction of an impact-initiated RM specimen in a constant volume chamber. A general schematic of a vented calorimeter is shown in Figure 5.2. In using the vented calorimeter, an RM specimen is launched using a gas or powder gun system either through a target plate sealing a port on the calorimeter chamber or directly into the chamber through a small hole. In the case of a target plate impact, the specimen fragments on impact and the fragments then travel into the calorimeter. These fragments impact the anvil which causes further fragmentation and ignition of the fragments. In the case where no target plate is used, the specimen directly impacts the anvil which drives the fragmentation and subsequent combustion of produced fragments. The change in pressure of the working fluid (the gas inside the chamber) is measured using a pressure transducer and is used to estimate the energy release of the specimen[68], similar to energy release measurements using pressure measurements of the interior of combustion bombs[69].

Ames[68] provides a detailed discussion of the vented calorimeter methodology. In summary, application of the methodology assumes that only a small amount of the total mass of the specimen is represented as gas phase reaction products, the volume of the system remains constant, and energy flux outside of the volume through heat transfer is negligible due to the short timescales of

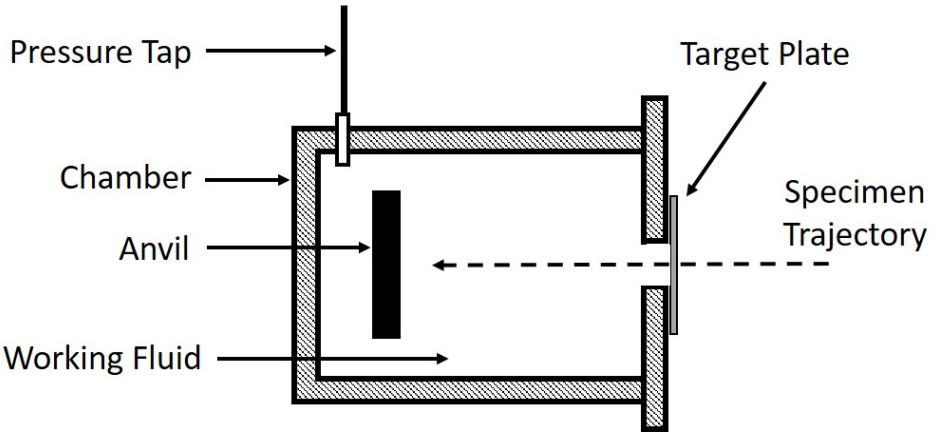

Figure 5.2: Schematic of a typical vented calorimeter system. Primary components and trajectory of the RM specimen are labeled.

the combustion event (<1 s). These assumptions imply the density of the working fluid (gas in the system) before impact and after impact of the specimen is equivalent. Assuming a calorically perfect gas and ideal gas behavior of the gas working fluid, the rate of heat addition from the impact and combustion event, dQ_{vc}/dt, is related to the rate of change in quasi-static pressure of the gas in the chamber, $\partial P_{vc}/\partial t$, and the change in mass of gas in the chamber (resulting from the mass flux through the perforated target plate), dm_{vc}/dt, as[68]:

$$\frac{dQ_{vc}}{dt} = \frac{\forall_{vc}}{\gamma - 1}\frac{\partial P_{vc}}{\partial t} + \frac{\gamma P_{vc}\forall_{vc}}{m_{vc}(\gamma - 1)}\frac{dm_{vc}}{dt} \tag{5.5}$$

Where $\forall_{vc}$ is the volume of the chamber and γ the ratio of specific heats of the working fluid. Here, quasi-static pressure refers to the pressure change induced by the combustion of the RM specimen and heating of the working fluid due to the propagation of the shock generated from the specimen impact with the anvil. The quasi-static pressure does not include the blast pressure associated with the shock[68].

Uncertainty analysis by Ames[68] showed that effects of mass loss through the hole the specimen passed through were negligible at short timescales as a result of choked flow at the hole and the short duration of the combustion event. Thus, in some cases it can be assumed that mass loss is negligible through venting such that $dm_{vc}/dt \approx 0$. Applying these assumptions and integrating Equation 5.5 yields[68]:

$$\Delta Q_{vc} = \frac{\Delta P_{vc}\forall_{vc}}{\gamma - 1} \tag{5.6}$$

Where ΔP_{vc} is the change in quasi-static pressure of the gas working fluid inside the chamber, such that $\Delta P_{vc} = P_{max,vc} - P_{ini,vc}$, and ΔQ_{vc} is the heat released into the chamber from the combustion of the specimen and kinetic energy, such that $\Delta Q_{vc} = Q_{comb,vc} + Q_{KE}$.

The use of the peak quasi-static pressure, $P_{max,vc}$, in the calculation of ΔP_{vc} implies the assumption that the reaction of the RM specimen is completed by the time $P_{max,vc}$ is reached. Consequently, if the chemical reaction of the specimen continues after the peak pressure is reached, this portion of the energy contribution to the total energy release is not accounted for using Equation 5.6. Ames[68] identified this issue, and states that for fast reacting RM systems Equation 5.6 may be appropriate, and for slow reacting systems Equation 5.5 should be used. No discussion of a reaction rate cutoff criteria is provided for making this determination. Other research efforts that have used vented calorimetry have not addressed the limitation of Equation 5.6 or discussed how energy released from the continued chemical reaction after the peak quasi-static pressure rise is accounted for in their reported measurements[70, 75, 86]. It is suspected that this lack of consideration may be an additional contributing factor to the deviations between experimental and theoretical results reported in these works as discussed in Section 1.4[70, 75, 86].

This work will assess the validity of Equations 5.5 and 5.6 for measuring the actual energy release of an RM reaction using the pressure measurements from the combustion bomb discussed in the previous section. Verification has not been performed of the methodology proposed by Ames[68] against a traditional energy release measurement such as bomb calorimetry. The pressure measurements of the interior of the combustion bomb made in this work allow the energy release to be calculated using the complete energy balance (Equation 5.5) and simplified form (Equation 5.6) proposed by Ames. Comparison of the calculated values can then be made to the energy release measurements by the bomb calorimetry method. Because bomb calorimetry is a true closed system, such that $dm/dt = 0$, the comparison permits assessment of the simple thermodynamic theory that governs the methodology proposed by Ames[68].

To maintain the calorically perfect gas assumptions in vented chamber calorimetry, argon is used for self-oxidizing RM systems as it has negligible specific heat variation with temperature[207]. For non-oxidizing RM systems, air is used as both the oxidizing agent and working fluid. The variation in specific heat of air is non-negligible at temperatures exceeding 600 K[68]. Expected temperatures in the vented calorimeter chamber are 500 K to >2000 K[68]. To account for the specific heat variation of air, the approach by Kline et al.[180] is followed in calculating the variation of the specific heat of air with temperature using a thermodynamic polynomial.

Following work by Ames[68], the mass flux through the hole the specimen passes through is described using isentropic flow and ideal gas relations. The flow through the perforated plate is choked when[68]:

$$P_{vc}(t) \geq P_{atm} \left(\frac{2}{\gamma + 1} \right)^{\frac{\gamma}{\gamma - 1}} \tag{5.7}$$

Where $P_{vc}(t)$ is the quasi-static pressure in the chamber at time t and P_{atm} is the ambient static pressure outside the chamber. When the condition given by Equa-

tion 5.7 is satisfied, mass flux through the perforated plate is[68]:

$$\frac{dm_{vc}}{dt} = A_h \sqrt{\frac{\gamma P_{vc}(t) m_{vc}(t)}{\cancel{V}_{vc}}} \left(\frac{2}{\gamma+1}\right)^{\frac{\gamma+1}{2(\gamma-1)}} \tag{5.8}$$

Where $m_{vc}(t)$ is the total mass of the working fluid in the chamber at time t and A_h is the area of the hole in the plate. This relation assumes that the hole area does not change during the venting process. When the condition given by Equation 5.7 is not satisfied, the flow is not choked and the mass flux through the hole is[68]:

$$\frac{dm_{vc}}{dt} = A_h \left(\frac{2\gamma}{\gamma-1} \frac{P_{vc}(t) m_{vc}(t)}{V} \left[\left(\frac{P_{vc}(t)}{P_{atm}}\right)^{\frac{2}{\gamma}} - \left(\frac{P_{vc}(t)}{P_{atm}}\right)^{\frac{\gamma-1}{\gamma}} \right] \right)^{\frac{1}{2}} \tag{5.9}$$

The vented calorimeter design used here is informed by the work by Ames[68]. The calorimeter chamber is a rectangular steel tube with 12.7 mm thick walls, interior dimensions of 178 mm in width and height and 305 mm in length, and an approximate volume of $9.66 \cdot 10^{-3}$ m^3. Eight 12.7 mm thick acrylic optical access ports allow visualization of the fragmentation and combustion events using the high speed focused shadowgraph imaging system. A 102B04 PCB Piezotronics pressure transducer is used for pressure measurements and is installed behind the replaceable anvil. Because the event times in these tests are on the order of 10^1 milliseconds, the discharge behavior of the piezoelectric transducer is not an issue. To minimize noise imparted in to the pressure measurements by the impact event, the anvil is attached to the rear of the vented calorimeter using four rubber isolaters. To provide damping mass, the anvil is a 127 mm tall, 76 mm wide, and 25.4 mm thick steel plate weighing $\sim$2kg.

The vented calorimeter is installed inside the stainless steel chamber and the 14 mm diameter, smooth bore powder gun is used to accelerate RM specimens into the calorimeter. The vented calorimeter installed in the stainless steel chamber is shown in Figure 5.3 with primary components labeled. Specimens are launched directly into the anvil and not through a target plate in this work. This is performed for two reasons: to avoid mass loss during the penetration of the target plate thus ensuring the mass entering the vented calorimeter is known; and to assess combustion of the fragments produced directly from the bulk specimen. It is desirable to look at fragments produced from the impact of the bulk specimen with the anvil as this is readily comparable to results from the impact tests performed here by accounting for the increase in strain rate. Conversely, when launching specimens into target plates, measurements are made of the combustion of fragments produced from fragments that impacted the anvil. This secondary fragmentation and combustion event are not explored here.

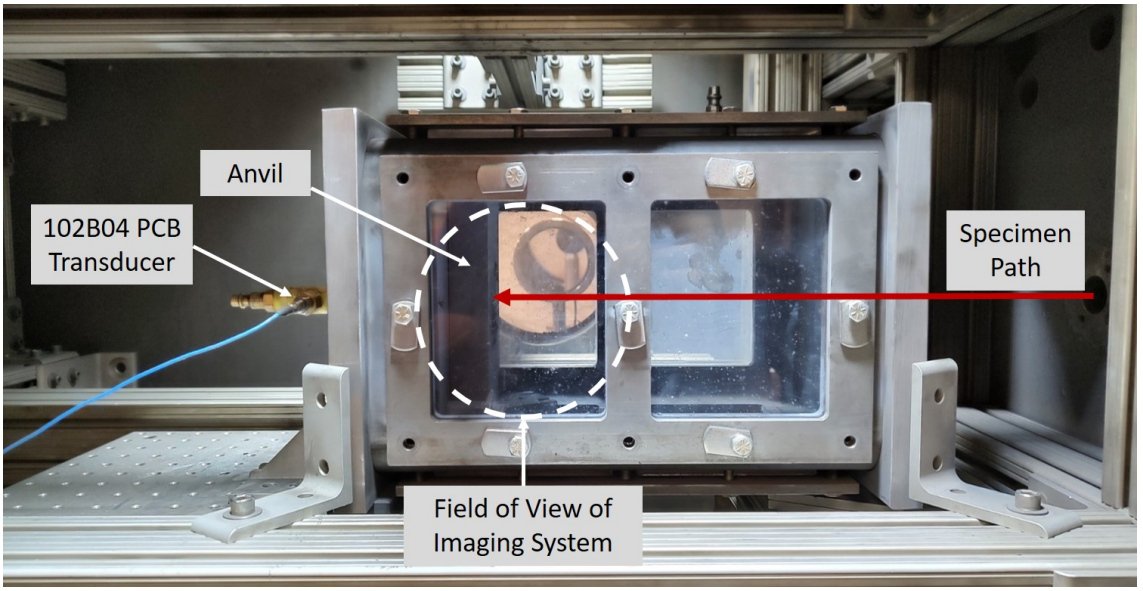

Figure 5.3: Vented calorimeter installed inside stainless steel chamber used in impact tests. Primary components, trajectory of RM specimen, and approximate field of view of the imaging system are labeled.

CHAPTER 6

EVALUATED REACTIVE MATERIAL SYSTEMS AND MANUFACTURING OF SPECIMENS

Multiple RM systems were evaluated prior to selecting the final RM systems for study in this work. The selected systems were evaluated from the perspective of manufacturability, such that the porosity and particle size distribution of the constituent powders showed potential for controlled variation. The final RM systems selected for this work and experimental design are discussed.

6.1 Evaluated RM systems

This work will consider three non-sintered RM systems: Al, Al/PTFE and Al/Fe_2O_3/PTFE. The Al RM system is selected as the material properties and fragmentation behavior of the system are well studied in literature[5, 11, 27, 180]. This facilitates comparison of results in this work to existing research efforts. The non-sintered forms of Al/PTFE and Al/Fe_2O_3/PTFE are chosen as they are under-represented in the RM field of research. The material, fracture, and energy release behaviors of sintered Al/PTFE compositions are well studied in literature [8, 224–232]. These works, however, have limited comparability to non-sintered Al/PTFE as the sintering process significantly changes the microstructure of the material[229, 231]. Studies of the Al/Fe_2O_3/PTFE system have become more prominent, with the mechanical and energy release behaviors of sintered Al/Fe_2O_3/PTFE systems reported[72, 231, 233]. Fragmentation behavior of the Al/Fe_2O_3/PTFE system has been discussed qualitatively, but quantitative fragmentation studies are lacking. As with the Al/PTFE system, these works have limited comparability to non-sintered Al/Fe_2O_3/PTFE as the sintering process significantly changes the microstructure of the material[229, 231].

The stoichiometric compositions of the Al, Al/PTFE, and Al/Fe_2O_3/PTFE systems are approximated here analytically. For these reactions, the global equilibrium state is considered such that the reaction products have returned to the initial temperature of the reactants. Subscripts are used to denote the phase assumed of the species with g and s denoting gas and solid phases, respectively. For the aluminum RM system, combustion can only occur in an oxidizing environment. This work will consider air for the oxidizing environment. The stoi-

chiometric equation for Al reacting with air is[234]:

$$4\mathrm{Al}(s) + 3\mathrm{O_2}(g) + 11.3\mathrm{N_2}(g) \rightarrow 2\mathrm{Al_2O_3}(s) + 11.3\mathrm{N_2}(g) \tag{6.1}$$

Note that reactions between aluminum and the nitrogen in the air are assumed negligible[234, 235]. The stoichiometric equation for Al/PTFE is given as:

$$4\mathrm{Al}(s) + 3(\mathrm{C_2F_4})_n(s) \rightarrow 4\mathrm{AlF_3}(s) + 6\mathrm{C}(s) \tag{6.2}$$

Which corresponds to the mass fraction composition of 26.45% Al and 73.55% PTFE. Determination of the true stoichiometric composition of the Al/Fe_2O_3/PTFE system is non-trivial analytically as the presence of two oxidizers introduces multiple reaction paths. The stoichiometric composition for the Al/Fe_2O_3/PTFE system is approximated in this work assuming independent stoichiometric reactions between Al and Fe_2O_3 and Al and PTFE, such that:

$$[2\mathrm{Al}(s) + \mathrm{Fe_2O_3}(s)] + [4\mathrm{Al}(s) + 3(\mathrm{C_2F_4})_n(s)] \rightarrow \\ [2\mathrm{Fe}(s) + \mathrm{Al_2O_3}(s)] + [4\mathrm{AlF_3}(s) + 6\mathrm{C}(s)] \tag{6.3}$$

Which corresponds to the Al/Fe_2O_3/PTFE mass fraction composition of 26.03% Al, 25.69% Fe_2O_3, and 48.28% PTFE. This approximation is assumed to locate the general region of the stoichiometric Al/Fe_2O_3/PTFE composition for selecting the non-stoichiometric compositions for fragmentation and vented calorimetry studies as discussed in the next section.

Manufacturing trials were performed to determine obtainable porosities of Al, Al/PTFE, and Al/Fe_2O_3/PTFE RM specimens. Compositions were considered viable if consolidation was possible at porosities equal to and less than the 20% porosity limit imposed by the developed analytical theory. It was determined from these trials that the porosity could be varied between$\sim$5% and $\sim$20% for the Al and Al/PTFE compositions and a minimum of 20% porosity was obtainable for Al/Fe_2O_3/PTFE compositions with less than 33.33% Fe_2O_3 by volume. The consolidation limit of the Al/Fe_2O_3/PTFE system restricts evaluation of the composition and particle size dependencies of the system to the 20% porosity condition. As such, this work will examine all three compositions to evaluate composition and particle size dependencies, and will use the Al and Al/PTFE systems to evaluate porosity dependencies.

6.2 Experimental design

Specific Al/PTFE and Al/Fe_2O_3/PTFE compositions are chosen in order to map the composition, porosity, and particle size dependencies of a portion of the Al/PTFE and Al/PTFE/Fe_2O_3 compositional space. This compositional space is shown in Figure 6.1. Experimental measurements will provide data for which the developed theory in this work can be validated against. Subsequently, the

developed theory can be applied to map the experimentally unexplored compositional space bounded by the evaluated compositions. Nine non-stoichiometric compositions that are evenly distributed over the volume fraction compositional space will be evaluated in addition to two stoichiometric compositions. Two of the non-stoichiometric compositions are the individual constituents Al and PTFE. The constituent Fe_2O_3 will not be evaluated in this work as manufacturing trials demonstrated that Fe_2O_3 could not be consolidated on its own without causing severe damage to pressing equipment. The location of evaluated compositions in the Al/PTFE and Al/Fe_2O_3/PTFE compositional space are shown in Figure 6.1. The evaluated compositions, applied porosity and particle size variation, and applied experimental methods are summarized in Table 7.1.

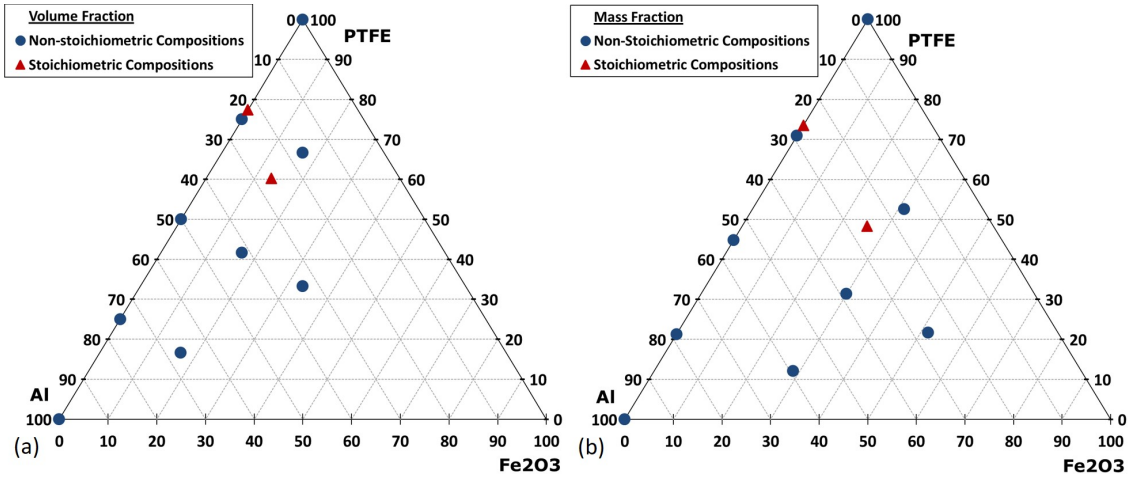

Figure 6.1: The compositional space of the Al/PTFE and Al/Fe_2O_3/PTFE RM systems presented in (a) volume fraction compositional space and (b) the equivalent mass fraction compositional space. The non-stoichiometric and stoichiometric compositions to be studied in this work are indicated.

The material, fragmentation, and energy release behavior of the systems will be evaluated for two porosities and two particle size ranges. The two evaluated porosities will be the nominally 5% and nominally 20% porosity conditions. Due to manufacturing limitations, only the Al and Al/PTFE systems will be evaluated at both 5% and 20% porosity conditions, and the Al/Fe_2O_3/PTFE system will be evaluated at 20% porosity only. The 5% porosity case corresponds to the equipment limit observed during manufacturing trials of the Al system, and the 20% porosity case corresponds to the limit associated with the developed theory and the manufacturing limit of the Al/Fe_2O_3/PTFE system.

The two evaluated particle size ranges are referred to here as ”coarse” and ”fine” for simplicity. The coarse particle size range corresponds to commercially available powders that have a supplier reported particle size range of $<$44 µm (-325 mesh). The fine particle size range corresponds to commercially available

Table 6.1: Summary of evaluated compositions and the applied porosity variation, particle size variation, and experimental methods

Composition by Volume Fraction	Applied Variations	Applied Experimental Methods
100Al 75Al/25PTFE 50Al/50PTFE 25Al/75PTFE 100PTFE	5% and 20% Porosity Particle Size Range: Coarse and Fine	Quasi-static Compression Tests (Sec. 3.1) Fracture Toughness Tests (Sec. 3.2) Wave Speed Measurements (Sec. 3.3)
66.70Al/16.65Fe_2O_3/16.65PTFE 41.68Al/16.65Fe_2O_3/41.68PTFE 33.33Al/33.33Fe_2O_3/33.33PTFE 16.65Al/16.65Fe_2O_3/66.70PTFE	20% Porosity Particle Size Range: Coarse and Fine	Quasi-static Compression Tests (Sec. 3.1) Fracture Toughness Tests (Sec. 3.2) Wave Speed Measurements (Sec. 3.3)
100Al 25Al/75PTFE 100PTFE	5% Porosity Particle Size Range: Coarse and Fine	Kolsky Compression Tests (Sec. 3.4) High Velocity Impact Tests (Sec. 3.5)
100Al 25Al/75PTFE 22.60Al/77.4PTFE 16.65Al/16.65Fe_2O_3/66.70PTFE 26.35Al/13.45Fe_2O_3/60.20PTFE	Particle Size Range: Fine	Bomb Calorimetry (Sec. 5.1)
100Al 25Al/75PTFE	5% Porosity Particle Size Range: Coarse and Fine	Vented Calorimetry (Sec. 5.2)

powders that have a supplier reported particle size range of 1-5 µm. Exact measurements of the particle size distributions of the constituent powders are made using the scanning optical microscope and discussed in the subsequent section. The effects of mixing of the two size ranges of the constituents powders will not be considered by this work. As such, each RM specimen evaluated for a range will be comprised entirely of constituent powders that have particles within the size range.

Statistical considerations are often lacking for quantitative results of RM systems reported in literature[5, 11, 12, 27, 231, 233]. This work will approach statistics of experimental results from the perspective of confidence intervals. A confidence interval is a range within which the true population mean of a parameter

of interest (e.g. elastic modulus, fracture toughness, characteristic fracture size, etc.) is expected to reside[236]. Mathematically this can be described using a two-tailed hypothesis test where the true population mean, μ_{TP}, lies in a range defined by the sample mean, $\bar{x}$, and error of estimation, δ:

$$\bar{x} - \delta \leq \mu_{TP} \leq \bar{x} + \delta \tag{6.4}$$

The confidence interval is given by the bounds $\bar{x} - \delta$ and $\bar{x} + \delta$, and a reduced interval range corresponds to reduction in δ, implying a better understanding of where the true population mean resides. Minimization of δ can be accomplished by increasing the sample size, η, or reducing the confidence level, CL, for the interval. The confidence level of the interval represents the probability that the true value of the population parameter lies within the range given by the confidence interval and is typically 90% or 95%[209, 236].

This work will use a standard confidence level of $CL = 90\%$[209, 236] to determine a minimum sample size for experimental testing. Two methods are applied in this work in determining δ, and subsequently the range of the confidence interval. Both methods assume a normal distribution of the population. The first method is given by the NIST and SEMATECH Engineering Statistics Handbook[209] using a single theoretical sample set from a population. The confidence interval and error of estimation of the NIST method are:

$$\bar{x} - \delta_{NIST} \leq \mu_{TP} \leq \bar{x} + \delta_{NIST} \tag{6.5}$$

$$\delta_{NIST} = \sigma_{SD} \frac{t_{dist(1-\Theta/2,\eta-1)}}{\sqrt{\eta}} \tag{6.6}$$

Here σ_{SD} is the standard deviation of the respective sample set, η is the number of samples, and t_{dist} the two-tailed t-distribution for the significance level, $\Theta = 1 - CL$, with degrees of freedom determined by η.

The second method compares the difference in means (DIM) of two theoretical sample sets from two similar populations with equal number of samples taken[236]. This would be equivalent to comparing the means of a material property from two different sample sets of RM specimens that have the same composition, porosity, and particle size distribution, but are from different manufacturing batches. The confidence interval and error of estimation of the DIM method are[236]:

$$\bar{x}_1 - \bar{x}_2 - \delta_{DIM} \leq \mu_{TP,1} - \mu_{TP,2} \leq \bar{x}_1 - \bar{x}_2 + \delta_{DIM} \tag{6.7}$$

$$\delta_{DIM} = \frac{\sigma_{SD,1} + \sigma_{SD,2}}{2} \frac{t_{dist(1-\Theta/2,2\eta-2)}}{\sqrt{2/\eta}} \tag{6.8}$$

The corresponding bounds of the confidence intervals, determined using both methods, are given as multiples of the standard deviation of the sample sets as a function of sample size for a confidence level of 90% in Figure 6.2.

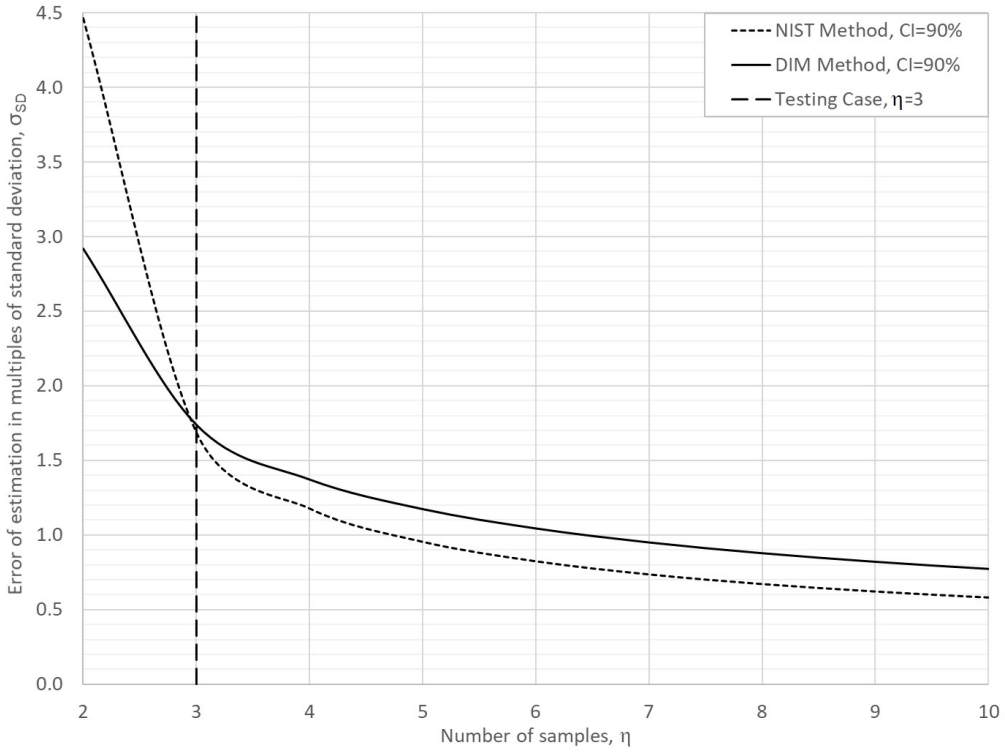

Figure 6.2: Error of estimation in multiples of standard deviations as a function of the number of samples in a sample set of a population.

The DIM method provides the more conservative estimate of δ for $\eta \geq 3$. For the DIM method, $\eta = 3$ yields $\delta \leq 1.75\sigma_{SD}$, $\eta = 4$ yields $\delta \leq 1.4\sigma_{SD}$, and $\eta = 7$ yields $\delta \leq 0.95\sigma_{SD}$. The selection of a sample set now becomes a balance of statistical need and temporal practicality. This work will aim to utilize three samples ($\eta = 3$) per test as it provides an understanding of the statistical representation of the data at a manageable scope of required experimental work.

6.3 Manufacturing of specimens

Specimens for experimental testing are manufactured in lab facilities located in the Energetic Materials Research and Testing Center (EMRTC) Field Lab. Powder compositions are prepared by blending the constituent powders in 30 g or 100 g batches. The raw powders are loaded into steel jars and 10 mm steel ball bearings are added to improve mixing of the constituent powders at a 5 to 1 ratio of mass of balls to mass of powder. Hexane is added to promote blending of the PTFE and prevent agglomeration. For 30 g batches, 75 ml of hexane is added, and for 100g batches 250ml of hexane is added. The loaded jars are rolled at 60 RPM for 2 hours using a US Stoneware roller machine. After rolling, the powders are

placed in a fume hood to allow the remaining hexane to evaporate. Once dried, the ball bearings are removed.

The blended constituent powders are consolidated using double action uniaxial pressing into the desired specimen shape. Two types of consolidated powder specimens are manufactured for this work. The dimensions of the specimens and use in experiments are summarized in Table 6.2. A Natoli NP-RD10A hydraulic single stage press with Natoli manufactured dies is used for consolidating the 6.35 mm cylinders. A Model-C Carver lab press is used for consolidating the 12.7mm discs with MTI Corp. dies. Pressing force, and thus peak uniaxial stress developed in the specimen, was varied to obtain the desired porosity of the compositions. Typical peak uniaxial stresses applied here are between 8 MPa (1 ksi) and 271 MPa (39 ksi), with the upper limit dictated by the capabilities of the dies. It is noted that unconsolidated powder is used for bomb calorimetry experiments and the grooved-disk specimens for fracture toughness measurements are cut separately using a ball end mill as discussed in Section 3.2.

Table 6.2: Dimensions of manufactured specimens and experimental purpose

Specimen Type	Dimensions	Applied Experimental Method
Cylinder	Diameter: 6.35 mm Length: 6.35 mm	Quasi-static Compression Tests (Sec. 3.1) Wave Speed Measurements (Sec. 3.3) Kolsky Compression Tests (Sec. 3.4) High Velocity Impact Tests (Sec. 3.5) Vented Calorimetry (Sec. 5.1)
Disc	Diameter: 12.7 mm Thickness: 4 mm	Fracture Toughness Tests (Sec. 3.2)

To ensure safe handling and manufacturing of specimens, a sensitivity testing series[237] was performed on stoichiometric mixtures of Al/Fe_2O_3/PTFE and Al/Fe_2O_3 with the 1-5 µm particle size range. Friction sensitivity was assessed using the BAM friction test, electro-static discharge (ESD) sensitivity assessed using an ESD tester, and impact sensitivity assessed using a Type-12 drop hammer[237]. The evaluated compositions did not demonstrate impact or friction sensitivity. The Al/Fe_2O_3 composition demonstrated ESD sensitivity, but the presence of PTFE in Al/Fe_2O_3/PTFE was found to reduce ESD sensitivity. Because of this, the sensitivity testing series[237] was not performed on the Al/PTFE system as it was considered insensitive to friction, ESD, and impact stimuli due to the presence of PTFE at the considered particle size ranges. All handling procedures enforce ESD sensitivity considerations using appropriate grounding equipment.

6.4 Constituent Powders

This work will uses aluminum powder sourced from Atlantic Equipment Engineers (AEE), PTFE sourced from Micro Powders Inc. (MPI), and Fe_2O_3 sourced from AEE and Alfa-Aesar for manufacturing specimens. The constituents, source, and reported properties are summarized in Table 6.3. These powders were selected based on availability and similarities in characteristic particle sizes.

Table 6.3: Supplier reported properties of constituent powders

Constituent	Product Name	Supplier	Purity %	Density g/cm^3	Size Range μm
Course Al	Al-101	AEE	99.8	2.7	<44
Fine Al	Al-100	AEE	99.9	2.7	1-5
Course PTFE	Fluo 625F	MPI	>99.9	2.2	<44
Fine PTFE	Fluo 300XF	MPI	>99.9	2.2	2-4
Course Fe_2O_3	Iron(III) Oxide	Alpha Aesar	98	5.24	<44
Fine Fe_2O_3	FE-601	AEE	>99.9	5.24	1-5

Reported densities were verified using an Anton Parr Ultrapyc 5000 pycnometer with a measurement accuracy of $\pm 0.1\%$. Effects of the blending process on the constituent densities were evaluated by comparing measurements of the powders before and after being individually subjected to the blending protocol. Differences in measured densities were below the measurement accuracy of the machine and therefore negligible. The measured densities of the constituents and deviation from values reported by the manufacture are summarized in Table 6.4.

Table 6.4: Reported and measured densities of constituent powders

Constituent	Product Name	Reported Density g/cm^3	Measured Density g/cm^3	Difference %
Course Al	Al-101	2.70	2.698	-0.07
Fine Al	Al-100	2.70	2.720	0.75
Course PTFE	Fluo 625F	2.20	2.280	3.63
Fine PTFE	Fluo 300XF	2.20	2.278	3.55
Course Fe_2O_3	Iron(III) Oxide	5.24	4.832	-7.79
Fine Fe_2O_3	FE-601	5.24	4.890	-6.68

The reported densities of the aluminum constituents align well with the density measurements presented here. The PTFE constituents exhibit a small difference between the measured and reported values which is consistent for both

powder sizes. The largest difference in the measured and reported density values was for the Fe_2O_3 powders. Prior works have reported similar observations of measurements of Fe_2O_3 failing to align with theoretical predictions[238]. The reported purity of the Fe_2O_3 powders would indicate contamination to be unlikely, so the observations here align with literature. Reported experimentally measured densities of Fe_2O_3 range from 4.69 g/cm^3[238] to 4.90 g/cm^3[239] and align well with the measurements made in this work. Theoretically calculated densities reported in literature range from 5.27 g/cm^3[238] to 5.30 g/cm^3[239] and align with the densities reported by the supplier technical data sheets. Poor alignment of measured densities to calculated theoretical densities has been observed for other iron oxides[238, 239]. The differences between measured and reported densities of the PTFE and the Fe_2O_3 powders highlights the importance of measuring the properties of constituent powders when received. Without the measurements made here, significant error would have been introduced into the calculations of theoretical maximum density of the compositions and porosity of the specimens.

Characteristic particle sizes of the powders were determined through size analysis of images of the powder particles taken using the scanning light microscope. To better represent particle conditions present in the blended composition and to break up large particle agglomerates the powders were individually blended according to the procedures discussed in Section 6.3 before analysis. Any remaining large particle agglomerates were manually selected for exclusion from analysis and smaller agglomerates were segmented by the watershed algorithm during analysis.

The final particle size distributions are assembled by averaging observance frequency distributions of particle sizes measured from a minimum of five microscope images. For each distribution more than 10^4 particles were analyzed. The spatial resolution of these images is 0.82 µm/pixel, and the spatial error of these measurements is conservatively taken as twice the discretization uncertainty, or $\pm$1µm. Per typical reporting standards[192, 240, 241], characteristic particle sizes are determined from the cumulative volume distributions of the particles. These characteristic sizes for volume distributions are $D10$, $D50$, and $D90$ which represent the particle sizes for which 10%, 50%, and 90% of particles are below in size, respectively. These values, along with the mean particle size determined from the volume distributions are reported in Table 6.5.

For each constituent powder, microscope images representative of typical particles and the normalized observation frequency and cumulative volume distributions are shown in Figures 6.3-6.8. Inspection of the observation frequency distributions show a large number of small particles below 10 µm are consistently observed for all powders. However, the presence of larger particles results in a cumulative volume distributions that is biased towards larger particle sizes. As such, the $D50$ and mean particle size values do not align with the particle sizes most frequently observed. This lack of alignment between the two distributions is not unexpected[192, 241]. By the concepts of the general rule of mixtures and volumetric influences of constituents discussed previously in Section 2.4, it

Table 6.5: Characteristic particle sizes of constituent powders

Constituent	Product Name	$D10$ μm	$D50$ μm	$D90$ μm	Mean Particle Size μm
Course Al	AL-101	14	26	38	27
Fine Al	AL-100	5	10	15	11
Course PTFE	Fluo 625F	14	27	40	28
Fine PTFE	Fluo 300XF	6	11	16	12
Course Fe_2O_3	Iron(III) Oxide	10	26	38	26
Fine Fe_2O_3	FE-601	4	8	14	10

seems logical that particle size parameters determined from a volume distribution would best represent the particle sizes that control mechanical properties. This work will utilize the mean particle size as the characteristic particle size of the constituents for the material models developed in this work. These measurements show the course particle size range is defined by a max particle size less than $<$44 µm (-325 mesh) and average mean particle size of $\sim$27 µm. The fine particle size range is defined by powders with a max particle size of $\leq$16 µm and average mean particle size of $\sim$10 µm. These results should be comparable to measurements from sieve or laser diffraction methods as it has been shown minimal difference exists between methods when analyzing particles on the order of 10^{-2} mm in size [242].

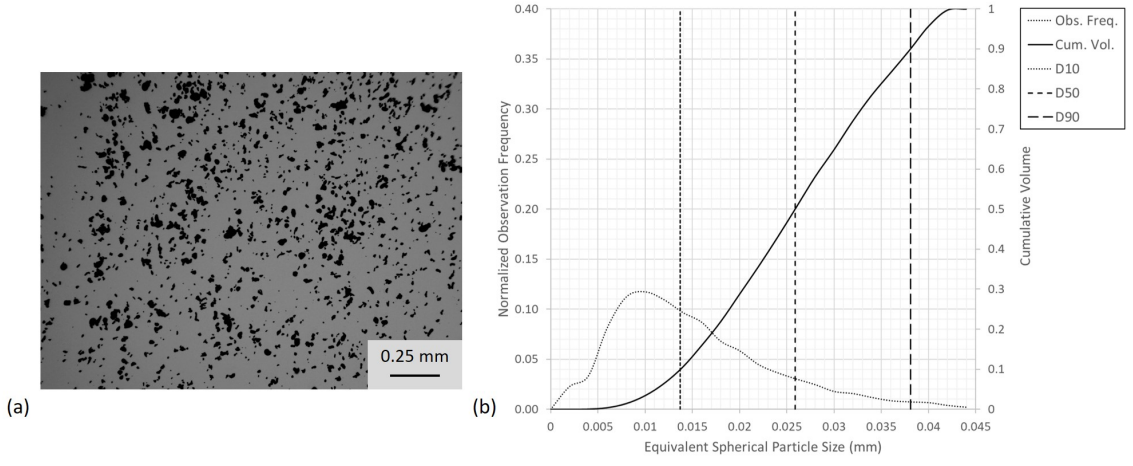

Figure 6.3: Particle analysis of the coarse aluminum constituent AL-101. (a) a microscope image of the typical particles that comprise AL-101 and (b) a plot of the measured normalized observation frequency and cumulative volume distributions. The values of $D10$, $D50$, and $D90$ are indicated on the plot.

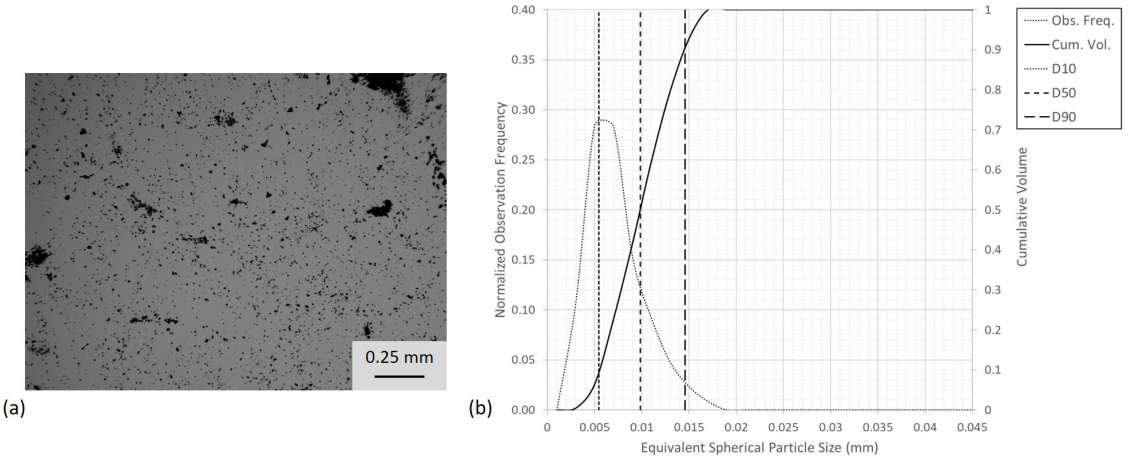

Figure 6.4: Particle analysis of the fine aluminum constituent AL-100. (a) a microscope image of the typical particles that comprise AL-100 and (b) a plot of the measured normalized observation frequency and cumulative volume distributions. The values of $D10$, $D50$, and $D90$ are indicated on the plot.

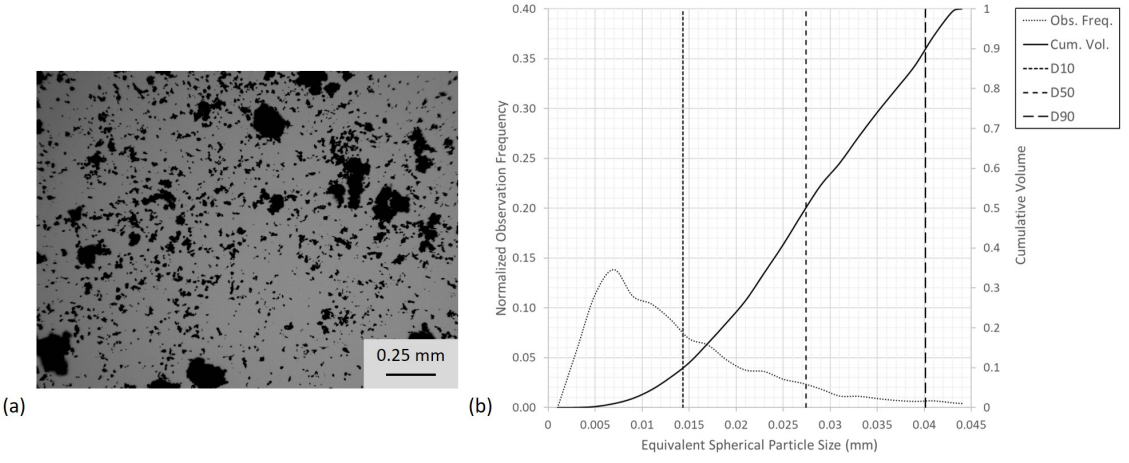

Figure 6.5: Particle analysis of the coarse PTFE constituent Fluo 625F. (a) a microscope image of the typical particles that comprise Fluo 625F and (b) a plot of the measured normalized observation frequency and cumulative volume distributions. The values of $D10$, $D50$, and $D90$ are indicated on the plot.

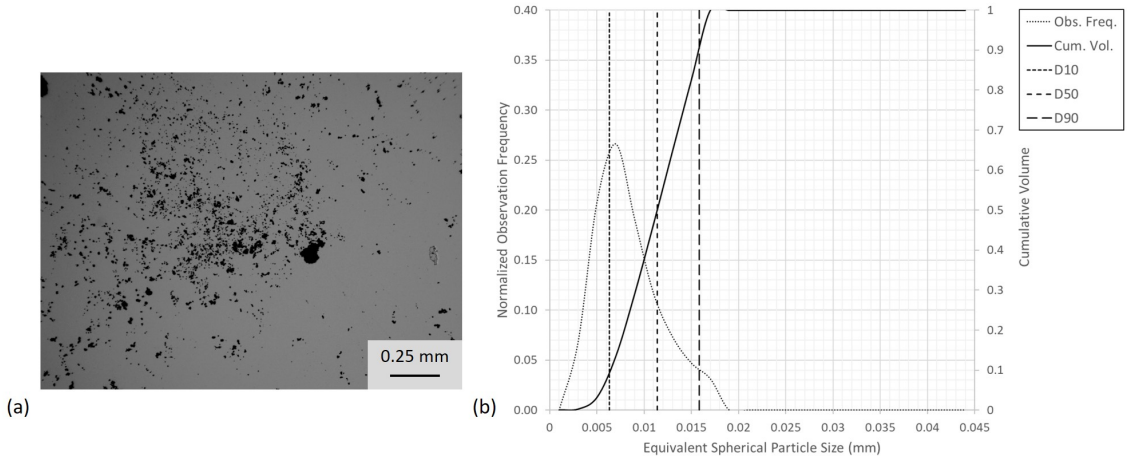

Figure 6.6: Particle analysis of the fine PTFE constituent Fluo 300XF. (a) a microscope image of the typical particles that comprise Fluo 300XF and (b) a plot of the measured normalized observation frequency and cumulative volume distributions. The values of $D10$, $D50$, and $D90$ are indicated on the plot.

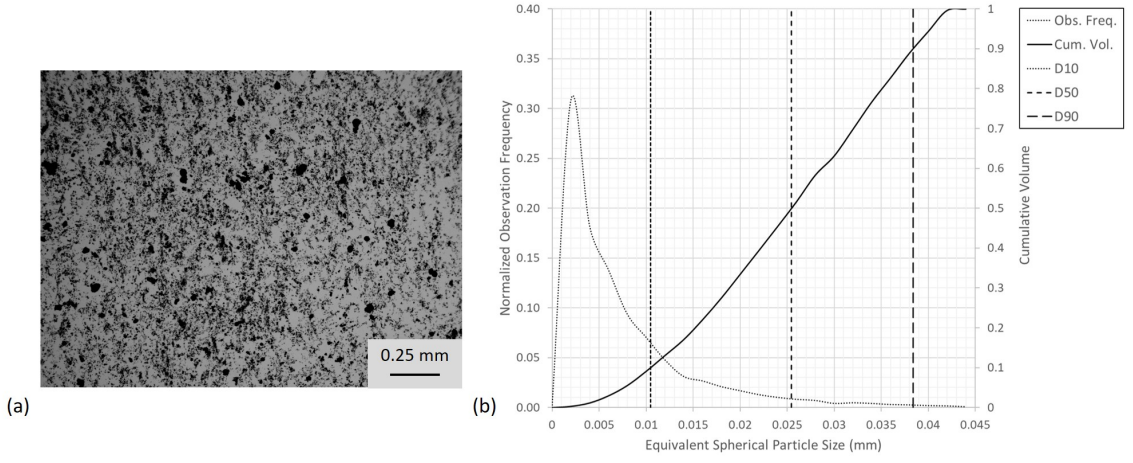

Figure 6.7: Particle analysis of the coarse Fe_2O_3 constituent Iron(III) Oxide. (a) is a microscope image of the typical particles that comprise Iron(III) Oxide and (b) is a plot of the measured normalized observation frequency and cumulative volume distributions. The values of $D10$, $D50$, and $D90$ are indicated on the plot.

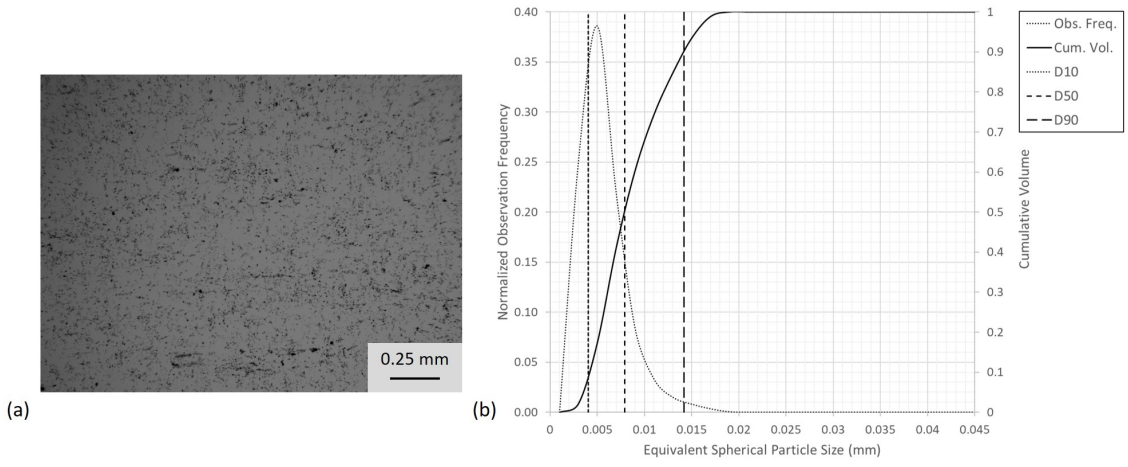

Figure 6.8: Particle analysis of the fine Fe_2O_3 constituent FE-601. (a) is a microscope image of the typical particles that comprise FE-601 and (b) is a plot of the measured normalized observation frequency and cumulative volume distributions. The values of $D10$, $D50$, and $D90$ are indicated on the plot.

CHAPTER 7

MEASUREMENTS OF MECHANICAL RESPONSE AND EVALUATION OF ANALYTICAL FRAGMENTATION THEORY

Experimental measurements were performed on the majority of the proposed Al/PTFE compositions with porosity and particle size variations applied. No testing was performed on the 100PTFE composition with nominally 20% porosity and fine particles due to specimen fragility preventing handling after consolidation. Kolsky bar tests were limited to specimens with nominally 5% porosity as specimens with nominally 20% porosity were determined not to be suitable for the method based on observations from the quasi-static compression tests. Additionally, all of the 25Al/75PTFE and 100PTFE compositions that were subjected to quasi-static compression tests were found to be too weak to survive launch in the 14 mm gun system. Therefore only the pure Al specimens were subjected to high velocity impact and vented calorimetry tests.

The $Al/Fe_2O_3/PTFE$ systems were not evaluated due to manufacturing challenges. Prior manufacturing trials of Fe_2O_3 containing compositions had shown consolidation was possible through the manufacture of single specimens. During manufacturing of the specimens for actual testing, the specimens containing Fe_2O_3 presented difficulties in repeatable consolidation. Before these consolidation issues could be resolved, irreparable damaged occurred to a Natoli die set due to binding of the punch in the die body. Conversations with the manufacture confirmed that binding of die parts can occur when the constituent powders consist of particles smaller than 5 μm. The hardness of Fe_2O_3 prevents breaking or yielding of the particles binding the die components, thus making separation of die components without damage highly unlikely. To avoid damaging the remaining dies, manufacturing of Fe_2O_3 containing compositions ceased.

For conciseness going forward, the following shorthand is used to describe compositions with applied variations: Composition - nominal porosity - particle size. For porosity variation, the nominal porosity conditions 5% and 20% are denoted by 5 and 20, respectively. For particle size variation, coarse and fine particle sizes are denoted by C and F, respectively. For example, the shorthand for the 25Al/75PTFE composition with nominally 5% porosity and coarse particles is 25Al/75PTFE-5-C. Alternatively, for cases where all variations of particle size or porosity are referred to, the $*$ symbol is used to denote all conditions. For example, the shorthand for the 25Al/75PTFE composition with fine particles and both porosity conditions is 25Al/75PTFE-$*$-F. The final list of evaluated compositional

variants and applied experimental methods is presented in Table 7.1.

Table 7.1: Summary of evaluated composition variants and applied experimental methods for evaluation of mechanical response and fragmentation behaviour

Evaluated Compositional Variants	Applied Experimental Methods
100Al-∗-∗ 75Al/25PTFE-∗-∗ 50Al/50PTFE-∗-∗ 25Al/75PTFE-∗-∗ 100PTFE-∗-C 100PTFE-5-F	Quasi-static Compression Tests (Sec. 3.1) Fracture Toughness Tests (Sec. 3.2) Wave Speed Measurements (Sec. 3.3)
100Al-5-∗ 25Al/75PTFE-5-∗ 100PTFE-5-∗	Kolsky Compression Tests (Sec. 3.4) High Velocity Impact Tests (Sec. 3.5)
100Al-5-∗	High Velocity Impact Tests (Sec. 3.5)

7.1 Experimental Uncertainty

The experimental results discussed in this chapter have an uncertainty associated with the measurement. These uncertainties were discussed in Chapter 3. The measurement uncertainty is in addition to the statistical uncertainty (error of estimation) associated with the sample size and standard deviation of a collection of measurements. This work will report the uncertainty of a measurement as the larger of the average measurement uncertainty or error of estimation for the specimen sample set. The governing uncertainty will be indicated when discussing results.

For measurements that characterize specimens and the compositions, the analysis methodology detailed by Taylor[160] is used in determining the

measurement uncertainties. For propagated uncertainties specific to specimen characteristics (e.g. mass fraction, TMD, etc), properties associated with the 50Al/50PTFE composition are used to describe the general measurement uncertainty for all specimens. The measurement uncertainties associated with the specimens and compositions are summarized in Table 7.2. The propagated uncertainties of the calculated properties of the specimens and compositions are summarized in Table 7.3.

Table 7.2: Summary of measurement uncertainties associated with the compositions and manufactured specimens

Measurement	Notation	Reported Uncertainty	Method of Determination
Length	δL_o	$\pm$0.02 mm	Digital caliper resolution
Diameter	δD_s	$\pm$0.02 mm	Digital caliper resolution
Mass	δm_s	$\pm$0.001g	Digital scale resolution
Constituent Density	$\frac{\delta \rho_i}{\rho_i}$	$\pm$0.1%	Pycnometer Reported Uncertainty

Table 7.3: Summary of propagated uncertainties associated with the compositions and manufactured specimens

Calculated Parameter	Notation	Reported Uncertainty	Uncertainty Equation
Specimen Density	$\frac{\delta\rho_s}{\rho_s}$	$\pm 0.8\%$	$\frac{\delta\rho_s}{\rho_s} = \sqrt{\left(\frac{\delta m_s}{m_s}\right)^2 + \left(\frac{2\delta D_s}{D_s}\right)^2 + \left(\frac{\delta L_o}{L_o}\right)^2}$
Mass Fraction	$\frac{\delta Y_i}{Y_i}$	$\pm 0.003\%$	$\frac{\delta Y_i}{Y_i} = \sqrt{(N+1)\left(\frac{\delta m_s}{m_s}\right)^2}$
Volume Fraction	$\frac{\delta \forall_i}{\forall_i}$	$\pm 0.2\%$	$\frac{\delta \forall_i}{\forall_i} = \sqrt{(N+1)\left[\left(\frac{\delta Y_i}{Y_i}\right)^2 + \left(\frac{\delta \rho_i}{\rho_i}\right)^2\right]}$
Theoretical Maximum Density	$\frac{\delta\rho_{TMD}}{\rho_{TMD}}$	$\pm 0.5\%$	$\frac{\delta\rho_{TMD}}{\rho_{TMD}} = \sqrt{N\left[\left(\frac{\delta \forall_i}{\forall_i}\right)^2 + \left(\frac{\delta \rho_i}{\rho_i}\right)^2\right]}$
Porosity	$\frac{\delta p}{p}$	$\pm 1\%$	$\frac{\delta p}{p} = \sqrt{\left(\frac{\delta\rho_s}{\rho_s}\right)^2 + \left(\frac{\delta\rho_{TMD}}{\rho_{TMD}}\right)^2}$

Slight variation exists between the final volume fraction of the compositions and the volume fractions proposed in Section 6.3. This is due to the use of manufacturer reported densities in the initial determinations of mass fractions for blending the compositions. Density measurements of the constituent powders discussed in Section 6.4 are used in calculating the final volume fractions of the blended compositions. For consistency the proposed compositional volume fractions will still be used to identify compositions, but calculations will be performed using the calculated volume fraction values. The proposed values and final values of volume fractions as well as the calculated TMD of the compositions are summarized in Table 7.4.

Table 7.4: Calculated volume fractions and TMDs of the as blended Al/PTFE compositions studied in this work

Composition	Al Volume Fraction %	PTFE Volume Fraction %	TMD g/cm^3
Uncertainty:	$\pm$0.2%	$\pm$0.2%	$\pm$0.5%
100Al	100	0	2.70
75Al/25PTFE	75.7	24.3	2.60
50Al/50PTFE	51.0	49.0	2.49
25Al/75PTFE	25.7	74.3	2.39
100PTFE	0	100	2.28

7.2 Quasi-static mechanical response of specimens

Quasi-static compression tests were performed on all of the Al/PTFE specimen variants except the 100PTFE-20-F variant due to specimen fragility. Tests were initially performed for all specimens using the EMS 1500 UTM. Due to compliance of the machine and limits of the displacement resolution, it was not possible to resolve the linear-elastic portion of the stress strain curve for 100Al specimen variants. Additional tests were performed on newly manufactured 100Al specimens using the ATS 905 which provided the needed resolution to resolve the linear-elastic response of the material. In total 72 specimens were subjected to compression tests: four specimens for all variants of the compositions 100Al, 100PTFE, and 25Al/75PTFE; four specimens for 100Al-5-F ultimate strength measurements; and three specimens for all variants of the compositions 75Al/25PTFE and 50Al/50PTFE. Typical stress-strain responses of the specimens of the different variants are shown in Figure 7.1. Stress and strain data is shown for the specimen up to failure, where failure of the specimens was indicated by a sharp drop in carried load. Note that for the 100Al-5-F variant, the linear elastic regime is given by the ATS 905 measurements and the remainder of the stress-strain response before failure is approximated using EMS 1500 measurements.

The stress-strain responses shown in Figures 7.1(a) and 7.1(c) demonstrate a clear non-linear relationship with the variation in constituent volume fractions which is not unexpected given the mismatch in moduli of the Al and PTFE constituents[144]. From Figure 7.1(c), it is seen that for the coarse particle variants containing more than 50% PTFE by volume, the response is effectively dictated by the PTFE. For the fine particle variants in Figure 7.1(a), the stress-strain response is also strongly dictated by the PTFE. However, the peak stresses obtained clearly increases with the increase in volume fraction of aluminum. This difference between the fine and coarse particle compositions is due to the volume distribution of the particles in the mixtures. For the fine particle variants,

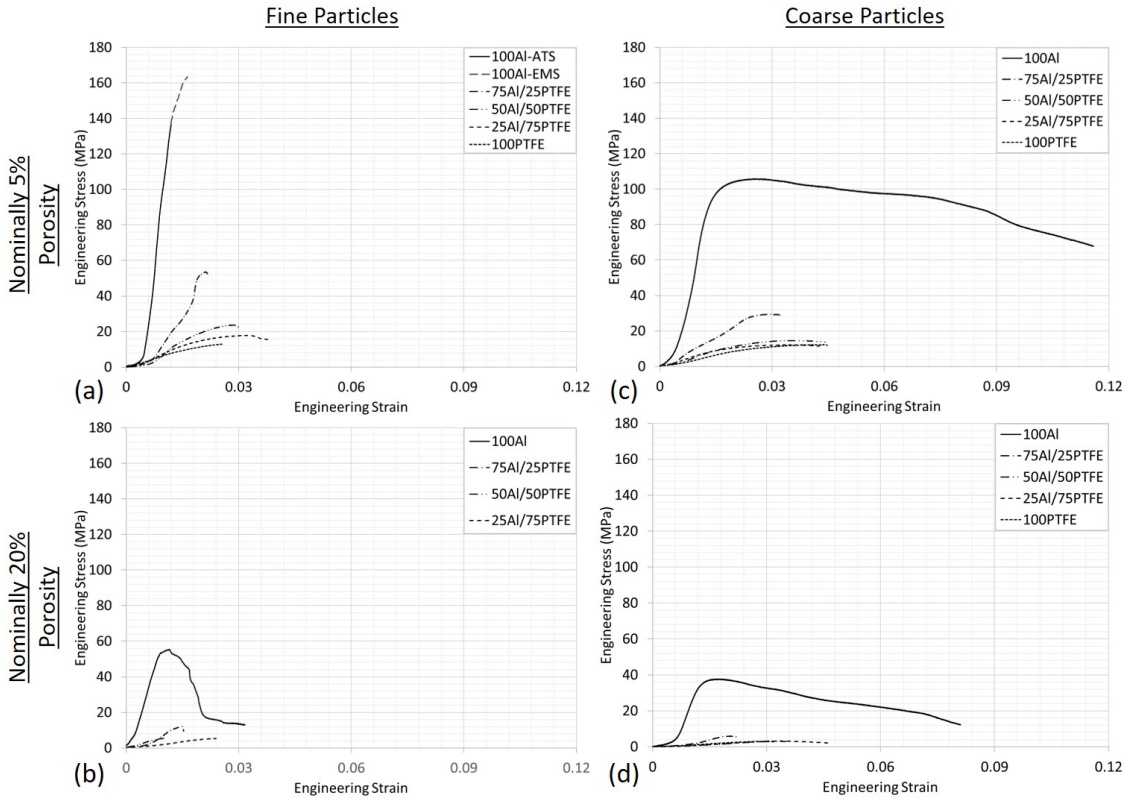

Figure 7.1: Typical stress and strain response of Al/PTFE compositions comprised of: (a) fine particles with nominally 5% porosity; (b) fine particles with nominally 20% porosity; (c) coarse particles with nominally 5% porosity; and (d) coarse particles with nominally 20% porosity.

the particles more uniformly distributed in the volume. This leads to the bulk of the particle interactions occurring between dissimilar particles (aluminum to PTFE) instead of similar particles (aluminum to aluminum or PTFE to PTFE). Thus a combined response is observed. Alternatively, the larger particles in the coarse particle variants reduce uniform volumetric distribution of the particles promoting interaction of material similar particles. From the measured response, these interactions appear to be predominately PTFE to PTFE particle interactions.

The comparison of 100Al stress-strain responses in Figures 7.1(a) and 7.1(c) shows that the 1.7x reduction in mean particle size and 2.6x reduction in max particle size (D90) of the aluminum powder provides considerable improvement to strength (60% increase), but yields a brittle granular material with reduced ductility (85% decrease in strain before failure). The addition of PTFE significantly weakens the material regardless of particle size, but does provide some improvement to ductility for the fine particle variants. These effects are non-linear in nature. Figures 7.1(b) and 7.1(d) show increased porosity causes a significant re-

duction in strength and elastic modulus of the materials which is expected. This sizable degradation in strength and modulus is observed for both particle size ranges, though the degradation on the strength of the Al/PTFE compositions seems more pronounced for the coarse particle variants. As with the compositional and particle size effects, the porosity effects are non-linear in nature.

Measurements of elastic modulus, yield strength, and ultimate strength were obtained from the measured stress-strain response of each specimen. In cases where the intersection of 0.2% offset line with the stress-strain curve could not be determined, yield stress is not reported. This occurred for the variants 75Al/25PTFE-5-F, 75Al/25PTFE-20-F, 50Al/50PTFE-20-F, and 50Al/50PTFE-20-C. For 100Al-5-F, the stress-strain response could not be resolved on one machine as the ATS 905 load limits were exceeded before the material yielded. Therefore it was not possible to determine the intersection of 0.2% offset line. Average values of the quasi-static properties from a specimen set of a variant are summarized in Table 7.5. For the strength measurements, the statistical uncertainty governs as given by the DIM method. For the elastic modulus measurements, the DIM statistical uncertainty governs for all variants except 25Al/75PTFE-20-C, 100PTFE-20-C, and 100PTFE-5-C where the measurement uncertainty was larger than the statistical uncertainty. Measurements of individual specimens are summarized in Appendix B.

Table 7.5: Average measurements and uncertainty of elastic modulus (E_c), yield strength ($\sigma_{c,y}$), and ultimate strength ($\sigma_{c,u}$) of evaluated compositions. Average porosity (p_{avg}) of sample sets is also given

Composition	Variant	p_{avg}	E_c		$\sigma_{c,y}$		$\sigma_{c,u}$	
		%	GPa	Uncert.	MPa	Uncert.	MPa	Uncert.
100Al	5-F	7	24.4	±19%	-	-	169.4	±6%
	5-C	6	18.5	±14%	105.5	±8%	116.2	±12%
	20-F	19	8.2	±14%	60.9	±16%	61.3	±16%
	20-C	21	6.4	±19%	36.5	±6%	37.3	±7%
75Al/25PTFE	5-F	4	3.7	±28%	-	-	53.3	±5%
	5-C	2	1.3	±15%	28.7	±3%	29.0	±3%
	20-F	20	1.3	±26%	-	-	11.7	±8%
	20-C	19	0.63	±17%	5.72	±4%	5.8	±4%
50Al/50PTFE	5-F	4	2.0	±14%	15.7	±10%	23.6	±5%
	5-C	4	0.88	±35%	10.2	±7%	14.5	±7%
	20-F	21	0.49	±11%	-	-	5.5	±4%
	20-C	20	0.13	±39%	-	-	3.0	±8%
25Al/75PTFE	5-F	4	0.99	±23%	12.6	±12%	17.5	±9%
	5-C	3	0.86	±36%	10.1	±13%	13.5	±18%
	20-F	21	0.28	±19%	5.0	±6%	5.2	±7%
	20-C	20	0.15	±9%	3.1	±11%	3.4	±9%
100PTFE	5-F	5	0.66	±10%	10.2	±11%	12.8	±5%
	5-C	3	0.56	±13%	9.0	±9%	12.4	±4%
	20-C	23	0.15	±10%	2.6	±10%	2.9	±8%

The elastic modulus, yield strength, and ultimate strength measurements presented in Table 7.5 are used in determining the parameters of the analytical models discussed in Chapter 2 and for evaluating the models. For the material strengths, the subscripts denoting yield and ultimate strength are y and u, respectively. For convenience, the analytical models proposed in Chapter 2 for the quasi-static properties are repeated here:

$$E_c = \frac{2}{\left[\sum_{i=1}^{N}(\forall_{f,i}E_i)\right]^{-1} + \sum_{i=1}^{N}(\forall_{f,i}/E_i)}(1-p)^{1/J_E} \tag{7.1}$$

$$\sigma_{c,y} = \frac{2}{\left[\sum_{i=1}^{N}(\forall_{f,i}\sigma_{y,i})\right]^{-1} + \sum_{i=1}^{N}(\forall_{f,i}/\sigma_{y,i})}(1-p)^{1/J_{\sigma_y}} \tag{7.2}$$

$$\text{where : } \sigma_{y,i} = (\sigma_{y,1\mu m,i} * (S_{c,i}/1\mu m)^{-n_{\sigma_{y,i}}}) \tag{7.3}$$

$$\sigma_{c,u} = \frac{2}{\left[\sum_{i=1}^{N}(\forall_{f,i}\sigma_{u,i})\right]^{-1} + \sum_{i=1}^{N}(\forall_{f,i}/\sigma_{u,i})}(1-p)^{1/J_{\sigma_u}} \tag{7.4}$$

$$\text{where} : \sigma_{u,i} = (\sigma_{u,1\mu m,i} * (S_{c,i}/1\mu m)^{-n_{\sigma_{u,i}}}) \tag{7.5}$$

A standard least-squares fit governed by the generalized reduced gradient algorithm is used in determining the parameters of the analytical models. Intuitively it may appear reasonable to determine all of the parameters that comprise the models at once. However, fitting all the parameters at the same time can result in an artificial goodness of fit due to the large number of free-fitting parameters in this approach[148]. As a consequence the determined parameter values may not appropriately represent the dependency for which they are intended to describe. When determining the parameters here, a systematic approach was used to ensure parameters were correctly determined for the dependency they were designed to represent.

First the full-density material properties (E_o, $\sigma_{y,o}$, $\sigma_{u,o}$) and the respective fractal parameters (J_E, J_y, J_u) are determined to describe the porosity dependencies. The full-density material properties are then used in determining the 1 µm mean particle size material properties ($E_{1\mu m}$, $\sigma_{y,1\mu m}$, $\sigma_{u,1\mu m}$) and particle size sensitivity parameter (n_E, n_y, n_u). This process ensures the particle size parameters represent only the particle size effects and not the combined porosity/particle size effects. Evaluation of the analytical models is then made by assessing the individual dependency functions in representing the specific experimentally observed behavior they were designed to represent.

The determined full-density properties and respective fractal parameters are summarized in Table 7.6. Because the yield strength could not be determined for 100Al-5-F, the average of the strength fractal parameters of the other 100Al variants was used in the determination of the 100Al-F full-density yield strength. This is justified based on the observation that the fractal parameter of the ultimate strength of 100Al-5-F is similar to the fractal parameters for the yield and ultimate strengths of 100Al-C. For the 100PTFE-F variant, parameters were determined based on the porosity variation of the nominally 5% porosity specimen set as the 20% nominal porosity specimen set could not be tested. The average of the root mean square percentage error[243] (RMSPE) for the three material properties is provided for perspective on the alignment of the predictions to the experimental results. The RMSPE values were found to be on the order of, or less than, the uncertainty bounds of the experimental measurement indicating acceptable alignment of the predictions to the data.

Table 7.6: Calculated full-density material properties and fractal parameters that best describe the porosity dependencies of the compositions comprised of fine and coarse particles.

Composition	Variant	E_o GPa	$\sigma_{y,o}$ MPa	$\sigma_{u,o}$ MPa	J_E	J_y	J_u	Average RMSPE
100Al	F	37.1	267.7	269.7	0.143	0.144	0.144	8.6%
	C	28.3	162.2	177.2	0.153	0.144	0.145	6.5%
75Al/25PTFE	F	4.5		71.5	0.181		0.122	8.5%
	C	1.4	34.7	35.0	0.254	0.144	0.114	3.6%
50Al/50PTFE	F	2.9		32.7	0.133		0.132	20.4%
	C	1.3		20.1	0.091		0.117	7.1%
25Al/75PTFE	F	1.3	15.4	22.7	0.167	0.212	0.161	12.2%
	C	1.2	12.4	17.1	0.091	0.155	0.131	10.9%
100PTFE	F	1.1	15.3	20.7	0.104	0.135	0.115	3.0%
	C	0.7	10.9	15.4	0.166	0.186	0.158	4.2%

From the full-density properties it is clear the compositions comprised of the fine powders have a higher elastic modulus and are stronger. This behavior is likely related to better mixing and distribution of particles within the the volume of the specimen[16, 43]. Typically the elastic modulus of a material is assumed to be independent of particle or grain size[132]. Prior works have demonstrated this is a reasonable assumption for sintered granular compacts[44] or homogeneous metals[147]. However, both the measurements of the elastic modulus of the constituents in Table 7.5 and the full-density elastic moduli in Table 7.6 indicate a non-negligible dependency on particle size exists. For the aluminum constituents, the difference in elastic modulus is nominally 30% between the fine and coarse powders. For the PTFE constituents, the difference in elastic modulus is nominally 60% between the fine and coarse powders. This variation due to particle size propagates into the combined compositional response as demonstrated by the variation of the full-density parameters in Table 7.6. Therefore, it is necessary to modify the analytical model for the elastic modulus to account for particle size dependencies of the constituents. The modified model takes the form:

$$E_c = \frac{2}{\left[\sum_{i=1}^{N}(\forall_{f,i}E_i)\right]^{-1} + \sum_{i=1}^{N}(\forall_{f,i}/E_i)}(1-p)^{1/J_E} \tag{7.6}$$

$$\text{where : } E_i = (E_{1\mu m,i} * (S_{c,i}/1\mu m)^{-n_{E,i}}) \tag{7.7}$$

To explore the potential for a universal fractal parameter that describes this system the minimum, maximum, and mean values of the fractal parameters for the three material properties are evaluated. These values are presented in Table

7.7. The mean values of J_E and J_y are within 5% of one another, and within 12% and 15% of J_u, respectively. Conversely, the minimum values of J_y and J_u are the same and within $\sim$20% of J_E. The maximum values show greater variation, with J_u and J_y differing by 24%, J_E and J_y differing by 20%, and J_E and J_u differing by $\sim$60%. While the observed differences are non-negligible, the minimum, maximum, and mean values are on average within 20% of one another.

Table 7.7: Minimum, maximum, and average values of the fractal parameters for the elastic modulus, yields strength, and ultimate strength

Value	J_E	J_y	J_u
Minimum	0.091	0.114	0.114
Mean	0.149	0.156	0.132
Maximum	0.254	0.212	0.161

It is interesting that the fractal parameters for the elastic moduli and strengths tend to be similar in value for the compositions. A reasonable approach in describing a universal fractal parameter for the Al/PTFE system appears to be to take the average of the mean values as the nominal value of the universal parameter and take the average values of the minimum and maximum values to establish bounds for the value of the universal parameter. These values are: $J_{nom} = 0.15$ for the nominal value, $J_{low} = 0.11$ for the lower bound, and $J_{high} = 0.21$ for the upper bound. The porosity dependency dictated by these values of the fractal parameter are plotted alongside the experimentally measured material property normalized by the full-density property in Figures 7.2, 7.3, and 7.4. The experimental values are plotted by composition only and particle size is not indicated. The error bars applied to a particular experimental measurement are conservatively taken as the average uncertainty of all measurements of that type for a composition.

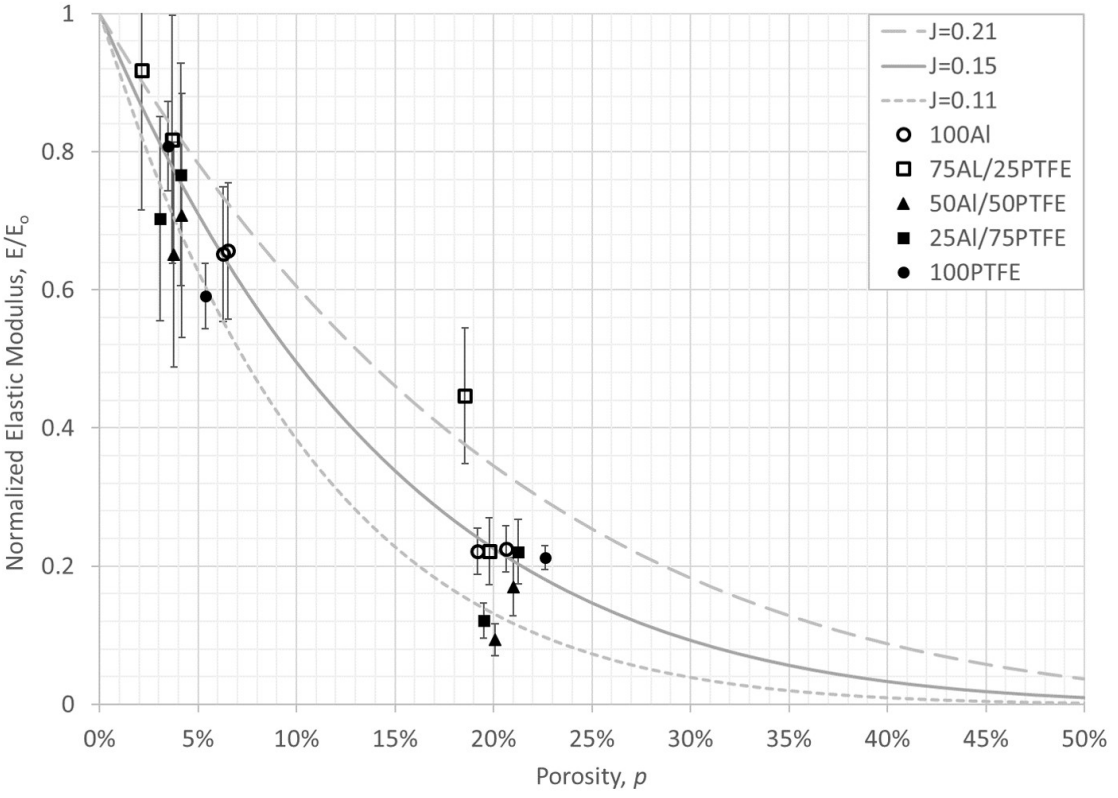

Figure 7.2: Measured elastic modulus response to porosity normalized by the calculated full-density elastic modulus. Predicted response for fractal parameter values of $J_{high} = 0.21$, $J_{nom} = 0.15$ and $J_{low} = 0.11$ are plotted for comparison.

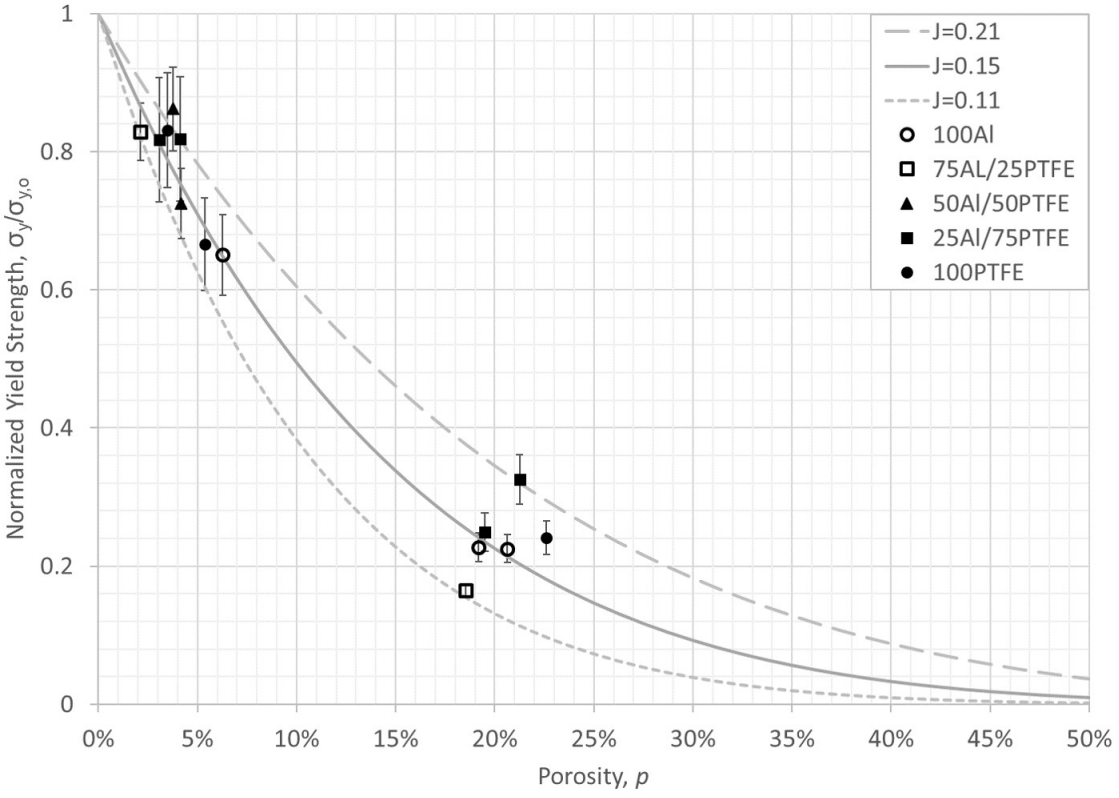

Figure 7.3: Measured yield strength response to porosity normalized by the calculated full-density yield strength. Predicted response for fractal parameter values of $J_{high} = 0.21$, $J_{nom} = 0.15$ and $J_{low} = 0.11$ are plotted for comparison.

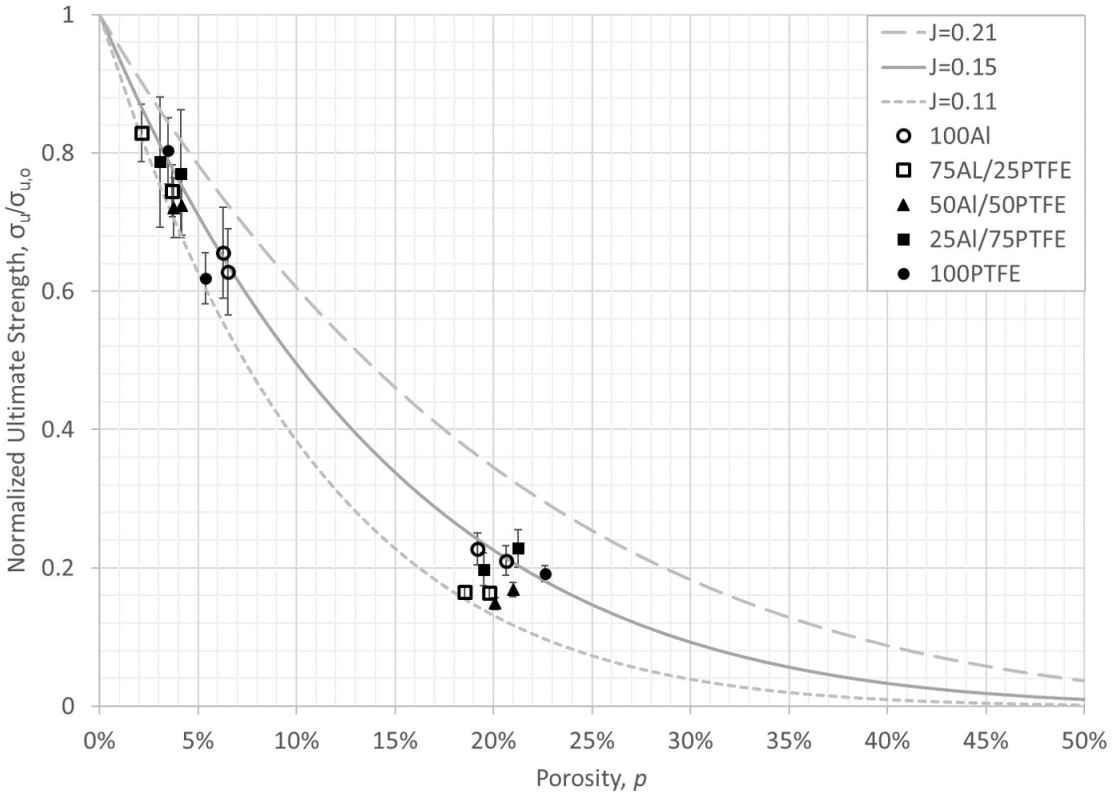

Figure 7.4: Measured ultimate strength response to porosity normalized by the calculated full-density ultimate strength. Predicted response for fractal parameter values of $J_{high} = 0.21$, $J_{nom} = 0.15$ and $J_{low} = 0.11$ are plotted for comparison.

The proposed values of J_{low} and J_{high} reasonably bound the mechanical response of the Al/PTFE system for all compositions and particle sizes evaluated. Furthermore, J_{nom} appears to well approximate the porosity dependence of the elastic modulus and material strengths of the Al/PTFE system. This indicates the porosity effects can be described relatively independent of the particle size and compositional effects supporting the concept of the parameterized models employed here. The fractal parameter value of 0.15 aligns well with the reported fractal parameter value of 0.14 for compressive strengths of granular Cu/Cu_2O composites[43] and the value of 0.146 reported for the elastic modulus of brittle composite alumina-magnesia ceramics[43]. This reinforces $J_{nom} = 0.15$ as an appropriate estimate of the universal fractal parameter to describe the porosity dependency of the Al/PTFE system explored here, and as a possible universal value for other granular composites. However, $J_{nom} = 0.15$ does deviate from other reported values for elastic moduli of 0.24-0.33 for granular compacts[43, 132]. It is possible this deviation for elastic modulus is related to the type of testing performed on the materials as a number of the reported values originate from works performing tensile tests[43] or transverse bending strength tests[44]. Regardless, the results here demonstrate viable values of the fractal parameter that describe

the Al/PTFE system response to porosity.

By definition of the fractal parameter[43], similarities in fractal parameter values suggest similar micromechanical behavior. From this perspective, the comparisons in Figures 7.2, 7.3, and 7.4 suggest similarity in the micromechanical mechanisms that dictate the porosity dependency across the Al/PTFE RM system. This behavior is observed despite the order of magnitude difference in elastic modulus and strengths of the constituents. If this behavior extends to other RM systems, or granular composite materials in general, it would indicate a general set of micromechanical mechanisms govern the bulk material response to porosity. If this general set of mechanisms does exist and could be characterized, improvements to general mesoscale modeling of RMs[16, 38, 134] could be made. While extensive work would be needed to verify, determine, and represent this set of mechanisms, it could be a worthy endeavor for future works.

Comparison of these experimental results to analytical work by Budiansky [137] provides some insight to the heterogeneities that may influence the micromechanical mechanisms governing the bulk material response to porosity observed here. Budiansky[137] extended the work by Eshelby[244] using a self-consistent methodology to derive analytical models for the shear modulus and bulk modulus of a heterogeneous composite material. Budiansky derived these models assuming uniform distribution of the constituent particles with nominally spherical particle shape, elastic behavior of the constituents, and homogeneous and isotropic behavior of the bulk material[137]. For a porous material, the ratio of the porous shear modulus G_p to the full density shear modulus G_o as a function of porosity is given by[137]:

$$\frac{G_p}{G_o} = \frac{3(1-2p)}{3-p} \tag{7.8}$$

Following the homogeneous, isotropic assumption employed by Budiansky [137], the ratio of the porous elastic modulus to the full density elastic modulus is related to the shear modulus ratio by:

$$\frac{E_p}{E_o} = \frac{G_p}{G_o}\frac{(1+\nu_p)}{(1+\nu_o)} \tag{7.9}$$

Where ν_p is the Poisson's ratio of the porous material and ν_o is the Poisson's ratio of the full density material. Experimental measurements of the Poisson's ratio dependence on porosity of granular metals, metal oxides, and ceramics have shown relative insensitivity to porosity variation for porosities less than 20%[149, 245]. Theoretical modeling of an idealized material using the Mori-Tanaka model[139] and Differential Effective Medium Model have also affirmed this behavior[246]. Assuming negligible Poisson's ratio variation with porosity, the elastic modulus ratio is then given by:

$$\frac{E_p}{E_o} \approx \frac{G_p}{G_o} = \frac{3(1-2p)}{3-p} \tag{7.10}$$

The predicted elastic modulus response using Equation 7.10 is shown in Figure 7.5 alongside the predicted response from the GRM model with $J = 0.15$, the experimentally measured elastic modulus of the compositional variants in this work, and experimental measurements of the elastic modulus of porous glass manufactured from fused spherical glass beads[43, 247]. Reasonable agreement of Budiansky's model[137] to the measured elastic modulus response of the porous glass is observed. The porous glass consists of uniformly dispersed spherical particles within the volume. Furthermore, due to the sintering process used to fuse the glass beads[247] the cohesive forces between the particles are expected to be reasonably uniform[24, 106]. These characteristics suggest homogeneous, isotropic behavior of the porous glass can be expected[24, 31]. As such, the microstructural characteristics of the porous glass align with the assumptions that govern Budiansky's model[137] and thus good agreement is expected[130].

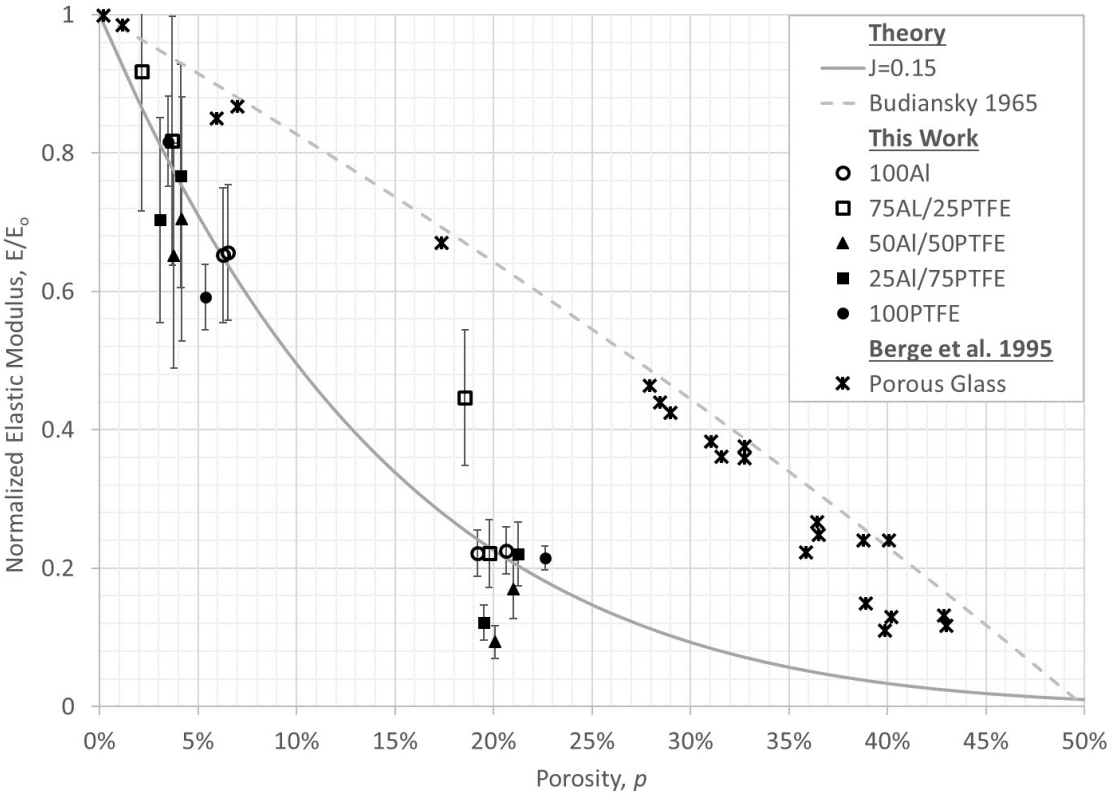

Figure 7.5: Measured elastic modulus response of Al/PTFE and porous glass[43, 247] to porosity normalized by the calculated full-density elastic moduli of the materials. Predicted responses by Budiansky's model[137] and the GRM model with a fractal parameter value $J_{nom} = 0.15$ are plotted for comparison.

Unsurprisingly, Budiansky's model[137] does not align with the elastic modulus response to porosity of the Al/PTFE granular composites. This indicates the

microstructure characteristics of the Al/PTFE variants strongly deviate from the assumptions of Budiansky's model. The microstructure of the Al/PTFE variants is characterized by non-spherical particles, non-spherical pores, likely varying cohesive forces between particles[106], and possible agglomeration of constituents leading to non-uniform distribution of consistent particles. With regards to the Al/PTFE mixtures, the significant contrast in elastic moduli of the constituents likely results in the PTFE, which is the more compliant constituent, experiencing large deformation locally leading to plastic behavior. As a result, the idealized assumptions of Budiansky's model[137] do not represent the Al/PTFE variants studied here. This observation then suggests that the micromechanical mechanisms that govern the bulk material response to porosity for these materials are related to particle morphology, pore shape, variation in cohesive forces between particles, uniformity of the distribution of particles in the volume, and potentially the elastic moduli of the constituents.

Using the calculated full-density material properties and mean particle sizes of the constituents, the 1 µm mean particle size material properties and sensitivity parameters were determined for the 100Al and 100PTFE systems. These values are summarized in Table 7.8. The RMSPE is not included in the table as the average RMSPE for the constituents is less than 0.01% indicating acceptable alignment to the data.

Table 7.8: 1 µm mean particle size material properties and sensitivity parameters that describe the particle size dependencies of the constituents

Composition	$E_{1\mu m}$ GPa	$\sigma_{y,1\mu m}$ MPa	$\sigma_{u,1\mu m}$ MPa	n_E	n_y	n_u
100Al	76.5	312.4	828.0	0.301	0.199	0.467
100PTFE	4.6	41.3	49.0	0.566	0.400	0.346

Values of the sensitivity parameters fall within the range of expected values reported in literature[44, 148]. Comparison of the calculated 1 µm mean particle size values to properties of the homogeneous forms of the pure constituents does provide some interesting insights. The 1 µm mean particle size elastic modulus of the 100Al composition is close to the typical homogeneous, isotropic value reported in industry for 1100 series aluminum (commercially pure 99% aluminum) of 68.9 GPa[248]. However, deviation of the 1 µm mean particle size yield and ultimate strengths are observed when comparing to the strengths of 1100 series aluminum with similarly mean grain size. The 1 µm mean particle size yield strength is 1.6x greater than the reported value of 190 MPa for 1 µm mean grain size 1100 series aluminum[249]. Similarly, the 1 µm mean particle size ultimate strength is 2.4x greater than the reported value of 245 MPa reported for 1 µm mean grain size 1100 series aluminum[248]. Similar poor alignment of all of the

1 μm mean particle size material properties to the homogeneous properties for the PTFE are observed. Here the calculated elastic modulus, yield strength, and ultimate strength for the 100PTFE composition exceed the maximum industry reported values for homogeneous extruded PTFE[248] by at least 70%.

It is not expected the values calculated here to fully align with the values of non-granular equivalents due to the vast differences in homogeneity of the materials. However, the calculated 1 μm mean particle size properties are consistently higher than the homogeneous material equivalents which shows these granular materials behave in a manner that is not derivative of their homogeneous counterparts. This is indicative of differences in micromechanical mechanisms that dictate the material response between the heterogeneous and homogeneous constituents. Without further exploration of particle size variation, with particular focus on granular materials approaching the 1 μm mean particle size, perspective on physical meaning and predictive capability of the particle size dependency parameters is limited. However, it is clear that the use of homogeneous material properties in the particle size dependency function is not appropriate.

Compositional dependency predictions by the Isotropic V/R model are evaluated by comparisons to the experimental results for the 5% and 20% nominal porosity and fine and coarse powder conditions. For these comparisons, the 5% and 20% constituent material properties for the different powder sizes are calculated using the 100Al and 100PTFE parameters in Table 7.6. The Voigt and Reuss bounds are plotted in addition to the average of the two models as the average is recommended in literature for describing the compositional dependency of composites[31]. Comparison of predictions to experimental measurements of elastic modulus, yield strength, and ultimate strength are shown in Figures 7.6, 7.7, and 7.8, respectively. Note that for all figures the average porosity of the specimen set of the measurement is indicated.

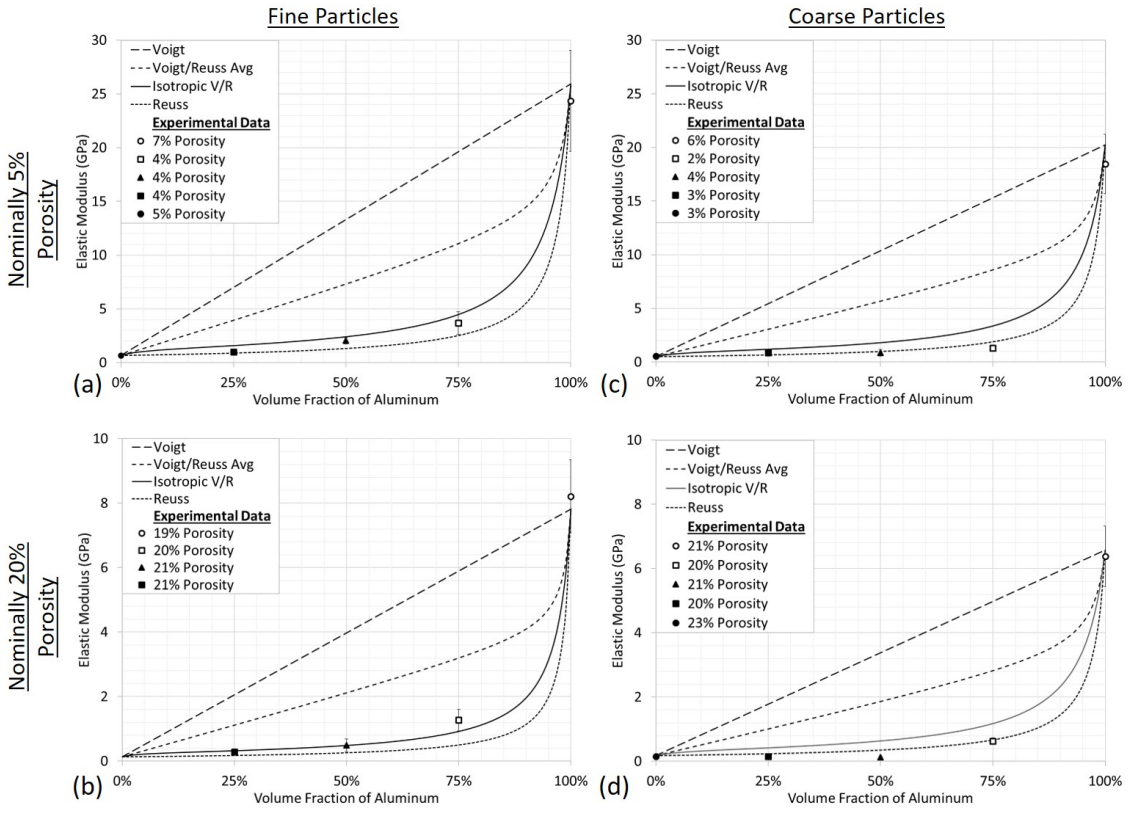

Figure 7.6: Predictions by GRM models of elastic modulus response to compositional variation compared to the measured response of the Al/PTFE system for: (a) fine particles with nominally 5% porosity; (b) fine particles with nominally 20% porosity; (c) coarse particles with nominally 5% porosity; and (d) coarse particles with nominally 20% porosity. Note that the scale of the 20% porosity plots is 1/3 of the 5% porosity plots

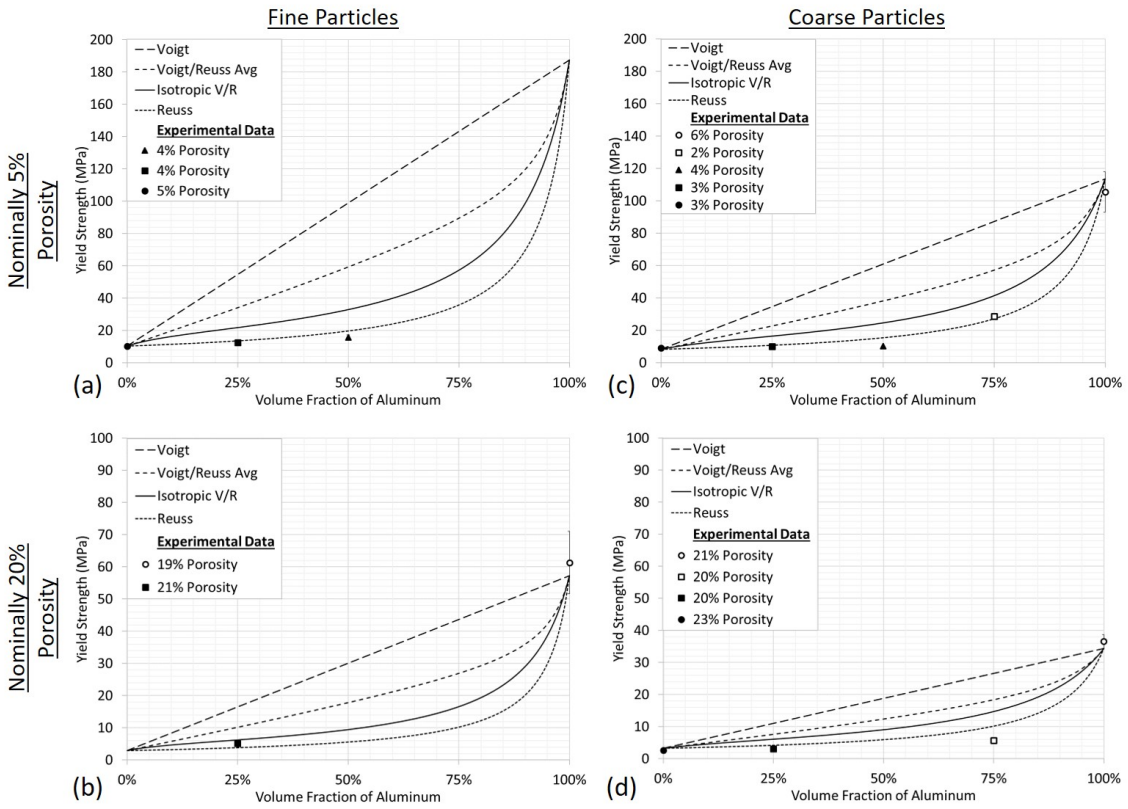

Figure 7.7: Predictions by GRM models of predicted yield strength response to compositional variation compared to the measured response of the Al/PTFE system for: (a) fine particles with nominally 5% porosity; (b) fine particles with nominally 20% porosity; (c) coarse particles with nominally 5% porosity; and (d) coarse particles with nominally 20% porosity. Note that the scale of the 20% porosity plots is $\frac{1}{2}$ of the 5% porosity plots.

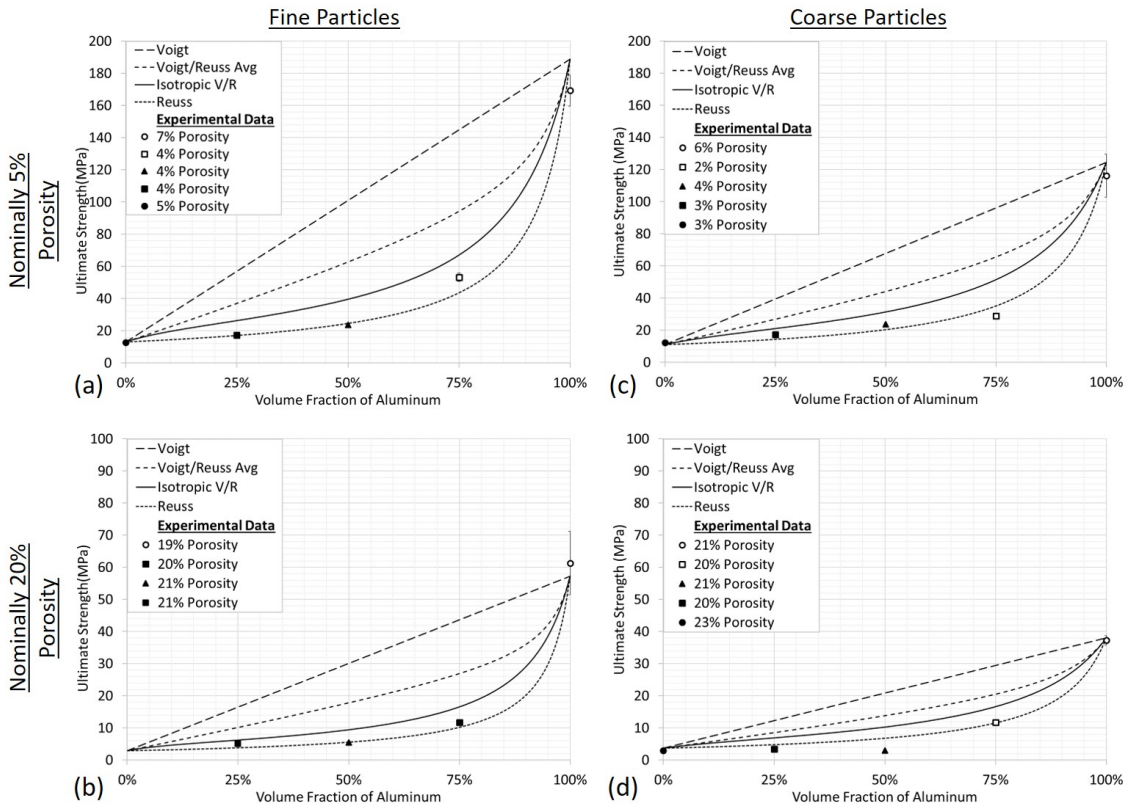

Figure 7.8: Predictions by GRM models of predicted ultimate strength response to compositional variation compared to the measured response of the Al/PTFE system for: (a) fine particles with nominally 5% porosity; (b) fine particles with nominally 20% porosity; (c) coarse particles with nominally 5% porosity; and (d) coarse particles with nominally 20% porosity. Note that the scale of the 20% porosity plots is $\frac{1}{2}$ of the 5% porosity plots.

For the fine particle variants, the measured elastic modulus response to compositional changes generally falls between the Reuss bound and Isotropic V/R predictions. However, the strengths of the fine particle variants best align with the Reuss bound. Similarly, the measured elastic modulus and strengths of the coarse particle variants align best with the Reuss bound. These results suggest that the Al/PTFE system is primarily behaving under isostress conditions given the alignment to the Reuss bound. A possible explanation for this behavior is associated with the mismatch in material strengths and elastic moduli of the constituents. Consider two particles in contact: one particle is the compliant constituent PTFE and the other particle is the stiff constituent Al. As opposing forces are applied to the particles in contact, intuitively the compliant constituent will deform more than the stiff constituent. As a result the total deformation of the two particles is biased to the weaker constituent. Looking at a cross sectional plane at the interface of the two particles that is perpendicular to the direction of loading, at force equilibrium the 2D contact area is the same between the particles implying equal stress development within the particles. This behavior is likely why the system collapses to the isostress Reuss bound as the compliant constituent PTFE dictates the bulk mechanical response until a critical volume fraction is reached at which point Al particles predominately interact and dominate the response. This behavior has been shown by Nesterneko et al.[16] and Herbold et al.[38] in modeling Al/W and Al/W/PTFE RM systems.

The complete parameterized models using the Isotropic V/R model are compared to the experimental measurements using the parameters in Tables 7.6 and 7.8. For the 50Al/50PTFE variant where porosity parameters for the yield strength could not be determined, the proposed universal fractal parameter value of 0.15 is used. The results of these comparisons are summarized in Table 7.9.

These results indicate the proposed analytical models for elastic modulus and material strengths using the Isotropic V/R model do not fully resolve the complexity of the bulk material behavior. Good alignment of the model forms is observed for the constituents 100Al and 100PTFE, with average absolute prediction errors for the elastic modulus and ultimate strength less than 5% and less than 10% for yield strength. However, as expected significant error is observed for the mixtures. This is not surprising given the mixtures tend towards alignment with the Reuss bound instead of the Isotropic V/R model. Other works[31] have suggested the average of the Voigt and Reuss bounds as a reasonable general approximation for the compositional dependency of materials, but it is clear the approximation does not adequately describe the compositional dependence here. While it is expected that by combining the dependency functions the error associated with each function compounds, it is clear the primary source of error is associated with the Isotropic V/R model in describing the compositional dependencies. The average absolute error between the predictions and measurements of elastic modulus, yield strength, and ultimate strength predictions is 55%, 29.2%, and 50.1%, respectively.

Table 7.9: Prediction error by the parameterized models using the Isotropic V/R model to describe the compositional dependencies of elastic modulus (E_c), yield strength ($\sigma_{c,y}$), and ultimate strength ($\sigma_{c,u}$) of the evaluated compositions

			E_c		$\sigma_{c,y}$		$\sigma_{c,u}$	
Composition	Variant	p_{avg}	Measured	Prediction	Measured	Prediction	Measured	Prediction
		%	GPa	Error	MPa	Error	MPa	Error
100Al	5-F	7	24.4	-8%	-	-	169.4	-4%
	5-C	6	18.5	-2%	105.5	0%	116.2	0%
	20-F	19	8.2	4%	60.9	-26%	61.3	2%
	20-C	21	6.4	-5%	36.5	-14%	37.3	-6%
75Al/25PTFE	5-F	4	3.7	59%	-	-	53.3	39%
	5-C	2	1.3	237%	28.7	73%	29.0	112%
	20-F	20	1.3	65%	-	-	11.7	42%
	20-C	19	0.63	229%	5.72	132%	5.8	100%
50Al/50PTFE	5-F	4	2.0	47%	15.7	120%	23.6	93%
	5-C	4	0.88	84%	10.2	151%	14.5	118%
	20-F	21	0.49	39%	-	-	5.5	89%
	20-C	20	0.13	68%	-	-	3.0	121%
25Al/75PTFE	5-F	4	0.99	108%	12.6	98%	17.5	83%
	5-C	3	0.86	38%	10.1	81%	13.5	75%
	20-F	21	0.28	128%	5.0	99%	5.2	83%
	20-C	20	0.15	-4%	3.1	70%	3.4	60%
100PTFE	5-F	5	0.66	5%	10.2	2%	12.8	4%
	5-C	3	0.56	4%	9.0	3%	12.4	3%
	20-C	23	0.15	-4%	2.6	3%	2.9	2%

The nature of the parameterized models permits ready exchange of dependency functions. Recognizing the alignment of the compositional dependency of the Al/PTFE system to the Reuss bound, replacing the Isotropic V/R model with the Reuss bound in the parameterized models yields:

$$E_c = \left[\sum_{i=1}^{N}(\forall_{f,i}/E_i)\right]^{-1}(1-p)^{1/J_E} \tag{7.11}$$

$$\text{where : } E_i = (E_{1\mu m,i} * (S_{c,i}/1\mu m)^{-n_{E,i}}) \tag{7.12}$$

$$\sigma_{c,y} = \left[\sum_{i=1}^{N}(\forall_{f,i}/\sigma_{y,i})\right]^{-1}(1-p)^{1/J_{\sigma y}} \tag{7.13}$$

$$\text{where : } \sigma_{y,i} = (\sigma_{y,1\mu m,i} * (S_{c,i}/1\mu m)^{-n_{\sigma_{y},i}}) \tag{7.14}$$

$$\sigma_{c,u} = \left[\sum_{i=1}^{N}(\forall_{f,i}/\sigma_{u,i})\right]^{-1}(1-p)^{1/J_{\sigma u}} \tag{7.15}$$

$$\text{where : } \sigma_{u,i} = (\sigma_{u,1\mu m,i} * (S_{c,i}/1\mu m)^{-n_{\sigma_{u},i}}) \tag{7.16}$$

The revised parameterized models using the Reuss bound that are given by Equations 7.11-7.16 are compared to the experimental measurements using the parameters in Tables 7.6 and 7.8. As before, where porosity parameters for the yield strength could not be determined the proposed universal fractal parameter value of 0.15 is used. The results of these comparisons are summarized in Table 7.10.

Table 7.10: Prediction error by the parameterized models using the Reuss bound to describe the compositional dependencies of elastic modulus (E_c), yield strength ($\sigma_{c,y}$), and ultimate strength ($\sigma_{c,u}$) of the evaluated compositions. Average porosity (p_{avg}) of sample sets is also given

			E_c		$\sigma_{c,y}$		$\sigma_{c,u}$	
Composition	Variant	p_{avg}	Measured	Prediction	Measured	Prediction	Measured	Prediction
		%	GPa	Error	MPa	Error	MPa	Error
100Al	5-F	7	24.4	-8%	-	-	169.4	-4%
	5-C	6	18.5	-2%	105.5	0%	116.2	0%
	20-F	19	8.2	4%	60.9	-26%	61.3	2%
	20-C	21	6.4	-5%	36.5	-14%	37.3	-6%
75Al/25PTFE	5-F	4	3.7	-11%	-	-	53.3	-9%
	5-C	2	1.3	85%	28.7	10%	29.0	42%
	20-F	20	1.3	-7%	-	-	11.7	-7%
	20-C	19	0.63	80%	5.72	47%	5.8	33%
50Al/50PTFE	5-F	4	2.0	-20%	15.7	37%	23.6	20%
	5-C	4	0.88	-1%	10.2	52%	14.5	38%
	20-F	21	0.49	-24%	-	-	5.5	17%
	20-C	20	0.13	-10%	-	-	3.0	41%
25Al/75PTFE	5-F	4	0.99	18%	12.6	30%	17.5	20%
	5-C	3	0.86	-23%	10.1	16%	13.5	18%
	20-F	21	0.28	30%	5.0	31%	5.2	20%
	20-C	20	0.15	-47%	3.1	9%	3.4	7%
100PTFE	5-F	5	0.66	5%	10.2	2%	12.8	4%
	5-C	3	0.56	4%	9.0	3%	12.4	3%
	20-C	23	0.15	-4%	2.6	3%	2.9	2%

Using the Reuss bound to describe the compositional dependency reduces the average absolute error between the predictions and measurements of elastic modulus, yield strength, and ultimate strength to 19%, 14%, and 15%, respectively. This alignment of the predictions to the measured behavior is compelling. Not only has the complexity of multiple heterogeneity effects been reasonably described using a single model, this has been accomplished for the Al/PTFE RM system which represents an extreme mechanical response case due to the mismatch in material properties.

The use of the Reuss bound is not broadly applicable to other RM systems based on comparisons in literature[31, 144]. While the Isotropic V/R model has been shown to provide reasonable agreement for tungsten carbide (WC) and cobalt (Co) and glass-epoxy granular composites[144], it is not applicable for the extreme case the Al/PTFE system represents. Therefore, to provide analytical

models that have general applicability for RM systems, it is necessary to propose application regimes for the compositional dependency functions defined by the Reuss bound and Isotropic V/R model for use in the parameterized models.

This work will consider a potential bounding ratio of the models to be the ratio of elastic moduli, E_S/E_W, between the stiff constituent, E_S, and compliant constituent, E_W. The elastic moduli ratio is chosen here because of the prevalence of comparisons of measured elastic moduli of composites to compositional dependency models in literature[144]. However, this is not to suggest other material property ratios are not appropriate for use, but sufficient experimental data is not available here to make assessment of other material property ratios.

For the WC-Co composite evaluated by Luo[144], $E_S/E_W = 3.4$. For the glass-epoxy composite $E_S/E_W = 25$. Here, the ratio between the full density elastic modulus of the fine and coarse Al and PTFE constituents is $E_S/E_W = 34$ and $E_S/E_W = 40$, respectively. Therefore, somewhere between elastic moduli ratios of 25 and 34 a transition of the compositional dependency to the Reuss bound (pure isostress) occurs. For $E_S/E_W > 34$, the Reuss bound provides the better representation of the compositional dependency, with the elastic modulus and material strengths described by Equations 7.11-7.16. For $E_S/E_W < 25$, the Isotropic V/R model provides the better representation of the compositional dependency, with the elastic modulus described by Equations 7.6 and 7.7 and the material strengths described by Equations 7.2-7.5. For $25 < E_S/E_W < 34$, the material response to compositional changes transitions from being described by the Isotropic V/R model to the Reuss bound. The exact nature of this transition is unknown and warrants further investigation.

This is arguably the first demonstration of a predictive capability of the mechanical response of RM systems using analytical models. Based on the alignment of these results to prior works[43, 144] showing the applicability of the dependency functions to a wide variety of granular mixtures, it is anticipated these models are applicable to other RM systems. However, the results here do not provide definitive verification of the proposed parameterized models. Further exploration of the proposed parameterized models is needed for other RM systems, porosity ranges, and particle sizes to affirm broad applicability.

7.3 Fracture toughness of specimens

Fracture toughness was measured for all Al/PTFE specimen variants except the 100PTFE-20-F variant due to specimen fragility. During manufacturing it was determined that the consolidation forces necessary to obtain the 5% nominal porosity conditions led to a number of compositions sticking to the punch faces of the die. As a consequence specimens could not be removed from the die without damage at the nominal 5% condition. It was suspected that the manufacture surface finish of the dies was too rough, as the behavior could not be mitigated using release agents. The 100Al composition, 25Al75PTFE composition, and 100PTFE-5-F variant all demonstrated an inability to consolidate without sticking to the

die punch faces. Therefore it was necessary to increase the nominal porosity condition to 10% for the fracture toughness measurements.

Average values of the fracture toughness measurements from a specimen set of a variant are summarized in Table 7.11. For these measurements, the statistical uncertainty given by the DIM method governs as the calculated maximum measurement uncertainty is <2%. A number of specimens failed during the notch sharpening process using the razor blade. As a result only two specimens were able to be tested for the following variants: 50Al/50PTFE-∗-C, 50Al/50PTFE-5-F, 25Al/75PTFE-5-F, and 100PTFE-5-F. In these case where $\eta = 2$, the uncertainty by the DIM method is $\leq 2.9\sigma_{SD}$ which yields a high uncertainty as seen in Table 7.11. Measurements of individual specimens are summarized in Appendix B.

Table 7.11: Average measurements and uncertainty of fracture toughness of evaluated compositions. Average porosity (p_{avg}) of sample sets is also given

Composition	Variant	p_{avg}	$K_{IC,c}$	
		%	MPa $m^{1/2}$	Uncertainty
100Al	5-F	11	10.2	±5%
	5-C	9	7.2	±12%
	20-F	21	4.3	±28%
	20-C	18	2.5	±8%
75Al/25PTFE	5-F	7	3.6	±9%
	5-C	7	1.3	±22%
	20-F	20	0.95	±31%
	20-C	19	0.25	±11%
50Al/50PTFE	5-F	7	2.3	±47%
	5-C	7	1.6	±7%
	20-F	20	0.75	±20%
	20-C	20	0.22	±22%
25Al/75PTFE	5-F	12	0.81	±125%
	5-C	11	0.78	±15%
	20-F	18	0.42	±53%
	20-C	20	0.35	±20%
100PTFE	5-F	10	0.88	±28%
	5-C	7	1.5	±8%
	20-F			
	20-C	21	0.34	±24%

The fracture toughness of the evaluated variants range from <1 MPa $m^{1/2}$ to >10 MPa $m^{1/2}$. The fracture toughness of the materials responds to composition, porosity, and particle size in a manner similar to the quasi-static elastic modulus and strengths. The highest fracture toughness is associated with the 100Al

composition and the addition of PTFE reduces the fracture toughness of the material with a non-linear proportionality. Similarly, the porosity has a non-linear decremental effect on the fracture toughness of the materials.

A distinct inverse relationship between particle size and the fracture toughness is observed for all compositional variants except 100PTFE. The 1.7x reduction in mean particle size and 2.6x reduction in max particle size (D90) of the Al constituent leads to a 40% increase in fracture toughness for 100Al specimens with nominally 10% porosity and 70% increase in fracture toughness for the 100Al specimens with nominally 20% porosity. For the PTFE constituent, the opposite behavior is observed. A similar reduction in particle sizes yields a 40% decrease in fracture toughness for the nominally 10% porosity condition. However, this behavior is likely not indicative of the true relationship between the PTFE constituent and particle size. The qualitative alignment of the fracture toughness response of the other variants to that of the quasi-static material properties suggests an inverse relationship to particle size is most likely. This would align with literature observations[44, 65]. While the statistical uncertainty does not directly explain the discrepancy, the observed behavior of the 100PTFE is most likely the result of natural variation in the measurements combined with a reduced sample size.

The fracture toughness response to particle size of the 100Al is particularly interesting as it is in direct contrast to observations drawn from work by Kline and Hooper[11] and Kline et al.[180]. Kline and Hooper[11] reported fracture toughness values of 0.6 to 1.8 MPa $m^{1/2}$ for RM specimens comprised of aluminum powder with a mean particle size of 3.5 µm, and mean porosity of 6.3%. Annealing of the specimens was performed, with an increase in fracture toughness associated with increasing annealing time. Subsequent work by Kline et al.[180] studying RM specimens comprised of aluminum powder with mean particle size of 16 µm and mean porosity of 5.2% reported the fracture toughness of the materials to be 3.1 ± 0.5 MPa $m^{1/2}$. The results by the two works would indicate that increasing the mean particle size of aluminum powder by 4.3x should increase the fracture toughness by $\sim$2.6x. However, this work has shown that decreasing the mean particle size by 1.7x will yield an increase in fracture toughness of 1.4x for a material with slightly higher porosity. In addition, higher overall values for fracture toughness are reported here despite evaluation of compositions with larger particles and higher porosity.

The discrepancy between the results here and results by Kline et al.[11, 180] is important to address. Both theory and experimental results of granular material properties[31, 44, 65] dictate that the typical response of a material property is to increase with decreasing particle size and decrease with increasing particle size. While this behavior is observed in the results here, the opposite behavior is observed by comparing the results from Kline and Hooper[11] and Kline et al.[180]. Fracture toughness has been shown to peak at particular particle sizes for composite ceramics[132], however the results discussed here are for a single component metallic granular material.

It is believed that the discrepancy of the results lies in how the fracture tough-

ness of the materials was measured. Testing performed here utilized the SVDCT method which has been shown to provide consistent results that are comparable to fracture toughness measurements obtained through other methods[121, 164]. Kline and Hooper[11] and Kline et al.[180] used ASTM E399 three-point bend tests to determine fracture toughness. The three-point bend test method has been reported by others to be poorly suited to granular compacts due to manufacturing challenges and material inconsistencies[111, 162–164]. Given the nature of granular materials, material inconsistencies can lead to weakening of the bulk material aligning with the lower measurements of fracture toughness reported using the three-point bend test[11, 180] when compared to the results here. Furthermore the values reported by Kline and Hooper[11] and Kline et al.[180] do not include the number of tests performed and thus lack evaluation of the statistical representation of the measurements. In contrast, the statistical uncertainty of the fracture toughness values reported here has been characterized. Because the experimental method used here has been shown to provide reliable results for granular compacts and the statistical uncertainty of the measurements has been characterized, it is believed that the fracture toughness results in this work are not only the best representation of the 100Al system, but also that of the general compositional, porosity, and particle size dependencies of the Al/PTFE system.

The fracture toughness measurements presented in Table 7.11 are used in determining the parameters of the analytical model discussed in Chapter 2 and for evaluating the predictions by the model. For convenience, the analytical model for fracture toughness is repeated here:

$$K_{IC,c} = \frac{2}{\left[\sum_{i=1}^{N}(\forall_{f,i}K_{IC,i})\right]^{-1} + \sum_{i=1}^{N}(\forall_{f,i}/K_{IC,i})}(1-p)^{1/J_K} \tag{7.17}$$

$$where: K_{IC,i} = (K_{1\mu m,i} * (S_c, i/1\mu m)^{-n_{K,i}}) \tag{7.18}$$

A standard least-squares fit governed by the generalized reduced gradient algorithm is used to determine the parameters of the analytical model for fracture toughness. This process follows the same systematic approach as applied to the elastic moduli and material strengths. The full density fracture toughness and respective fractal parameters are summarized in Table 7.12.

Due to the lack of porosity variation and restricted statistical representation of the 100PTFE fine particle variant, determination of both the full density fracture toughness and fractal parameter is not feasible using a least squares fit. An estimate of the full density fracture toughness is needed to constrain the system for determining the fractal parameter. The difference between the 100PTFE fine and coarse particle variant full density elastic modulus, yield strength, and ultimate strength are similar at 1.57x greater, 1.40x greater, and 1.34x greater, respectively. It is also recognized that the proportional difference between the measured fracture toughness of the 100PTFE-5-C and 100PTFE-20-C variants is similar to the proportional difference between their respective ultimate strengths for similar

values of porosity. Given these similarities, it is assumed that the known proportionalities of the 100PTFE fine particle variant full density elastic modulus and material strengths are similar for the fracture toughness. The full density fracture toughness of the 100PTFE fine particle variant is therefore estimated as 1.40x that of the full body density of the 100PTFE coarse particle variant, or 4 MPa $m^{1/2}$.

Table 7.12: Calculated full density fracture toughness and fractal parameters that best describe the porosity dependencies of the compositions comprised of fine and coarse particles.

Composition	Variant	$K_{IC,o}$ MPa $m^{1/2}$	J_k	RMSPE
100Al	F	22.7	0.144	15.4%
	C	17.3	0.105	6.6%
75Al/25PTFE	F	7.1	0.110	4.9%
	C	2.8	0.085	11.5%
50Al/50PTFE	F	4.0	0.130	10.6%
	C	3.5	0.083	7.1%
25Al/75PTFE	F	2.5	0.113	31.5%
	C	1.8	0.135	10.7%
100PTFE	F	4.0	0.067	13.3%
	C	2.9	0.114	16.9%

The full density fracture toughness values in Table 7.12 demonstrate that the fracture toughness has an inverse relationship to particle size reinforcing observations from the measurements in Table 7.11. This relationship can be explained by considering the fracture process zone[102]. This zone represents the region ahead of the traction free crack tip and thus the volume of material that most readily dictates the crack growth behavior. The fracture process zone can be estimated as the plastic zone size, r_y, described using the Irwin approach[102]:

$$r_y = \frac{1}{6\pi}\left(\frac{K_I}{\sigma_y}\right)^2 \tag{7.19}$$

Where K_I is the stress intensity factor. At crack tip advancement occurs, $K_I = K_{IC}$. Assuming the plastic zone size for the Al/PTFE system is bounded by the zone size of the constituents, the full density yield strengths and fracture toughness of the 100Al and 100PTFE variants are used to calculate the potential size range of the fracture process zone. The process zone size has a range between 0.4 mm and 4 mm dictated by the 100Al and 100PTFE, respectively. The size of the plastic zone is between one and two orders of magnitude larger than the constituent particle sizes, indicating the crack growth behavior should be dictated by the combined response of the particles. For the fine particle variants, $\sim$ 17x more

particles by volume are inside the fracture process zone compared to the coarse particle variants. This suggests the fracture toughness relationship to particle size is not only due to improved distribution of particles[16, 43], but also the increase in particle contact area within the fracture process zone[106, 120].

An interesting thing of note is the size of the process zone relative to the distance between the crack tip and the unnotched face of the SVDCT specimen which is 3 mm. For the 100Al compositions, the process zone is 15% of this distance indicating the process zone is fully contained within the material. For the 100PTFE compositions, the process zone is larger than the distance between the crack tip and the unnotched face of the SVDCT specimen. This interaction of the process zone with the specimen boundary could influence the fracture toughness measurements of the 100PTFE composition and potentially the other PTFE containing compositions[250]. However, this is not expected to be the case for the 100Al compositions as the size of the fracture process zone falls within in limits proposed by Hu and Duan[250] for when specimen boundary effects can be considered negligible. Now that values of fracture toughness and yield strength have been established for these materials, a worthy future endeavor would be to explore the effects of specimen geometry on these measurements and alignment to ASTM E99 specimen geometry standards.

The RMSPE values are on the order of, or are less than, the uncertainty bounds of the experimental measurement indicating acceptable alignment of the predictions to the data. As with the measurements of elastic moduli and material strengths, a nominal universal fractal parameter is taken as the mean value of the fractal parameters, the lower bound as the minimum value of the fractal parameters, and the upper bound as the maximum value of the fractal parameters. These values are: J_{nom}=0.11 for the nominal value, J_{low}=0.07 for the lower bound, and J_{high}=0.14 for the upper bound. These values are lower than the group values for the elastic modulus and material strengths of the Al/PTFE system, indicating the fracture toughness is more sensitive to material porosity. Similarly, the smaller fractal parameter values for the coarse particle variants indicate these compositions are more sensitive to porosity than the fine particle variants. The porosity dependency dictated by these values of the fractal parameter are plotted alongside the experimentally measured fracture toughness normalized by the full density fracture toughness in Figures 7.9. The experimental values are plotted by composition only and particle size is not indicated. The error bars represent the average uncertainty of all specimen measurements for a variant.

Using the calculated full density fracture toughness and mean particle sizes of the constituents, the 1 μm mean particle size fracture toughness and sensitivity parameter were determine for the constituents 100Al and 100PTFE. For 100Al, $K_{1\mu m}$ = 46.9 MPa $m^{1/2}$ and n_K = 0.303. For 100PTFE, $K_{1\mu m}$ = 10.8 MPa $m^{1/2}$ and n_K = 0.398. The RMSPE values of the predictions for the constituents is less than 0.01% indicating acceptable alignment to the data.

Comparisons to fracture toughness values for the homogeneous forms of the constituents is challenging due to limited fracture toughness data for the pure ho-

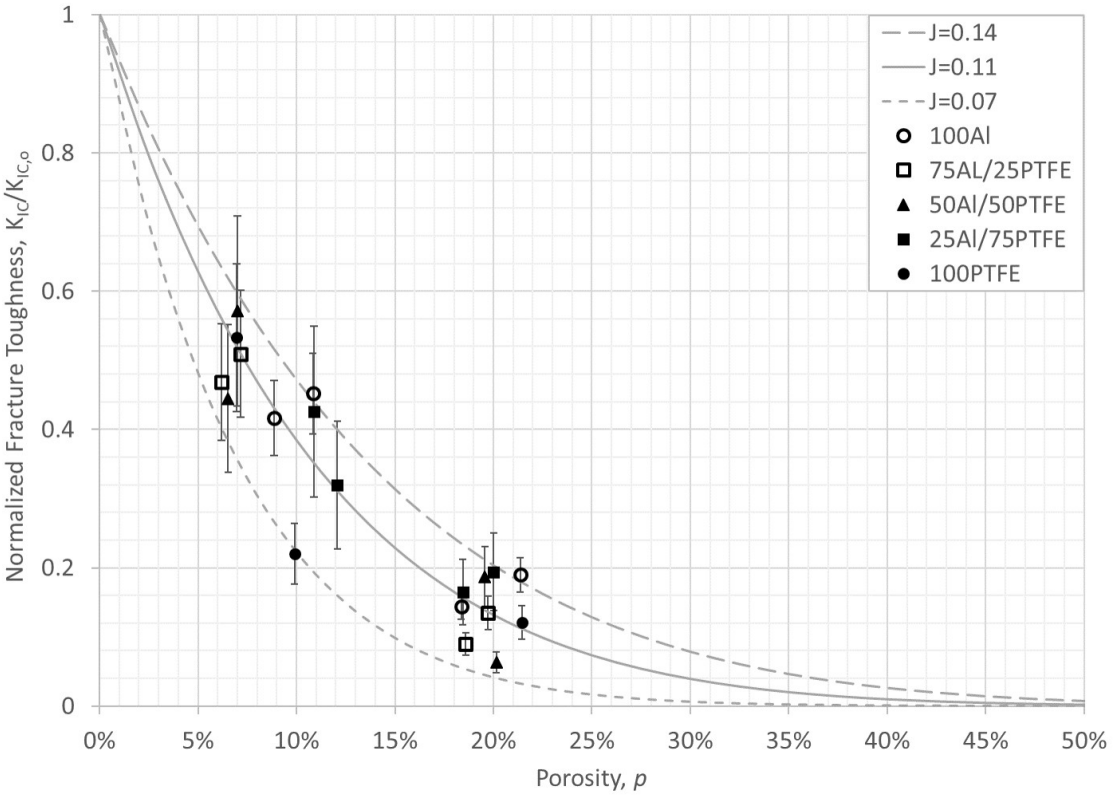

Figure 7.9: Measured fracture toughness response to porosity normalized by the calculated full density fracture toughness. Predicted response for fractal parameter values of $J_{high} = 0.14$, $J_{nom} = 0.11$ and $J_{low} = 0.07$ are plotted for comparison.

mogeneous forms of the constituents. Values of K_{IC} for homogeneous PTFE are lacking due to measurement challenges associated with the viscoelastic behavior at room temperature[251]. Similarly, K_{IC} values of the commercially pure 1100 series aluminum are also lacking due to the ductility of the material[252]. Comparing K_{IC} values of 2024 series aluminum, which is the most similar in response to 1100 series in tension[252], the $K_{1\mu m}$ value for 100Al is 2.1x greater. This reaffirms the observation that the bulk behavior of these granular materials is not derivative of their homogeneous counterparts and the use of homogeneous properties to estimate the 1 µm mean particle size fracture toughness is misguided. Without further exploration of particle size variation, with particular focus on materials approaching the 1 µm mean particle size, perspective on physical meaning and predictive capability of the particle size dependency parameters for fracture toughness is limited.

Predictions of the compositional dependency of the fracture toughness are evaluated by comparisons to the experimental results. Theoretical predictions are made for the 10% porosity condition and the 10% and 20% constituent mate-

rial properties for the different powder sizes are calculated using the 100Al and 100PTFE particle size dependency parameters. The Isotropic V/R model is plotted along with the Voigt and Reuss bounds and the average of the two models. Comparison of predictions to experimental measurements of fracture toughness are shown in Figures 7.10. Note that for all figures the average porosity of the specimen set of the measurement is indicated.

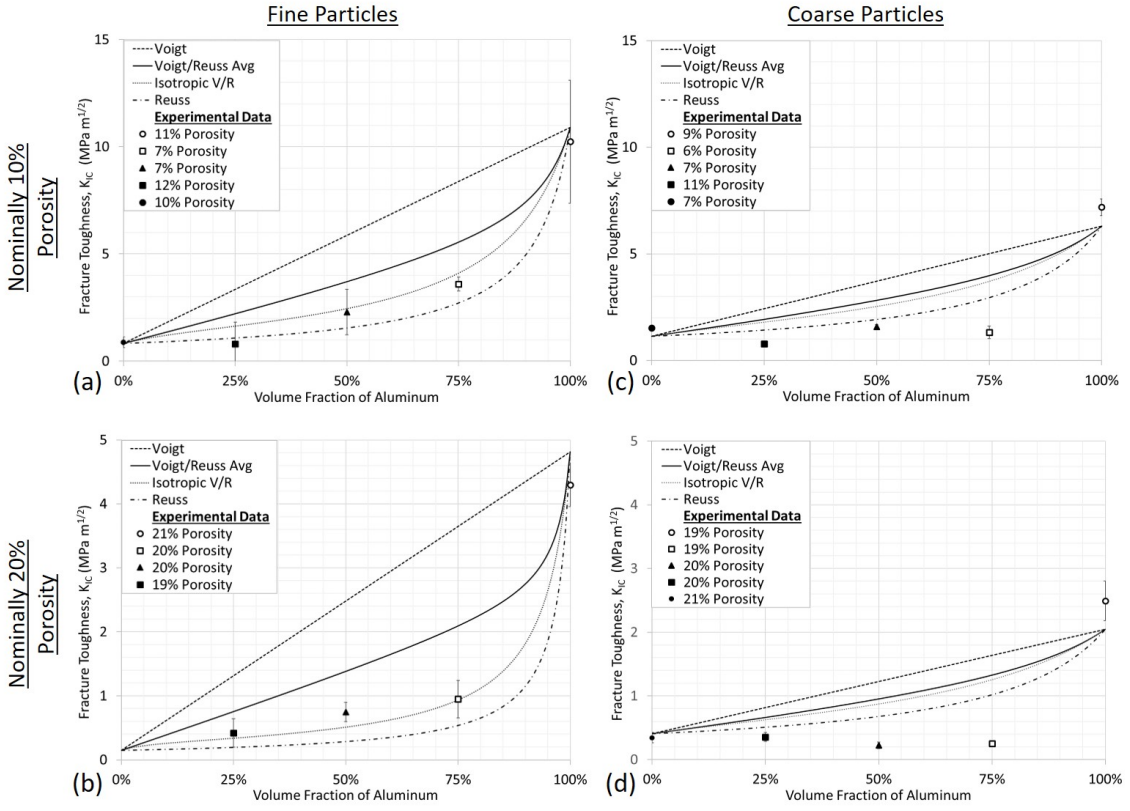

Figure 7.10: Predictions by GRM models of predicted of fracture toughness response to compositional variation compared to the measured response of the Al/PTFE system for: (a) fine particles with nominally 10% porosity; (b) fine particles with nominally 20% porosity; (c) coarse particles with nominally 10% porosity; and (d) coarse particles with nominally 20% porosity. Note that the scale of the 20% porosity graphs is 1/3 of the 10% porosity graphs.

For the fine particle variants, the measured fracture toughness response to compositional variation falls between the Reuss bound and Isotropic V/R model for both porosity conditions. This is similar to the observed behavior of the elastic modulus of the fine particle variants. The opposite is true for the coarse particle variants, which do not align to any of the compositional dependency models. This is indicative of unknown micromechanical behaviors that overshadow the compositional effects. The addition of Al for the coarse particle variants is also

seen to reduce the fracture toughness of the mixtures as compared to the fracture toughness of the 100PTFE coarse particle variants. The fracture toughness of granular materials is known to be strongly dependent on the interface strength and the distribution of area between the particles[29, 106, 120]. For the coarse particle variants the addition of aluminum may lead to a reduction in the interface strength between particles due to the presence of larger dissimilar particles and poor mixing. This behavior is not observed for the fine particle variants, likely due to better mixing and increased interface strength between particles. Because the particle sizes of the constituents are similar it seems unlikely these effects are related to a spatial scale changes due to mixing of the particles. This is reinforced by the order of magnitude differences in size bounds of the fracture process zone relative to the constituent particle sizes.

Using the determined parameters for the porosity and particle size dependencies, fracture toughness predictions by the full parameterized model are compared to the experimental measurements in Table 7.13. As with the elastic moduli and material strengths, the analytical model proposed here for fracture toughness does not fully resolve the complexity of the bulk material behavior. Good alignment of the model for the constituents is observed with an average absolute prediction error of 3% for the 100Al system and 4% for the 100PTFE system. This indicates that the combined porosity and particle dependency functions adequately describe the fracture toughness response for the single constituents. The prediction error is significant for the mixtures. This is expected based on the response of the fine particle variants falling between the Isotropic V/R and Reuss bound predictions and the coarse particle variants failing to align to any of the evaluated compositional models. Average absolute prediction error is 4% for the constituent variants and 138% for the mixed compositional variants reinforcing the primary source of error is related to predictions of the compositional dependencies.

The nature of the parameterized models permits ready exchange of dependency functions. Recognizing the alignment of the compositional dependency of the Al/PTFE system to the Reuss bound, replacing the Isotropic V/R model with the Reuss bound in the parameterized models yields:

$$K_{IC,c} = \left[\sum_{i=1}^{N} (\Psi_{f,i}/K_{IC,i})\right]^{-1} (1-p)^{1/J_K} \tag{7.20}$$

$$\text{where : } K_{IC,i} = (K_{1\mu m,i} * (S_{c,i}/1\mu m)^{-n_{K,i}}) \tag{7.21}$$

The revised parameterized models using the Reuss bound that are given by Equations 7.20 are compared to the experimental measurements using the parameters in Tables 7.12 and particle size dependency parameters. The results of these comparisons are summarized in Table 7.14.

Using the Reuss bound to describe the compositional dependency reduces the average absolute prediction error to 85% for the mixed compositional variants. While this is an improvement, the compositional dependencies are still not

Table 7.13: Prediction error by the parameterized models using the Isotropic V/R model to describe the compositional dependencies of fracture toughness (K_{IC}) of evaluated compositions. Average porosity (p_{avg}) of sample sets is also given

Composition	Variant	p_{avg}	$K_{IC,c}$	
			Measured	Prediction
		%	MPa $m^{1/2}$	Error
100Al	5-F	11	10.2 ±5%	-1%
	5-C	9	7.2 ±12%	-2%
	20-F	21	4.3 ±28%	3%
	20-C	18	2.5 ±8%	4%
75Al/25PTFE	5-F	7	3.6 ±9%	90%
	5-C	7	1.3 ±22%	221%
	20-F	20	0.95 ±31%	83%
	20-C	19	0.25 ±11%	228%
50Al/50PTFE	5-F	7	2.3 ±47%	124%
	5-C	7	1.6 ±7%	72%
	20-F	20	0.75 ±20%	116%
	20-C	20	0.22 ±22%	104%
25Al/75PTFE	5-F	12	0.81 ±125%	154%
	5-C	11	0.78 ±15%	150%
	20-F	18	0.42 ±53%	162%
	20-C	20	0.35 ±20%	153%
100PTFE	5-F	10	0.88 ±28%	-6%
	5-C	7	1.5 ±8%	1%
	20-C	21	0.34 ±24%	6%

fully resolved. However, both the Isotropic V/R model and Reuss bounds qualitatively capture the compositional dependencies of the fine particle variants.

This is the first known demonstration of an analytical model to describe the compositional, porosity, and particle size effects of the fracture toughness of granular materials. The porosity and particle size dependency functions have been shown to provide good description of the bulk behavior of single constituent granular compacts as evident by the small average prediction error for the constituents. Assessment of these functions over a broader range of porosity and particle sizes would fully verify their applicability and is warranted. The Isotropic V/R model and Reuss bounds both failed to provide a complete quantitative description of the fracture toughness response of the materials, but did show qualitative description for the fine particle variants. Recognizing the the Al/PTFE RM system represents an extreme mechanical response case due to the mismatch in material properties of the constituents, the ability of these models to represent

Table 7.14: Prediction error by the parameterized models using the Reuss bound to describe the compositional dependencies of fracture toughness (K_{IC}) of evaluated compositions. Average porosity (p_{avg}) of sample sets is also given

Composition	Variant	p_{avg}	$K_{IC,c}$	
			Measured	Prediction
		%	MPa $m^{1/2}$	Error
100Al	5-F	11	10.2 ±5%	-1%
	5-C	9	7.2 ±12%	-2%
	20-F	21	4.3 ±28%	3%
	20-C	18	2.5 ±8%	4%
75Al/25PTFE	5-F	7	3.6 ±9%	50%
	5-C	7	1.3 ±22%	150%
	20-F	20	0.95 ±31%	45%
	20-C	19	0.25 ±11%	156%
50Al/50PTFE	5-F	7	2.3 ±47%	69%
	5-C	7	1.6 ±7%	28%
	20-F	20	0.75 ±20%	63%
	20-C	20	0.22 ±22%	51%
25Al/75PTFE	5-F	12	0.81 ±125%	101%
	5-C	11	0.78 ±15%	95%
	20-F	18	0.42 ±53%	107%
	20-C	20	0.35 ±20%	97%
100PTFE	5-F	10	0.88 ±28%	-6%
	5-C	7	1.5 ±8%	1%
	20-C	21	0.34 ±24%	6%

the behavioral trends of both the mixtures and the constituents is inspiring. While the proposed analytical model for fracture toughness of RM systems clearly does not fully resolve the complexities of the granular materials, further evaluation is warranted in both application to other RM systems and developing an understanding of the particle interaction changes induced by mixing constituents.

7.4 Wave speeds of specimens

Wave speed measurements were attempted for all Al/PTFE specimen variants, but attenuation of the ultrasonic waves by the material presented challenges. The shear wave speeds of the materials could not be measured as the Olympus 45MG could not detect a reflected wave. While measurements of dilational wave speed were obtainable for the 5% porosity specimens, measurements

of the 20% porosity specimens also could not be obtained as the Olympus 45MG could not detect a reflected wave. The exception to this was the 100Al variant for which wave speeds of the nominally 20% condition were obtained. Measurements of at least four specimens were made for each variant, and the average values of the dilational wave speed measurements from a specimen set are summarized in Table 7.15.. For these measurements, the statistical uncertainty given by the DIM method governs as the calculated maximum measurement uncertainty is <1%. Measurements of individual specimens are summarized in Appendix B.

Table 7.15: Average measurements and uncertainty of dilational wave speed of the evaluated compositions. Average porosity (p_{avg}) of sample sets is also given

Composition	Variant	p_{avg} %	$C_{d,c}$ m/s	$C_{d,c}$ Uncertainty
100Al	5-F	7	5091	±5%
	5-C	6	4785	±10%
	20-F	19	3614	±2%
	20-C	21	1993	±4%
75Al/25PTFE	5-F	4	2215	±11%
	5-C	2	1766	±17%
50Al/50PTFE	5-F	4	1751	±8%
	5-C	4	1326	±9%
25Al/75PTFE	5-F	4	1263	±11%
	5-C	3	1430	±13%
100PTFE	5-F	5	1273	±3%
	5-C	3	1089	±4%

A direct assessment of the porosity dependency of the dilational wave speed for the Al/PTFE system is not possible due to the lack of measurements for the 20% porosity condition. However, the 100Al variant shows a distinct decrement in dilational wave speed due to porosity. From the observed response of the elastic modulus to porosity in this work, the relationships between wave speeds and moduli, and prior works investigating seismic wave speeds of granular rock[43] it is expected the porosity dependency is of the power-law GRM form. From the least squares fit methodology applied here, the full density dilational wave speed of the 100Al fine and coarse particle variants are 5918 m/s and 6684 m/s, respectively. The fractal parameters of the 100Al fine and coarse particle variants are 0.434 and 0.189, respectively. RMSPE for these parameters is $< 4\%$ indicating good agreement of the power-law GRM model. The lower fractal parameter value of 100Al coarse particle variant compared to the fine particle variant indicates the coarse particle variant is considerably more sensitive to porosity. This explains why the 100Al-C has a higher full density wave speed than the 100Al-F variant. The difference in fractal parameters indicates the two variants

do not share a linear proportionality to porosity affirming the use of the power-law GRM. This power law dependency likely extends to all of the variants based on the behavior of the elastic modulus previously discussed.

An inverse particle size dependency is evident for all variants, with decreasing dilational wave speed associated with increasing mean particle size. This behavior aligns with observations by works modeling microstructural influences on wave speeds in granular materials[136, 152] and is due to enhanced attentuation due to the reduced particle contact area associated with the coarse particles. The particle size dependency parameters cannot be determined for the variants that lack full density dilational wave speeds. Additionally, the particle size parameters cannot be determined for the 100Al as the full density dilational wave speed of the 100Al fine particle variant is lower than the full density value for the 100Al coarse particle variant. Based on these 100Al results, the dilational wave speed dependencies on the interface conditions between particles[136, 152] appears to preclude the use of a simple analytical model to describe the particle size dependencies.

Predictions of the compositional dependency of the dilational wave speed are evaluated by comparisons to the experimental results. Theoretical predictions are made for the 5% porosity condition. These predictions use the full density dilational wave speed and fractal parameters for determining the Al constituent properties and the mean of the dilational wave speeds measured for the 100PTFE variant for the PTFE constituent properties. The Isotropic V/R model is plotted along with the Voigt and Reuss bounds and the average of the two models. Comparison of predictions to the experimental measurements of dilational wave speed are shown in Figures 7.11. Note that for all figures the average porosity of the specimen set of the measurement is indicated. It is clear from the comparisons in Figure 7.11 that the dilational wave speed has a non-linear compositional dependency. Thus, the proposed linear form of the analytical model for dilatiational wave speed is not the appropriate representation of the actual compositional dependency of the Al/PTFE system.

The proposed analytical model for dilational wave speed that represents the compositional and porosity dependencies of granular materials as linear functions is not representative of the material behavior observed here. Additionaly, there is a clear particle size dependency that was not accounted for by the proposed analytical model. To avoid misrepresenting the use of a simple analytical model to describe the dilational wave speed compositional, porosity, and particle size dependencies, a revised model will not be proposed. Instead, the dependency behaviors are reported here to guide future works. These results suggest the porosity dependency is best described using a power-law relation. While it is clear the dependency on particle size is significant, this relationship is more complex than can be described by the generalized Spriggs equation proposed for other material properties in this work. This is likely due to the attenuation effects associated with the interface conditions of the particle[136, 152]. From the experimental results, the compositional dependencies are clearly not linear. While the measured dilational wave speeds of the fine particle variants align somewhat

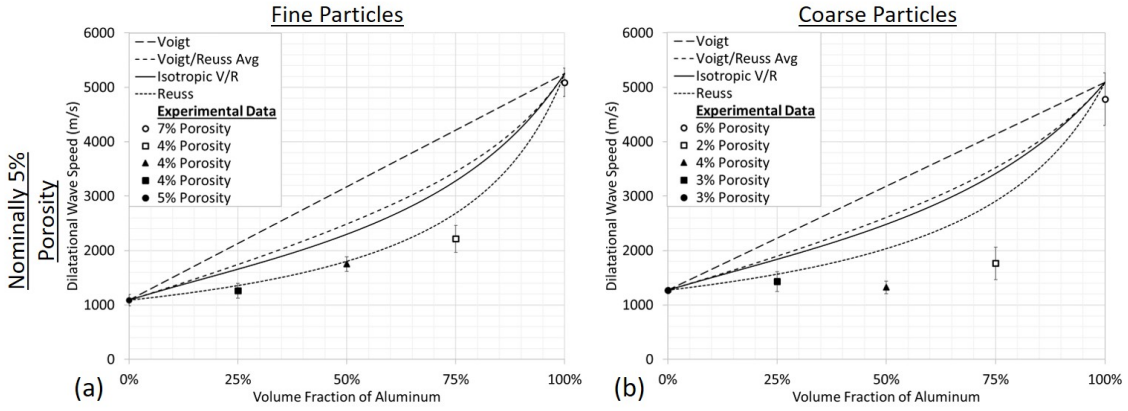

Figure 7.11: Predictions by GRM models of predicted of dilational wave speed response to compositional variation compared to the measured response of the Al/PTFE system for: (a) fine particles with nominally 5% porosity and (b) coarse particles with nominally 5% porosity.

to the Reuss bound, the coarse particle variants do not align well to any of the models describing compositional dependencies. As with the particle size dependencies, this behavior is likely associated with the interface conditions between particles which these models do not describe. From these observations, the lack of verified analytical models for wave speeds in literature is understandable.

7.5 Dynamic response and fragmentation behavior observed in Kolsky bar compression tests

Kolsky bar tests were used to dynamically load specimens to failure in an effort to explore the fragmentation behavior of the Al/PTFE system. Dynamic compression tests were performed on the following variants: 100AL-5-F, 100Al-5-C, 100PTFE-5-F, 100PTFE-5-C, 25Al/75PTFE-5-F, 25Al/75PTFE-5-F. Because all variants are of the same nominal porosity condition, for the discussions in this section they will be referred to by only the composition and particle size designations for simplicity. The selection of these variants for testing were informed by the quasi-static compression testing results. The constituents 100Al and 1000PTFE provide insight into particle size effects on the dynamic material response without interference from compositional influences. The 25Al/75PTFE compositional variant was selected because it is the near stotichiometric mixture for the Al/PTFE system and provides insight on the compositional effects. Porosity effects on the dynamic response were not explored because the low material strength determined in the quasi-static compression tests indicated specimens at the 20% porosity condition were ill suited for Kolsky bar tests due to the inability to isolate the transmitted wave for calculations and the potential for high-speed collision of the bars.

Three specimens per variant were loaded dynamically for a total of 18 Kolsky bar tests. The average strain rate for these tests was $2.3{\cdot}10^3$ s^{-1}. Peak engineering compressive stress, $\sigma_{d,max}$, and average engineering axial strain rate of the specimens are summarized in Table 7.16. The dynamic increase factor (DIF) is reported as a metric comparing the measured the peak dynamic compressive stress to the quasi-static ultimate compressive strength, given by $\sigma_{d,max}/,\sigma_{c,u}$. The engineering compressive stress-strain response of specimens representative of the typical response of the variants are shown in Figure 7.12. For clarity, the stress and strain data are smoothed using a moving average with a window size of 20.

Table 7.16: Average strain rate ($\bar{\dot{\varepsilon}}_s$) and peak compressive stress ($\sigma_{d,max}$) for specimens subjected to Kolsky bar tests. The dynamic increase factor (DIF), given by $\sigma_{d,max}/\sigma_{c,u}$, is reported for the specimen variants. Porosity (p) of the samples is also given.

Variant	Specimen	p	$\bar{\dot{\varepsilon}}_s$		$\sigma_{s,max}$		DIF
		%	10^3 s^{-1}	Uncert.	MPa	Uncert.	
100Al-5-F	1	6	2.0	±2.4%	185	±2.5%	1.09
	2	5	2.3		212		1.25
	3	6	2.1		197		1.16
100Al-5-C	1	4	2.1	±2.4%	136	±2.5%	1.17
	2	5	2.2		131		1.15
	3	5	2.2		138		1.19
25Al/75PTFE-5-F	1	5	2.4	±2.4%	29	±2.5%	1.66
	2	4	2.3		32		1.83
	3	4	2.4		36		2.06
25Al/75PTFE-5-C	1	4	2.4	±2.4%	44	±2.5%	3.26
	2	3	2.3		35		2.60
	3	3	2.4		28		1.77
100PTFE-5-F	1	7	2.3	±2.3%	30	±2.5%	2.34
	2	5	2.3		64		5.0
	3	8	2.4		24		1.9
100PTFE-5-C	1	4	2.5	±2.3%	33	±2.5%	2.66
	2	5	1.9		26		2.10
	3	5	2.4		28		2.26

The individual variants demonstrate consistency in response of their respective specimens to the applied dynamic loading. As with the quasi-static compression results, the 100Al variants has the highest strength under dynamic loading. The 25AL/75PTFE variants demonstrate similar strength and response to the 100PTFE variants, indicating the PTFE is controlling the bulk response. The DIF values show all variants are sensitive to strain rate and exhibit strain rate

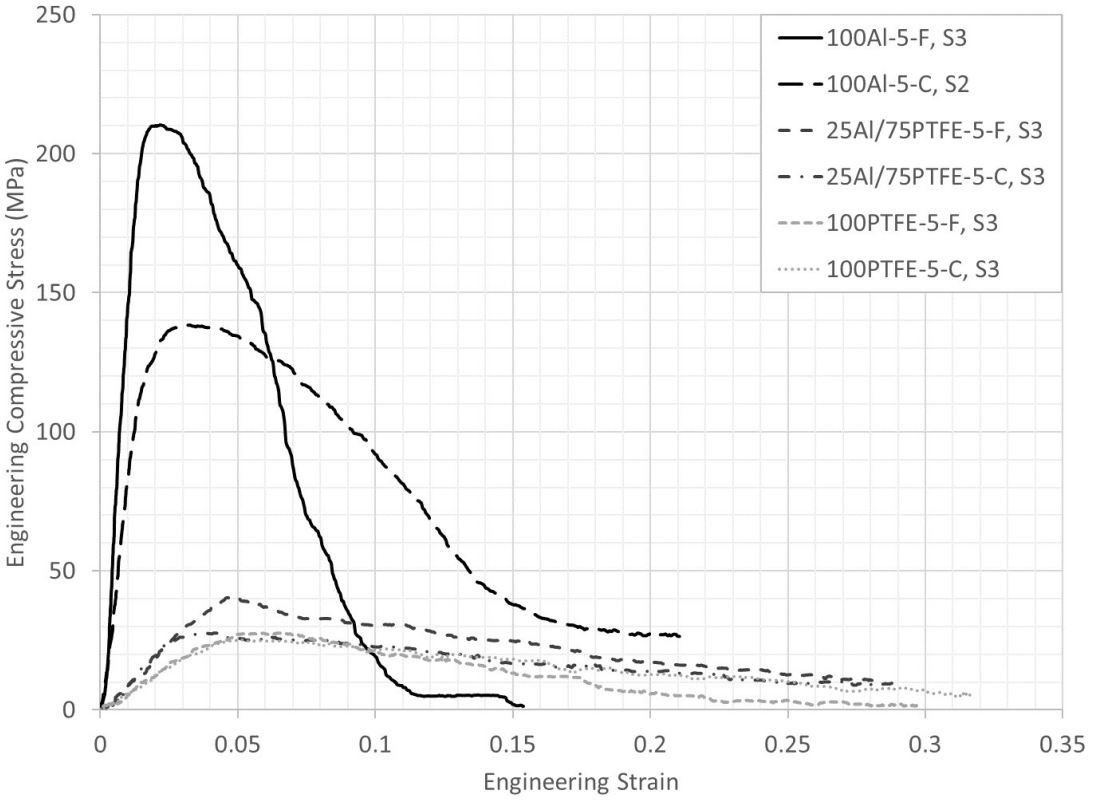

Figure 7.12: Engineering stress and strain response of representative specimens of the 100Al, 100PTFE, and 25Al/75PTFE particle size variants subjected to Kolsky bar tests. The variant type and specimen number are indicated. Porosity of the specimens is nominally 5%.

hardening behavior to some degree. The 100Al-5-F and 100Al-5-C variants show the least sensitivity to strain rate with an average DIF value of 1.2x. The variants containing PTFE are significantly more sensitive to strain rate as indicated by their higher DIF values. The 100PTFE-5-F and 100PTFE-5-C variant peak stresses obtained under dynamic loading are on average 3x and 2.5x greater, respectively, than the measured quasi-static compression strengths. While the addition of Al suppresses the strain rate hardening effects to a small degree for the 25Al/75PTFE variants, the 25Al/75PTFE-5-F and 25Al/75PTFE-5-C peak stresses obtained under dynamic loading are on average 1.9x and 2.5x greater, respectively, than the measured quasi-static compression strengths.

The loading and failure of all specimens was captured using the HPV-X2 camera. From the HPV-X2 footage, the failure of all specimens was observed to occur during the first loading pulse. Three images from the HPV-X2 high-speed footage are assembled for the specimens whose stress-strain responses are shown in Figure 7.12: The first image is of the specimen at the onset of loading; the

second image is of the specimen at peak stress, and the third image is of the failing specimen when the stress has decreased to 20% of the peak stress. These images are considered representative of the general response all the other specimens of the variant. These image sets for the 100Al, 100PTFE, and 25Al/75PTFE variants are shown in Figures 7.13, 7.14, and 7.15, respectively.

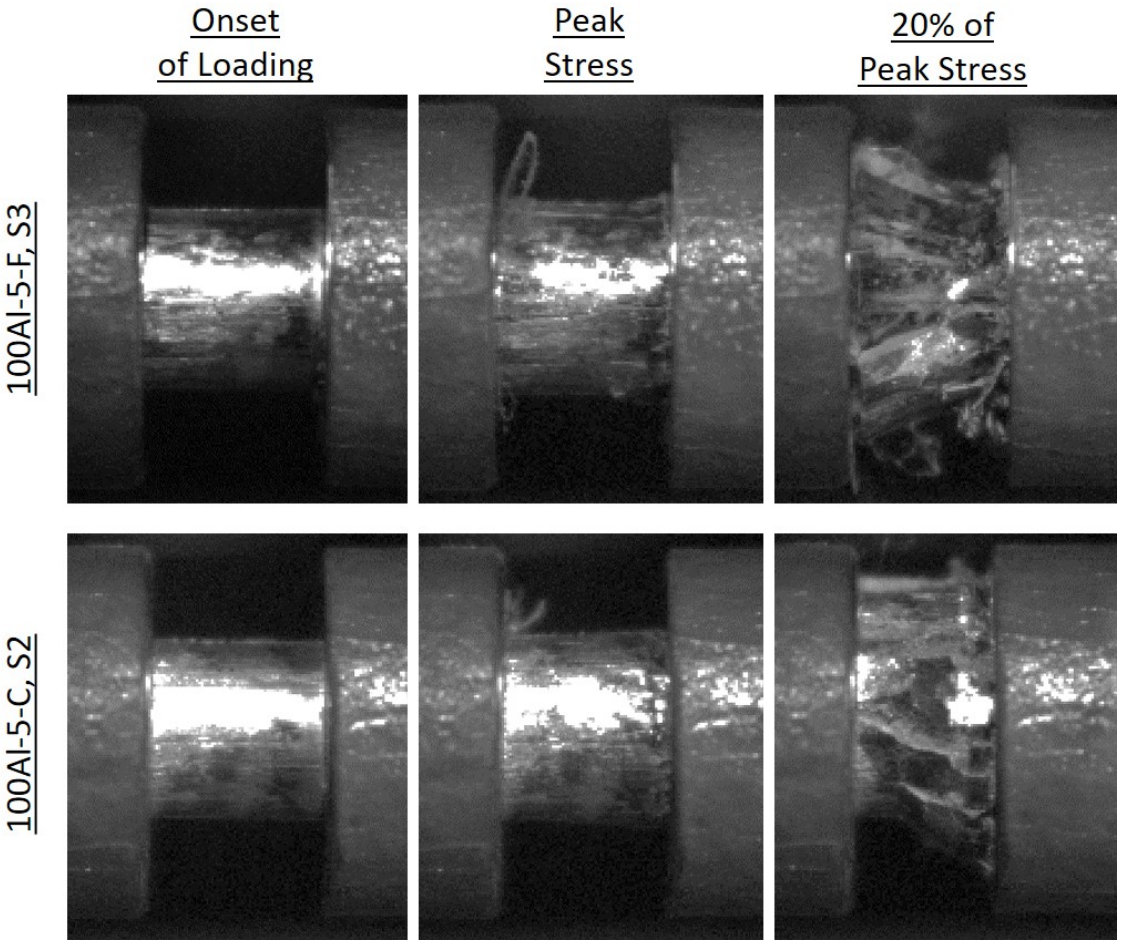

Figure 7.13: High-speed images of the dynamic loading event of 100Al specimens subjected to Kolsky bar tests. Images from left to right correspond to: onset of loading, peak stress, and 20% of peak stress, post-peak. Variant and specimen number are indicated for the image sets.

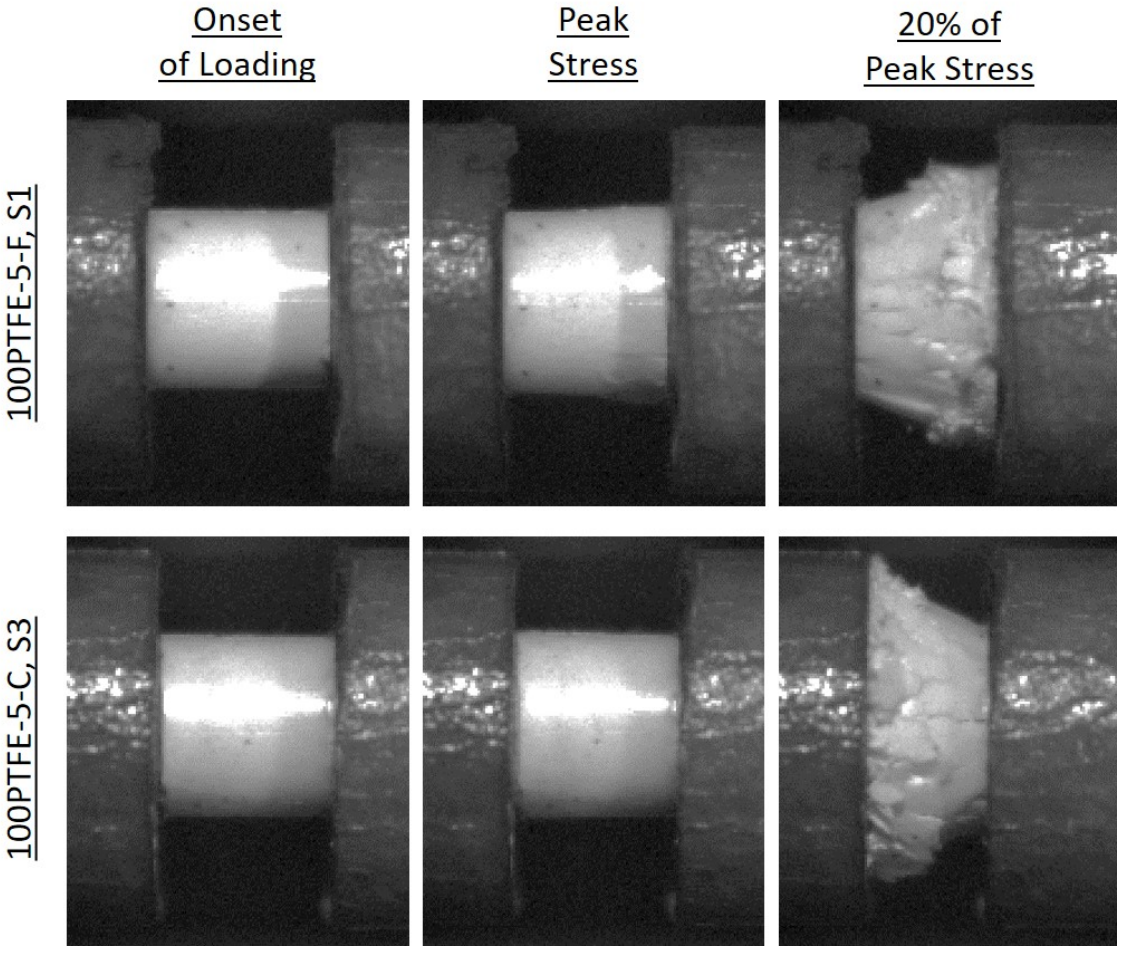

Figure 7.14: High-speed images of the dynamic loading event of 100PTFE specimens subjected to Kolsky bar tests. Images from left to right correspond to: onset of loading, peak stress, and 20% of peak stress, post-peak. Variant and specimen number are indicated for the image sets.

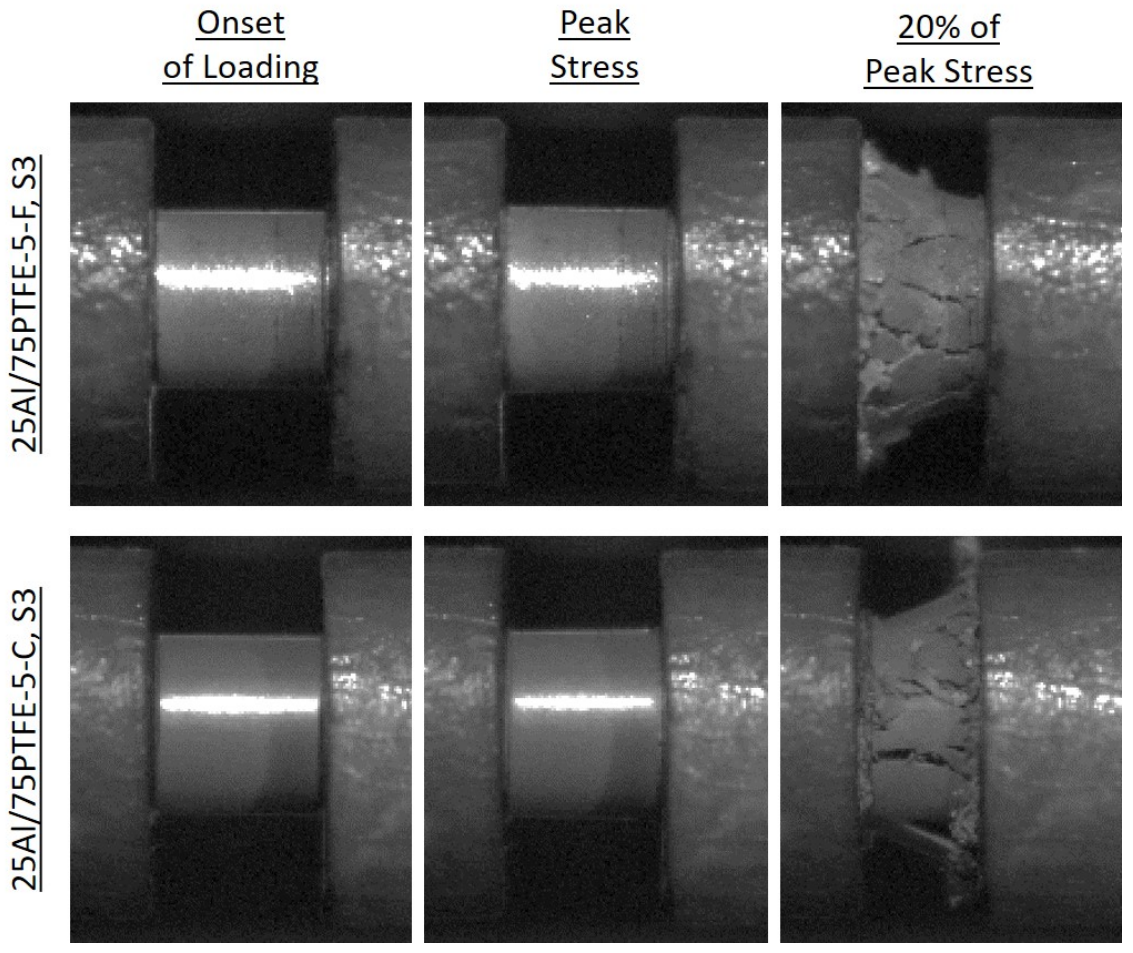

Figure 7.15: High-speed images of the dynamic loading event of 25Al/75PTFE specimens subjected to Kolsky bar tests. Images from left to right correspond to: onset of loading, peak stress, and 20% of peak stress, post-peak. Variant and specimen number are indicated for the image sets

Specimens in Figures 7.13, 7.14, and 7.15 all expanded radially during loading. Failure of the specimens occur through the formation of circumferential cracks parallel to the direction of axial loading. This behavior could be indicative of tensile failure of the surface material due to hoop stress development as a result of the radial expansion. This would be a similar failure mode to what has been observed in high velocity impact tests[11, 12]. However, the formation of these cracks can also be the result of fractures that propagate off of weak slip planes called wing cracks which have been observed in the dynamic failure of brittle materials under compressive loads[253]. As the specimens fail, fragments are ejected radially outward from the specimen center. This mode of failure has been observed in high-velocity impact tests[11, 12] supporting comparison of the Kolsky bar results here to high velocity impact tests.

The 100Al variants display similar behavior at the peak stress condition with developing circumferential cracks along the surface, although the 100Al-5-F variant appears to have accumulated more damage by this stage of loading. Upon failure, the 100Al-5-F specimen fails rapidly, indicated by the rapid drop in stress in Figure 7.12. This behavior is reflected in the images at the 20% of peak stress condition, where the 100Al-5-F variant has shattered into small fragments while the 100Al-5-C variant has failed into what appears to be larger fragments.

The PTFE variants are similar in their stress-strain response. However, at peak stress, the 100PTFE-5-F is beginning to develop circumferential surface cracks while no visible crack development is observed for the 100PTFE-5-C variant. At the 20% of peak stress condition, the failed specimen condition is nearly indistinguishable between the fine and coarse particle size variants. Circumferential crack formation is not apparent at the peak stress condition for the 25Al/75PTFE particle size variants. At the 20% of peak stress condition, the failed specimen conditions are also nearly indistinguishable.

Fragments were recovered for all Kolsky tests. Recovered fragment masses ranged from 50% to 80% of the original specimen mass. Primary mass loss was associated with ejection of fragments from the enclosure. For the PTFE containing variants, some of the recovered material was not suitable for size analysis as it had been crushed between the contact faces of the bars. This compacted material was removed so as not to be considered by the size analysis here. Some fragment mass was also lost during removal of residual lubricant from between the specimen and bar faces. For 100Al-5-F and 100Al-5-C specimens, fragments representing $\sim$82% and $\sim$50% of the original mass were analyzed, respectively. For 100PTFE-5-F and 100PTFE-5-C specimens, fragments representing $\sim$58% and $\sim$65% of the original mass were analyzed, respectively. For 25Al/75PTFE-5-F and 25Al/75PTFE-5-C specimens, fragments representing $\sim$67% and $\sim$78% of the original mass were analyzed, respectively.

Size analysis of the recovered fragments was performed using traditional sieve analysis and optical analysis of images from the scanning microscope. Only fragments $>$150 µm could be properly dispersed for scanning and optical analysis. Dispersal of fragments $<$150 µm was not optimal for analysis due to electrostatic charge build up from particle interactions during handling[254]. Compari-

son of size distributions from the optical and sieve analysis methods of fragments >150 µm revealed the optical analysis methods consistently returned mass-size distributions biased towards larger fragments. As an example of this behavior, distributions determined by the two methods are compared in Figure 7.16(a). The stitched microscope image used for optical analysis of the fragments is shown in Figure 7.16(b). These distributions are for Specimen 1 of the 100PTFE-5-C variant.

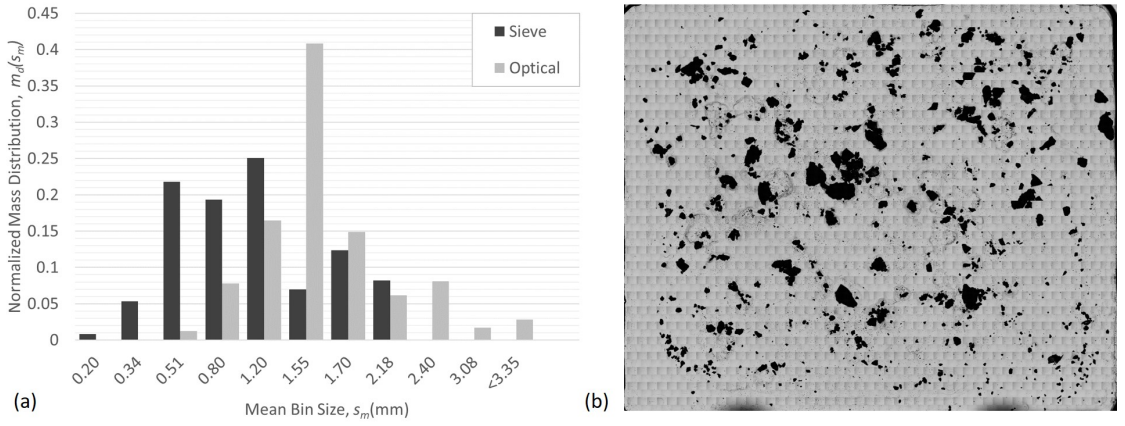

Figure 7.16: (a) Comparison of normalized mass-size distributions from the sieve and optical analysis methods for specimen 1 of the 100PTFE-5-C variant. (b) Stitched microscope image used for optical analysis of the fragments.

Some of the larger fragments (>2.4 mm) identified by the optical analysis methods can be attributed to insufficient segmentation of fragments in the image. However, this was not the case with fragments <2.4 mm. From Figure 7.16(a), the distribution mean for the optical method is ∼0.7 mm greater than the mean from the sieve analysis which is significant. In considering the non-spherical nature of the fragments seen in Figure 7.16(b), it is intuitive that this bias is associated with the equivalent spherical particle assumption used in transforming from a spatial based distribution to a mass based distribution. When comparing optical methods to sieve measurements of non-spherical particles, the error associated with the spatial to mass basis transformation using the equivalent spherical assumption has been shown to be minimal when analyzing particles on the order of 10^{-2} mm in size [242]. However, the results here indicate this is not the case when analyzing particles that range from 10^{-1} to 10^{0} mm which are common sizes in distributions of RM fragments[11, 12, 27, 180, 186]. As such, mass-size distributions from the sieve analysis are considered the best representation of the fragmentation behavior of the specimens and will be used going forward. Scanned images of specimen fragments <150 µm are included in Appendix C. This is for future works that may consider exploring alternative means to determine mass-size distributions from optical images of fragments. The fragment mass-size distributions for the 100Al, 100PTFE, and 25Al/75PTFE particle size

variants subjected to Kolsky bar compression tests are presented in Figure 7.17, Figure 7.18, and Figure 7.19, respectively.

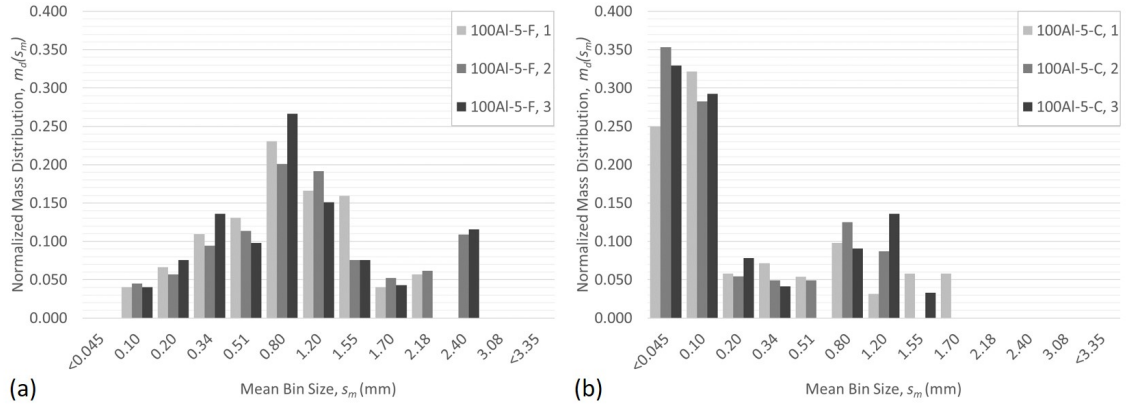

Figure 7.17: Normalized mass-size distributions of the fragments recovered from 100Al specimens subjected to Kolsky bar compression tests consisting of (a) fine particle powder and (b) coarse particle powder.

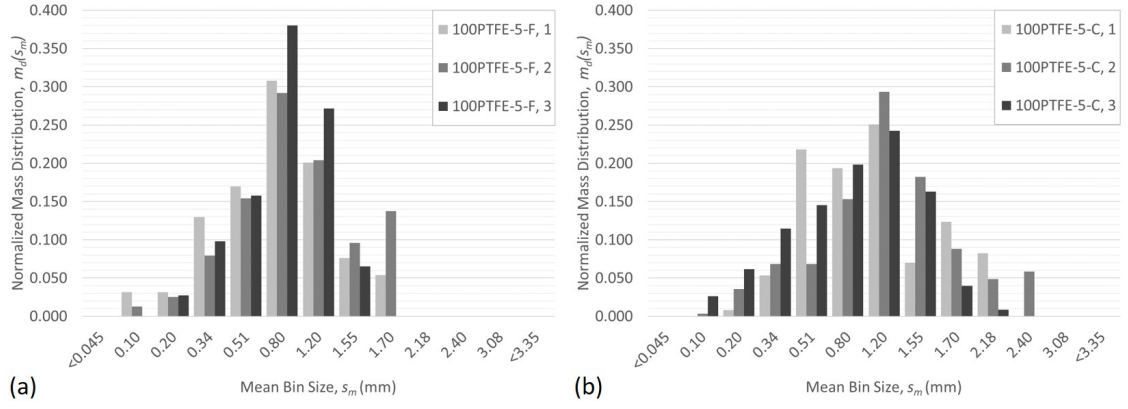

Figure 7.18: Normalized mass-size distributions of the fragments recovered from 100PTFE specimens subjected to Kolsky bar compression tests consisting of (a) fine particle powder and (b) coarse particle powder.

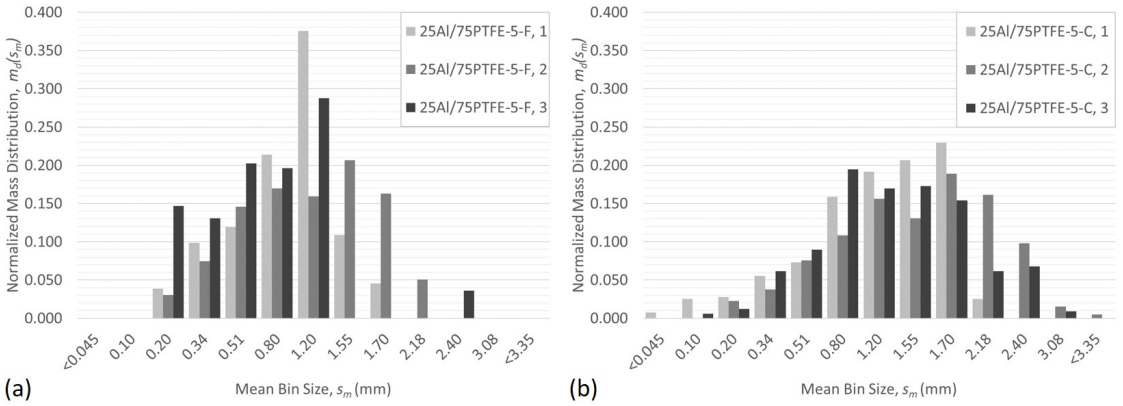

Figure 7.19: Normalized mass-size distributions of the fragments recovered from 25Al/75PTFE specimens subjected to Kolsky bar compression tests consisting of (a) fine particle constituents and (b) coarse particle constituents.

The mass-size distributions are reasonably consistent in shape and peak location across the three specimens of the variants. This consistency in the distributions aligns with the conformity of the quasi-static material properties measured here. This behavior is observed despite the dynamic nature of the fragmentation event and aligns with prior works that have shown the explosive driven fragmentation behavior of the Al/PTFE system to be repeatable and consistent[186, 190]. From the distributions, a distinct lack of fine fragments is apparent for all variants except 100Al-5-C. For all variants except 100Al-5-C, 80% of the fragment mass is typically between 0.3 mm and 1.7 mm. The fragment distributions of the 100Al-5-F, 100PTFE-5-F, 100PTFE-5-C, and 25Al/75PTFE-5-F variants could be reasonably described using a Weibull distribution function, which is a common distribution model used in describing fragment size distributions from fragmenting warheads[56]. The distributions of the 25Al/75PTFE-5-C variant is biased towards larger fragments, and could be reasonably described using a Beta type distribution[255]. These distribution behaviors are in contrast to impact[27] and explosive experiments[186] that typically see distributions exhibiting exponential and/or power-law type behavior. This difference is not unexpected given the strain rate for these tests is at least an order of magnitude less than what is typically seen in impact or explosive tests where the higher strain rates drive finer fragment production[27, 60].

The mass-size distributions of the 100Al-5-C specimens shown in Figure 7.17(b) demonstrate bi-model type behavior. The majority of the fragment mass is associated with fragments $<$0.2 mm, but a smaller secondary peak exists around 1 mm. The highest concentration of fragment mass is associated with fragments $<$0.045 mm, which is effectively the constituent particle size. The form of this distribution appears to be a combination of exponential and Weibull distribution behaviors.

The observed distribution behavior of the 100Al-5-C variant is in contrast to

the observations from the high speed footage where the 100Al-5-C variant appeared to produce larger fragments than the 100Al-5-F variant. The secondary peak does align with observations of large fragment production from the high-speed images, but the primary peak indicates the majority of the specimen failed into fragments near the constituent particle size. This fragmentation behavior could be a result of a core-shell structural behavior. Here the outer shell fails under tensile loading into the larger fragments observed in the high-speed images. Once the shell fails, the inner core of the material catastrophically disassembles into small fragments approaching the constituent powder size. This core-shell structural behavior likely stems from non-uniform compaction of the 100Al-5-C variant where the shell develops due to increased particle compaction at the powder-die surface interface[22].

It is important to discuss the potential effects of the missing fragment mass on these distributions. While the missing mass could influence the shape of the distribution, it would not decrease the amount of large fragments observed. In these tests, fragments were observed to eject from the enclosure through clearance openings for the incident and transmitted bars and underlying support structure of the Kolsky bar system. The demonstration of fine fragment recovery for 100Al-5-C would suggest the mass loss is not associated with ejection of fine fragments, but instead medium to large fragments. Recognizing the ejection of fragments should be a random statistical event, the corresponding fragment mass loss should have a randomly varying effect on the mass-size distributions. If the effects of this mass loss were significant, the distributions would be expected to display significant random variation. The lack of significant random variation, and thus consistency of these results, support that the mass-size distributions are representative of the fragmentation behavior of the specimens.

The general fragment mass-size distribution form proposed by Hooper[27] has shown good agreement to RM fragment distributions from high-velocity impact[11, 12, 27] and explosive tests[186]. While the application of the distribution form to RM fragment distributions from Kolsky bar tests has not been reported on in literature, the underlying principles that govern the derivation of the distribution form should not preclude it from application. Because this distribution form is used in describing the 100Al fragment distributions from high velocity impact tests discussed later in this chapter, it seems appropriate to assess the application of the distribution form to the 100Al fragment distributions here. For convenience, the Hooper distribution form previously discussed in Section 2.6 is repeated here[27]:

$$m_d(s) = \Pi \frac{1}{s_o}\left(\frac{s}{s_o}\right)^{-\Lambda} \frac{\exp(-(\beta s)^{\Psi})}{f_{exp}(\beta s_o)} + (1-\Pi)\frac{1}{6\mu_c}\left(\frac{s+2/\beta}{\mu_c}\right)^3 \exp\left[-\left(\frac{s+2/\beta}{\mu_c}\right)\right] \quad (7.22)$$

$$where: \Lambda = (2\Psi - (\Psi k_s + 1)) \quad (7.23)$$

A standard least-squares fit governed by the generalized reduced gradient algorithm is used to determine the following parameters: k_s, β, Π, and the exponential characteristic length, μ_c. These parameters are determined as the best fit to the distributions associated with the three specimens of a variant. Because of the large number of free-fitted parameters, it is necessary to impose value ranges to the parameters to guide the solver. Per literature observations of $k_s \approx 5/3 = 1.667$[27, 186], the permitted range for k_s is conservatively taken as $\pm$50% such that $0.83 < k_s < 2.5$. Per the assumptions employed in deriving the distribution (which are discussed in Chapter 1), the permitted ranges for Π is $0 < \Pi < 1$. Intergranular fracture can be expected for granular aluminum composites[11]. Therefore, it is intuitive that μ_c is restricted by the particle size of the constituents. Here that limit is taken as the D90 term for the constituent powders. For 100Al-5-F the limit is $\mu_c > 0.015$ mm. For 100Al-5-C the limit is $\mu_c > 0.038$ mm These parameters are determined as the best fit to all three distributions of a 100Al variant.

The resulting fit parameters are summarized in Table 7.17. The mean fragment size, s_{avg}, and D50 values are taken as simple characteristic length scales of the distributions that the parameters of the distributions can be compared too. These characteristic values are included in Table 7.17. The distribution fits are plotted alongside fragment distributions of the 100Al-5-F and 100Al-5-C variants in Figure 7.20.

Table 7.17: Distribution fit parameters determined for the 100Al-F and 100Al-C fragment distributions from Kolsky bar tests. The s_{avg} and D50 values are also reported as simple characteristic length scales of the distributions

Variant	Π	k_s	$1/\beta$	μ_c	s_{avg}	D50
			mm	mm	mm	mm
100Al-F	0.187	2.14	0.39	0.020	1.03	0.72
100Al-C	0.046	1.33	2.81	0.199	0.35	0.07

The distribution form proposed by Hooper[27] provides reasonable description of the fragmentation behavior for both 100Al variants. However, the peak of the distribution fit is biased towards smaller fragments compared to the peak of the measured 100Al-5-F distributions. Similarly, the secondary peak of the fitted distribution is biased towards smaller fragments compared to the measured secondary peak for the 100Al-5-C system. This bias towards smaller fragment sizes seems reasonable given the distribution form was intended to represent exponential and power-law type distribution behaviors where the bias of the distributions is towards smaller fragments.

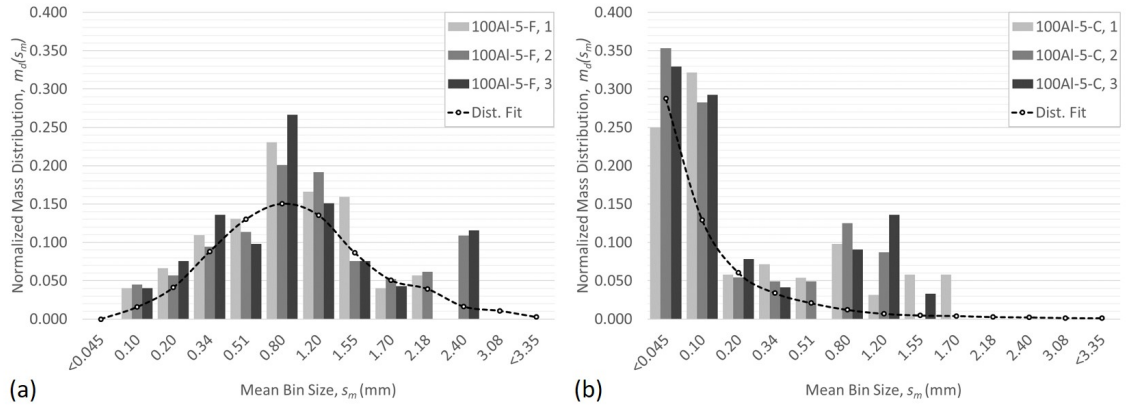

Figure 7.20: Distribution fit to normalized mass-size distributions of the fragments recovered from 100Al specimens subjected to Kolsky bar compression tests consisting of (a) fine particle powder and (b) coarse particle powder.

The determined parameter values appear to have little physical meaning. Here, the values of k_s deviate $\pm 30\%$ from the universal value of $k_s \approx 1.667$ suggested by others[27, 57, 58, 186]. Characteristic length scale values of the distributions, μ_c and $1/\beta$ do not appear to have physical meaning when compared to the characteristic length scales of the distribution, s_{avg} and D50. The characteristic length scales parameters also do not appear to align to any specific features of the distribution.

The evaluated distribution form was derived on physical principles to represent exponential and power-law type fragment distribution associated with high-velocity impacts[27]. Given the distributions here are from Kolsky bar compression tests and display limited exponential and/or power law behavior, it is not expected that the distribution form would provide physically meaningful parameters here. What is shown is that the distribution form is appropriately general enough to reasonably describe distributions outside the original use case for high-velocity impact tests. However, there is an implication of the observed generality of the distribution fit: the distribution form proposed by Hooper[27] can be forced to fit virtually any experimental distribution as a result of the number of free-fitting parameters[148]. In doing so the parameters can lose their physical meaning as observed here. Thus, predicting the parameters of the distribution is not possible for the 100Al distributions here.

Predictions of characteristic fragment sizes are made using the the analytical model discussed in Chapter 2. Predictions by minimizing energy of the dilating bulk (λ_{MEB}) are not included as the bulk wave speed of the materials is not able to be measured. For convenience, the applied analytical models are summarized in Table 7.18.

Table 7.18: Summary of analytical models used for predicting the nominal (characteristic) fragment size of for the Kolsky bar tests. Note that the λ_{MED} model corresponds to the Grady model

Approach	Equation
Minimizing Energy Density of Fragment	$\lambda_{MED} = \left(\frac{\sqrt{20}K_{IC}}{\sqrt{\rho E}\dot{\varepsilon}}\right)^{2/3}$
Minimizing Energy of Fragment	$\lambda_{MEF} = \left(\frac{4K_{IC}}{\sqrt{\rho E}\dot{\varepsilon}}\right)^{2/3}$

The models in Table 7.18 assume a tension driven fracture. The reported strain rates of the Kolsky bar tests in Table 7.16 are for axial compression. Therefore, it is necessary to estimate an equivalent tensile strain rate for use in these models. For cylindrical specimens the radial strain rate can be used, $\bar{\dot{\varepsilon}}_{vr}$, given by $\bar{\dot{\varepsilon}}_{vr} = V_{rad}/r_s$[12, 42]. V_{rad} is the radial expansion velocity of the cylinder and r_s the radius of the specimen. Estimates of V_{rad} are made from the high-speed images immediately prior to the specimen achieving peak stress and failing. The uncertainty of the radial velocity measurements is high due to the radial displacements being on the order of the spatial resolution of the HPV-X2 camera. However, these measurements provide reasonable estimates of the order of magnitude of the radial strain rate experienced by these specimens. The average radial strain rate for the 100PTFE and 25Al75PTFE variants was estimated as $1.5{\cdot}10^3$ s^{-1} and the average radial strain rate for the 100Al variants was estimated as $1.7{\cdot}10^3$ s^{-1}.

The calculated values of λ_{MED} and λ_{MEF} values are presented in Table 7.19. These values are calculated using fracture toughness and elastic modulus values determined for the average porosity of the specimen set using the porosity dependency function parameters in Table 7.19. Density for the variants is the average for the specimen set.

Table 7.19: Predictions of characteristic fragment sizes by the λ_{MED} and λ_{MEF} models. Fracture toughness, elastic modulus, density, and strain rate values used in the calculations are reported

Variant	p_{avg}	K_{IC}	E	ρ	$\dot{\varepsilon}$	λ_{MED}	λ_{MEF}
	%	MPa $m^{1/2}$	GPa	g/cm^3	10^3 s^{-1}	mm	mm
100Al-5-F	6	15.15	24.68	2.55	1.7	29.3	27.2
100Al-5-C	5	10.98	20.72	2.57	1.7	25.0	23.2
25Al/75PTFE-5-F	4	1.69	1.06	2.30	1.5	24.7	22.9
25Al/75PTFE-5-C	3	1.40	0.97	2.32	1.5	30.5	28.3
100PTFE-5-F	7	1.43	0.57	2.13	1.5	21.9	20.3
100PTFE-5-C	5	1.91	0.525	2.17	1.5	19.8	18.4

The predicted characteristic fragment sizes in Table 7.19 are greater than the specimen dimensions by an order of magnitude. However, this is not unusual as severe over prediction of characteristic fragment sizes by minimum energy state fragmentation models has been demonstrated elsewhere[42, 60, 63]. This behavior is indicative that the fragmentation is no longer driven purely by the kinetic energy associated with the expansion of the material. In some cases this can be the result of elastic strain energy participating in driving fracture at lower strain rates[63, 64]. As a result, the fragment size that corresponds to balancing the kinetic energy is larger than the actual fragment sizes as not all of the energy of the process has been accounted for[63]. As discussed in Section 2.2 and other works[42, 64] this behavior and the conditions for transition from kinetic energy only driven fragmentation are material and loading rate specific.

To assess if the elastic strain energy contribution resolves the discrepancies observed here, the minimum energy state of the fragment given by Equation 2.40 in Section 2.2 is used. Equation 2.40 is repeated here for convenience, but reformed to be a function of λ_{MEF} :

$$dE'_{FE}(\lambda_{MEF})/d\lambda_{MEF} = 0 = (\lambda_{MEF}/2)^3 + \frac{\sigma_y^2}{\rho\dot{\varepsilon}^2 E}(\lambda_{MEF}/2) - \frac{2K_{IC}^2}{\rho\dot{\varepsilon}^2 E} \tag{7.24}$$

Using the reformed version of Equation 2.40, the calculated characteristic fragment sizes of the variants, accounting for both kinetic energy and elastic

strain energy, are summarized in Table 7.20. The fracture toughness, elastic modulus, density, and strain rate values from Table 7.19 are used for these calculations. The yield strength of the variants is determined for the average porosity of the specimen set using the porosity dependency function parameters in Table 7.19. Density for the variants is the average for the specimen set.

Table 7.20: Predictions of characteristic fragment sizes, accounting for both kinetic energy and elastic strain energy, by the λ_{MEF} model. Fracture toughness, elastic modulus, yield strength, density, and strain rate values used in the calculations are reported

Variant	p_{avg}	K_{IC}	E	$\sigma_{c,y}$	ρ	$\dot{\varepsilon}$	λ_{MEF}
	%	MPa $m^{1/2}$	GPa	MPa	g/cm^3	10^3 s^{-1}	mm
100Al-5-F	6	15.15	24.68	179	2.55	1.7	9.5
100Al-5-C	5	10.98	20.72	116	2.57	1.7	9.1
25Al/75PTFE-5-F	4	1.69	1.06	11.4	2.30	1.5	10.1
25Al/75PTFE-5-C	3	1.40	0.97	11.4	2.32	1.5	13.0
100PTFE-5-F	7	1.43	0.57	18.4	2.13	1.5	8.2
100PTFE-5-C	5	1.91	0.53	13.8	2.17	1.5	7.9

Accounting for the elastic strain energy contribution to the fracture process is seen to improve the predictions to a degree, with the characteristic fragment sizes now the same order of magnitude as the specimen dimensions. However, these characteristic fragment size values are still non-physical as they are larger than the specimen dimensions. These predictions are not in line with the observed alignment of the analytical models to literature fragmentation data discussed in Chapter 2, and would suggest that there are additional factors influencing the fragmentation of these specimens. It is speculated these factors are related to uncharacterized defects associated with the heterogeneity of the material[42]. Defect size and distributions have been shown to have significant effects on the dynamic fragmentation of brittle materials[42, 109, 111]. However, exploring these effects are outside the scope of this work.

The dynamic response and fragmentation results from these Kolsky bar tests support several important observations regarding the dynamic fragmentation behavior of RM systems and predictive capabilities. The response of the variants

have been shown to be consistent both in the stress-strain response and fragmentation behavior under dynamic loading, inline with observations by other works of the Al/PTFE system[186, 190]. This is important as it indicates the material behavior is repeatable, and thus the concept of predicting behaviors possible. However, the general mass-size distribution form regularly used in RM studies[11, 12, 27, 186] cannot provide representation of the fragment distribution behavior observed here with parameters that have physical meaning. This would suggest the predictive capability using the general distribution form proposed by Hooper[27] is not possible for fragment size distributions that do not display exponential and/or power-law type behavior.

For these materials subjected to Kolsky bar compression tests, the fragmentation event is not purely kinetic energy driven. While accounting for the elastic strain energy contribution shifts the results closer to what was observed here experimentally, the characteristic fragment sizes were still larger than the specimens which is non-physical. Considering the alignment of the models to fragmentation data of heterogeneous and homogeneous materials in Chapter 2, it seems likely that defects associated with the heterogeneity of the materials here have a non-negligible role in influencing the fragmentation of these specimens at these strain rates. It is possible these observations are unique to the materials studied here; However, the similarities of these materials to other RM systems studied in literature would suggest the observed behavior is not exclusive to this work.

7.6 Fragmentation behavior observed in high velocity impact test

High velocity impact tests were used to explore the fragmentation behavior the RMs studied here at higher strain rates. Due to mechanical strength limits determined from quasi-static and Kolsky bar tests, the 100Al-5-F and 100Al-5-C variants were considered the only viable candidates for surviving the launch conditions of the 14 mm gun system.

High velocity launch tests were conducted to assess the post-launch condition of the 100Al specimens at the planned impact velocity of approximately 1 km/s. These tests were performed for two reasons: to assess the viability of the variants for high velocity impact tests, and to have knowledge of expected specimen condition post-launch. The latter was necessary as early testing in the vacuum environment showed exact specimen condition in flight could be partially obscured by the small fragments resulting from the stripping process. This was due to the lack of drag in the vacuum environment that normally decelerates the small particles causing them to fall behind the specimens when testing in gaseous atmospheres. These verification tests were conducted in air to ensure aerodynamic drag would decelerate residual small fragments typical of the stripping process. This ensured a clear view of the specimen condition could be obtained. Images typical of the specimen condition from these tests are shown in Figure 7.21.

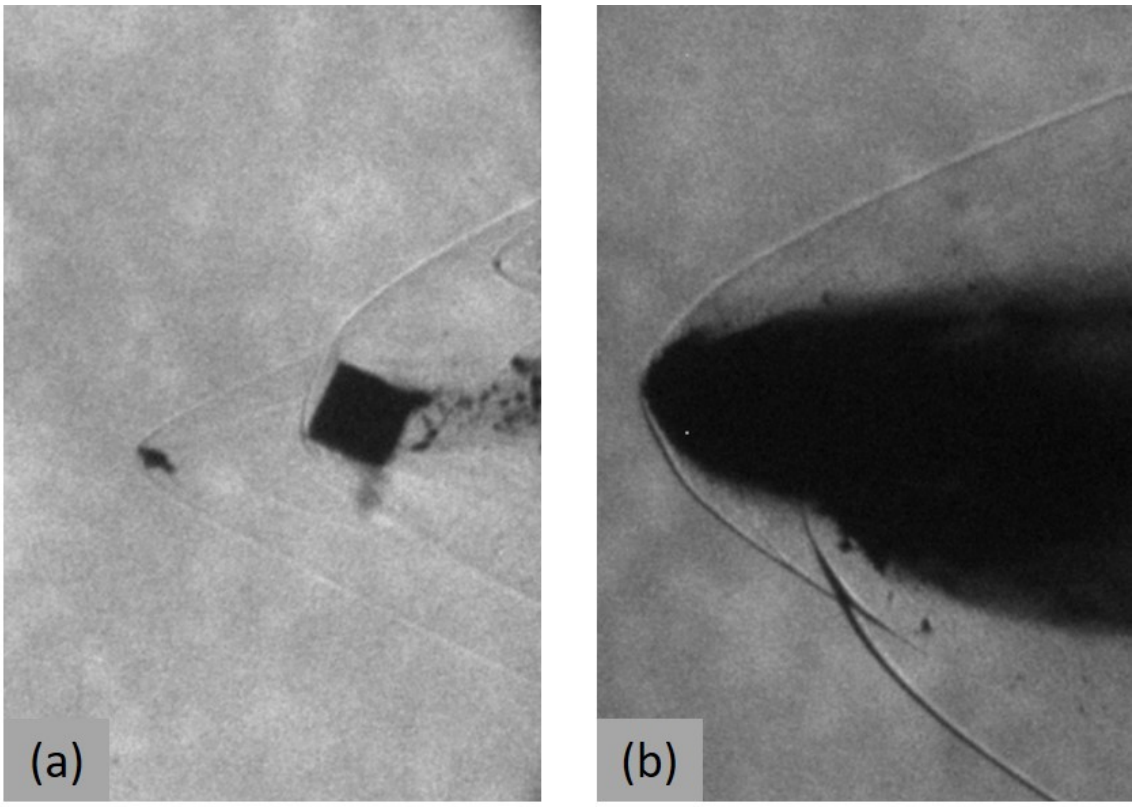

Figure 7.21: Example images of specimen conditions post-launch from the 14 mm gun of the (a) 100Al-5-F and (b) 100Al-5-C variants. Travel is right to left. Tilting of the specimens is due to the sabot stripping process.

The 100Al-5-F variant, as seen in Figure 7.21(a), is fully intact with some small fragment production as expected from the stripping process. This behavior was consistent over three tests providing confidence that the 100Al-5-F variant reliably survives launch from the 14 mm gun. However, the 100Al-5-C variant was observed to fail catastrophically when launched from the 14 mm gun as seen in Figure 7.21(b). This was the consistent behavior over three tests indicating the 100Al-5-C variant could not be reliably tested. Inspection of the nylon buffer revealed heavy aluminum powder deposits in the nylon for the 100Al-5-C tests, indicative of specimen failure from the high loading during launch. For reference, peak acceleration during acceleration in the 14 mm barrel is $1.51 \cdot 10^6$ m/s^2.

Three high velocity impact tests were performed with the 100Al-5-F specimens. For these tests, impact velocity was not able to be calculated from the high-speed footage due to insufficient frames clearly showing the specimen before impact. Instead, the velocity was calculated using the time of flight of the specimens between the muzzle end of the nylon arrestor in the sabot stripper and the target plate. This distance was measured to be 430 mm $\pm$4 mm. Time

of flight was determined as the time between the impact of the sabot with the nylon arrestor and the impact of the specimen with the target plate. The sabot impact with the nylon arrestor is determined from the resultant ringing in the sabot stripper measured using a PCB transducer. All data acquisition was triggered using the same signal so the transducer measurement and camera share the same zero time. with This method compared well to optical velocity measurements from the verification tests, with calculated velocities within 4% of the optical velocity measurements. Given the optical velocities measurements have a measurement uncertainty of 0.3%, the uncertainty of the velocity measurements here are conservatively taken as $\pm$ 5%.

These specimens were launched at an average velocity of 1080 m/s into 0.51 mm thick 1008 cold rolled steel target plates. These target plates were manufactured by Gardco (Part Number: PP-01-04x06) and have an average reported ultimate tensile strength of 380 MPa by the manufacturer. The specimen specifics and impact velocity are summarized in Table 7.21. Image sets from the SIM-X framing camera showing the impact and penetration event of Specimens 1, 2, and 3 are presented in Figures 7.22, 7.23, and 7.24, respectively. The first frame of each figure is the approximate time of impact for each test. The thin plate is observed as a vertical line and both the impact side and penetration side of the plate are imaged. The specimen can be observed on the impact side before impact and the fragmentation is observed on the penetration side.

Table 7.21: Summary of 100Al-5-F specimens and target plate impact velocity for high velocity impact tests

Variant	Specimen	p %	D_s mm	L_o mm	m_s g	V_{Im} m/s
Uncertainty		$\pm$1%	$\pm$0.02 mm	$\pm$0.02 mm	$\pm$0.001 g	$\pm$5%
100Al-5-F	1	6	6.33	6.22	0.501	1019
	2	5	6.32	6.33	0.513	1058
	3	6	6.33	6.32	0.507	1090

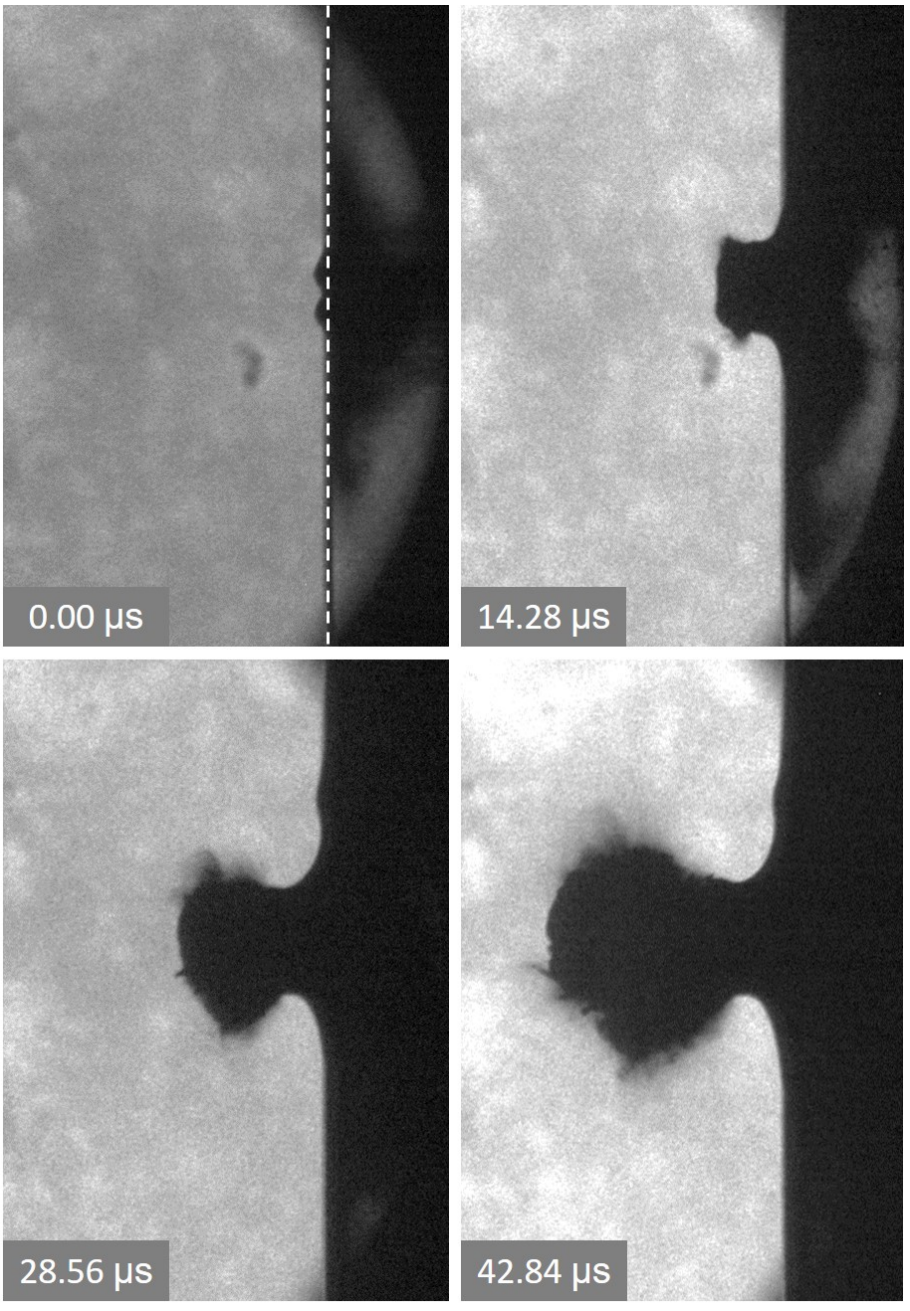

Figure 7.22: Image set from SIM-X framing camera of the impact event of Specimen 1 with travel from right to left. The target plate is indicated by a white dashed line. Interframe time is indicated to show temporal progression of event, with time 0.00 µs aligning with the image closest to impact. The specimen is observed to uniformly penetrate target and then radially fragment.

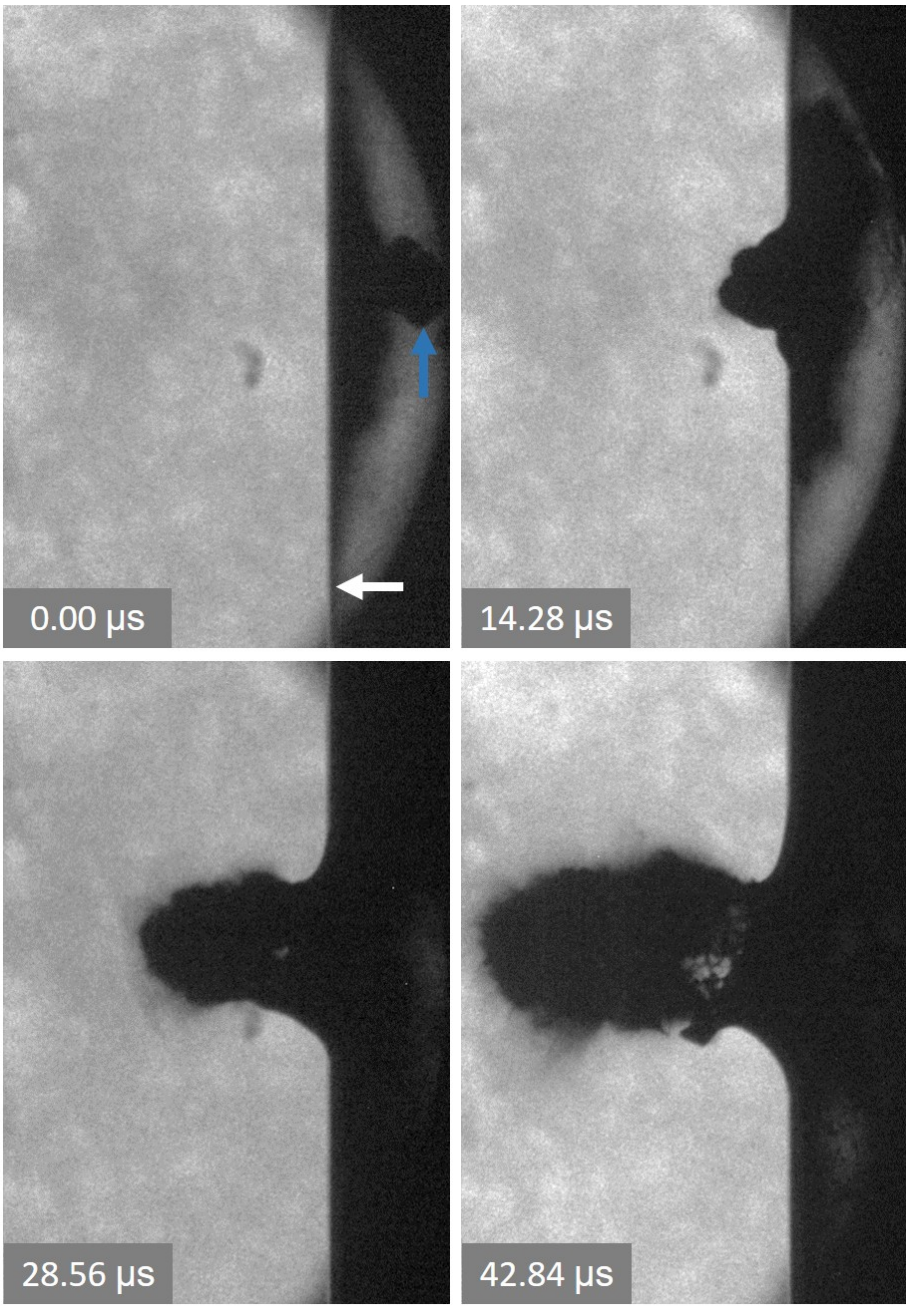

Figure 7.23: Image set from SIM-X framing camera of the impact event of Specimen 2 with travel from right to left. The target plate is indicated by a white arrow. Interframe time is indicated to show temporal progression of event, with time 0.00 µs aligning with the image closest to impact. The specimen is indicated by blue arrow, and is observed to impact target plate at an angle. This impact condition is reflected in the non-symmetrical penetration through the target.

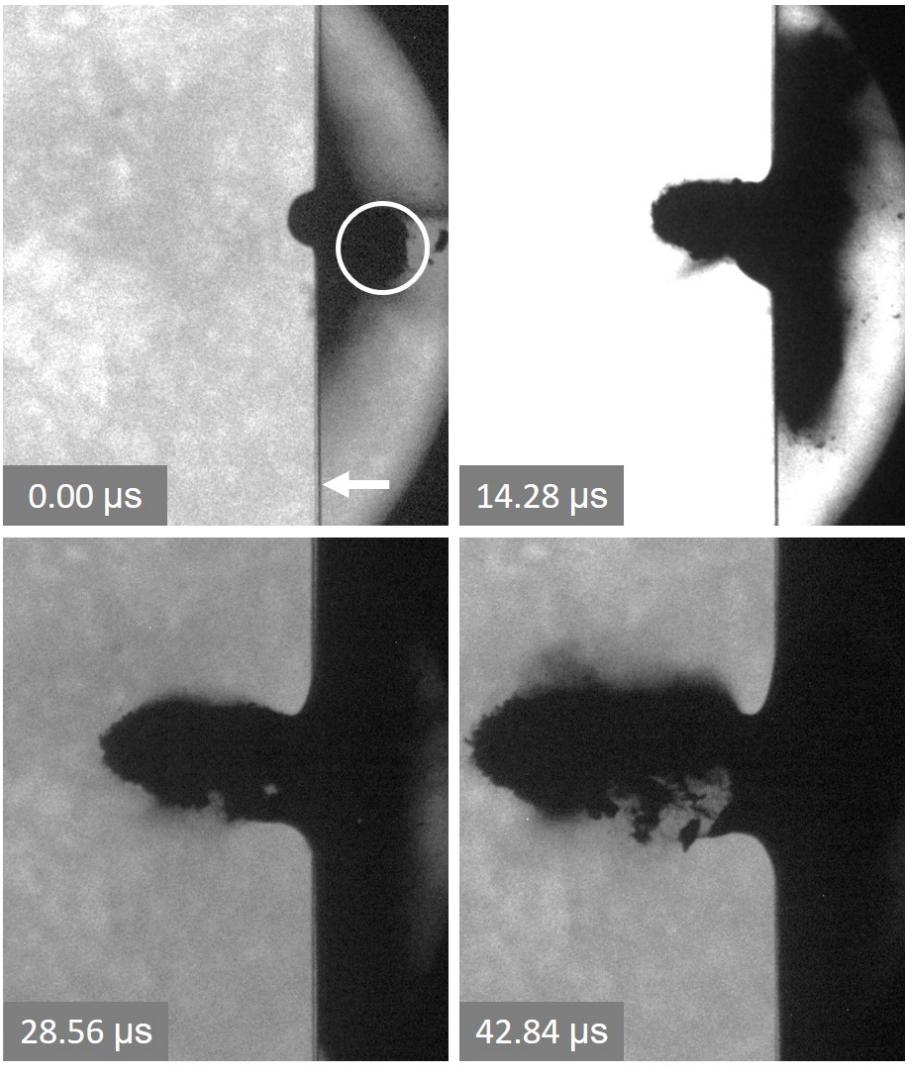

Figure 7.24: Image set from SIM-X framing camera of the impact event of Specimen 3 with travel from right to left. The target plate is indicated by white arrow. Interframe time is indicated to show temporal progression of event, with time 0.00 µs aligning with the image closest to impact. A large material piece is observed to trail the impact of the RM specimen and is circled. It is believed this is a piece of nylon that escaped the sabot stripper. Impact angle of the specimen is unclear, but is believed to be angled. Over exposure of the image at 14.28 µs was due to intensifier tube variation in the SIM-X camera.

An image was not captured of Specimen 1 prior to impact, but the penetration of Specimen 1 shown in Figure 7.25 indicates the specimen face was parallel to the target plate face at impact. At time 14.28 µs, the specimen has just penetrated the plate and is observed to be radially symmetric with a nominally flat face that is parallel to the target plate. The specimen has also started to fragment. Following the initial penetration of the plate at 14.28 µs, the specimen has fully failed and fragments of the specimen are observed to radially expand. This is typical behavior of thin plate penetration of cylindrical specimens with non-angular impact at high velocities[11, 12]. High fragment production on the impact side of the plate is observed during penetration of the target plate. By 28.56 µs after impact, the field of view on the impact side of the target plate has been obscured by fine fragment production.

Specimen 2 was observed to be at an angle right before impact as seen in Figure 7.26 at time 0.00 µs. The angle between the centerline of the specimen and the face of the target plate was estimated to be approximately 50°. This angled impact of the specimen is reflected in the non-symmetrical penetration of the plate observed at time 14.28 µs. By time 42.84 µs the fragment cloud has regained some symmetry as it expands after penetration of the plate.

An image was not captured of Specimen 3 prior to impact, but the similarities in fragment cloud evolution at times 28.56 µs and 42.84 µs in Figure 7.27 compared to the same times for Specimen 2 in Figure 7.26 suggest an angular impact was likely for Specimen 3. Angling of the specimens results from the sabot stripping process and as seen some specimens are affected while others are not. Figure 7.27 also reveals Specimen 3 was followed by a large material fragment during impact with the target plate at time 0.00 µs. This large material fragment impacts below the main penetration site of the RM specimen. This material piece is believed to be nylon from the sabot and/or arrestor that escaped the sabot stripping process. This is based on the lack of fine fragment production from the penetration of this material as seen at time 42.84 µs.

Image sets from the SIM-X framing camera are shown for the fragment cloud development after penetration of the target plates for Specimens 1, 2, and 3 in Figures 7.25, 7.26, and 7.27, respectively. Individual images in each of these series are the same as shown in Figures 7.25, 7.26, and 7.27, respectively. High fragment production is observed on the impact side of the plate for all specimens.

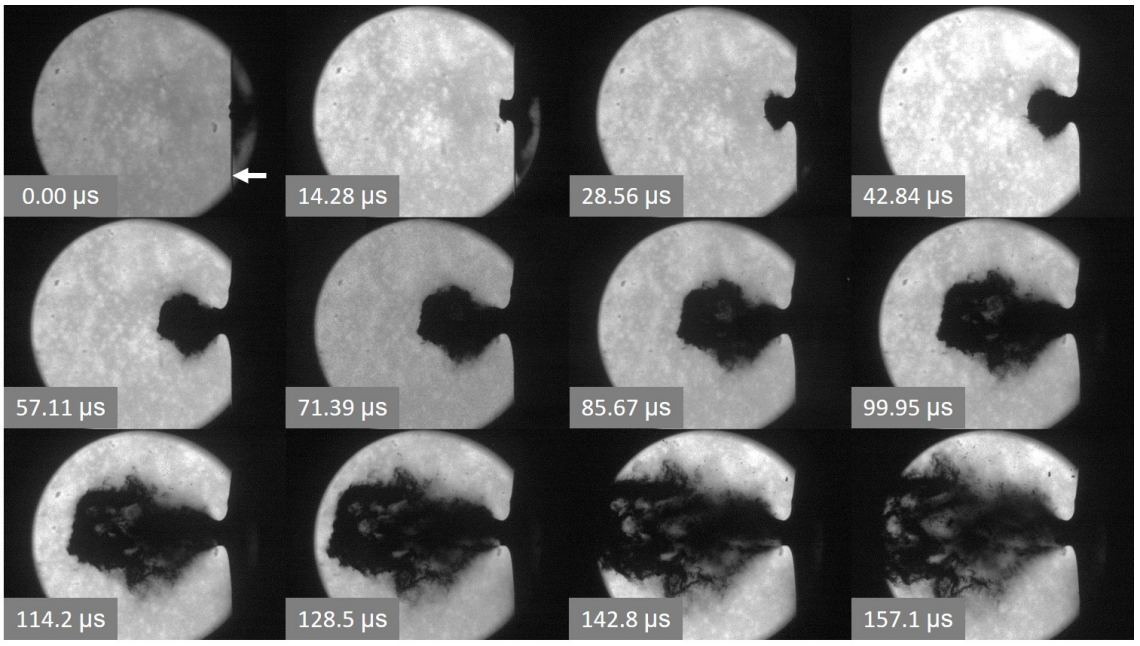

Figure 7.25: Evolution of the fragment cloud of Specimen 1 after penetration of the target plate with the travel of specimen from right to left. The target plate is indicated by the white arrow. The fragment cloud evolves to rectilinear in shape reflecting the specimen condition post-penetration.

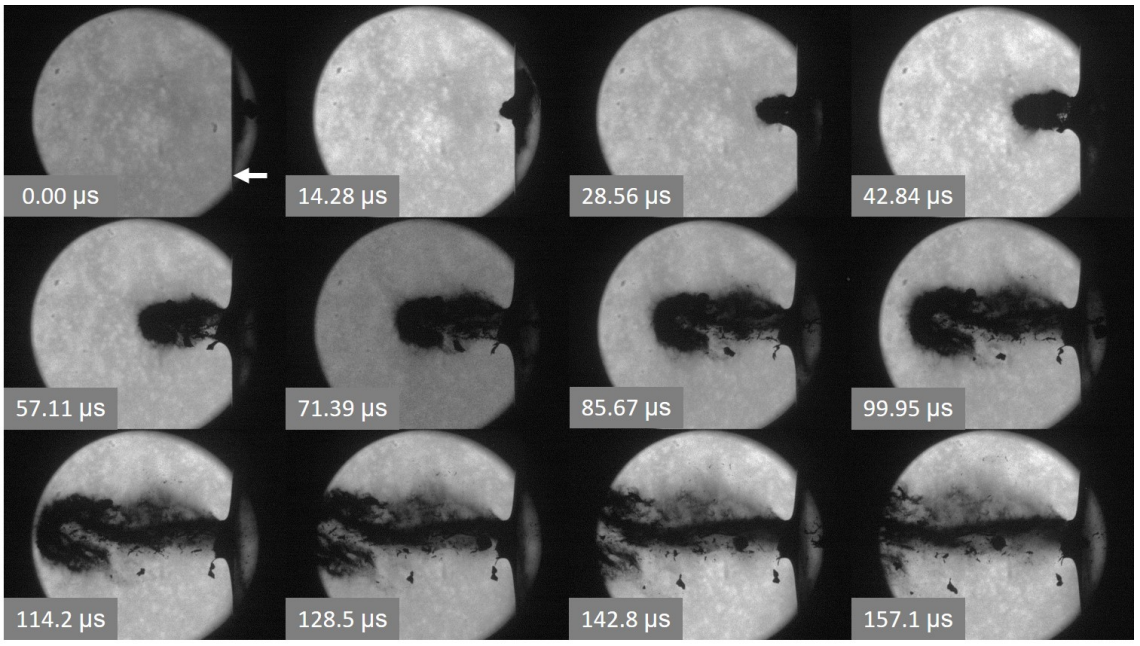

Figure 7.26: Evolution of the fragment cloud of Specimen 2 after penetration of the target plate with the travel of specimen from right to left. The target plate is indicated by the white arrow. The fragment cloud evolves to asymmetrical in shape reflecting the asymmetry of the penetration of the target by the specimen.

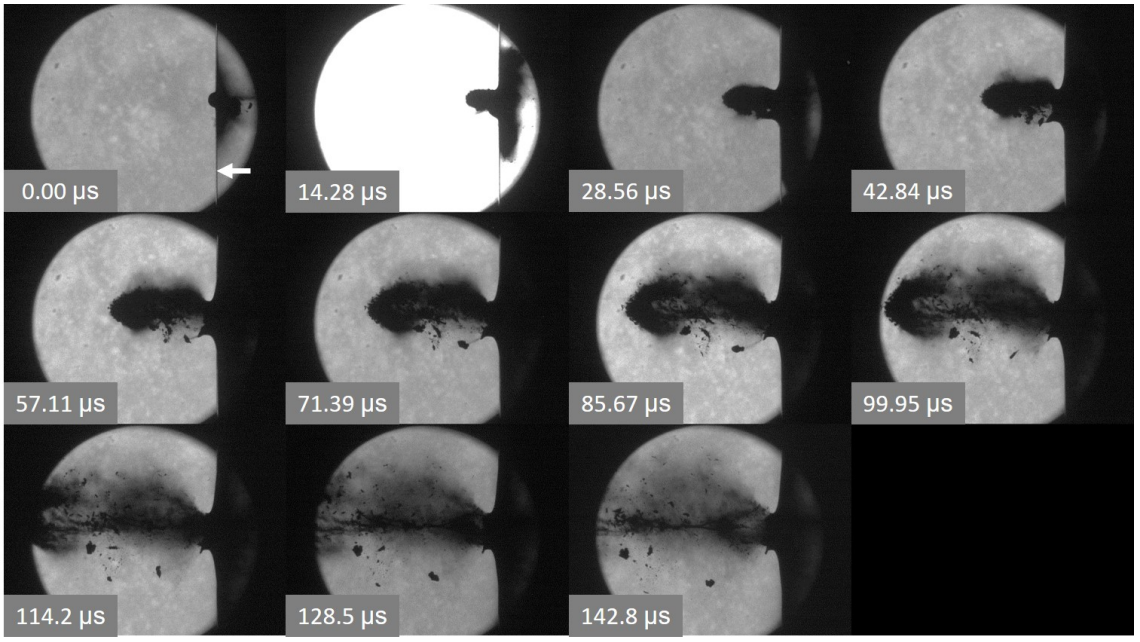

Figure 7.27: Evolution of the fragment cloud of Specimen 3 after penetration of the target plate with the travel of specimen from right to left. The target plate is indicated by blue arrow. The fragment cloud evolves to a reasonably symmetrical U-shape.

The evolution of the fragment clouds of the specimens display reasonable symmetry in expansion at early times. For Specimen 1 in Figure 7.25, the front of the fragment cloud is planar and has a rectilinear shape. Immediately after penetration of the plate, the radial expansion of the fragment cloud is observed to be reasonably symmetric. For Specimen 2 in Figure 7.26, the fragment cloud has symmetrical attributes as it expands after 25.56 μs, indicating reasonable symmetry in the radial expansion of the fragments after the penetration of the plate. However, by time 85.67 μs the fragment cloud has evolved into a distinct hook shape. For Specimen 3 in Figure 7.27, the fragment cloud has symmetrical attributes as it expands after 25.56 μs, indicating reasonable symmetry in the radial expansion of the fragments after the penetration of the plate. The front of the fragment cloud of Specimen 3 has clearly evolved into a reasonably symmetric U-shape by time 85.67 μs. This suggests the asymmetry of the impact of Specimen 3 was not as severe as Specimen 2, but was not a planar impact as with Specimen 1.

Radial expansion and residual velocity measurements were measured from the HPV-X2 high-speed images using the calculated displacement data from the phase correlation stitching routine. Based on the observations of the fragment cloud evolution after penetration, measurements of radial expansion velocity of the fragment cloud and residual velocity of the specimen bulk will begin immediately after penetration of the target plate by the specimens. Reported velocities will be determined as the average velocity calculated over eight frames from the HPV-X2. In the absence of drag forces, as is the case here, and at these time scales the measured velocities are essentially the same between frames. This is due to the lack of forces acting on the fragments that would normally decelerate them. Simple averaging of the measurements is taken to provide the best representation of the velocity of interest as some variation is inherent in the calculated displacement of the fragment cloud by the phase correlation routine. As an example, the HPV-X2 image set analyzed in determining the radial and residual velocity for Specimen 1 is shown in Figure 7.28. Because of the early time symmetry of the fragment cloud evolution, only a portion of the image is analyzed by the phase correlation routine for determining the displacement of the fragment cloud between frames. The interrogation window for the phase correlation routine is indicated in Figure 7.28.

Note that focal limitations of the auxiliary port on the SIM-X camera and lower resolution of the HPV-X2 camera reduces visible detail in the images. However, these images are well suited for radial expansion and residual velocity measurements as the edges of the fragment cloud are well defined and high temporal resolution exists for these images sets which were captured at 200,000 fps for Specimen 1 and 500,000 fps for Specimens 2 and 3. Similar sets of eight images were used to calculate the radial and residual velocities for Specimens 2 and 3. The calculated average residual and radial velocities for the specimens are presented in Table 7.22. These results compare well to velocities calculated by manual tracking of the fragment cloud boundaries.

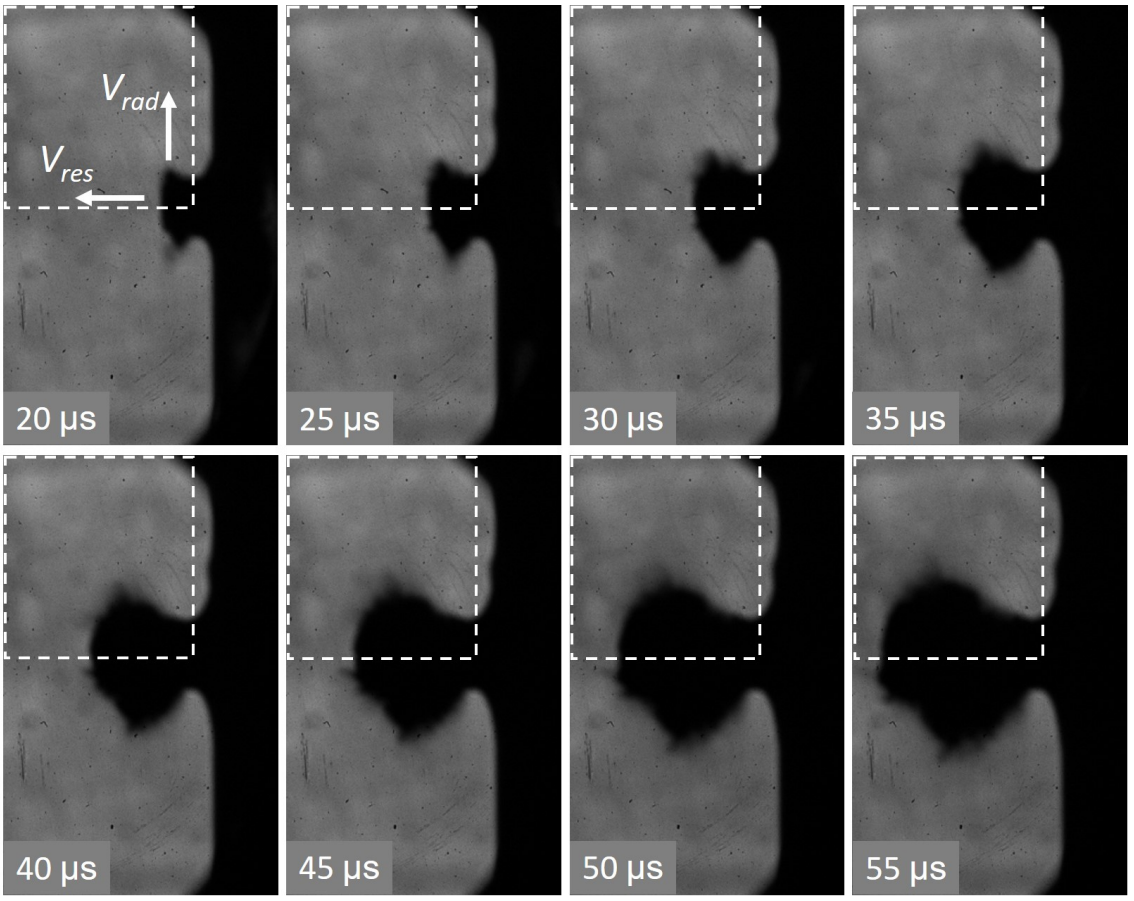

Figure 7.28: Image set from HPV-X2 used for radial and residual velocity measurements for Specimen 1. Dotted box indicates interrogation window for phase correlation routine. Directionality of the radial expansion velocity, V_{rad}, and residual velocity, V_{res}, are indicated.

Table 7.22: Calculated residual velocities, V_{res}, and radial expansion velocities, V_{rad}, for specimens subjected to high velocity impact. Impact velocity, V_{Im} is included for reference.

Variant	Specimen	V_{Im} m/s	V_{res} m/s	V_{rad} m/s
Uncertainty		±5%	±5%	±5%
100Al-5-F	1	1019	375	235
	2	1058	513	165
	3	1090	495	138

Estimates of average bulk strain rates of the specimens are calculated from

the measured velocities. The strain rate of interest for these tests is the radial strain rate associated with the expansion of the specimen due to the dynamic compressive load. Typically, the radial strain rate has been related to the longitudinal strain and estimated as a function of the difference in residual and impact velocities using $\bar{\dot{\varepsilon}}_{vir} = (V_{Im} - V_{res})/r_s$[12]. However, in this work the optical imaging permits radial expansion velocity of the fragment to be determined after penetration. In the absence of drag forces, as is the case here, conservation of momentum supports the radial expansion velocity of fragments as a reasonable approximation of the radial expansion rate of the body at onset of fracture. As with the Kolsky bar tests, the radial strain rate is a function of the radial expansion velocity and is given by $\bar{\dot{\varepsilon}}_{vr} = V_{rad}/r_s$. Using the velocities in Table 7.22 and specimen dimensions in Table 7.21, the calculated estimates of strain rates are reported in Table 7.23.

Table 7.23: Calculated average bulk strain rate for tests using the difference between impact and residual velocities, $\bar{\dot{\varepsilon}}_{vir}$, and alternatively the optically measured radial expansion velocity, $\bar{\dot{\varepsilon}}_{vr}$

Variant	Specimen	$\bar{\dot{\varepsilon}}_{vir}$ 10^5 s^{-1}	$\bar{\dot{\varepsilon}}_{vr}$ 10^4 s^{-1}
100Al-F	1	2.04	7.40
	2	1.72	5.20
	3	1.88	4.36

The approximation proposed by Tang and Hooper[12] for $\bar{\dot{\varepsilon}}_{vir}$ is on average 3.5 times higher than the actual radial strain rate, $\bar{\dot{\varepsilon}}_{vr}$, measured here optically. The generalized radial strain rate relation proposed in Section 3.5 is used to calculate the Poisson's ratio of the specimen that resolves the difference between the methods (i.e. the value of ν_{RM} that yields $\dot{\varepsilon}_{vir,g} = \bar{\dot{\varepsilon}}_{vr}$). For convenience, the relation is repeated here:

$$\bar{\dot{\varepsilon}}_{vir,g} = \nu_{RM} \frac{V_{Im} - V_{res}}{L_o} \tag{7.25}$$

For Specimens 1, 2, and 3, the Poisson's ratio that resolves the difference is 0.73, 0.6, 0.46, respectively. While these values of Poisson's ratio are less than 1 and approach 0.5, they are outside the expected bounds for linear elastic materials. However, this is not unexpected given the complexity of the impact event for which this simple relation is applied. This is the first known assessment of the relation proposed by Tang and Hooper[12] to estimates of radial strain rate calculated from direct measurements of the radial expansion rate. The relation proposed by Tang and Hooper is clearly not appropriate for the high velocity impact tests here. When direct estimates of radial strain are not possible, the generalized radial strain rate relation proposed in this work provides the correct

order of magnitude estimate of the radial strain rate assuming an incompressible material with a Poisson's ratio value of 0.5.

Optical size analysis was not performed on the high-speed images of the fragment clouds due to the dense clustering of the fragments. Fragments were recovered for these three tests using the snow soft catch and sieve analysis was used to measure mass-size distributions. For Specimen 1, only 50% of the specimen mass was recovered. For Specimen 2 and 3, 68% of the original specimen mass was recovered. Inspection of the soft catch after each test did not reveal any fragments missing the soft catch opening or impacting the soft catch tube walls. As such, the recovered fragment mass in the soft catch is believed to accurately represents the mass that passed through the target plate during penetration. From the high speed images in Figures 7.22, 7.23, and 7.24 showing penetration of the target plate by the specimens, high production of fine fragments was observed on the impact side of the plate. It is suspected the remainder of the specimen mass was ejected as fine fragments at the impact side of the target plate during penetration. Significant mass on the impact side of the target plate is not unusual and has been reported elsewhere[68] As with the size analysis of the fragments recovered from the Kolsky bar tests, optical size analysis of the scanned images of the specimen fragments did not compare favorably to the sieve analysis. As such, mass-size distributions from the sieve analysis are considered the best representation of the fragmentation behavior of the specimens and will be used going forward. Scanned images of specimen fragments $>$150 µm are included in Appendix C.

The general distribution form proposed by Hooper[27] is applied to the fragment distributions measured here for high velocity impact. A standard least-squares fit governed by the generalized reduced gradient algorithm is used to determine the following parameters: k_s, β, Π, and the exponential characteristic length, μ_c. These parameters are determined as the general best fit to the three distributions of the specimens. As with the size analysis of the fragments from the Kolsky compression tests, the same value ranges of the parameters are imposed to guide the solver: $0.83< k_s <2.5$; $0< \Pi <1$; and $\mu_c > 0.015$ mm. The resulting fit parameters are summarized in Table 7.24. s_{avg} and D50 values are included as simple comparable characteristic length scales of the distributions. The measured size distributions and distribution fit are presented in Figure 7.29.

The normalized mass-size distributions are remarkably consistent despite the differences in orientation of specimens at impact and the total recovered fragment mass between the specimens. Notably, the distributions for Specimens 2 and 3 are very similar in their characteristic sizes of their distributions as seen in Table 7.24. The characteristic sizes of the distribution of Specimen 1 are slightly higher than those for Specimens 2 and 3 due to the small number of fragments associated with the 1.70 mm size range. However, production of fragments below 1.55 mm in size is consistent for all specimens. The similarities in the distributions suggest insensitivity of the fragmentation behavior to impact angle. This is likely due to the differences in spatial scales between the specimen geometry, impact orientation of the specimens, and the strain rates associated with these events.

Table 7.24: Summary of parameters that represent a general distribution fit to the fragment mass-size distributions of the three specimens subjected to high velocity impact tests. Characteristics sizes of the distributions are reported

Specimen	s_{avg}	D50	General Fit Parameters			
			Π	k_s	$1/\beta$	μ_c
	mm	mm			mm	mm
1	0.45	0.17				
2	0.25	0.13	0	-	0.714	0.218
3	0.26	0.14				

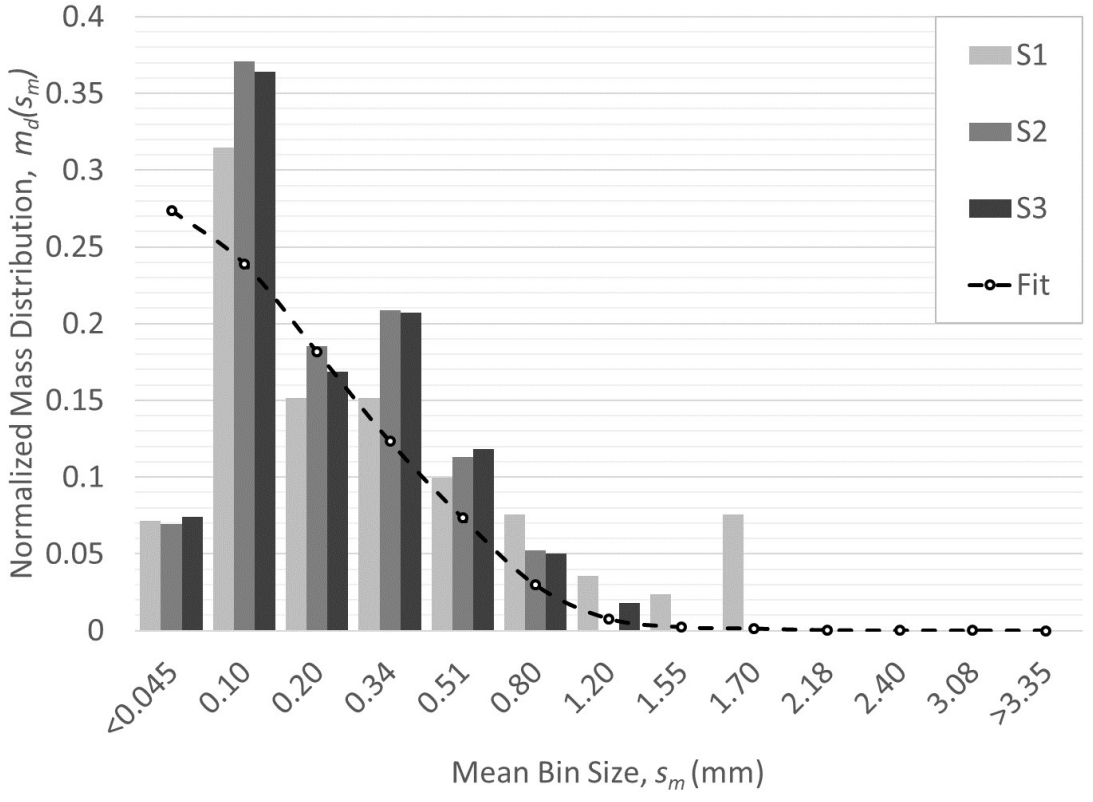

Figure 7.29: Normalized mass-size distributions of the fragments recovered from the 100Al specimens subjected to high velocity impact tests. Distribution fit for each specimen is also plotted.

Without comparisons to additional mass-size distributions of specimens impacting the target face-on, a specific conclusion regarding these differences cannot be

drawn as they may simply result from the natural variation in the fragmentation process.

From the distribution fit parameters, the mass-size distributions of the specimens are represented by exponential distribution behavior ($\Pi = 0$). The distribution form defaulting to an exponential form suggests that there should be higher production of fine fragments less than 0.045 mm in size. From the distribution fit, up to 30% of the fragment mass could be associated with fragments less than 0.045 mm in size. The lack of observed fragments less than 0.045 mm in size is likely associated with the mass loss at the impact side of the target plate during penetration.

The characteristic length scale describing the power law behavior, $1/\beta$, does not appear to align to any physical characteristic of the distributions by itself, which seems reasonable given the predominantly exponential distribution of fragment sizes. Because no power-law behavior is represented by the distribution fit β simply becomes a free-fitting parameter that aligns with the general length scales of the distributions. The value of the exponential characteristic length, μ_c, aligns to s_{avg} of the distributions for Specimen 2 and Specimen 3 and aligns closer to the D50 value for Specimen 1. As predominately exponential behavior is observed for the three specimens, μ_c aligning to physical characteristics of the distributions is reasonable. Using the fracture toughness and elastic modulus values of the 100Al-5-F variant from Table 7.20, the specimen specifics in Table 7.21, and calculated radial strain rate in Table 7.23 the calculated values of λ_{MED} and λ_{MEF} are summarized in Table 7.25.

Table 7.25: Predictions of characteristic fragment sizes by the λ_{MED} and λ_{MEF} models for the fragmentation of 100Al-5-F specimens subjected to high-velocity impact tests. Fracture toughness, elastic modulus, density, and strain rate values used in the calculations are reported

Variant	p_{avg}	K_{IC}	E	ρ	$\dot{\varepsilon}$	λ_{MED}	λ_{MEF}
	%	MPa $m^{1/2}$	GPa	g/cm^3	10^4 s^{-1}	mm	mm
1	6	15.15	24.68	2.55	7.4	2.37	2.20
2	5	16.29	26.57	2.57	5.2	3.06	2.84
3	6	15.15	24.68	2.54	4.4	3.35	3.11

The predicted characteristic fragment sizes in Table 7.25 are smaller than the specimen dimensions indicating they are physically possible, but are an order of magnitude larger than the characteristic length scales of the measured fragment distributions. This discrepancy seems unlikely to be resolved by accounting for

elastic strain energy. This is because the elastic strain energy is unlikely to be a contributing factor to the fracture process given the strain rates observed in these tests[63, 64] and evaluation of energy contributions to the fracture process in Section 2.2 using Weimer and Rodgers' fragmentation data[115].

Interestingly, if the estimate of $K_f = 1$ MPa m$^{1/2}$ regularly reported in literature[5, 11, 27] is used, the kinetic energy only predictions of a characteristic fragment size fall between the values of $1/\beta$ and μ_c of the fitted distributions. This may be coincidental, but could be an indication of heterogenity effects reducing the ability of the material to resist fracture under dynamic loading. As with the fragmentation results from the Kolsky bar experiments, it is speculated these effects are related to the defects associated with the heterogeneity of the material[42]. As such, minimization of energy methods cannot solely resolve the characteristic length scales of the fragmentation behavior here.

The observed exponential type distribution behavior of these high velocity impact tests is significant. This exponential dominant behavior has been observed for the 25Al/75PTFE systems of the same mean particle size, porosity, and specimen size subjected to explosive loading with similar order of magnitude in strain rate[186]. This indicates the exponential behavior is not uncommon at these strain rates or for materials with similar microstructure characteristics as well as differing composition. However, prior work using the distribution form has reported power-law dominate behavior for fragment distributions of similar Al RM specimens subjected to strain rates on the order of 10^4 s^{-1} using impact tests[11].

These impact tests by Kline and Hooper[11] used Al specimens that were 10 mm diameter cylinders manufactured from Valimet H-2 aluminum powder which has a volumetric size distribution similar to that of the Al-100 used for the 100Al-5-F specimens. The specimens had 6% porosity, a $K_{IC} \approx 0.6$ MPa m$^{1/2}$ measured using three-point bend tests, and elastic modulus of 58 GPa calculated from measurements of dilatational and shear wave speeds. Reported characteristic length scales of the distributions were $>$1 mm; an order of magnitude difference in scale compared to the length scales of the distributions here. This discrepancy is counter intuitive given the order of magnitude smaller K_{IC} value and higher elastic modulus than the measured values in this work. From the λ_{MED} and λ_{MEF} minimum energy models, the length scale of the characteristic fragment sizes observed by Kline and Hooper should be an order of magnitude smaller and of the same length scale as observed for the distributions here. This suggests the reported fracture toughness and elastic modulus do not align with the actual material properties of the Al specimens studied by Kline and Hooper.

There are several potential explanations for the differences between the fragmentation behavior observed here and that observed by Kline and Hooper[11]. Differences in the fragmentation behavior could be associated with variation in the heterogeneity of the granular materials as a result of potential differences in morphology of the constituent powder particles. This could result in variations in defects[42] and particle cohesion[106] between the granular Al composite studied here and the Al composite studied by Kline and Hooper[11].

Alternatively, geometrical scaling of the dynamic fragmentation process could also be a factor. The concept of geometrical scaling effects in dynamic fragmentation processes was briefly explored by Grady[256]. Grady reported that fracture driven failure of ductile materials have shown dependencies on the length scale of the fragmenting system (e.g. specimen length scale). Similar studies for granular materials are not known. However, a similar order of magnitude difference between specimen length scale and characteristic fragment length scale is observed here and in the work by Kline and Hooper[11]. While this could be coincidental, it may indicate a scaling behavior of the dynamic fragmentation process exists for the Al RM system. Exploration of these effects and potential influence on the fragmentation behavior of RM systems is warranted by future works.

CHAPTER 8

MEASUREMENTS OF ENERGY RELEASE AND EVALUATION OF THEORETICAL PREDICTIONS

Bomb calorimetry tests were performed on the stoichiometric composition of 22.6Al/77.4PTFE nd near stoichiometric composition of 25Al/75PTFE. The near stoichiometric condition corresponds to the 25Al75PTFE composition evaluated in Chapter 7. The mass fractions of these compositions are reported in Section 6.1. Bomb Calorimeter tests were attempted for the 100Al composition in air and the Fe_2O_3 compositions, but these compositions could not be ignited using a hot wire ignition method. For the 100Al, the hot wire would melt before reaching a temperature sufficient enough to cause the powder to react with the air. For the Fe_2O_3 compositions, charring of the powder was observed where the hot wire was in contact with the powder, but no bulk ignition could be obtained.

Vented calorimetry tests were only performed on the 100Al-5-F variant. All of the 25Al/75PTFE variants were determined to have insufficient strength to survive the loading during launch by the 14 mm gun. Similarly, the 100Al course particle size variants and 100Al-20-F variant did not have sufficient strength to survive launch. For the compositions subjected to bomb calorimetry, no porosity or particle size designation are given as only loose fine particle powders were tested. The final list of evaluated compositional variants and applied experimental methods is presented in Table 8.1.

Table 8.1: Summary of evaluated composition variants and applied experimental methods for evaluation of energy release behavior

Evaluated Compositional Variants	Applied Experimental Methods
25Al/75PTFE 22.6Al/77.4PTFE	Bomb Calorimetry (Sec. 5.1)
100Al-5-F	Vented Calorimetry (Sec. 5.2)

8.1 Bomb calorimetry measurements of total energy release

Challenges arose in attempting to ignite the powdered Al/PTFE compositions. Initial trials revealed that the standard 0.25 mm (30 gauge) nichrome wire used by the Parr 6200 system did not provide sufficient heating duration to ignite the Al/PTFE powder. The capacitive discharge ignition system of the Parr 6200 would burn out the 0.25 mm wire before the powder could ignite. An alternative solution was developed using a 0.82 mm (20 gauge) nichrome wire shaped into a coil. An image of this coil is shown in Figure 8.1(a). The stainless crucible containing the sample powder was installed beneath the coil with the coil in contact with the powder. An image of the coil in the powder is shown in Figure 8.1(b). An ohmmeter was used to ensure the coil was not in contact with the conductive crucible.

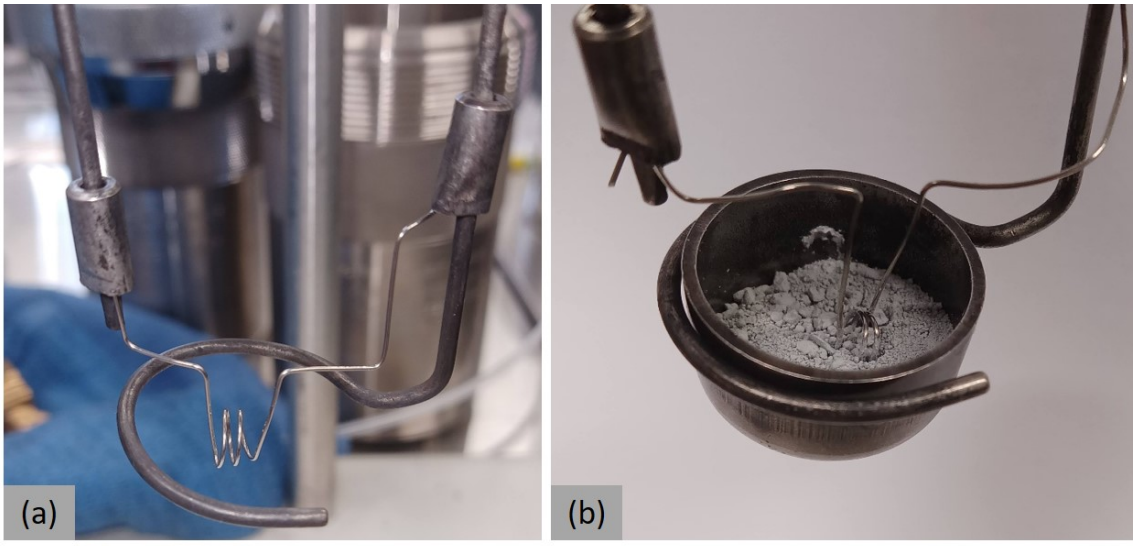

Figure 8.1: Hot wire set up for igniting the powders in the Parr 1108 bombs.(a)0.82 mm nichrome wire coil installed on the wire posts of the 1108 lid. (b) Coil in place in the powder sample after installation of stainless crucible.

To heat the coil, an external power supply was used rather than the ignition system of the Parr 6200. Typical peak voltage and current applied was 6 V at 6.5 A, respectively. To conduct a test, the Parr 6200 automated test procedures were initiated and power supplied to the coil on the audible alert from the Parr 6200 signaling the system was preparing to fire the capacitive ignition system. Typical time from application of power to ignition of the powder was approximately 8 s. Upon ignition, the hot combustion products from the Al/PTFE reaction would melt the hot wire, stopping any additional energy input from the hot wire. The exact voltage and current applied to the coil was recorded to calculate the electrical energy input into the coil up to ignition of the powder. The energy used to heat the wire also heats the system and is subtracted from the reported

energy measurement by the Parr 6200. For these tests, the average energy input was 350 J. For all tests, mass of the recovered remnants of the original wire were within 2 mg of the original wire mass. Therefore, any interaction of the nichrome with the reaction of the Al/PTFE is believed to be negligible.

Thirteen bomb calorimetry tests were performed across the two compositions. A total of 10 calorimetry tests were performed on the 22.6Al/77.4PTFE stoichiometric composition and three calorimetry tests were performed on the 25Al/75PTFE composition. All tests were conducted in an argon environment at 85 kPa absolute pressure and 293 K. These conditions corresponding to the atmospheric conditions at the time of testing. In addition to the energy release measurements, internal pressure measurements of the Parr 1108 bomb were made for select tests. These pressure measurements are all reported as gauge pressure. These measurements were: peak pressure, P_p, residual pressure at thermal equilibrium , P_r, (as indicated by the Parr 6200), and internal bomb pressure as a function of time for 100 s (at 1400 samples per second). The measurement uncertainty of these pressure results is $\pm$3.4 kPa.

The residual pressure in the bomb after the tests was small, with an average value of 10 kPa for all tests. Measurements of residual pressure were taken approximately 10 minutes after the combustion of the specimen. The change in enthalpy of the system is given by $\Delta H = \Delta U + (\forall dP)_{cb}$ as discussed in Section 5.1. For the 0.342 L volume of the Parr 1108 bombs this residual pressure corresponds to a value of $(\forall dP)_{cb}$ = 3.4$\pm$1.1 J. The energy associated with this change in pressure of the bomb is less than the measurement uncertainty of the energy release measurements. As such, it is considered negligible for the results here and $\Delta H = \Delta U$. The final energy release measurements are summarized in Table 8.2. The individual pressure measurements are also summarized in Table 8.2 and pressure responses for select tests are shown in Figure 8.2.

Table 8.2: Energy release (ΔH), peak pressure (P_p), and residual pressure (P_r) measurements of the combustion of the 22.6Al/77.4PTFE (stoichiometric) and 25Al/75PTFE (near-stoichiometric) compositions from bomb calorimetry tests. All pressures are reported as gauge pressure

Composition	Test Number	Sample Mass g	ΔH kJ/g	P_p kPa	P_r kPa
Uncertainty:		0.001g	0.1%	4 kPa	4 kPa
22.6Al/77.4PTFE	1	1.049	7.55	413	-
	2	1.050	7.67	495	-
	3	1.052	7.66	485	-
	4	1.004	7.93	-	-
	5	1.001	7.63	-	-
	6	1.052	7.80	-	-
	7	1.05	7.75	-	-
	8	1.000	7.69	532	7
	9	1.000	7.70	498	10
	10	0.999	7.89	633	10
25Al/75PTFE	1	1.001	7.71	517	13
	2	1.000	7.88	-	-
	3	0.999	8.07	495	10

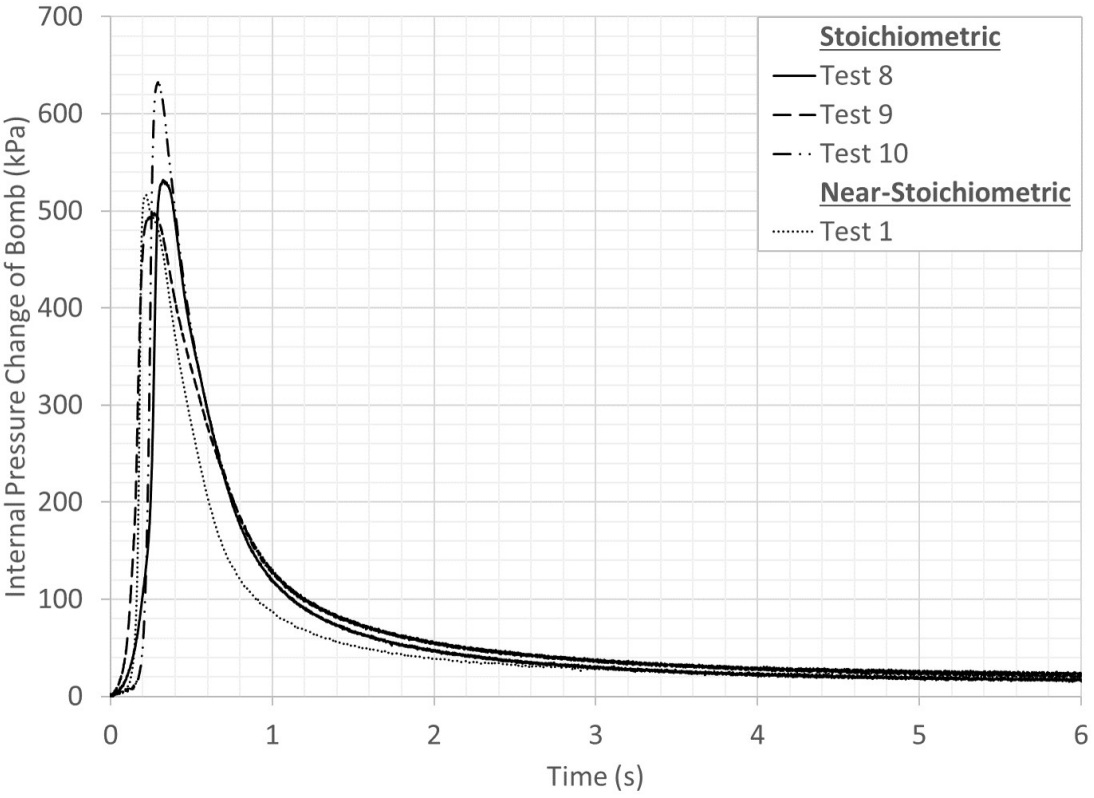

Figure 8.2: Internal pressure change of the bomb for Tests 8, 9, and 10 of the 22.6Al/77.4PTFE composition (Stoichiometric) and Test 1 for the 25Al/75PTFE composition (Near-Stoichiometric). The start of the pressure trace aligns with the breaking of the hot wire associated with the ignition of the Al/PTFE Powder. Only 6 s of the 100 s pressure trace is plotted here.

The measured energy release and pressure responses of the compositions are consistent. As seen in Figure 8.2, peak pressure for the compositions is obtained between 100 ms and 200 ms after ignition of the powder. The internal pressure of the bomb decays to 90% of the peak pressure after 2 seconds. The remainder of the pressure decay to the final residual pressure is over a 10 minute period as the interior of the Parr 1108 bomb comes to thermal equilibrium with the Parr 6200 system. The low residual pressure values reported in Table 8.2 are indicative of minimal gas phase products at thermal equilibrium. Thus, at thermal equilibrium with the environment controlled by the Parr 6200, condensed phase reaction products are expected for the Al/PTFE compositions evaluated here. This is not unexpected based on observations from prior works[79, 257] and aligns with the heavy soot formation observed on the inside of the bomb as shown in Figure 8.3.

Figure 8.3: Soot formation in Parr 1108 bomb resulting from the Al/PTFE reaction.

From the energy release results in Table 8.2, the total energy release for the stoichiometric composition 22.6Al/77.4PTFE is 7.40$\pm$0.05 kJ/g. The total energy release for the near-stoichiometric composition 25Al/75PTFE is 7.89$\pm$0.25 kJ/g. Note that the statistical uncertainty given by the DIM method is reported here.

The near-stoichiometric composition has a slightly higher energy release, even when considering the statistical uncertainty of the measurement. Higher energy release associated with a slightly-fuel rich condition is a known real world behavior in other combustion systems[258] and is typically associated with increasing molecular dissociation as the stoichiometric condition is approached due to elevated temperatures. Based on the slight differences in energy release observed here, this behavior appears to extend to the multi-phase combustion of the Al/PTFE compositions studied here.

Comparison of these results to other works is limited. This is due to the lack of studies that have specifically investigated the energy release of the stochiometric reaction of Al/PTFE in an inert atmosphere using bomb calorimetry. Xiao et al.[257] explored the energy release of the stoichiometric Al/PTFE composition in air[257]. Unsurprisingly, higher energy release of 10.65 kJ/g is reported due to the carbon reaction with the oxygen in the air[257]. The results here are believed to be the first reported experimental values of the total energy release of the stoichiometric reaction of Al/PTFE with no interaction with the surrounding atmosphere.

The pressure measurements of the interior of the combustion bomb permit a comparison between the bomb calorimetry measurements and Ames' methodology for calculating energy release from pressure measurements[68]. For convenience, the governing energy balance derived by Ames[68] and discussed in Section 5.2 is repeated here as Equation 8.1. Because bomb calorimtry is a closed system, $dm_{vc}/dt = 0$, reducing the second half of Equation 8.1 to zero.

$$\frac{dQ_{vc}}{dt} = \frac{\forall_{vc}}{\gamma - 1}\frac{\partial P_{vc}}{\partial t} + 0 \tag{8.1}$$

Ames[68] also proposed a simplified equation assuming the combustion reaction of a RM is complete by the time the peak quasi-static pressure is obtained. For convenience, this form discussed in Section 5.2 is repeated here as Equation 8.2.

$$\Delta Q_{vc} = \frac{\Delta P_{vc}\forall_{vc}}{\gamma - 1} \tag{8.2}$$

For these bomb calorimetry tests $\forall_{vc}$ =3.42·10^{-4} m^3 and γ =1.66. Applying Equation 8.1 to the measured pressure histories for Tests 8, 9, and 10 yields an intuitive result for the three cases: $\Delta Q_{vc} \approx 0$. This corresponds to the fact that $\frac{\partial P_{vc}}{\partial t} > 0$ until the peak pressure condition is obtained. For times after the peak pressure condition, the pressure is declining and as such $\frac{\partial P_{vc}}{\partial t} < 0$. Because the pressure of the interior of the bomb approaches the nominal starting pressure by 100 s, $\Delta Q_{vc} \approx 0$.

For this system, there are two competing energy flows: the heat released into the bomb from the reaction of Al/PTFE, Q_R; and the heat loss through heat transfer to the bomb walls, Q_W. For times when $\frac{\partial P_{vc}}{\partial t} > 0$, $Q_R > Q_W$. Conversely, when

$\frac{\partial P_{vc}}{\partial t} < 0$, $Q_R < Q_W$. The implication of this is that the reaction may continue to release energy into the bomb, but that release is not reflected by an increase in pressure. This behavior was addressed by Ames[68]. However, for Ames the primary source of energy loss from the working fluid corresponded to the mass loss from the venting process of the calorimeter. Here, the primary source of energy loss corresponds to heat transfer to the bomb walls. Without characterization of the heat transfer rate to the bomb walls, application of Equation 8.1 has limited use here.

Alternatively, using Equation 8.2 yields an average energy release for Tests 8, 9, and 10 of 0.287 kJ/g. This is equivalent to the energy released from 4% of the sample mass used in the bomb calorimeter tests here. This indicates that either the remainder of the energy from the reaction is associated with the times when $\frac{\partial P_{vc}}{\partial t} < 0$ which cannot be characterized here, or the governing assumptions of the methodology by Ames[68] have been violated.

Work by Xiao et al.[257] would suggest both; in their study, Xiao et al. investigated the energy release characteristics of Al/PTFE combustion in a closed vessel containing air as the working fluid. While not a direct analog to this work, some important insights can be gained in comparing results. Xiao et al.[257] observed temperatures greater than 1000 K at the peak pressure condition using transient pyrometry. Work by Zhang et al.[71] showed that the Al/PTFE reaction is still reacting at temperatures greater than 1000 K, but Xiao et al.[257] pyrometry measurements suggest the reaction is near completion. As such, it is reasonable to expect some additional energy release from the Al/PTFE reaction after the peak pressure. Xiao et al.[257] calculated energy release from the pressure measurements in a manner similar to the methodology by Ames[68]. These calculations were compared to the total internal energy change of the system determined from measurements of the chamber temperature. At peak pressure the calculated energy using the pressure measurement corresponded to approximately 75% of the total energy release measured for the reaction. However, precipitation of condensed product species in the working fluid during the time leading up to the peak pressure condition were estimated to retain 18% of the the total energy released in addition to the approximately 75% calculated from the pressure measurement. This

Xiao et al.[257] used a chamber with a volume 26 times that of the Parr 1108 volume here, but used 10 g of Al/PTFE instead of the 1 g here. Comparing the ratio of the chamber volume to sample mass ratio, the chamber used by Xiao et al. was 2.5 times the volume to mass ratio for these bomb calorimeter tests. It is expected the effects of precipitation of solid phase products would be more significant for the results here given the reduced proportional difference between the chamber and sample mass. While it is likely the Al/PTFE reaction continues past the peak pressure condition, it seems unlikely that 96% of the energy is released after the peak pressure condition based on the results by Xiao et al.[257]. Given the large amount of soot formation observed here, it seems reasonable to conclude that the primary source of error associated with results from Equation 8.2 is with the precipitation of solid phase products from the reaction that absorb

energy instead of the argon working fluid.

These comparisons and subsequent discussion are not to be taken as a repudiation of the methodology by Ames[68], but instead a demonstration of the limits of the methodology. These results, in combination with Xiao et al.[257] results, indicate that interaction of the reaction products with the working fluid can have significant effects that lead to non-representative calculations of energy release using the simple thermodynamic theory applied by Ames[68]. This is because the presence of both gas phase products and finely dispersed solid phase products in the working fluid creates a mixture with a mass and thermodynamic response that differs from what is assumed. Xiao et al.[257] showed that increasing the volume to specimen mass ratio reduces the error associated with the reaction products interacting with the working fluid. This is logical as there is a higher proportion of working fluid to reaction products, thus reducing the dilution of the working fluid. These effects and imposing limitations have not been explored in literature.

8.2 Predicted energy release of the Al/PTFE compositional space

The phase compliant equilibrium solver was used to explore the energy release associated with the global equilibrium state (heat of combustion) and adiabatic flame temperature of a portion of the Al/PTFE compositional space under inert atmospheric conditions at 101 kPa absolute pressure and 298 K. The assembled phase compliant thermodynamic data set used by the solver contains 18 species, of which 12 were gas phase and 6 were condensed phase. The selection of these species was based on elemental availability dictated by the Al/PTFE system and availability of thermodynamic data. The considered gas phase species were: Al, AlF, AlF_2, AlF_3, C_2F_4, C_2F_2, CF, CF_2, CF_3, CF_4, F, F_2. The condensed phase species were: Al(L), AlF_3(s). Al_4C_3(s), C_2F_4n(s), C(s). The phase compliant thermodynamic data set used here is provided in Appendix D. The phase compliant equilibrium solver MATLAB script is provided in Appendix E.

Phase compliant equilibrium solutions were determined for Al/PTFE mixtures containing between 10% and 45% Al. These equilibrium solutions were for the fixed HP condition, which corresponds to the unconstrained reaction of the Al/PTFE system. For these solutions convergence errors reported by the solver were less than 1%. Phase compliant solutions for Al/PTFE mixtures containing less than 10% and greater than 45% Al could not be determined. This was due to continuity and energy conservation constraints that could not be satisfied by the solver with the 18 species considered. This suggests additional species must be considered to resolve reactions associated with the compositional ranges outside 10% and greater than 45% Al by mass. The determination of what these additional species are was not possible here due to lack of available research that has explored product species in the range. Predicted adiabatic flame temperature and the corresponding product species that represent 99% of the total product species by mole fraction are presented in Figure 8.4. The heat of combustion and

corresponding product species that represent 99% of the total product species by mole fraction for the global equilibrium state are presented in Figure 8.5.

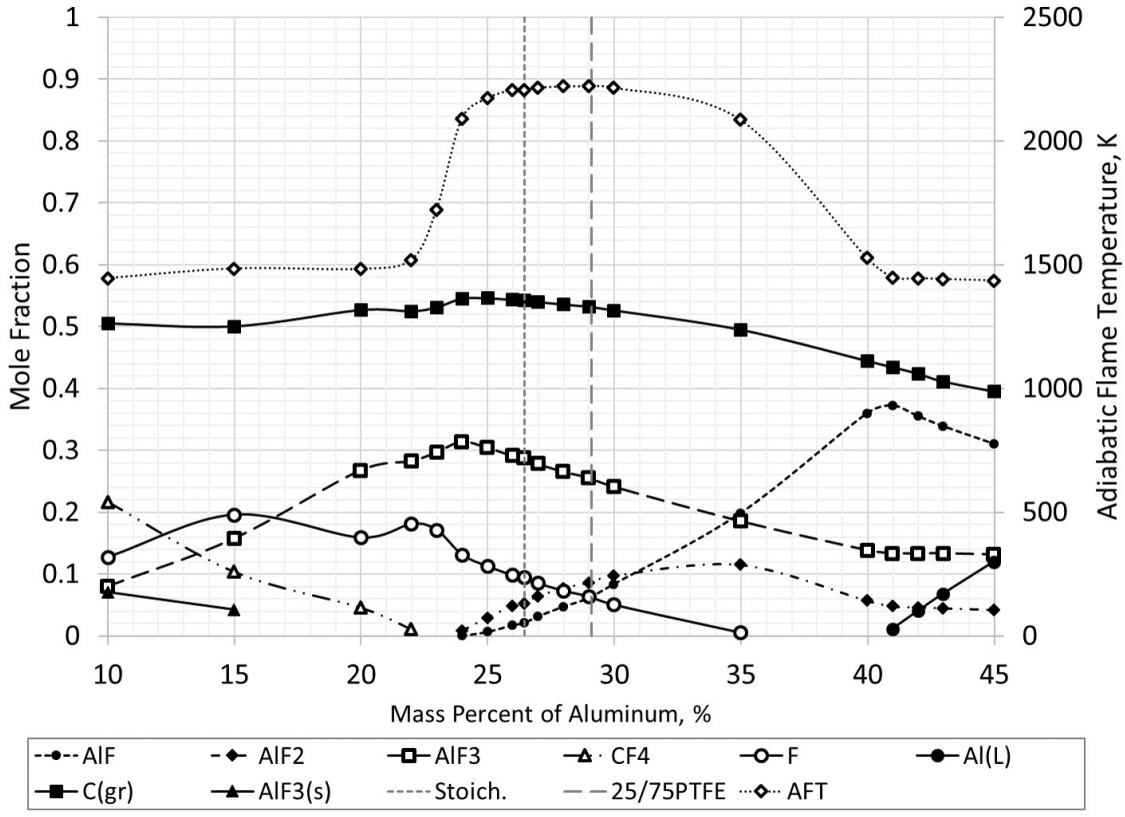

Figure 8.4: Phase compliant predictions of adiabatic flame temperature (AFT) and equilibrium reaction products for a portion of the Al/PTFE compositional space. The reaction products shown represent 99% of the product species by mole fraction. The stoichiometric and near-stoichiometric compositions evaluated using bomb calorimetry are indicated by dashed vertical lines. Markers indicate specific compositions evaluated by the solver.

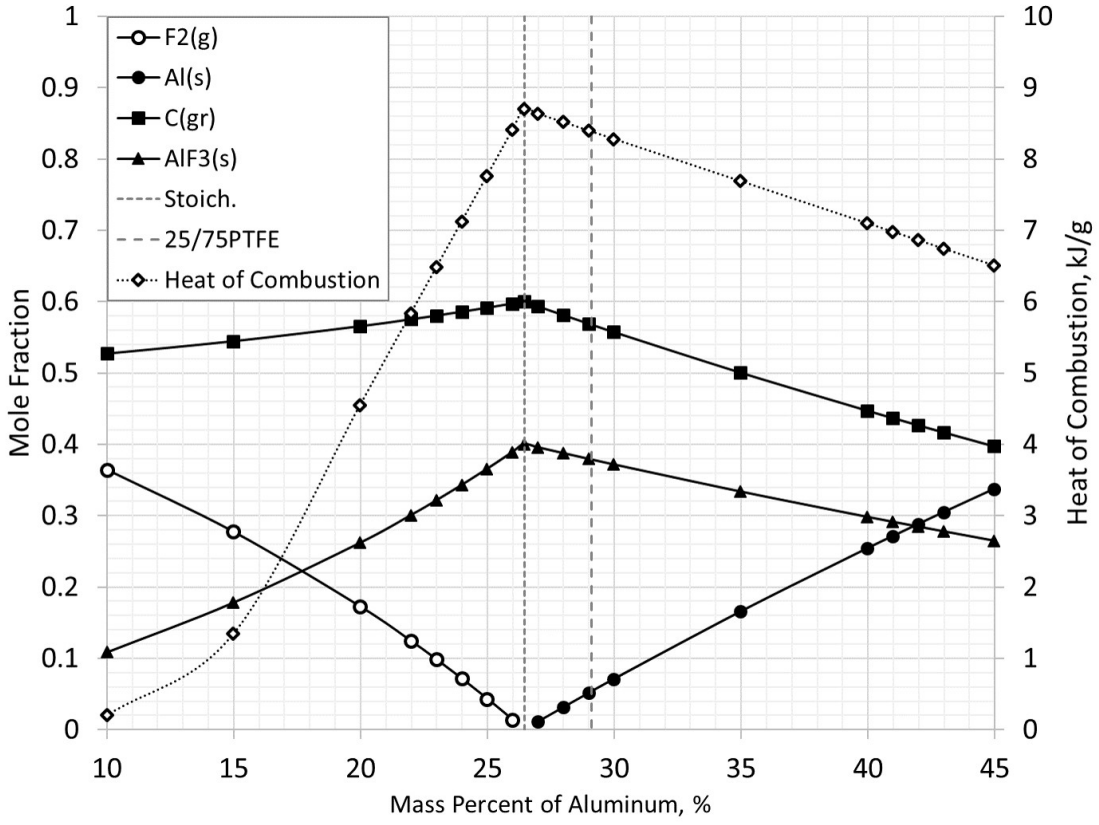

Figure 8.5: Phase compliant predictions of heat of combustion and equilibrium reaction products at the global equilibrium state for a portion of the Al/PTFE compositional space. The reaction products shown represent 99% of the product species by mole fraction. The stoichiometric and near-stoichiometric compositions evaluated using bomb calorimetry are indicated by dashed vertical lines. Markers indicate specific compositions evaluated by the solver.

Figure 8.4 reveals that reaction products at the adiabatic flame temperature condition are largely gas phase aluimnum-flouride compounds except for solid carbon which is the most prevalent product species. Mole fractions of solid carbon range between 0.4 and 0.55. Carbon being the most prevalent product species aligns with observations of high soot formation in the bomb calorimetry results. Critical assessment of the importance of phase compliancy is limited due to the lack of phase transitions near the adiabatic flame temperature condition. However, phase compliancy is upheld indicating these results are physically viable.

The predicted adiabatic flame temperature behavior aligns with predictions by Koch[67]. Peak adiabatic flame temperature was calculated to be 2220 K, occurring for the fuel rich composition containing 28% Al by mass. This aligns with the peak location predicted by Koch, but is nearly 1300K lower than the temperature Koch predicted using CEA. This is a reflection of the use of the

thermodynamic data for PTFE here. The predicted adibatic flame temperature by the phase compliant equilibrium solver for the stoichiometric mixture compares well to 2300 K reported in literature for the mixture using pyrometry measurements[257]. The pyrometry measurements were performed on Al/PTFE combusting in air and are expected to be slightly higher due to the carbon reaction with the air[257].

Figure 8.5 showing the global equilibrium state reveals the product species are condensed except F_2 which forms under lean conditions. This aligns with the low residual pressure observed in the combustion bomb after testing. The heat of combustion for the Al/PTFE system is predicted to peak at 8.7 kJ/g for the stoichiometric composition. The heat of combustion peaking for the stoichiometric condition deviates from the higher energy release measured for the fuel rich 25Al/75PTFE composition, although the peak at 26.4% Al by mass is about 2.5% lower than the mass percentage of Al in the 25Al/75PTFE. This difference is considered negligible given the reduced level of complexity considered by the solver compared to the real world combustion behavior of Al/PTFE. While the fixed UV equilibrium condition represents the early time reaction in the combustion bomb, comparison of the fixed HP equilibrium predictions to the bomb calorimetry measurements is considered appropriate as the pressure measurements of the interior of the bomb indicated negligible pressure change at thermal equilibrium. The predicted heat of combustion for the stoichiometric Al/PTFE composition is 18% higher than the measured energy release of 7.4$\pm$0.05 kJ/g from the bomb calorimtry tests.

Acknowledging the likely error associated with using graphite thermodynamic data to approximate the carbon/soot reaction products[216, 217] and the complexities of multiphase reactions, alignment of the predictions here to the experimental measurements is considered satisfactory. This supports that the predictions presented here are reasonably representative of the equilibrium, adiabatic flame temperature, and energy release of the Al/PTFE compositional space.

8.3 Vented calorimetry measurements of impact driven combustion

Vented calorimetry tests were used to measure the energy release from the impact driven reaction of 100Al-5-F specimens. These tests involved launching the specimens directly into a steel anvil at approximately 1 km/s in air. For these tests a no target plate on the front of the calorimeter was used. Instead the specimen passed through a 25.4 mm hole to impact the anvil directly. This ensured the mass entering the vented calorimeter was known and combusting fragments were produced directly from the specimen due to impact with the anvil. The specimen specifics and impact velocities are summarized in Table 8.3. Two vented calorimeter tests were successfully conducted with specimens that were intact at impact. The vented calorimeter was filled with air at 85.4 kPa absolute pressure and 293 K for these tests. These conditions correspond to the atmopsheric conditions during these tests. Image sets from the SIM-X framing camera

showing the impact and fragmentation events of Specimens 1 and 2 are presented in Figures 8.6 and 8.7, respectively.

Table 8.3: Specifics of the 100Al-5-F specimens for vented calorimetry tests

Variant	Specimen	p %	D_s mm	L_o mm	m_s g	V_{Im} m/s
Uncertainty		±1%	±0.02 mm	±0.02 mm	±0.001 g	±5%
100Al-5-F	1	6	6.33	6.38	0.513	1044
	2	6	6.33	6.29	0.503	1095

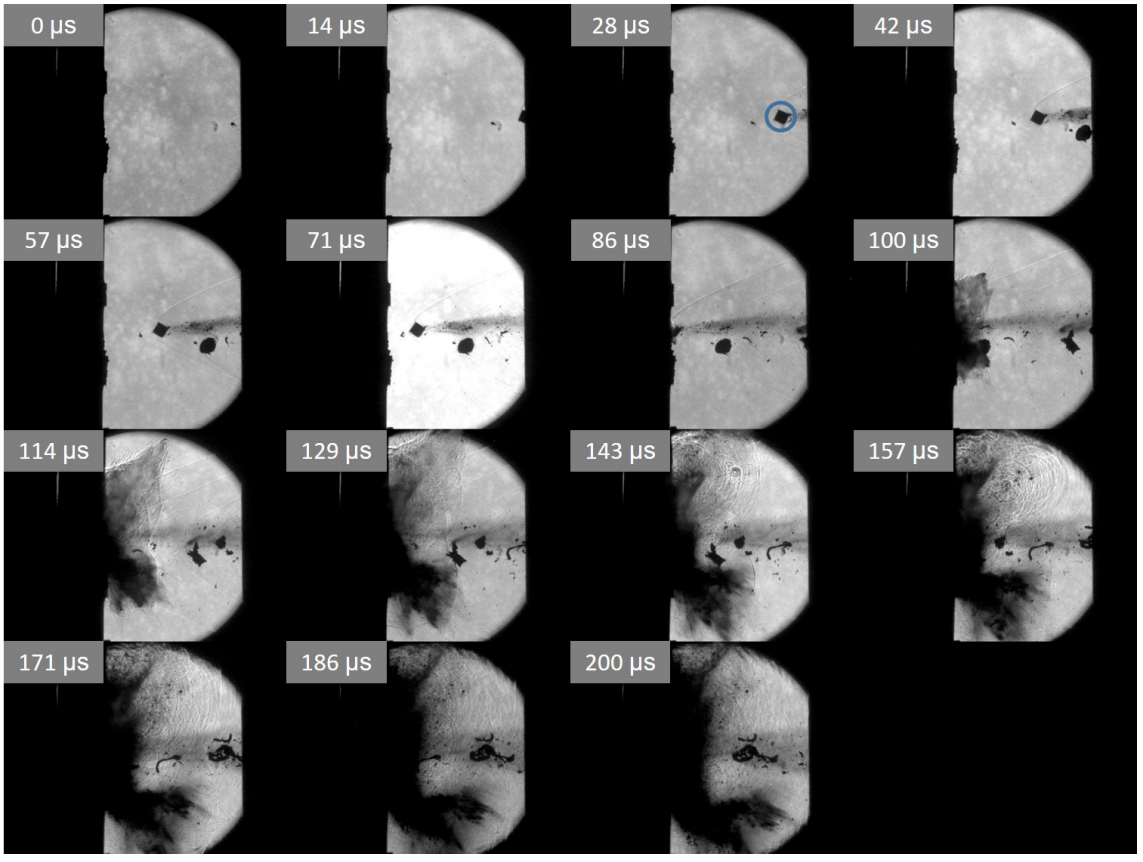

Figure 8.6: Image set from SIM-X framing camera of the impact event of Specimen 1. Interframe time is indicated to show temporal progression of event, with time 0 µs aligning with the image closest to impact. The specimen is circled in blue in the frame at 28 µs. Material pieces that precede or follow the specimen are nylon remnants that escaped the sabot stripper.

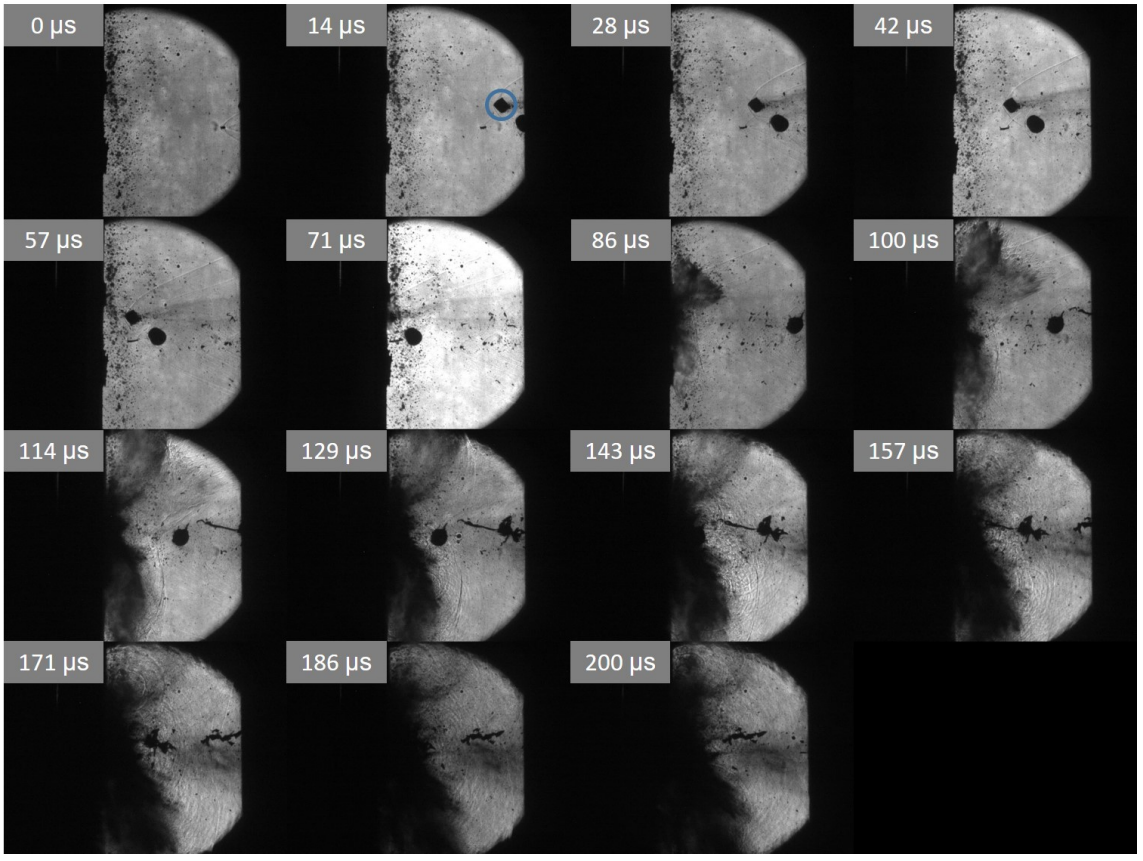

Figure 8.7: Image set from SIM-X framing camera of the impact event of Specimen 2. Interframe time is indicated to show temporal progression of event, with time 0 µs aligning with the image closest to impact. The specimen is circled in blue in the frame at 14 µs. Material pieces that precede or follow the specimen are nylon remnants that escaped the sabot stripper. Dark dots in the image at time 0.0 µs are from fragment impacts with the windows from previous testing.

As seen in Figures 8.6 and 8.7, the specimens impacted at an angle, with the cylindrical edge of the specimen contacting the anvil first. The angling of the specimen was a result of mechanical interaction during the sabot stripping process. Specimen 1 and 2 impacted at an angle of 45° and 55°, respectively. These angles correspond to the angle between the centerline of the specimen and the face of the anvil. These are similar angles to the two specimens that impacted at approximately 50° in the high velocity impact tests in Section 7.6. Upon impact, both specimens were observed to pulverize into fine fragments that ejected at high velocity from the anvil surface. These fine fragments approach the imaging resolution of the SIM-X system and the density of the fine fragment cloud prevents optical size analysis of the fragments. Estimates of the strain rate that drives the fragmentation of the specimens were made using the generalized ra-

dial strain rate relation as discussed in Section 7.6. Taking the residual velocity of the anvil impact condition to be zero[12] and assuming incompressible behavior of the specimens (ν_{rm}=0.5), the radial strain rates of these impacts are on the order of $8.5 \cdot 10^4$ s^{-1} which is approximately 50% higher than the radial strain rates associated with the high velocity impact tests.

Light emission from a combustion event was not observed in Figures 8.6 and 8.7, but this is not indicative of a lack of combustion of the fragments. The use of parallel light and fixed wavelength laser illumination with the SIM-X camera reduces the appearance of any direct illumination associated with combustion. High speed images from the HPV-X2 clearly show combustion of the fragments occurring after impact. Images showing light emission from fragment combustion immediately after impact of Specimen 1 and 2 are presented in Figure 8.8(a) and 8.8(b), respectively. Light emission was no longer observed in the HPV-X2 images after 1.2 ms for both tests.

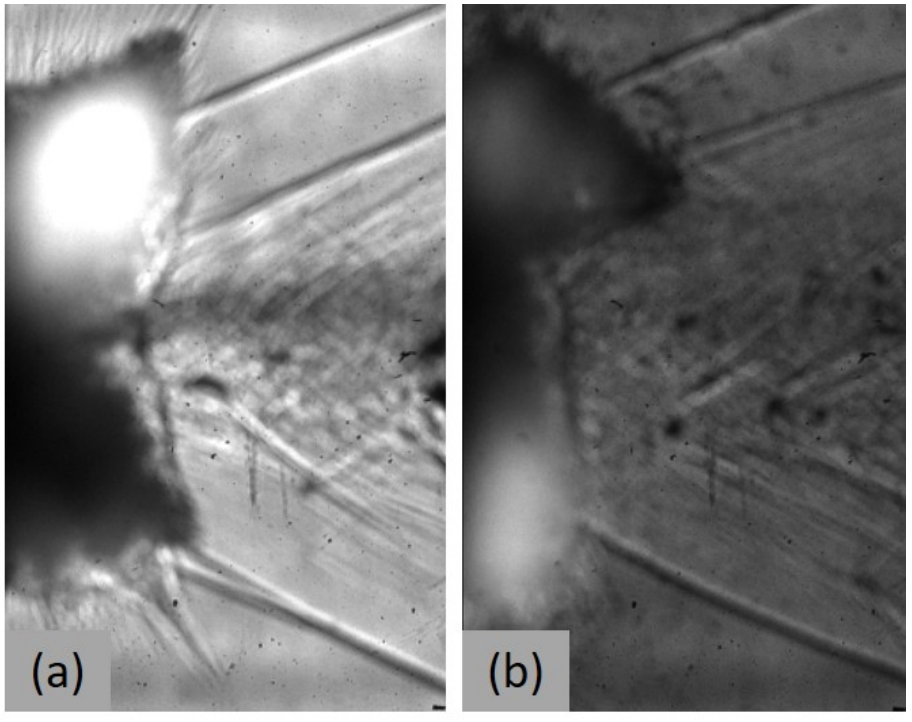

Figure 8.8: Light emission observed in HPV-X2 images after impact that is indicative of combustion for (a) Specimen 1 and (b) Specimen 2. Anvil face is in line with left edge of the frame for both images.

Pressure of the working fluid (air) in the calorimeter was recorded for a duration of 140 ms at 500,000 samples per second. Significant noise was observed in the pressure measurement due to mechanical ringing of the calorimeter and wave reflections in the working fluid after impact. This noise is typical of vented

calorimetry pressure measurements[68, 70] and post processing is necessary to estimate the quasi-static pressure evolution over time. A Fast Fourier Transform (FFT) was used to remove high frequency noise that corresponded to frequencies greater than 10^4 Hz. The measured pressure, filtered of high frequency noise, is shown in Figure 8.9(a) for Specimen 1 and Figure 8.9(b) for Specimen 2. A Gaussian moving average with a window size of 1200 was used to smooth the data and remove the pressure oscillations associated with waves reflecting in the calorimeter. The smoothed measurements estimating the quasi-static pressure are overlaid on the measured pressure of the working fluid in Figures 8.9(a) and 8.9(b). Peak pressure $P_{max,vc}$, time to peak pressure $t_{max,vc}$ and peak temperature $T_{max,vc}$ are reported in Table 8.4. The estimate of peak temperature is calculated using the ideal gas law for the peak pressure condition and $\forall_{vc} = 9.66 \cdot 10^{-3}$ m^3.

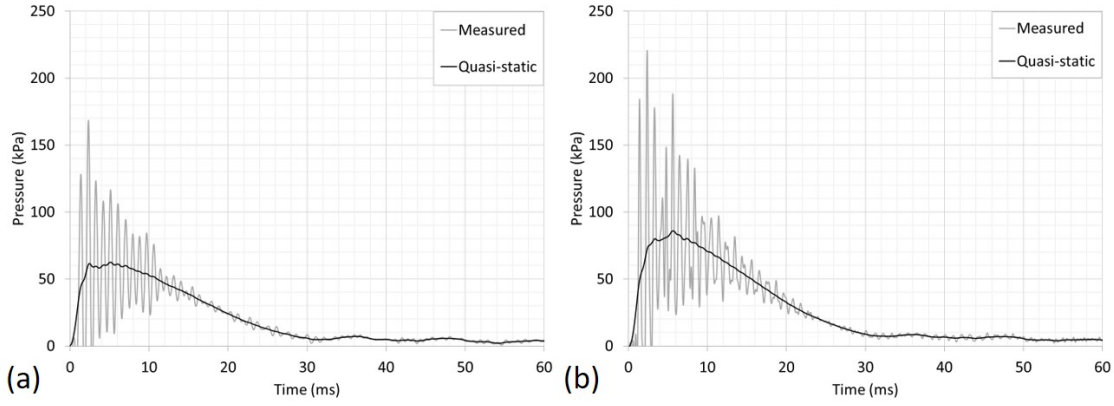

Figure 8.9: Measured pressure of the working fluid (air) and estimated quasistatic pressure for (a) Specimen 1 and (b) Specimen 2. Note the time scale of these graphs is in milliseconds and not µs as in the SIM-X image sets.

Table 8.4: Peak quasi-static pressure $P_{max,vc}$, time to peak pressure $t_{max,vc}$ and peak temperature $T_{max,vc}$, determined from the measured pressures of the working fluid in the vented calorimetry for Specimen 1 and Specimen 2

Variant	Specimen	$P_{max,vc}$ kPa	$t_{max,vc}$ ms	$T_{max,vc}$ K
100Al-F	1	62.5	5.2	509
	2	85.3	5.9	585

The estimated peak temperature provides important insights regarding how to proceed with calculations of energy release using the methodology by Ames[68]. At these temperatures the change in specific heat of air is less

than 4% for both cases. This error is small relative to other uncertainties of the measurement (e.g. exact quasi-static pressure) and thus can be considered negligible[68]. This maintains the calorically perfect gas assumption used in Ames' methodology. The calculated temperature is also below the reported auto-ignition temperature of 750 K for dispersed fine aluminum particles (>1 µm) in air[259], indicating that combustion of aluminum particles is not favorable at the peak pressure condition. Because no further light emission was observed after 1.2 ms, the temperature of the working fluid indicates the combustion reaction was completed before the peak pressure was reached for both tests. Because the calorically perfect gas assumption is maintained and combustion is assumed to end before the peak pressure condition, the use of Equation 5.6 from Section 5.2 is appropriate. This equation is repeated here for convenience:

$$\Delta Q_{vc} = \frac{\Delta P_{vc} \forbidden{V}_{vc}}{\gamma - 1} \tag{8.3}$$

Equation 8.3 does not account for mass loss due to venting. However, the average time to peak pressure of 5.5 ms aligns with the pressure rise times reported by Ames[68] suggesting mass loss should be negligible. Using the methodology discussed in Section 5.2, the calculated mass loss due to venting by the time peak pressure is reached equates to less than a 1% change in the mass of the working fluid. This confirms mass loss through venting can be assumed negligible[68].

As discussed in Section 8.1, calculations of energy release using Ames' methodology[68] can fail to represent actual energy release measurements due to the presence of reaction products in the working fluid. To affirm the calculated energy release is representative of the reactions here, the change in mass of the working fluid due to the presence of reaction products needs to be assessed. As a worse case scenario, full combustion of the specimen is assumed. This corresponds to 0.5 g of reaction products by mass continuity. Only the total mass of reaction products is considered as both the gas phase products and fine dispersed condensed phase products mixing with the working fluid can effect the results. This was observed in the bomb calorimetry tests in Section 8.1. For the vented calorimeter here, approximately 0.34 moles of air are present, corresponding to 9.8 g of working fluid. The change in mass of the working fluid assuming complete combustion of the Al specimen is less than 5%. This falls within the the range reported by Ames[224] to have minimal impact on the calculations. As such, the use of Equation 8.3 is expected to provided reasonable estimates of the energy release of the impact driven combustion of these Al RM specimens. Verification of test conditions for using the methodology by Ames[68] is rarely discussed in other works[49, 70, 180]. This verification is necessary to ensure the energy release calculated from these pressure measurements is representative of the energy release actually associated with the impact driven combustion event.

Both the energy released from the combustion reaction and deposition of kinetic energy of the specimens heat the working fluid[68]. The portion of the kinetic energy that heats the working fluid not only depends on the specimen

impact, but also the work done on the ejected fragments by the working fluid through drag and subsequent impact of these fragments with the calorimeter walls[11]. Some works have assumed complete conversion of the kinetic energy when calculating energy release from pressure measurements[180], while others have reported less than 20% of the kinetic energy of the projectile was converted to heating the working fluid[70] in vented calorimetry tests. The vented chamber calorimetry method measures the total energy change of the working fluid, assuming combustion energy release and kinetic energy deposition. Conversion of the kinetic energy to heating of the working fluid leads to an apparent reduction in the amount of energy released from the combustion event.

For the calculations here, maximum and minimum values of energy release are reported which should bound the actual energy release from the reaction of the Al specimen fragments. The maximum energy release of the reaction corresponds to no conversion of the kinetic energy of the specimens into heating the fluid. The minimum energy release of the reaction corresponds to full conversion of the kinetic energy of the specimens into heating the fluid. The kinetic energy of the specimens and maximum and minimum values of energy release associated with the combustion of the Al fragments are summarized in Table 8.5.

Table 8.5: Calculated energy for the impact driven combustion of Specimen 1 and Specimen 2. The maximum energy release of the reaction bound corresponds to no conversion of the projectile kinetic energy to heat. The minimum energy release corresponds to full conversion of the projectile kinetic energy to heat. Kinetic energy of the specimens is reported.

Variant	Specimen	Kinetic Energy kJ	ΔQ_{vc} Max kJ	ΔQ_{vc} Min kJ
100Al-F	1	0.26	1.51	1.25
	2	0.30	2.05	1.75

The energy release for Al reacting with air has been reported to be approximately 31 kJ per gram of Al[6, 88]. For full combustion of the 0.5 g specimens, a maximum energy release of 15.5 kJ would be expected. Here the energy release for Specimen 1 and Specimen 2 were calculated as 1.25-1.51 kJ/g and 1.75-2.05 kJ/g of Al. This indicates that only between 8% and 10% of the mass of Specimen 1 reacted and between 11% and 13% of the mass of Specimen 2 reacted. Despite the large production of fine fragments observed in Figures 8.6 and 8.7, only a small portion of these fragments appear to have reacted with the air.

Exploring the characteristic timescales of the combustion events here can provide some insight to spatial scales that may limit combustion of the fragments. Beckstead[234] provides a thorough review of timescales of Al particle combustion in air. Typically the combustion timescales of an Al particle are described

using a power-law relation of the burning particle diameter[234]:

$$t_c = \frac{D_b^{n_b}}{\beta_b} \tag{8.4}$$

Where the timescale of combustion t_c, is a function of the burning particle diameter D_b, scaled by a constant β_b. Beckstead[234] suggests values of 1.5 to 1.8 for n_b and β_b=0.003 as values that provide reasonable estimates of the timescales of Al particle combustion. If the time to peak pressure, which is approximately 5.5 ms for these tests, corresponds to the end of the combustion event then only fragments less than 60 µm can be fully burned[234]. If the duration of light emission, which is approximately 1.2 ms for these tests, corresponds to the end of the combustion event then only fragments less than 25 µm can be fully burned[234]. This establishes that fragments less than 60 µm could have combusted in these vented calorimetry tests, and that fragments less than 25 µm were primarily associated with the early time combustion event that produced light.

The fragmentation behavior of the specimens here is expected to be similar to the fragmentation behavior observed in the high velocity impact tests in regards to high production of fine fragments less than 44 µm. This is based on the insensitivity of the fragmentation behavior to impact angle that was observed in the high velocity impact tests and the higher strain rate associated with these anvil impact test. From the high velocity impact tests, it was estimated from the distribution fit that at least 30% of the fragment mass is associated with fragments less than 44 µm in size. As such, 30% of the original Al mass should be available for combustion within the constraints of the time and spatial scales identified here, but due to other limitations only a portion of this fragment mass actually reacted with the air. Similar behavior has been observed in explosive tests of Al RM casing[180] suggesting it is not a unique phenomenon.

The resolution of the size analysis methods here do not permit exploration of the size distribution of fragments below 44 µm. This impedes directly correlating energy release to a particular mass percentage of fragments based on the timescales of events here. However, prior works have shown cooling due to gas impingement and formation of an oxide cap on the burning aluminum particles can suppress and even fully quench the combustion of the particle[234, 260]. Timescales of the oxide cap formation are on the order of 10^{-1} ms for the particle sizes discussed here[260]. Therefore, it seems very likely the burning of fragments is inhibited by the oxide cap formation on the surface of the particle. These results suggest that predicting the energy release of an impact driven combustion event of an RM can not be described solely knowing the mass-size distribution of the fragments and timescales of particle combustion. To actually predict energy release from these types of impact events, temporal and spatial modeling of the burning characteristics of the ejected fragments is needed to resolve the fragment mass of the specimens that is actually consumed. This undertaking is outside the scope of this work.

CHAPTER 9

CONCLUSIONS AND RECOMMENDATIONS FOR FUTURE WORK

Knowledge of the fragmentation and energy release behavior of RMs is critical for effective design and application of RM based munition systems. This includes understanding the roles that composition, microstructure, and loading have on fragmentation behavior and energy release [8–12]. A systematic approach was applied in this work to characterize the macro-scale mechanical, fragmentation, and combustion behavior of aluminum and Al/PTFE granular RM composite systems. The Al/PTFE system was evaluated using five compositions, which included aluminum only RMs, with controlled variation of porosity and particle size. Quasi-static compression, Kolsky bar compression, and high velocity impact tests were used to explore the quasi-static response, dynamic response, and fragmentation behavior of these materials. Bomb calorimetry and theoretical equilibrium predictions were used to explore the energy release behavior of the Al/PTFE composition and vented calorimetry tests were used to assess the impact driven combustion behaviors of granular aluminum RMs.

General predictive theory for mechanical properties of granular RM composites was found to be lacking. As such, a new parameterized model was developed here to provide general predictive capability of density, elastic modulus, fracture toughness, yield strength, and compressive strength for these materials. The model was comprised of three dependency functions representing the effects composition, porosity, and particle size have on the considered material properties. Measurements of these material properties were used to validate the individual dependency functions as well as the predictions of combined response by the parameterized model. These dependency functions were individually shown to provide reasonable representation of the effects associated with the variation of composition, porosity, and particle size. A methodology has been provided for determining parameters of the functions and identifying which forms of the compositional dependency function to use. These dependency functions are important tools for designing granular RM composites as they can inform the selection of compositions, constituent particle size, and porosity to meet a specific application need.

The parameterized model further extends the predictive capabilities of material properties by providing a means to assess the combined response to composition, porosity, and particle size variations. Predictions by the parameterized

model agreed well with measurements of density, elastic modulus, and yield and compressive strength of the evaluated RMs. The successful demonstration of the parameterized model represents a major step forward in expanding the engineering capabilities of granular RM composites. By providing a means to theoretically evaluate the mechanical response of an RM variant before testing, experimental efforts can be focused on the most viable RM candidates for the application.

The parameterized model failed to quantitatively capture the compositional effects on the Mode-I fracture toughness, but did provide qualitative representation of the response to compositional variation. Thus, the model still has utility in describing the proportional change of the fracture toughness in relation to composition, porosity, and particle size variations. Application for dilatational wave speed was also explored, but the models did not demonstrate appropriate representation of the material property. Important insights have been gained on additional heterogeneity characteristics that influence granular RM composites as the fracture toughness and dilatational wave speed have known sensitivities to the interface conditions between particles[29, 106, 120, 136, 152].

Predictive capability of the fragmentation of granular RM composites was explored using minimization of energy models for calculations of characteristic fragment sizes. The minimization of energy model proposed in later works by Grady[61], and regularly used in RM research, was found to have a mathematical error by this work. In correcting this error, a revised model was also derived to account for kinetic energy and elastic strain energy contributions to fragmentation without dependency on material wave speeds. This model was validated using fragmentation data from literature of explosively loaded steel cases.

Using the developed parameterized model to account for porosity and particle size variations of the RM specimens, material properties were calculated for use in the minimization of energy models. Predictions of characteristic fragment sizes by the models were compared to characteristic length scales of fragment mass-size distributions from the Kolsky bar and high velocity impact tests conducted here. The models were found to consistently overpredict characteristic fragment sizes of the mass-size distributions by an order of magnitude. It is believed this behavior is not associated with the use of non-representative material properties, but instead reflects the inability of the models to fully resolve the mechanical processes associated with the dynamic fragmentation of the RM materials studied here. It is expected that this stems from defects associated with the heterogeneity of the material[42] and interface conditions between particles which can influence the fragmentation behavior[106].

Because of the similarities in heterogenity between the RMs here and granular RMs elsewhere in literature, it is expected that minimization of energy methods are not generally appropriate for predicting the characteristic length scales of the fragmentation of granular RMs. These results challenge the prevalent use of minimization of energy models by other works attempting to predict the fragmentation behavior of these RMs. Furthermore, a need has been demonstrated for additional research into alternative models for predicting characteristic length scales of the fragment distributions of RMs.

The use of general distribution fits was also explored in this work for predicting fragmentation behavior of RMs. Intuitively, predictive application of a distribution fit depends on the ability to predict the fit parameters. As such, physical meaning of the parameters is needed to be able to relate back to material properties and loading conditions that drive the fragmentation process of RMs. The general mass-size distribution form proposed by Hooper[27] has shown potential for predictive application. However, this work found Hooper's distribution form to have limited use as a predictive tool of RM fragment distributions. This was because the four parameters that define the distribution form are susceptible to free-fitting behavior. This demonstrates a fundamental limitation of distributions fits: general applicability of a fit obtained through multiple parameters can lead to free-fitting behavior which precludes physical representation of the fragmentation process by the parameters. While continued research in developing distribution forms that represent RM fragmentation is needed, the limitations of physical representation by the parameters cannot be ignored.

Review of prior predictive efforts of RM energy release found systemic errors in thermodynamic data sets and a lack of consideration for phase transitions of the reaction products. As a result, non-representative predictions of energy release for RMs is common. In response, a phase compliant minimization of Gibbs free energy solver was developed and a methodology demonstrated for verifying thermodynamic data to improve energy release predictions of RMs. This solver was verified against energy release measurements from bomb calorimetry and adiabatic flame temperature measurements of the stoichiometric reaction of Al/PTFE. Predictions of the adiabatic flame temperature and energy release for the stoichiometric Al/PTFE composition were 2220 K and 8.7 kJ/g, respectively. These predictions compared well to temperature measurements from literature[257] and the measured energy release of 7.40 ± 0.05kJ/g from the bomb calorimetry experiments.

The phase compliant equilibrium solver was used to predict the energy release, adiabatic flame temperature, and product species for a portion of the Al/PTFE compositional space. Predictions of equilibrium products were phase compliant thus affirming the physical validity of the solutions. These results challenge predictions of the Al/PTFE reaction by other works[67]. It was determined that thermodynamic data for PTFE has not been properly incorporated into existing thermodynamic data sets and it is suspected this has led to the incorrect use of thermodynamic data for the gas phase monomer, C_2F_4, for PTFE. The thermodynamic data reported for PTFE by Lau et al.[212] which was used here successfully should be incorporated into other existing equilibrium codes such as CEA and CHEETAH to support future PTFE combustion studies. The developed phase complaint equilibrium solver and use of verified thermodynamic data represents a major improvement to predictive capabilities of energy release, reaction temperatures, and equilibrium compositions associated with the combustion of RMs.

Vented calorimetry tests were performed on granular aluminum RM specimens directly impacting an anvil at approximately 1 km/s. In evaluating the

timescales of the reactions for these vented calorimetry tests, only fragments below 44 μm in size were determined to be available for combustion. Based on the high velocity impact tests, approximately 30% of the original aluminum specimen mass was expected to be represented by fragments in this size range. However, only 8% to 13% of the original specimen mass was calculated to have reacted based on the energy release measurements. This discrepancy is believed to stem from the combustion of the small ejected fragments being inhibited by impingement of the oxidizing working fluid and development of an oxide shell which can occur at the timescales of the combustion event[260]. The inhibited combustion behavior observed here reveals that the energy release can not be described knowing only the mass-size distributions of fragments and timescales of the combustion process. To accurately predict the energy release from these types of RM impact events, additional research is needed in developing an understanding of the temporal and spatial burning characteristics of the ejected fragments to resolve the total fragment mass consumed through combustion.

The present research has expanded the general understanding of mechanical response, fragmentation behavior, and energy release of granular RM composites. New methods have been established for predicting the mechanical response and combustion behavior of these RMs. A systematic methodology has also been demonstrated that represents a general baseline evaluation of the mechanical response, fragmentation, and energy release behaviors needed in assessing the application and viability of different RM systems. The experimental results from this methodology supported the validation of the new predictive methods and also the determination of limitations of existing analytical theories. While unifying theories for describing the fragmentation behavior of granular RM composites could not be determined, knowledge gaps and limitations of existing methods have been identified here. This establishes new areas for future works to focus efforts in expanding predictive capabilities and general knowledge of RM behaviors.

9.1 Future work

One of the enduring challenges in the field of RM research has been the lack of comparability between research efforts and materials. Rarely are similar materials tested under similar experimental conditions between works in literature. Granted, this does support both application development and a potential broad scale understanding of RM behaviors. However, the lack of heterogeneity characterization limits the comparison of results as researchers cannot identify the differences in size distributions of the constituent powders, morphology of constituent particles, and the measured bulk material properties. Failing to identify these characteristic aspects of a material restricts identification of general behavioral trends that may be associated with granular RM composites. Research efforts could improve the understanding of RM behavior by additional characterization of size and morphology of constituent particles and reporting quasi-static

measurements of moduli, strengths, and fracture toughness. In doing so, more informed comparisons of results between works can be made.

Additional characterization of microscale effects on the mechanical behavior of granular RM composites is needed. Heterogeneity characteristics such as particle cohesion and contact area have been identified as additional influencing factors that warrant further exploration. Incorporation of these effects into the parameterized model could improve predictions of material properties. This in turn supports predictive capability of fragmentation behavior. Understanding the role of defects associated with the heterogeneity of the material[42] and potentially geometrical scaling effects[256] have on the fragmentation behavior of RMs would support development of improved fragmentation models. In doing so, consideration is needed of the application of models that account for both energy and heterogeneity effects on the fragmentation process, such as the ZMR model[42].

Further work is needed in exploring discrepancies between the fracture toughness measurements here and those reported in literature. This should include further verification of the single V-notch diametrical compression test (SVDCT) method used by this work. A comparative study of fracture toughness measurements methods prevalent in RM literature would improve comparability between research efforts. In addition, while this work has shown the behavior of RMs can be expected to be consistent and repeatable, this should not be taken for granted. The nature of granular RM compacts predisposes them to inconsistencies and natural variation in behavior between specimens. Multiple tests of a material variant under similar conditions should become a standard in the field to ensure a representative estimate of the general behavior is obtained.

Work is also needed in resolving discrepancies in thermodynamic data sets used for theoretical calculations of energy release and thermochemical equilibrium. This not only would improve the understanding of the multiphase reactions associated with RMs, but also the assessment of combustion efficiency of the materials in application. Verification of these efforts requires additional experimental measurements of energy release, reaction temperatures, and equilibrium products. For energy release measurements, future works should adopt the calorimetry methods developed here to ensure measured energy release is representative of the studied RMs.

This dissertation has focused on the application of the experimental and theoretical methods to the study of RMs; however, there is broad application potential for use of the methods in other fields. The experimental methodologies and uncertainty analysis for measurements of quasi-static material properties and fracture toughness have use in the general study of heterogeneous materials such as granular composite compacts, geological materials, or metal foams. Similarly, the parameterized model developed in this work has potential use in the field of composite engineering and research. The experimental methods and analysis for high velocity impact demonstrated in this work could have general application in ballistic impact studies that may include projectile or armor development. Also, the phase compliant equilibrium approach demonstrated here has

potential for improving predictions of adiabatic flame temperature and energy release in other works studying multiphase combustion processes such as rocket propulsion and other energetic materials.

REFERENCES

[1] W. H. Wilson, F. Zhang, and K. Kim. Fine fragmentation distribution from structural reactive material casings under explosive loading. volume 1973. Shock Compression of Condensed Matter, AIP Conference Proceedings, 2015.

[2] D. A. Kotei. Aluminum reactive material warhead casings. Master's thesis, Naval postgraduate school, Monterey, Ca., 2018.

[3] F. Zhang, M. Gauthier, and C. Cojocaru. Sub-fragmentation of structural reactive material casings under explosion. volume 1793. Shock Compression of Condensed Matter, AIP Conference Proceedings, 2015.

[4] P. J. Hooper, C. I. Milby, R. J. Lee, and R. J. Jouet. High-velocity impact fragmentation of brittle, granular aluminum spheres. *Procedia Engineering*, 58:663–671, 2013.

[5] S. C. Thuot, J. Wilkinson, R. J. Lee, J. R. Carney, J. Hooper, J. M. Lightstone, J. R. Juoet, and J. G. Rogerson. Impact fragmentation and ballistics of pressed aluminum powder projectiles. volume 1195. Shock Compression of Condensed Matter, AIP Conference Proceedings, 2009.

[6] S. H. Fischer and M. C. Grubelich. Theoretical energy release of thermites, intermetallics, and combustible metals. Technical report, Sandia National Laboratories, SAND98-1176C, 1998.

[7] E. L. Dreizen and M. Schoenitz. Correlating ignition mechanisms of aluminum-based reactive materials with thermoanalytical measurements. *Progress in Energy and Combustion Science*, 50:81–105, June 2015.

[8] C. Ge, Q. Yu, H. Zhang, Z. Qu, H. Wang, and Y. Zheng. On dynamic response and fracture-innduced initiation characteristics of aluminum particle filled PTFE reactive material using hat-shaped specimens. *Materials and Design*, 188, January 2020.

[9] H. Zhang, H. Wang, and C. Ge. Characterization of the dynamic response and constitutive behavior of PTFE/Al/W reactive materials. *Propellants, explosives, pyrotechnics*, 45, 2020.

[10] E. R. Wainwright, M. A. Mueller, K. R. Overdeep, S. V. Lakshman, and T. P. Weihs. Measuring heat production from burning Al/Zr and Al/Mg/Zr composite particles in a custom micro-bomb calorimeter. *Materials*, 13(2745), 2020.

[11] J. Kline and J. P. Hooper. The effect of annealing on the impact fragmentation of a pure aluminum reactive material. *Journal of Applied Physics*, 125, May 2019.

[12] M. Tang and J. P. Hooper. Impact fragmentation of a brittle metal compact. *Journal of Applied Physics*, 123, April 2018.

[13] S. H. Youngblood, B. Miller, C. Schmittle, M. J. Hargather, J. Kimberley, S. Thoma, and P. Martellaro. Study of reactive material fragmentation behavior in gun- and explosive- launched systems. 49th Combustion Conference, JANNAF, June 2019.

[14] E. L. Dreizen. Metal-based reactive nanomaterials. *Progress in Energy and Combustion Science*, 35:141–167, September 2008.

[15] M. J. Hargather, J. Kimberley, and S. G. Thoma. Failure and fragmentation of pressed bi-metallic composites. volume 1979 of *1*. Shock Compression of Condensed Matter, AIP Conference Proceedings, July 2018.

[16] V. F. Nesterenko, P. Chiu, C. Braithwaite, A. Collins, D. Williamson, K. L. Olney, D. B. Benson, and F. McKenzie. Dynamic behavior of particulate/-porous energetic materials. volume 1426, pages 533–538. Shock Compression of Condensed Matter, AIP conference proceedings, 2012.

[17] T. W. Schoenitz and E. L. Dreizen. Preparation of energetic metastable nanocomposite materials by arrested reactive milling. volume 800. Symposium AA - synthesis, characterization, and properties of energetic/reactive nanomaterials, Materials Research Society, 2004.

[18] S. G. Hashemabad. *Hybrid bimetallic-thermite reactive compositesl ultrasonic powder consolidation, ignition characterization and application to soldering*. PhD thesis, Northeastern University, December 2015.

[19] K. J. Blobaum, M. E. Reiss, J. M. Plitzko, and T. P. Weihs. Deposition and characterization of a self-propagating CuOx/Al thermite reaction in a multilayer foil geometry. *Journal of applied physics*, 94(5):2915–2922, 2003.

[20] G. Hammes, C. Binder, A. Galiotto, A. N. Klein, and H. A. Al-Qureshi. Relationship between cold isostatic pressing and uniaxial compression of powder metallurgy. Technical report, Federal University of Santa Catarina, Florianopolis, Brasil, December 2014.

[21] Rainer Oberacker. *Ceramics science and technology; volume 3: synthesis and processing*, chapter Part 1: Powder compaction by dry pressing, pages 1–34. Wiley-VCH, 2011.

[22] S. Sundaresh. A mesoscopic approach towards modeling of compaction process in powder metallurgy. Master's thesis, Ohio State University, 2014.

[23] K. P. Keefe. Comparison of uniaxial and isostatic compaction behavior. Technical report, Alfred University, 2013.

[24] M. N. Rahaman. *Ceramic processing and sintering*. CRC Press, New York, New York, 2 edition, July 2003.

[25] S. A. Tsukerman. *Powder metallurgy*. Pergamon Press, 1 edition, January 1965.

[26] H. W. Chandler, C. M. Sands, J. H. Song, P. J. Withers, and S. A. McDonald. A plasticity model for powder compaction processed incorporating particle deformation and rearrangement. *International journal of solids and structures*, 45:2056–2076, October 2008.

[27] J. P. Hooper. Impact fragmentation of aluminum reactive materials. *Journal of Applied Physics*, 112:1–7, 2012.

[28] R. D. Carneim. *Characterization of uniaxial compaction in spray dried ceramic powders*. PhD thesis, Pennsylvania state university, December 2000.

[29] M. Takahashi, S. Suzuki, and M. Kosakai. Dependence of intergranular fracture strength of a compact of pressed granules on their deformation characteristics. *Journal of the American Cerami Society*, 1986.

[30] I. M. Hutchings. Manufacturing engineering tripos: Powder processing. Technical report, University of Cambridge, Cambridge, England, 2012.

[31] R. German. Manipulation of strength during sintering as a basis for obtaining rapid densification without distortion. *Materials Transactions*, 42(7):1400–1410, 2001.

[32] K. L. Olney, P. H. Chiu, C. W. Lee, V. F. Nesterenko, and D. J. Benson. Role of material properties and mesostructure on dynamic deformation and shear instability in Al-W granular composites. *Journal of Applied Physics*, 110, 2011.

[33] L. Ding, J. Zhou, W. Tang, X. Ran, and Y. Hu. Impact energy release characteristcs of PTFE/Al/CuO reactive materials measured by a new energy release testing device. *Polymers*, 11, January 2019.

[34] P. Chiu, K. L. Olney, C. Braithwaite, A. Jardine, A. Collins, D. J. Benson, and V. F. Nesterenko. Mechanisms of fragmentation and microstructure of debris generated furing explosive testing of Al-W granular composite rings. volume 50. Shock Compression of Condensed Matter, Journal of Physics: Conference Series, 2014.

[35] D. M. Bond and M. A. Zikry. Differentiating between intergranular and transgranular fracture in polycrystalline aggregates. *Journal of material science*, 53:5786–5798, 2017.

[36] T. Watanabe. Grain boundary engineering: historical perspective and future prospects. *Journal of material science*, 46:4095–4115, 2011.

[37] J. Cai. *Properties of heterogeneous energetic materials under high strain, high strain rate deformation*. PhD thesis, University of California, San Diego, 2007.

[38] E. B. Herbold, V. F. Nesterenko, D. J. Benson, J. Cai, K. S. Vecchio, F. Jiang, S. Addiss, M. Walley, and W. G. Proud. Particle size effects on strength failue and shock behavior in polytetrafluroethylene-Al-W granular composite materials. *Journal of Applied Physics*, 104, August 2008.

[39] H. Kolsky. An investigation of the mechanical properties of materials at very high rates of loading. *Proceedings of the physical society*, 62:676–700, 1949.

[40] P. H. Chiu and V. F. Nesterenko. Dynamic behavior and fracture of granular composite Al-W. volume 2, pages 947–953. DYMAT, 9th international conference on the mechanical and physical behavior of materials under dynamic loading, 2009.

[41] L. Zhou, L. Yang, Y. Peng, L. Fei, and X. Zhu. Comparative study on constitutive models to predict flow stress of Fe-Cr-Ni preform reinforced Al-Si-Cu-Ni-Mg composite. *Journal of Wuhan University of Technology - Material Science Edition*, 32(2):666–676, 2017.

[42] K. T. Ramesh, J. D. Hogan, J. Kimberley, and A. Stickle. A review of mechanisms and models for dynamic failure, strength, and fragmentation. *Planetary and Spae Science*, 107:10–23, 2014.

[43] S. Ji and Q. Gu. Porosity dependence of mechanical properties of solid materials. *Journal of material science*, 41:1757–1768, 2006.

[44] R. M. Spriggs, J. B. Mitchell, and T. Vasilos. Mechanical properties of pure, dense aluminum oxide as a function of temperature and grain size. *Journal of American Society of Ceramics*, 47(7):323–327, 1964.

[45] S. C. Carniglia. Working model for porosity effects on the uniaxial strength of ceramics. *Journal of the American Ceramic Society*, 55(12):610–618, 1972.

[46] G. R. Johnson and W. H. Cook. A constitutive model and data for metals subjected to large strains, high strain rates, and high temperatures. pages 541–547, The Hague, 1983. Seventh Inernational Ballestics Symposium.

[47] J. Gao. Split-Hopkinson pressure bar testing and constitutive model evaluation for 7050-T7451 aluminum, IN718 superalloy, and 300M steel. Master's thesis, McGill University, Montreal, Quebec, Canada, 2017.

[48] Y. Shen. *The chemical and mechanical behaviors of polymer/reactive metal systems under high strain rates*. PhD thesis, Georgia institute of technology, 2012.

[49] X. F. Zhang, J. Zhang, L. Qiao, A. S. Shi, Y. G. Zhang, Y. He, and Z. W. Guan. Experimental study of the compression properties of Al/W/PTFE granular composites under elevated strain rates. *Material Scienc and Engineering A*, 581:48–55, 2013.

[50] S. Doddamani and M. Kaleemulla. Review of experimental fracture toughness (KIC) of aluminum alloy and aluminum MMCs. *International journal of fracture and damage mechanics*, 1(2):38–51, 2016.

[51] J. Kimberley, R. T. Ramesh, and N. P. Daphalapurkar. A scaling law for the dynamic strength of brittle solids. *Acta Materials*, 61:3509–3521, 2013.

[52] D. E. Grady and M. E. Kipp. Geometric statistics and dynamic fragmentation. *Journal of Applied Physics*, 58(3):1210–1222, 1985.

[53] D. E. Grady. Particle size statistics in dynamic fragmentation. *Journal of Applied Physics*, 68(12):6099–6105, 1990.

[54] M. F. Mott and S. H. L:infoot. A theory of fragmentation. Technical Report AC 3348, Bristol University, England, 1943.

[55] D. Grady. *Fragmentation of Rings and Shells*. Springer, 2006.

[56] P. Elek and S. Jaramaz. Fragment mass distribution of naturally fragmenting warheads. *FME Transactions*, 37:129–135, 2009.

[57] J. A. Astrom, F. Ouchterlony, R. P. Linna, and J. Timonen. Universal dynamic fragmentation in D dimensions. *Physical Review Letters*, 92(24), 2014.

[58] L. Oddershede, P. Dimon, and J. Bohr. Self-organized criticality in fragmenting. *Physical Review Letters*, 71(19):3107–3110, 1993.

[59] T. Tang, G. Ren, Z. Guo, and Q. Li. An improved technique of expanding metal ring experiment under high explosive loading. *Review of scientific instruments*, 84, 2013.

[60] D. E. Grady. Local inertial effects in dynamic fragmentation. *Journal of applied physics*, 53(322):322–325, 1982.

[61] D. E. Grady. The spall strength of condensed matter. *Journal of the mechanics and physics of solids*, 36(3):353–384, 1988.

[62] D. E. Grady and M. E. Kipp. Fragmentation properties of metals. *International Journal of Impact Engineering*, 20:293–308, 1997.

[63] L. A. Glenn and A. Chudnovsky. Stain-energy effects on dynamic fragmentation. *Journal of Applied Physics*, 59(1379):1379–1380, 1986.

[64] L. A. Glenn, B. Y. Gommerstadt, and A. Chudnovsky. A fracture mechanics model of fragmentation. *Journal of Applied Physics*, 59(1379):1224–1226, 1986.

[65] Y. Li, C. Jiang, Z. Wang, and P. Luo. Experimental study on reaction charcteristics of PTFE/Ti/W energetic materials under explosive loading. *Materials*, 9(11), 2016.

[66] R. H. Warnes, R. R. Karpp, and P. S. Follansbee. The freely expanding ring test - a test to determine material strength at high strain rates. *Journal De Physique*, 5(46):583–589, 1985.

[67] E. Koch. *Metal-Fluorocarbon based energetic materials*. Wiley-VCH, 2012.

[68] R. G. Ames. Vented chamber calorimetry for impact-initiated energetic materials. 43rd AIAA Aerospace Sciences Meeting and Exhibit, AIAA, 2005.

[69] W. L. Perry, B. C. Tappan, B. L. Reardon, V. E. Sanders, and S. F. Son. Energy release characteristics of the nanoscale aluminum-tungsten oxide hydrate metastable intermolecular composite. *Journal of Applied Physics*, 101, 2007.

[70] P. Luo, Z. Wang, C. Jiang, L. Mao, and Q. Li. Experimental study on impact-initiated characters of W/Zr energetic fragments. *Materials and Design*, 84:72–78, 2015.

[71] J. Zhang, J. Huang, X. Fang, Y. Li, Z. Yu, Z. Gao, S. Wu, L. Yang, J. Wu, and J. Kui. Thermal decomposition and thermal reaction process of PTFE/Al/MnO2 fluorinated thermite. *Materials*, 2451, 2018.

[72] J. Lan, J. Liu, S. Zhang, C. Xue, X.and He, Z. Wu, Z. Yang, M. Yang, and S. Li. Influence of multi-oxidants on reaction characteristics of PTFE-Al-XmOy reactive material. *Materials and Design*, 186, 2020.

[73] S. K. Sahoo, S. M. Danali, and P. R. Arya. Ignition behavior Al/Fe2O3 metastable intermolecular composites. *International Journal of Engineering Research and Science*, 3(11), 2017.

[74] O. G. Cervantes, J. D. Kuntz, A. E. Gash, and Z. A. Munir. Heat of combustion of tantalum-tungsten oxide thermite composites. *Combustion and flame*, 157:2326–2332, 2010.

[75] J. M. Densmore, M. M. Biss, B. E. Holman, and K. L. McNesby. Impact initiated combustion of nickel-aluminum and aluminum-polytetrafluoroethylene. 15th International Detonation Symposium, Lawrence Livermore National Laboratory, 2014.

[76] M. A. Hobosyan, K. G. Kirakosyan, S. L. Kharatyan, and K. S. Martirosyan. PTFE-Al2O3 reactive interation at high heating rates. *Journal of Thermal Analysis and Calorimetry*, 119:245–251, 2015.

[77] J. M. Densmore, M. M. Biss, B. E. Homan, and K. L. McNesby. Thermal imaging of nickel-aluminum and aluminum-polytetrafluoroethylene impact initiated combustion. *Journal of Applied Physics*, 112, 2012.

[78] L. Zhou, S. Piekiel, S. Chowdhury, and M. R. Zachariah. Time-resolved mass spectrometry of the exothermic reaction between nanoaluminum and metal oxides: The role of oxygen release. *Journal of Physical Chemistry*, 114:14269–14275, 2010.

[79] E. S. Domalski and G. T. Armstrong. Heat of formation of aluminum fluoride by direct combination of the elements. *Journal of research of the National Bureau of Standards*, 69A(2):137–147, 1964.

[80] D. L. Hastings, M. Schoenitz, and E. L. Dreizin. High density reactive composite powders. *Journal of Allows and Compounds*, 735, 2018.

[81] E. W. Washburn. Standard states for bomb calorimetry. *Bureau of Standards Journal of Research*, pages 546–558, 1933.

[82] R. S. Jessup. Precise measurement of heat of combustion with a bomb calorimeter. Technical report, National Bureau of Standards, United States, 1960.

[83] E. S. Domalski and G. T. Armstrong. The heats of combustion of polytetrafluoethylene (Teflon) and graphite in elemental fluorine. *Institute for Basic Standards, National Bureau of Standards*, 1967.

[84] W. Ripley. Investigations into the calorimetric determination of the heat of combustion of a tertiary pyrotechnic composition. Technical report, United States Naval Ammuniation Depot, Crane IN, RDTR-13, 1960.

[85] V. P. Kobyakov, L. B. Mashkinov, and M. A. Sichinava. Heat release in combustion of burning composite thermite mixtures on the base of Fe2O3/TiO2/Al system. *High Temperature*, 47(1), 2009.

[86] X. F. Zhang, A. S. Shi, L. Qiao, J. Zhang, Y. G. Zhang, and Z. W. Guan. Experimental study on impact-initiated characters of multifunctional energetic structural materials. *Journal of Applied Physics*, 113, 2013.

[87] Cheetah 9.0: User's Manual. Technical report, Lawerence Livermore National Laboratory.

[88] A. V. Grosse and J. B. Conway. Combustion of metals in oxygen. *Industrial and Engineering Chemistry*, 50(4):663–672, 1958.

[89] E. Koch, R. Webb, and V. Weiser. Review on thermochemical codes. Rotterdam, Netherlands, 2009. 36th International Pyrotechnics Seminar.

[90] D. S. Stewart. A gibbs formulation for reactive materials with phase change. volume 1793. Shock Compression of Condensed Matter, AIP Conference Proceedings, 2015.

[91] F. C. Christo. Thermochemistry and kinetics models for magnesium/teflon/viton pyrotechnic compositions. Technical report, Defence Science and Technology Organization, 1999.

[92] L. V. de Yong and K. J. Smit. A theoretical study of the combustion of magnesium/Teflon/viton. Technical Report MRL-TR-91-25, Materials Research Laboratory, Australia, 1991.

[93] I. Glassman. Metal combustion processes. Technical report, Department of Aeronautical Engineering, Princeton University, 1959.

[94] D Lide, editor. *CRC Handbook of Chemistry and Physics*. CRC Press LLC, 81st edition, 2000.

[95] R. Smith. *Chemical Equilibrium Analysis: Theory and Algorithms*. Wiley, New York, 1982.

[96] D. Kondepudi and I. Prigogine. *Modern thermodynamics: From heat engines to dissipative structures*. John Wiley and Sons Ltd, West Sussex, England, 1998.

[97] Alexander Burcat. *Combustion Chemistry*, chapter Thermochemical data for combustion calculations, pages 455–473. Springer, New York, 1984.

[98] S. Gordon and B. J. McBride. Computer program for calculation of complex chemical equilibrium compositions, rocket performance, incident and reflected shocks, and Chapman-Jouget detonations. Technical Report NASA SP-273, NASA, 1976.

[99] B. J. McBride, S. Gordon, and M. A. Reno. Coefficients for calculating thermodynamic and transport properties of individual species. Technical report, NASA, Technical Memo 4513, 1993.

[100] D. G. Goodwin, R. L. Speth, H. K. Moffat, and B. W. Weber. Cantera: An object-oriented software toolkit for chemical kinetics, thermodynamics, and transport processes. *https://www.cantera.org*, 2018.

[101] G. Deffrennes, B. Gardiola, M. Allam, D. Chaussende, A. Pisch, J. Andrieux, R. Schmid-Fetzer, and O. Dezellus. Critical assessment and thermodynamic modeling of the al-c system. *Calphad*, 66, 2019.

[102] T. L. Anderson. *Fracture Mechanics: Fundamentals and Applications*. Taylor & Francis Group, Boca Raton, Florida, 4th edition, 2017.

[103] N. Pourmoghaddam, M. A. Kraus, J. Schneider, and G. Siebert. Relationship between strain energy and fracture pattern morphology of thermally tempered glass for the prediction of the 2D macro-scale fragmentation of glass. *Glass Structures & Engineering*, 4:257–275, 2018.

[104] X. F. Li, H. B. Li, Q. B. Zhang, J. L. Jiang, and J. Zhao. Dynamic fragmentation of rock material: Characteristic size, fragment distribution and pulverization law. *Engineering Fracture Mechanics*, 199:739–759, 2018.

[105] L. Gao, F. Gao, Y. Xing, and Z. Zhang. An energy preservation index for evalauting the rockburst potential based on energy evolution. *Energies*, 13(3636), 2020.

[106] A. Schmeink, L. Goerhing, and A. Hemmerle. Fracture of a model cohesive granular material. *Soft Matter, Royal Society of Chemistry*, 13(5):1040–1047, 2017.

[107] A. A. Griffith. The phenomena of rupture and flow in solids. *Philosophical Transactions of the Royal Society of London*, 221:163–198, 1920.

[108] J. H. Nielsen. Remaining stress-state and strain-energy in tempered glass fragments. *Glass Structures & Engineering*, 2(1):45–56, 2016.

[109] F. Zhou, J. Molinari, and K. T. Ramesh. Analysis of the brittle fragmentation of an expanding ring. *Computational Materials Science*, 37:74–85, 2006.

[110] D. E. Grady. Length scales and size distribtuions in dynamic fragmentation. *International Journal of Fracture*, 163:85–99, 2009.

[111] F. Zhou, J. Molinari, and K. T. Ramesh. Effects of material properties on the fragmentation of brittle materials. *International Journal of Fracture*, 139:169–196, 2006.

[112] L. T. Wilson, D. R. Reedal, M. E. Kipp, R. R. Martinez, and D. E. Grady. Comparison of calculated and experimental results of fragmenting cylinder experiments. Technical report, Sandia National Laboratories, SAND2000-1406C, 2000.

[113] M. E. Kipp, D. E. Grady, and J. W. Swegle. Experimental and numerical studies of high-velocity impact fragmentation. Technical report, Sandia National Laboratories, SAND93-0773, 1993.

[114] D. E. Grady and M. E. Kipp. Impact failure and fragmentation properties of metals. Technical report, Sandia National Laboratories, SAND98-0387, 1998.

[115] R. J. Weimer and H. C. Rogers. Dynamic fracture phenomena in high strength steels. *Journal of applied physics*, 50(12):8025–8030, 1979.

[116] A. I. Medved and A. E. Bryukhanov. The variation of young's modulus and the hardness with tempering of some quenched chromium steels. *Metal Science of Heat Treatment*, 11:706–708, 1969.

[117] S. Zhang, W. Jiang, and M. R. Tonks. Assessment of four strain energy decomposition methods for phase field fracture models using quasi-static and dynamic benchmark cases. *Materials Theory*, 6(6), 2022.

[118] B. Mitra, J. Hilden, and J. D. Litster. Effects of the granule composition on the compaction behavior of deformable dry granules. *Powder Technology*, 291:487–498, 2016.

[119] J. Kovacik. Correlation between young's modulus and porosity in porous materials. *Journal of Material Science Letters*, 18:1007–1010, 1999.

[120] D. Tromans and J. A. Meech. Fracture toughness and surface energies of minerals: theoretical estimates for oxides, sulphides, silicates, and halides. *Materials Engineering*, 15:1027–1041, 2002.

[121] J. K. Clobes and D. J. Green. Validation of single-edge V-notch diametral compression fracture toughness test for porous alumina. *Journal of Materials Science*, 37:2427–2434, 2002.

[122] J. Kovacik. Correlation between Young's modulus and porosity in porous materials. *Journal of Materials Science Letters*, 18:1007–1020, 1999.

[123] N. Ramakrishnan. Speed of sound in porous materials. *Bulletin Materials Science*, 17:499–504, 1994.

[124] B. Mitra, J. Hilden, and J. D. Litster. Compaction mechanics of plastically deformable dry granules. *Powder Technology*, 291:328–336, 2016.

[125] B. Mitra, J. Hilden, and J. D. Litster. Effects of the granule composition on the compaction behavior of deformable dry granules. *Powder Technology*, 291:487–498, 2016.

[126] R. M. German. Strength dependence on porosity for P/M compacts. *The International Journal of Powder Metallurgy and Powder Technology*, 13(4):259–271, 1977.

[127] J. Kovacik, L. Marsavina, and E. Linul. Poisson's ratio of closed-cell aluminum foams. *Materials*, 11(10), 2018.

[128] M. F. Ashby, A. G. Evans, N. A. Fleck, L. J. Gibson, J. W. Hutchinson, and H. N. G. Wadley. *Metal Foams: A Design Guide*. Butterworth-Heinemann, 2000.

[129] B. H. Smith, S. Szyniszewski, J. F. Hajjar, B. W. Schafer, and S. R. Arwade. Steel foam for structures: A review of applications, manufacturing and material properties. *Journal of Constructional Steel Research*, 7:1–10, 2012.

[130] J. P. Watt, G. F. Davies, and R. J. O'Connell. The elastic properties of composite materials. *Reviews of Geophysics and Space Physics*, 14(4):541–563, 1976.

[131] X. F. Zhang, L. Qiao, A. S. Shi, J. Zhang, and Z. W. Guan. A cold energy mixture theory for the equation of state in solid and porous metal mixtures. *Journal of Applied Physics*, 110, 2011.

[132] R. M. German. *Particulate Composites: Fundamentals and Applications*. Springer Nature, 2016.

[133] Z. Hashin. The elastic moduli of heterogenous materials. Technical report, Harvard University, Division of Engineering and Applied Physics, ONR Report No. 9, 1960.

[134] G. Heilig, N. Durr, M. Sauer, and A. Klomfass. Mesoscale mechanics of reactive materials for enhanced target effects. Technical Report I-69/12, Fraunhofer EMI, Freiburg, Germany, 2012.

[135] O. Mouraille. *Sounds propagation in dry granular materials: Discrete element simulations, theory, and experiments*. PhD thesis, University of Twente, Enshece, The Netherlands, 2009.

[136] S. R. Hostler. *Wave Propagation in Granular Materials*. PhD thesis, California Institute of Technology, Pasadena, California, 2005.

[137] B. Budiansky. On the elastic moduli of some heterogeneous materials. *Journal of the Mechanics and Physics of Solids*, 13:223–227, 1965.

[138] R. A. Hill. A self-consistent mechanics of composite materials. *Journal of the Mechanics and Physics of Solids*, 13:213–222, 1965.

[139] T. Mori and K. Tanaka. Average stress in matrix and average elastic energy of materials with misfitting inclusions. *Acta Metallurgica*.

[140] Y. Luo. Comparison of micromechanics models of particulate composites against microstructure-free finite element modeling. *Materials*, 15, 2022.

[141] J. A. Choren, S. M. Heinrich, and M. B. Silver-Thorn. Young's modulus and volume porosity relationships for additive manufacturing applications. *Journal of Materials Science*, 48:5103–5112, 2013.

[142] E. Pasternak and H. B. Muhlhaus. Generalised homogensisation procedures for granular materials. *Journal of Engineering Mathmatics*, 52:199–229, 2005.

[143] K. H. Kate, R. K. Enneti, S. J. Park, R. M. German, and S. V. Atre. Predicting powder-polymer mixture properties for PIM design. *Critical Reviews in Solid State and Materials Science*, 39(3):197–214, 2014.

[144] Y. Luo. Isotropized voigt-reuss model for prediction of elastic properties of particulate composites. *Mechanics of Advanced Materials and Structures*, 2021.

[145] J. Kovacik. Correlation between shear wave velocity and porosity in porous solids and rocks. *Journal of Powder Technology*, 2013, 2012.

[146] N. Hansen. Hall-Petch relation and boundary strengthening. *Scripta Materialia*, 51:801–806, 2004.

[147] J. W. Morris. The influence of grain size on the mechanical properties of steel. Technical report, Lawerence Berkeley National Lab, LBNL-47875, 2000.

[148] Y. Li, A. J. Bushby, and D. J. Dunstan. The hall-petch effect as a manifestation of the general size effect. *Proceedings of the Royal Society A*, 472, 2016.

[149] R. G. Munro. Analytical representations of elastic moduli data with simultaneous dependence on temperature and porosity. *Journal of Research of the National Institute of Standards and Technology*, 109:497–503, 2004.

[150] S. K. Datta, H. M. Ledbetter, and A. H. Shah. Ultrasonic-velocity studies of composite and heterogeneous materials. Technical report, University of Colorado, CUMER 87-1, 1986.

[151] P. Jonsen, H. A. Haggblad, and K. Sommer. Tensile strength and fracture energy of pressed metal powder by diametral compression test. *Powder Technology*, 176:148–155, 2007.

[152] C. Zhai, E. B. Herbold, and R. C. Hurley. The influence of packing structure and interparticle forces on ultrasound transmission in granular media. *Proceedings of the National Academy of Sciences*, 117(28):16234–16242, 2020.

[153] H. L. Ferrand. Modeling the effect of microstructure of elastic wave propagation in platelet-reinforced composites and ceramics. *Composite Structures*, 2019.

[154] K. Teramoto and H. Tano. Measurements of sound speed in granular materials simulated regolith. K. Lunar and Planetary Science XXXVI, Lunar and Planetary Institute, 2005.

[155] American Society for Testing and Materials. ASTM E9-19 Standard Test Methods of Compression Testing of Metallic Materials at Room Temperature. Technical report, ASTM, 2019.

[156] W. E. Luecke, L. Ma, S. M. Graham, and M. A. Adler. Repeatability and reproducibility of compression strength measurements conducted according to ASTM E9. Technical report, National Institute of Standards and Technology, NIST Technical Note 1679, 2009.

[157] American Society for Testing and Materials. ASTM E111-17 Standard test method for Young's modulus, tangent modulus, and chord modulus. Technical report, ASTM, 2017.

[158] J. G. Williams and C. Gamonpilas. Using the simple compression test to determine Young's modulus, Poisson's ratio and the Coulomb friction coefficient. *International Journal of Solids and Structures*, 45:4448–4459, 2008.

[159] K. T. Chau. Young's modulus interpreted from compression tests with end friction. *Journal of Engineering Mechanics*, 123(1), 1997.

[160] J. R. Taylor. *Introduction to Error Analysis: The study of uncertainties in physical measurements*. University Science Books, 2008.

[161] American Society for Testing and Materials. ASTM E1820-20b Standard Test Method for Measurement of Fracture Toughness. Technical report, ASTM, 2020.

[162] C. Keles and L. Tutluoglu. Investigation for proper specimen geometry for mode i fracture toughness testing with flattened Brazilian disc method. *Carbon*, 159:255–265, 2020.

[163] Y. Zhang and D. Yu. Comparative study on the test method for tensile elastic modulus of rock materials. *Advances in Civil Engineering*, 2019, 2019.

[164] A. A. Alabi, S. M. Tahir, M. A. Azmah Hanim, N. I. Zahari, and M. S. Anuar. Relationship between fracture toughness and relative density in iron and copper metal powder compacts. *Nigerian Journal of Engineering*, 26(3):77–90, 2019.

[165] J. Zhou, Y. Wang, and Y. Xia. Mode-I fracture toughness measurement of PMMA with the Brazillian disk test. *Journal of Material Science*, 41:5778–5781, 2006.

[166] American Society for Testing and Materials. ASTM E399 - 20a Standard Test Method for Plane-Strain Fracture Toughness of Metallic Materials. Technical report, ASTM, 2020.

[167] P. Jonsen. *Fracture and Stress in Powder Compacts*. PhD thesis, Lulea University of Technology, Lulea, Sweden, 2006.

[168] P. Jonsen and H. A. Haggblad. Fracture energy based constitutuve models for tensile fracture of metal powder compacts. *International Journal of Solids and Structures*, 2007.

[169] C. C. Degnan, P. H. Shipway, and A. R. Kennedy. Comparison of the green strength of warm compacted Astaloy CrM and Distaloy AR Densmix powder compacts. *Materials Science and Technology*, 20(6):731–738, 2004.

[170] D. Li and L. Wong. The Brazilian disc test for rock mechanics applications: Review and new insights. *Rock Mechanics and Rocke Engineering*, 46:269–287, 2012.

[171] M. R. Ayatollahi and M. R. M. Aliha. On the use of Brazilian disc specimen for calculating mixed mode I-II fracture toughness of rock materials. *Engineering Fracture Mechanics*, 2008.

[172] F. Carneiro. A new method to determine the tensile strength of concrete. In *Proceedings of the 5th meeting of the Brazilian Association for Technical Rules*, 1943.

[173] American Society for Testing and Materials. ASTM D3967-16 Standard Test Method for Splitting Tensile Strength of Intact Rock Core Specimens. Technical report, ASTM, 2016.

[174] G. Szendi-Horvath. Fracture toughness determination of brittle materials using small to extremely small specimens. *Engineering Fracture Mechanics*, 13(4):955–961, 1980.

[175] F. Liu, P. Xu, H. Zhang, C. Guan, D. Feng, and X. Wang. Use of time-of-flight ultrasound to measure wave speed in popular seedlings. *Forests*, 10, 2019.

[176] P. C. Hines, J. C. Osler, J. G. Scrutton, and L. J. Halloran. Time-of-flight measurements of acoustic wave speed in a sandy sediment at 0.6-20kHz. *IEEE Journal of Oceanic Engineering*, 35(3):502–515, 2010.

[177] K. T. Ramesh. *Springer Handbook of Experimental Solid Mechanics: Chapter 33. High Rates and Impact Experiments*. Springer, 2008.

[178] S. Lang. Design of a split Hopkinson bar apparatus for use with fiber reinforced composite materials. Master's thesis, Utah State University, Logan UT, 2012.

[179] D. Brizard, R. Ronel, and E. Jacquelin. Estimating measurement uncertainty on stress-strain curves from shpb. *Experimental Mechanics*, 57(5):735–742, 2017.

[180] J. C. Kline, B. P. Mason, J. P. Hooper, and R. J. Jouet. Energy release and fragmentation of brittle aluminum reactive material cases. *Propellants, Explosives, Pyrotechnics*, 46, 2021.

[181] J. A. Zukas. *High Velocity Impact Dynamics*. John Wiley & Sons, Inc., 1990.

[182] D. D. Anderson and K. D. Fickie. IBHVG2- A User's Guide. Technical report, Ballistic Research Laboratory, Aberdeen Proving Ground, MD, 1984.

[183] R. C. Ruff. Development of the materials division meteoroid simulation facility. Technical report, NASA Propulsion and Vehicle Engineering Laboratory, NASA TMX-53787, 1968.

[184] W. M. Mock and W. H. Holt. Nonaerodynamic sabot stripper for nswcdd 40-mm gas gun. Technical report, Naval Surface Warfare Center, NSWCDD/TR-92/447, 1992.

[185] F. Horz, M. J. Cintala, and E. L. Christiansen. Low-density sabot stripper: A feasibility study. *International Journal of Impact Engineering*, 153, 2021.

[186] S. H. Youngblood, S. Palmer, D. A. Avalos Violante, J. Kimberley, and M. J. Hargather. In situ measurement of the fragmentation behavior of al/ptfe reactive materials subjected to explosive loading, part 1: Fragment size measurements. *Propellants, Explosives, Pyrotechnics*, Forthcoming, 2022.

[187] E. L. Andreas. New estimates for the sublimation rate for ice on the moon. *Icarus*, 186:24–30, 2006.

[188] G. S. Settles. *Schlieren and shadowgraph techniques*. Springer-Verlag, 2001.

[189] R. Szeliski. *Computer Vision: Algorithms and Applications*. Springer, 2010.

[190] S. Palmer, S. H. Youngblood, J. Kimberley, and M. J. Hargather. In situ measurement of the fragmentation behavior of al/ptfe reactive materials subjected to explosive loading, part 2: Fragment velocity and trajectory measurements. *Propellants, Explosives, Pyrotechnics*, Forthcoming, 2022.

[191] S. Palmer. Three-dimensional fragment tracking and size estimation using stereo focused shadowgraphy. Master's thesis, New Mexico Tech, 2022.

[192] A. Jillavenkatesa, S. J. Dapkunas, and L. H. Lum. *Particle Size Characterization*. NIST, 2001.

[193] R. E. Pollard. Sieve test of metal powders. *Journal of Research of the National Bureau of Standards*, 39:487–505, 1947.

[194] Advantech Mfg. Test Sieving: Principles and Procedures. Technical report, Advantech Mfg. Manuals, 2001.

[195] American Society for Testing and Materials. Standard Specification for Woven Wire Test Sieve Cloth and Test Sieves. Technical report, ASTM, 2022.

[196] F. Meyer. Topographic distance and watershed lines. *Signal Processing*, 38:113–125, 1994.

[197] R. C. Gonzalez and R. E. Woods. *Digital Image Processing*. Pearson Education Inc., 2016.

[198] W. A. Johnson and R. F. Mehl. Reaction kinetics in processes of nucleation and growth. *Metals Technology*, 1939.

[199] S. R. Turns. *An Introduction to Combustion: Concepts and Applications*. McGraw-Hill, New York, NY, 2012.

[200] M. Huston. Flame propagation of Al/PTFE mechanically activated composites. Master's thesis, Iowa State University, Ames IA, 2017.

[201] M. Mayur, S. C. DeCaluwe, B. L. Kee, and W. G. Bessler. Modeling and simulation of the thermodynamics of lithium-ion battery intercalation materials in the open-source software Cantera. *Electrochimica Acta*, 323, 2019.

[202] D. A. Gunawardena and S. D. Fernando. Thermodynamic equilibrium analysis of methanol conversion to hydrocarbons using Cantera methodology. *Journal of Thermodynamics*, 2012, 2012.

[203] H. K. Moffat and C. F. Colon. Implementation of equilibrium aqueous speciation and solubility (EQ3 type) calculations into Cantera for electrolyte solutions. Technical report, Sandia National Laboratories, SAND2009-3115, 2009.

[204] J. Blecic, J. Harrington, and M. O. Bowman. TEA: A code for calculating thermochemical equilibrium abundances. *The Astrophysical Journal Supplement Series*, 225(4), 2016.

[205] S. H. Youngblood. Design and testing of a liquid nitrous oxide and ethanol fueled rocket engine. Master's thesis, New Mexico Institute of Mining and Technology, Socorro NM, 2015.

[206] G. Eriksson. Thermodynamic studies of high temperature equilibria, III. SOLGAS, a computer program for calculating the composition and heat condition of an equilibrium mixture. *Acta Chemica Scandinavica*, 21:1651–1658, 1971.

[207] D. R. Burgess. *NIST Chemistry WebBook, NIST Standard Reference Database Number 69*, chapter Thermochemical Data. National Institute of Standards and Technology, 2018.

[208] M. W. Chase, C. A. Davies, J. R. Downey, D. J. Frurip, R. A. McDonald, and A. N. Syverud. *NIST Standard Reference Database 13*, chapter NIST-JANAF Thermochemical Tables. National Institute of Standards and Technology, 1998.

[209] NIST and SEMATECH. e-Handbook of Statistical Methods. Technical report, National Institure of Standards and Technology, 2012.

[210] B. J. McBride, M. J. Zehe, and S. Gordon. NASA Glenn Coefficients for calculating thermodynamic properties of individual species. Technical report, NASA Glenn Research Center, TP2002-211556, 2002.

[211] F. Gozzo and G. Camaggi. Oxidation reactions of tetrafluorethylene and their products-I: Auto-oxidation. *Tetrahedron*, 22(6):1765–1770, 1966.

[212] S. F. Lau, H. Suzuki, and B. Wunderlich. The thermodynamic properties of polytetrafluoroethylene. *Journal of polymer science, polymer physics edition*, 22(3):379–405, 1983.

[213] J. B. Dunn, C. James, L. Gaines, K. Gallagher, Q. Dai, and J. C. Kelly. Material and energy flows in the production of cathode and anode materials for lithium ion batteries. Technical report, Argonne National Laboratory, 2015.

[214] J. Davis, E. Molnar, and I. Novosselov. Nanostructure transition of soot aggregrates to mature soot aggregates in diluted diffusion flames. *International Journal of Fracture*, 169:61–75, 2011.

[215] J. Xi, G. Yang, J. Cai, and Z. Gu. A review of recent research results on soot: The formation of a kind of carbon-based material in flames. *Frontiers in Materials*, 8, 2021.

[216] A. Dobrosavljevic, N. Perovic, and K. Maglic. Thermophysical properties of POCO AXM-5Q1 graphite in the 200 to 1800 K range. *High Temperatures-High Pressures*, 19:303–310, 1987.

[217] Y. Takahashi and E. Westrum. Glassy carbon low-temperature thermodynamic properties. *The Journal of Chemical Thermodynamics*, 2(6):847–854, 1970.

[218] H. A. Michelson, M. B. Colket, P. Bengtsson, A. D'Anna, P. Desgroux, B. S. Haynes, J. H. Miller, G. J. Nathan, H. Pitsch, and H. Wang. A review of terminology used to describe soot formation and evolution under combustion and pyrolytic conditions. *ACS Nano*, 14(10):12470–12490, 2020.

[219] K. A. Kroos and M. C. Potter. *Thermodynamics for engineers*. Cengage Learning, 2015.

[220] A. Williams, I. Shancitam, I. Altmanm, N. Tamura, and M. L. Pantoya. On the pressure generated by thermite reactions using stress-altered aluminum particles. *Propellants, Explosives, Pyrotechnics*, 46:99–106, 2020.

[221] L. Wang, D. Luss, and K. S. Martirosyan. The behavior of nanothermite reaction based on Bi2O3/Al. *Journal of Applied Physics*, 110, 2011.

[222] V. Baijot, L. Glavier, J. M. Ducere, M. D. Rouhani, C. Rossi, and A. Esteve. Modeling the pressure generation in aluminum based thermits. *Propellants, Explosives, Pyrotechnics*, 40(3):402–412, 2015.

[223] Richard Stone. *Introduction to internal combustion engines*. SAE International, Warrendale, PA, 3rd edition, 1999.

[224] R. G. Ames. Energy release characteristics of impact-initiated energetic materials. volume 896. Materials Research Society Symposium, 2006.

[225] B. Feng, X. Fang, Y. Li, S. Wu, Y. Mao, and H. Wang. Reactions of Al/PTFE under impact and quasi-static compression. *Advances in Materials Science and Engineering*, 2015, 2015.

[226] B. Feng, Y. Li, S. Wu, H. Wang, Z. Tao, and X. Fang. A crack-induced initiation mechanism of Al-PTFE under quasi-static compression and the investigation of influencing factors. *Materials and Design*, 108:411–417, 2016.

[227] B. Feng, X. Fang, H. Wang, W. Dong, and Y. Li. The effect of crystallinity on compressive properties of Al/PTFE. *Polymers*, 8(356), 2016.

[228] E. Hunt, S. Malcolm, M. Pantoya, and F. Davis. Impact ignition of nano and micron composite energetic materials. *International Journal of Impact Engineering*, 36:842–846, 2009.

[229] C. Jiang, S. Cai, L. Mao, and Z. Wang. Effect of porosity on dynaic mechanical properties and impact response characteristics of high aluminum content PTFE/AL energetic materials. *Materials*, 13(140), 2019.

[230] H. Ren, W. Li, and J. Ning. Effect of temperature on the impact ignition behavior of the aluminum/polytetrafluoroethylene reactive material under multiple pulse loading. *Materials and Design*, 189, 2020.

[231] J. Wu, Q. Liu, B. Feng, S. Wu, S. Chang, Z. Gao, Q. Yin, Y. Li, L. Ziao, and J. Huang. A comparative study on the mechanical and reactive behavior of three fluorine-containing thermites. *Royal Society of Chemistry Advances*, 10:5533–5539, 2020.

[232] H. Wang, Y. Zheng, Q. Yu, Z. Liu, and W. Yu. Impact-induced initiation and energy release behavior of reactive materials. *Journal of Applied Physics*, 110, 2011.

[233] J. Huang, Z. Fang, Y. Li, B. Feng, H. Wang, and K. Du. The mechanical and reaction behavior of PTFE/AL/Fe2O3 under impact and quasi-static compression. *Advances in materials science and engineering*, 2017, 2017.

[234] M. W. Beckstead. A summary of aluminum combustion. Internal Aerodynamics in Solid Rocket Propulsion, RTO/VKI special course, 2004.

[235] A. Rai, K. Park, L. Zhou, and M. R. Zachariah. Understanding the mechanism of aluminum nanoparticle oxidation. *Combustion Theory and Modeling*, 10(5):843–859, 2006.

[236] D. C. Montgomery. *Design and Analysis of Experiments*. John Wiley and Sons, Inc., 8th edition, 2012.

[237] P. Wang and G. Hall. Friction, impact, and electrostatic discharge sensitivities of energetic materials. Technical report, Monsanto Research Corporation, MLM-3252, 1985.

[238] M. Takeda, T. Onishi, S. Nakakubo, and S. Fujimoto. Physical properties of iron-oxide scales on Si-containing steels at high temperatures. *Materials Transactions*, 50(9):2242–2246, 2009.

[239] S. P. Jupp. *Fundamental Modeling of Friction During the Hot Rolling of Steel*. PhD thesis, University of Sheffield, Sheffield, England, 2005.

[240] Horiba. Application note: Particle size and shape of abrasives. Technical report, Horiba, AN187, 2022.

[241] Horiba. A guidebook to particle size analysis. Technical report, Horiba, 2022.

[242] J. G. Whiting, E. J. Garboczi, V. N. Tondare, J. H. Scott, M. A. Donmez, and S. P. Moylan. A comparison of particle size distribution and morphology data acquired using lab-based and commercially available techniques: Application to stainless steel powder. *Powder Technology*, 396:648–662, 2022.

[243] M. V. Shcherbakov, A. Brebels, N. L. Shcherbakova, A. P. Tyukov, T. A. Janovsky, and V. A. Kamaev. A survey of forecast error measures. *World Applied Sciences Journal 24 (Information Technologies in Modern Industry, Education & Society)*, pages 171–176, 2013.

[244] J. D. Eshelby. The determination of the elastic field of an ellipsoidal inclusion, and related problems. *Proceedings of the Royal Society of London. Series A, Mathematical and Physical Sciences*, 241:376–396, 1957.

[245] J. Kovacik. Correlation between poisson's ratio and porosity in porous materials. *Journal of Material Science*, 41:1247–1249, 2005.

[246] M. P. Lutz and R. W. Zimmerman. The effect of pore shape on the Poisson ratio of porous materials. *Mathematics and mechanics of solids*, 26(8):1191–1203, 2021.

[247] P. A. Berge, B. P. Bonner, and J. G. Berryman. Ultrasonic velocity-porosity relationships for sandstone analogs made from fused glass beads. *Geophysics*, 60:19–37, 1995.

[248] MatWeb LLC. Polytetrafluoethylene (PTFE), Extruded data sheet. *https://www.matweb.com/*, 2022.

[249] A. Mostafapor and V. Mohammadinia. Mechanical properties and microstructure evolution of AA1100 aluminum sheet processed by accumulative press bonding process. *Acta Metallurgica Sinica*, 29(8):735–741, 2016.

[250] X. Hu and K. Duan. Size effect: Influence of proximity of fracture process zone to specimen boundary. *Engineering Fracture Mechanics*, 74:1093–1100, 2007.

[251] P. J. Joyce and J. A. Joyce. Evaluation of the fracture toughness properties of polytetrafluoroethylene. *International Journal of Fracture*, 127(4):361–385, 2004.

[252] R. J. Bucci and E. A. Starke. Selecting aluminum alloys to resist failure by fracture mechanisms. *ASM Handbook, Volume 19: Fatigue and Fracture*, pages 771–812, 1996.

[253] N. P. Cannon, E. M. Schulson, T. R. Smith, and H. J. Frost. Wing cracks and brittle compressive fracture. *Acta Metallurgica et Materialia*, 38:1955–1962, 1990.

[254] L. Zhang, X. Bi, and J. Grace. Measurements of electrostatic charging of powder mixtures in a free-fall test device. *Procedia Engineering*, 102:295–304, 2015.

[255] M. Evans, N. Hastings, and B. Peacock. *Statistical Distributions, Ch. 5: Beta Distribution*. Wiley, 2016.

[256] D. E. Grady. Scaling issues in dynamic fragmentation. Technical report, Sandia National Laboratories, SAND94-3187C, 1994.

[257] J. Xiao, Z. Nie, Z. Wang, Y. Du, and E. Tang. Energy release behavior of Al/PTFE reactive materials powder in a closed chamber. *Journal of Applied Physics*, 127, 2020.

[258] S. H. Youngblood, M. J. Hargather, R. Morales, J. Phillip, J. Peguero, M. Grubelich, and W. V. Saul. Sea level performance of nitrous oxide and ethanol bipropellant rocket engines. *International Journal of Energetic Materials in Chemical Propulsion*, 21, 2022.

[259] Deng. J, J. Qu, Q. Wang, X. Zhai, Y. Xiao, Y. Cheng, and C. Shu. Minimum ignition temperature of aluminum dust clouds via the Godbert-Greenwald furnace. *Process safety and environmental protection*, 129:176–183, 2019.

[260] J. Liu, Q. Chu, and D. Chen. On modeling the combustion of a single micron-sized aluimnum particle with the effect of oxide cap. *ACS Omega*, 6:34263–34275, 2021.

NOMENCLATURE AND ABBREVIATIONS

Abbreviations

$(C_2F_4)_n$	Polymerized Tetrafluoroethylene (PTFE)
1D	One-dimensional
2D	Two-dimensional
3D	Three dimensional
AFT	Adiabatic flame temperature
Al	Aluminum
Al_2O_3	Aluminum oxide
ASTM	American Society for Testing of Materials
ATM	Applied Test Systems
B_2O_3	Boron trioxide
B_4C	Boron carbide
BMG	Browning machine gun
C_2F_4	Tetrafluoroethylene
CAD	Computer-aided design
CIP	Cold isostatic pressing
Co	Cobalt
CTOD	Crack tip opening displacement
Cu	Copper
Cu_2O	Copper(I) oxide
CuO	Copper oxide
DCTT	Diametrical compression testing technique
DIF	Dynamic increase factor

DIM	Difference of means
EMS	Engineered Materials Solutions
ERT	Expanding ring test
Fe	Iron
Fe_2O_3	Iron oxide
GRM	Generalized rule of mixtures
HIP	Hot isostatic pressing
HP	Fixed enthalpy and pressure equilibrium condition
IBHVG2	Interior ballistics of high velocity guns
Mg	Magnesium
MoO_3	Molybdenum oxide
Ni	Nickel
NIST	National Institute of Standards and Technology
PDV	Photon Doppler Velocimetry
RM	Reactive material
RMSPE	Root Mean Square Percentage Error
Sn	Tin
SVDCT	Single-edge V-notch diametrical compression test
TiC	Titanium carbide
TiO_2	Titanium dioxide
TMD	Theoretical maximum density
TOF	Time-of-flight
TP	Fixed temperature and pressure equilibrium condition
UTM	Universal testing machine
UV	Fixed internal energy and volume equilibrium condition
VCS	Villars-Cruise-Smith
VISAR	Velocity interferometer system for any reflector
W	Tungsten

WC	Tungsten carbide
WC	Tungsten-carbide
WO_3	Tungsten oxide
WO_3H_2O	Hydrated tungsten oxide
Zr	Zirconium
ZrO_2	Zirconium dioxide

Subscripts

c	Property of a composite material
cb	Property of the combustion bomb
e	Engineering
I	Incident
i	Index of a component or species of a mixture
j	Index of a chemical element in a mixture
JC	Johnson cook parameters
R	Reflected
T	Transmitted
t	True
ult	Ultimate value
VC	Property of the vented calorimeter

Variables

α	Half arc length angle
α_s	Stoichiometric coefficient
$\bar{\dot{\varepsilon}}$	Average strain rate of impact
$\bar{\dot{\varepsilon}}_{vir,g}$	Strain rate from generalized radial strain relation
$\bar{\dot{\varepsilon}}_{vir}$	Radial strain from impact and residual velocity difference
$\bar{\dot{\varepsilon}}_{vr}$	Radial strain from radial expansion velocity
$\bar{\sigma}_s$	Mean axial compressive stress

$\bar{r}$	Ratio of radial position over total radius
$\bar{x}$	Sample mean
β	Characteristic length scale of power-law fragment distribution
β_b	Scaling constant od particle burning power-law
β_m	Total number of moles of chemical element
ΔH	Change in enthalpy
ΔP_{vc}	Change in quasi-static pressure of vented calorimeter
ΔQ_{vc}	Heat released into vented calorimeter
ΔT	Change in temperature of thermodynamic system
ΔU	Change in internal energy
δV_G	General velocity uncertainty from images
δ	Error of estimation
$\Delta_f h_i^\circ$	Molar heat of formation of ith species at 298.15 K
$\dot{\rho}$	Rate in changing density
$\dot{\sigma}_s$	Mean axial strain rate
$\dot{\varepsilon}$	Strain rate
$\dot{\varepsilon}_{long}$	Longitudinal strain rate
$\dot{\varepsilon}_{rad}$	Radial strain rate
$\dot{\varepsilon}_{xx}$	Strain rate in the x-x direction
$\dot{\varepsilon}_{yy}$	Strain rate in the y-y direction
$\dot{\varepsilon}_{zz}$	Strain rate in the z-z direction
η	Number of samples
Γ	Total surface energy density of fragment element
γ	Ratio of specific heats
κ	Local kinetic energy density
λ	Nominal (characteristic) fragment size
λ_{co}	Activity of condensed phase species

λ_g	Activity of a gas species
λ_i	Activity of the ith species
$\lambda_{m,cu}$	Mott cubic fragment size
$\lambda_{m,sp}$	Mott spherical fragment size
λ_{MEB}	Characteristic fragment size by minimizing the energy of the dilating body
λ_{MED}	Characteristic fragment size by minimizing the energy density of fragment
λ_{MEF}	Characteristic fragment size by minimizing the energy of fragment
μ_i°	Standard state chemical potential of ith species
μ_c	Characteristic length scale of exponential fragment distribution
μ_i	Chemical potential of ith species
μ_m	Mott parameter
μ_{TP}	True population mean
ν_b	Poisson's ratio of Kolsky bar
ν_o	Poisson's ratio of a full density composite material
ν_p	Poisson's ratio of a porous composite material
ν_{rm}	Poisson's ratio of an RM
ν_r	Surface area to volume ratio of fragment element
$\partial P/\partial t$	Rate f quasi-static pressure change
Π	Weighting factor of fragment distribution
Ψ	Dimensionality of fragmenting object
ρ	Density
ρ_b	Density of Kolsly bar
ρ_c	Density of a composite material
ρ_{IP}	Density of impact plate
ρ_s	Density of RM specimen
σ_x°	Horizontal stress in SVDCT specimen

σ_{1um}	Empirical constant of generalized Spriggs equation for strength
σ_b	Average tensile stress of bulk body before fracture
σ_{comp}	Compressive stress
σ_{cr}	Critical stress state at failure of bulk body
σ_c	Composite material strength
$\sigma_{d,max}$	Peak dynamic compressive stress
σ_f	Failure stress
$\sigma_{o,d}$	Particle dislocation stress for Hall-Petch relation
σ_o	Material strength of a fully dense material
σ_p	Material strength of a porous material
σ_{SD}	Standard deviation of sample set
$\sigma_{t,max}$	Peak horizontal tensile stress in SVDCT specimen
σ_{TB}	Transverse bending strength
σ_{vm}	Von Mises stress
$\sigma_{y,db}$	Yield stress of the dilating body
$\sigma_{Y,TP}$	Yield strength of impact plate
σ_Y	Yield stress
Θ	Significance level
υ	Elastic strain energy density of fragment element
ε	Strain
ε_b	Average strain of bulk body before fracture
ε_b	Strain in Kolsky bar
ε_{long}	Longitudinal strain
ε_p	Plastic strain
ε_{rad}	Radial strain
$\forall$	Volume
$\forall_{f,i}$	Volume fraction of ith component

$\forall_{FE}$	Volume of fragment element
$\forall_g$	Volume of gas mixture
ζ	Surface energy
a	Radius of fragment element
A_{act}	Actual projected area of fragments
A_b	Cross-sectional area of bar
A_{FE}	Fragment element surface area
A_{frag}	Measured area of a fragment
A_h	Area of hole in impact plate of vented calorimeter
A_{obs}	Observed projected area of fragments
A_{reg}	Area of region that fully contains fragment cloud
A_s	Cross-sectional area of RM specimen
C	Wave speed
C_p°	Standard state constant pressure specific heat at 0.101 MPa
C_0	Bar wave speed used in Grady equations
C_b	Bulk wave speed
c_{cr}	Characteristic crack dimensions
C_d	Dilatational wave speed
C_o	Bar wave speed
c_{sv}	SVDCT notch depth
C_{sys}	Specific heat of thermodynamic system
C_s	Shear wave speed
C_w	Wave speed of interest for TOF measurements
CL	Confidence Level
d	Diameter
$D10$	Corresponding particle size when the cumulative percentage reaches 10%

$D50$	Corresponding particle size when the cumulative percentage reaches 50%
$D90$	Corresponding particle size when the cumulative percentage reaches 90%
D_b	Diameter of Kolsky bars
D_b	Diameter of burning particle
D_{eq}	Equivalent spherical diameter of a fragment
d_{sp}	Equivalent spherical diameter
D_s	Undeformed RM specimen diameter
dm/dt	Rate of change in mass
dQ/dt	Rate of heated addition
E	Elastic modulus
E'_{Fe}	Total energy of fragment element
E'_{KE}	Local kinetic energy of fragment element
E'_{PE}	Elastic strain energy of fragment element
E'_{SE}	Surface energy of fragment element
E_o	Elastic modulus of fully dense material
E_b	Elastic modulus of Kolsky bar
$E_{c,r}$	Reuss average of elastic modulus of a composite material
$E_{c,v}$	Voigt average of elastic modulus of a composite material
E_{db}	Total energy of dilating body
E_{FE}	Total energy density of fragment element
$E_{KE,db}$	Total kinetic energy in dilating body that is available for fragmentation
E_{KE}	Kinetic energy of bulk body
$E_{PE,db}$	Stored elastic energy in dilating body that is available for fragmentation
E_p	Elastic modulus of a porous material
$E_{SE,db}$	Total surface energy in dilating body that is available for fragmentation

E_S	Elastic modulus of stiff constituent
$E_{TP,c}$	Bulk thermodynamic property of composite material
$E_{TP,i}$	Thermodynamic property of ith component
E_w	Elastic modulus of compliant constituent
F	Load (force) applied to specimen by UTM crosshead
F_{ci}	Force at crack initiation
f_{exp}	Generalized exponential integral function
$F_{M,1}(C)$	Composition dependency function of a material property
$F_{M,2}(p)$	Porosity dependency function of a material property
$F_{M,3}(S_c)$	Particle size dependency function of a material property
F_s	Normal force at specimen/Kolsky bar interface
G	Fracture energy release rate
G_{cr}	Critical energy release rate during fracture
G_{IC}	Energy release associated with Mode-I crack growth
G_{mix}	Gibbs free energy of multiphase mixture
G_o	Shear Modulus of a full density composite material
G_p	Shear Modulus of a porous composite material
H°	Standard enthalpy at 0.101 MPa
$h^\circ_{298,i}$	Standard state molar entropy of ith species at 298.15 K
h°_i	Standard state molar entropy of ith species
h_{reacs}	Total molar enthalpy of reactants mixture
HC_{error}	Enthalpy convergence error
J	Fractal parameter for GRM
J_σ	Material strength fractal scaling parameter
J_E	Elastic modulus fractal scaling parameter
J_k	Fractal parameter for Mode-I fracture toughness
K	Stress intensity factor

k	Number of species in mixture
$K_{1\mu m}$	Empirical constant of generalized Spriggs equation for fracture toughness
K_b	Bulk Modulus
K_C	Fracture toughness
K_c	Critical stress intensity
K_f	Dynamic initiation fracture toughness
k_g	Gauge Factor
k_g	Hall-Petch sensitivity parameter
K_{IC}	Mode-I static fracture toughness
k_s	Power-law fragment distribution scaling exponent
$K_{y,db}$	Bulk modulus of the dilating body
L	Length
L_{arc}	Arc length for SVDCT specimens
L_b	Kolsky bar length
L_o	Undeformed RM specimen length
L_{pd}	Propagation distance of crack
L_w	Distance traveled by wave in TOF measurements
L_x	Travel in x direction
L_y	Travel in y direction
M	Bulk material property of interest
m	Mass
M_c	Bulk material property of composite material
$M_{d,o}$	Total mass of fragments in m_d
m_d	Normalized fragment mass distribution
m_f	Mass of fragment
M_i	Material property of ith component

M_p	Material property of material phase that comprises pores
m_{sys}	Mass of thermodynamic system
m_s	Mass of RM specimen
N	Total number of components (species)
n	Number of moles of gas in mixture
$n_{\sigma,i}$	Sensitivity parameter of $\sigma_{1um}$to particle or grain size
N_{bin}	Number of fragments observed for the bin size
$N_{d,o}$	Total number of fragments in N_d
N_d	Normalized fragment number distribution
N_f	Total number of fragments that can be volumetrically contained by the dilating body
$n_{g,i}$	Number of moles of ith gas species
$n_{g,mix}$	Total number of gas phase moles
n_i	Number of moles of ith species in mixture
$n_{K,i}$	Sensitivity parameter of Mode-I fracture toughness to particle or grain size
P	Pressure
p	Porosity of a material
P_{atm}	Ambient static pressure
$P_{ax,o}$	Applied axial pressure
P_{ax}	Realized axial pressure
$P_{g,i}$	Partial pressure of ith gas species
P_{ini}	Initial pressure
P_{max}	Max quasi-static pressure
P_{mix}	Total pressure of gas mixture
P_{Pr}	Pressing pressure
Q	Total net heat
Q_{comb}	Energy release of a combustion reaction

Q_{KE}	Heat addition to vented calorimeter from kinetic energy of specimen
Q_R	Heat released by a reaction
Q_W	Heat loss to the bomb walls
r	Radius of fragment element mass shells
R_{db}	Radius of dilating body
R_{sv}	Radius of SVDCT specimen
r_{sv}	Radial position on SVDCT specimen
r_s	Radius of cylindrical RM specimen
R_u	Ideal gas constant
r_y	Plastic zone size
s	Linear fragment size
S°	Standard entropy at 0.101 MPa
s_i°	Standard state molar entropy of ith species
S_c	Average particle (grain) size
s_{mean}	Mean fragment size
s_m	Mean equivalent diameter of the bin size
s_o	Minimum fragment size
T	Temperature
t	Time
T_*	Homologous temperature
t_{cr}	Time at failure of bulk body
t_c	Time scale of particle combustion
t_{dist}	Two-tailed t-distribution
t_{IP}	Thickness of impact plate
t_L	Temporal resolution of laser
$t_{max,vc}$	Time to peak pressure
T_{ref}	Reference state temperature

t_{sv}	Thickness of SVDCT specimen
t_t	Transit time of wave in TOF measurements
U	Internal energy
v	Particle velocity
V_{ex}	Excitation voltage
V_{Im}	Impact velocity
$V_{m,k}$	Measured kolsky strain gauge voltage
V_{rad}	Radial expansion velocity
V_{res}	Residual velocity
V_{sb}	Kolsky striker bar velocity
x	Displacement of UTM crosshead
x_cor	Corrected displacement of specimen
Y_i	Mass fraction of ith component
Y_K	Stress intensity constant

APPENDIX A

GRADY FRAGMENTATION MODEL SUPPLEMENTAL DERIVATIONS

Grady[60] originally proposed the kinetic energy density of a fragment element, κ, as a function of the surface area to volume ratio, ν, as:

$$\kappa = \frac{27}{10}\frac{\rho\dot{\varepsilon}^2}{\nu^2} \tag{A.1}$$

Where ρ is the density of the fragment element and $\dot{\epsilon}$ is the strain rate the element is subjected to. In subsequent work by Grady[61], Equation A.1 was reformed into a function of the nominal fragment size, λ, as:

$$\kappa = \frac{1}{120}\rho\dot{\varepsilon}^2\lambda^2 \tag{A.2}$$

The rederivation of the kinetic energy density of a fragment element, κ, following the fragmentation theory proposed by Grady[60] found that Grady[61] had made an error in reforming Equation A.1. As such, Equation A.2 reported by Grady[61] is incorrect. To reform Equation A.1 to be a function of λ, the relation for a spherical element $\nu = 3/a = 6/\lambda$[60] is applied to remove the dependency on ν, yielding:

$$\begin{aligned}\kappa &= \frac{27}{10}\frac{\rho\dot{\varepsilon}^2}{(6/\lambda)^2} \\ &= \frac{27}{10}\frac{\rho\dot{\varepsilon}^2\lambda^2}{36} \\ &= \frac{9}{120}\rho\dot{\varepsilon}^2\lambda^2\end{aligned}$$

Thus, the proper prefactor for κ as a function of λ is $9/120$, and not $1/120$ as reported by Grady[61].

APPENDIX B

INDIVIDUAL SPECIMEN MEASUREMENTS OF MECHANICAL RESPONSE AND FRAGMENTATION

Quasistatic Compression and Dilatational Wave Speed Measurements

Variant	Composition (Mass Fracs.)			Desired	6.35mm	Length	Diameter	Density	Porosity	Area	D TOF	D-Speed	E	σ_y	σ_c
	Al	Fe2O3	PTFE	Porosity	Cylinder #	mm	mm	g/cm3	%	mm2	us	m/s	Gpa	Mpa	Mpa
100Al-F	100%	0%	0%	5%	1a	6.16	6.35	2.553	6%	31.67	2.3	5356.522	24.4573	-	-
					2a	6.24	6.35	2.566	6%	31.67	2.53	4932.806	19.984	-	-
					3a	6.23	6.35	2.544	6%	31.67	2.5	4984	24.7735	-	-
					4a	6.44	6.36	2.493	8%	31.77	2.53	5090.909	28.1862	-	-
				20%	1a	6.01	6.34	2.182	19.7%	31.57	3.38	3556.213	7.6312	-	55.4595
					2a	6.27	6.34	2.198	19.1%	31.57	3.46	3624.277	8.2771	-	65.9184
					3a	6.28	6.34	2.199	19.0%	31.57	3.43	3661.808	7.6029	-	55.8931
					4a	6.29	6.34	2.201	19.0%	31.57	3.48	3614.943	9.335	-	67.845

Variant	Composition (Mass Fracs.)			Desired	6.35mm	Length	Diameter	Density	Porosity	Area	D TOF	D-Speed	E	σ_y	σ_c
	Al	Fe2O3	PTFE	Porosity	Cylinder #	mm	mm	g/cm3	%	mm2	us	m/s	Gpa	Mpa	Mpa
100Al-C	100%	0%	0%	5%	1a	6.12	6.37	2.523	6.4%	31.87	2.39	5121.339	16.7625	99.2833	109.587
					2a	6.1	6.37	2.531	6.1%	31.87	2.54	4803.15	19.4296	103.9417	114.3243
					3a	6.19	6.36	2.532	6.0%	31.77	2.62	4725.191	11.467	97.9311	105.8464
					4a	6.09	6.37	2.520	6.5%	31.87	2.75	4429.091	19.187	113.2986	124.615
				20%	1a	6.39	6.36	2.123	21.2%	31.77	6.74	1896.142	2.9304	-	31.3676
					2a	6.31	6.36	2.160	19.9%	31.77	6.2	2035.484	5.8198	-	37.6753
					3a	6.32	6.36	2.132	20.9%	31.77	6.58	1920.973	6.4157	-	36.6326
					4a	6.51	6.36	2.142	20.5%	31.77	6.44	2021.739	6.8986	-	38.7864

Quasistatic Compression and Dilatational Wave Speed Measurements

Variant	Composition (Mass Fracs.)			Desired	6.35mm	Length	Diameter	Density	Porosity	Area	D TOF	D-Speed	E	σ_y	σ_c
	Al	Fe2O3	PTFE	Porosity	Cylinder #	mm	mm	g/cm3	%	mm2	us	m/s	Gpa	Mpa	Mpa
100PTFE-F	0%	0%	100%	5%	1	6.1	6.32	2.153	5.4%	31.37069	11.2	1089.286	0.70855	10.5629	12.9034
					2	6.32	6.33	2.157	5.2%	31.47004	11.45	1103.93	0.63544	10.8584	13.2867
					3	6.22	6.33	2.156	5.2%	31.47004	11.25	1105.778	0.65643	9.529	12.58
					4	6.19	6.33	2.146	5.7%	31.47004	11.7	1058.12	0.64597	9.7972	12.4386
				20%	1	FAILED TO CONSOLIDATE									
					2										
					3										
					4										

Quasistatic Compression and Dilatational Wave Speed Measurements

Variant	Composition (Mass Fracs.) Al	Fe2O3	PTFE	Desired Porosity	6.35mm Cylinder #	Length mm	Diameter mm	Density	Porosity %	Area mm2	D TOF us	D-Speed m/s	E Gpa	σ_y Mpa	σ_c Mpa
100PTFE-C	0%	0%	100%	5%	1	6.17	6.32	2.201	3.6%	31.37069	9.8	1259.184	0.53234	9.3389	12.2726
					2	6.02	6.32	2.197	3.8%	31.37069	9.62	1251.559	0.50976	9.5728	12.3362
					3	6.07	6.31	2.234	2.2%	31.27149	9.14	1328.228	0.627	8.652	12.761
					4	6.1	6.32	2.184	4.4%	31.37069	9.75	1251.282	0.59303	8.6389	12.1944
				20%	1	6.57	6.34	1.760	22.9%	31.56955	UNABLE TO DETECT REFLECTED PULSE		0.14142	2.7262	2.9589
					2	6.56	6.34	1.769	22.5%	31.56955			0.14768	2.7115	3.0998
					3	6.55	6.32	1.767	22.6%	31.37069			0.1506	2.4525	2.818
					4	6.02	6.32	1.774	22.3%	31.37069			0.154	2.818	3.0998

Variant	Composition (Mass Fracs.) Al	Fe2O3	PTFE	Desired Porosity	6.35mm Cylinder #	Length mm	Diameter mm	Density g/cm3	Porosity %	Area mm2	D TOF us	D-Speed m/s	E Gpa	σ_y Mpa	σ_c Mpa
75Al/25PTFE-F	78.70%	0.00%	21.30%	5%	1	6.35	6.34	2.529	3.5%	31.56955	6.42	1978.193	3.088	-	51.1475
					3	6.38	6.34	2.537	3.2%	31.56955	5.3	2407.547	4.7303	34.7577	54.6701
					3	6.34	6.34	2.518	4.0%	31.56955	5.64	2248.227	3.21	-	53.5428
				20%	1	6.39	6.33	2.103	3.2%	31.47004	9.01	1418.424	1.4744	11.9169	12.1176
					2	6.44	6.34	2.100	4.0%	31.56955	9.92	1298.387	1.258	-	11.131
					3	6.39	6.34	2.106782	4.0%	31.56955	10.5	1217.143	1.093	-	11.836

Variant	Composition (Mass Fracs.) Al	Fe2O3	PTFE	Desired Porosity	6.35mm Cylinder #	Length mm	Diameter mm	Density g/cm3	Porosity %	Area mm2	D TOF us	D-Speed m/s	E Gpa	σ_y Mpa	σ_c Mpa
75Al/25PTFE-C	78.70%	0%	21.30%	5%	1	6.28	6.34	2.557	1.9%	31.57	6.92	1815.0	1.41	28.87	29.03
					2	6.21	6.34	2.550	2.2%	31.57	7.88	1576.1	1.25	28.09	28.60
					3	6.3	6.34	2.549	2.2%	31.57	6.61	1906.2	1.21	29.18	29.17
				20%	1	6.42	6.34	2.122	18.6%	31.57	UNABLE TO DETECT REFLECTED PULSE		0.58	-	5.92
					2	6.24	6.34	2.122	18.6%	31.57			0.70	-	5.78
					3	6.25	6.34	2.129	18.4%	31.57			0.60	-	5.64

Quasistatic Compression and Dilatational Wave Speed Measurements

Variant	Composition (Mass Fracs.)			Desired	6.35mm	Length	Diameter	Density	Porosity	Area	D TOF	D-Speed	E	σ_y	σ_c
	Al	Fe2O3	PTFE	Porosity	Cylinder #	mm	mm	g/cm3	%	mm2	us	m/s	Gpa	Mpa	Mpa
50Al/50PTFE-F	55.19%	0.00%	44.81%	5%	1	6.3	6.33	2.411	4.3%	31.47	7.81	1613.3	1.92	14.74	22.90
					2	6.36	6.33	2.413	4.2%	31.47	7	1817.1	1.89	16.56	23.61
					3	6.29	6.33	2.415	4.1%	31.47	6.92	1817.9	2.35	16.33	24.59
					4	6.4	6.33	2.414	4.2%	31.47	7.29	1755.8	2.01	15.20	23.46
				20%	1	6.39	6.33	2.103	20.8%	31.47	9.01	1418.4	1.47	11.92	12.12
					2	6.44	6.34	2.100	21.1%	31.57	9.92	1298.4	1.26	-	11.13
					3	6.43	6.33	1.992	20.9%	31.47	-	-	0.45	-	5.65
					4	6.34	6.33	1.984763	21.2%	31.47	10.5	1217.1	0.39	-	5.51

Variant	Composition (Mass Fracs.)			Desired	6.35mm	Length	Diameter	Density	Porosity	Area	D TOF	D-Speed	E	σ_y	σ_c
	Al	Fe2O3	PTFE	Porosity	Cylinder #	mm	mm	g/cm3	%	mm2	us	m/s	Gpa	Mpa	Mpa
50Al/50PTFE-C	55.19%	0.00%	44.81%	5%	1	6.32	6.34	2.406	4.2%	31.57	-	-	0.73	9.99	13.95
					2	6.32	6.34	2.426	3.4%	31.57	9.46	1336.15	1.07	10.30	15.08
					3	6.29	6.34	2.417	3.7%	31.57	-	-	0.83	10.36	14.51
				20%	1	6.39	6.35	1.996	20.5%	31.67	UNABLE TO DETECT REFLECTED PULSE		0.11	3.00	3.09
					2	6.32	6.35	2.013	19.8%	31.67			0.13	2.91	2.95
					3	6.33	6.35	2.010	19.9%	31.67			2.72	2.81	-
					4	6.37	6.35	2.008	20.0%	31.67			3.02	3.09	2.81

Variant	Composition (Mass Fracs.)			Desired	6.35mm	Length	Diameter	Density	Porosity	Area	D TOF	D-Speed	E	σ_y	σ_c
	Al	Fe2O3	PTFE	Porosity	Cylinder #	mm	mm	g/cm3	%	mm2	us	m/s	Gpa	Mpa	Mpa
25Al/75PTFE-F	29.11%	0.00%	70.89%	5%	1	6.1	6.32	2.315	3.7%	31.4	9.05	1348.1	1.04	13.75	17.87
					2	6.08	6.32	2.312	3.8%	31.4	9.03	1346.6	1.18	12.76	18.29
					3	6.18	6.32	2.295	4.5%	31.4	10.45	1182.8	0.93	11.91	17.30
					4	6.21	6.32	2.295	4.5%	31.4	10.58	1173.9	0.80	11.95	16.31
				20%	1	6.33	6.34	1.88	21.7%	31.6	NO ECHO DETECTED		0.31	4.80	4.93
					2	6.3	6.34	1.90	21.1%	31.6			0.25	5.07	5.21
					3	6.25	6.34	1.90	20.9%	31.6			0.30	5.15	5.35

Variant	Composition (Mass Fracs.)			Desired	6.35mm	Length	Diameter	Density	Porosity	Area	D TOF	D-Speed	E	σ_y	σ_c
	Al	Fe2O3	PTFE	Porosity	Cylinder #	mm	mm	g/cm3	%	mm2	us	m/s	Gpa	Mpa	Mpa
25Al/75PTFE-C	29.11%	0.00%	70.89%	5%	1	6.31	6.33	2.322	3.4%	31.47	10	1262.0	0.70	9.32	12.44
					2	6.17	6.33	2.343	2.5%	31.47	8.33	1481.4	0.89	10.60	14.28
					3	6.33	6.32	2.311	3.8%	31.37	9	1406.7	0.68	9.62	12.16
					4	6.24	6.33	2.342	2.5%	31.47	7.94	1571.8	1.16	10.84	14.98
				20%	1	6.22	6.34	1.910	20.5%	31.57	9.01	1418.4	0.14	2.95	3.24
					2	6.22	6.34	1.945	19.1%	31.57	9.92	1298.4	0.15	3.30	3.66
					3	6.24	6.34	1.949	18.9%	31.57	-	-	0.15	2.99	3.24

Fracture Toughness Measurements

Variant	Composition (Mass Fracs.)			Desired	12.7mm	Length	Diameter	Density	Porosity	Crack D.	Arc Len.	Alpha	Fmax	σ_tens	KIC
	Al	Fe2O3	PTFE	Porosity	Disc #	mm	mm	g	%	mm	mm		N	Mpa	Mpa*m^(1/2)
100Al-F	100%	0%	0%	10%	1a	4.09	12.75	2.472	8%	0.91	2	0.31	335.71	3.57	6.78
					2a	4.09	12.75	2.465	9%	0.91	1.95	0.31	363.20	3.89	7.37
					3a	4.11	12.75	2.456	9%	0.91	2	0.31	362.53	3.84	7.27
					4a	4.13	12.75	2.445	9%	0.91	1.9	0.30	363.29	3.88	7.35
				20%	1a	3.86	12.75	2.224	17.6%	0.91	1.27	0.20	114.99	1.41	2.67
					2a	3.93	12.75	2.194	18.7%	0.91	1.65	0.26	102.22	1.18	2.24
					3a	3.94	12.75	2.191	18.8%	0.91	1.78	0.28	119.08	1.35	2.57

Variant	Composition (Mass Fracs.)			Desired	12.7mm	Length	Diameter	Density	Porosity	Crack D.	Arc Len.	Alpha	Fmax	σ_tens	KIC
	Al	Fe2O3	PTFE	Porosity	Disc #	mm	mm	g	%	mm	mm		N	Mpa	Mpa*m^(1/2)
100Al-C	100%	0%	0%	10%	1a	3.99	12.75	2.414	10.5%	0.91	2.16	0.34	430.50	4.58	8.70
					2a	3.99	12.75	2.407	10.8%	0.91	1.78	0.28	545.26	6.13	11.60
					3a	3.98	12.75	2.395	11.2%	0.91	2.29	0.36	419.02	4.38	8.29
					4a	3.97	12.75	2.409	10.7%	0.91	1.78	0.28	578.80	6.53	12.37
				20%	1a	3.93	12.75	2.170	19.6%	0.91	1.27	0.20	185.58	2.23	4.23
					2a	4.02	12.75	2.124	21.3%	0.91	1.78	0.28	189.41	2.11	4.00
					3a	4.05	12.75	2.112	21.7%	0.91	2.032	0.32	225.70	2.41	4.57
					4a	4.13	12.75	2.082	22.8%	0.91	1.78	0.28	213.96	2.32	4.40

Variant	Composition (Mass Fracs.)			Desired	12.7mm	Length	Diameter	Density	Porosity	Crack D.	Arc Len.	Alpha	Fmax	σ_tens	KIC
	Al	Fe2O3	PTFE	Porosity	Disc #	mm	mm	g	%	mm	mm		N	Mpa	Mpa*m^(1/2)
100PTFE-F	0%	0%	100%	10%	1	3.92	12.75	2.040	10.5%	0.91	2.29	0.36	46.97	0.497971	0.943013
					2	3.9	12.75	2.069	9.3%	0.91	2.032	0.32	39.03	0.433365	0.820668
				20%	1	FAILED TO CONSOLIDATE									
					2										
					3										
					4										

Variant	Composition (Mass Fracs.)			Desired	12.7mm	Length	Diameter	Density	Porosity	Crack D.	Arc Len.	Alpha	Fmax	σ_tens	KIC
	Al	Fe2O3	PTFE	Porosity	Disc #	mm	mm	g	%	mm	mm		N	Mpa	Mpa*m^(1/2)
100PTFE-C	0%	0%	100%	10%	1	3.81	12.72	2.107	7.6%	0.91	2.24	0.35	70.85	0.78	1.48
					2	3.8	12.72	2.133	6.4%	0.91	2.11	0.33	74.72	0.84	1.60
					3	3.85	12.72	2.124	6.9%	0.91	2.18	0.34	71.33	0.79	1.49
				20%	1	4.1	12.75	1.767	22%	0.91	3.05	0.48	17.63	0.15	0.29
					2	3.94	12.75	1.803	21%	0.91	3.05	0.48	22.10	0.20	0.38
					3	3.96	12.75	1.814	20%	0.91	3.05	0.48	17.90	0.16	0.30
					4	4.03	12.75	1.780	22%	0.91	2.92	0.46	24.06	0.22	0.41

Fracture Toughness Measurements

Variant	Composition (Mass Fracs.)			Desired	12.7mm	Length	Diameter	Density	Porosity	Crack D.	Arc Len.	Alpha	Fmax	σ_tens	KIC
	Al	Fe2O3	PTFE	Porosity	Disc #	mm	mm	g	%	mm	mm		N	Mpa	Mpa*m^(1/2)
75Al/25PTFE-F	78.70%	0.00%	21.30%	10%	1	4.03	12.77	2.424	7%	0.91	1.520	0.24	157.82	1.81	3.42
					3	4.02	12.76	2.414	7.5%	0.91	1.78	0.28	179.71	2.00	3.79
					3	4.05	12.76	2.429	6.9%	0.91	1.65	0.26	167.92	1.89	3.57
				20%	1	3.92	12.76	2.133	18.3%	0.91	1.78	0.28	52.22	0.60	1.13
					2	4.01	12.76	2.083	20.2%	0.91	1.78	0.28	43.21	0.48	0.91
					3	4.02	12.76	2.068	20.8%	0.91	1.52	0.24	36.80	0.42	0.80

Variant	Composition (Mass Fracs.)			Desired	12.7mm	Length	Diameter	Density	Porosity	Crack D.	Arc Len.	Alpha	Fmax	σ_tens	KIC
	Al	Fe2O3	PTFE	Porosity	Disc #	mm	mm	g	%	mm	mm		N	Mpa	Mpa*m^(1/2)
75Al/25PTFE-C	78.70%	0%	21.30%	10%	1	4.04	12.77	2.439	6.5%	0.91	2.41	0.38	62.01	0.62	1.18
					2	4.03	12.77	2.453	6.0%	0.91	2.29	0.36	64.94	0.67	1.27
					3	4.02	12.77	2.451	6.1%	0.91	2.03	0.32	73.87	0.79	1.51
				20%	1	3.9	12.76	2.143	17.9%	0.91	2.24	0.35	11.74	0.13	0.24
					2	3.95	12.78	2.104	19.4%	0.91	2.24	0.35	13.52	0.14	0.27
					3	3.92	12.77	2.125	18.6%	0.91	2.24	0.35	12.37	0.13	0.25

Variant	Composition (Mass Fracs.)			Desired	12.7mm	Length	Diameter	Density	Porosity	Crack D.	Arc Len.	Alpha	Fmax	σ_tens	KIC
	Al	Fe2O3	PTFE	Porosity	Disc #	mm	mm	g	%	mm	mm		N	Mpa	Mpa*m^(1/2)
50Al/50PTFE-F	55.19%	0.00%	44.81%	10%	1	4.05	12.76	2.331	7.2%	0.91	2.29	0.36	131.27	1.35	2.55
					2	4.06	12.76	2.329	7.3%	0.91	2.29	0.36	104.85	1.07	2.03
				20%	1	3.95	12.76	2.015	19.7%	0.91	1.52	0.24	36.36	0.42	0.80
					2	3.96	12.76	2.018	19.6%	0.91	2.29	0.36	32.69	0.34	0.65
					3	3.95	12.76	2.025	19.3%	0.91	1.78	0.28	36.73	0.4	0.79

Variant	Composition (Mass Fracs.)			Desired	12.7mm	Length	Diameter	Density	Porosity	Crack D.	Arc Len.	Alpha	Fmax	σ_tens	KIC
	Al	Fe2O3	PTFE	Porosity	Disc #	mm	mm	g	%	mm	mm		N	Mpa	Mpa*m^(1/2)
50Al/50PTFE-C	55.19%	0.00%	44.81%	10%	1	4.05	12.75	2.357	6.1%	0.91	1.91	0.30	77.52	0.84	1.60
					2	4.06	12.76	2.336	7.0%	0.91	2.03	0.32	76.43	0.81	1.54
				20%	1	3.95	12.76	2.002	20.3%	0.91	2.29	0.36	11.84	0.12	0.24
					2	3.95	12.77	2.008	20.0%	0.91	2.54	0.40	11.13	0.11	0.21

Fracture Toughness Measurements

Variant	Composition (Mass Fracs.)			Desired	12.7mm	Length	Diameter	Density	Porosity	Crack D.	Arc Len.	Alpha	Fmax	σ_tens	KIC
	Al	Fe2O3	PTFE	Porosity	Disc #	mm	mm	g	%	mm	mm		N	Mpa	Mpa*m^(1/2)
25Al/75PTFE-F	29.11%	0.00%	70.89%	10%	1	4.08	12.77	2.113	12.0%	0.9	2.29	0.36	54.94	0.56	1.06
					2	4.06	12.76	2.111	12.1%	0.9	2.29	0.36	29.09	0.30	0.56
				20%	1	3.89	12.77	1.96	18.5%	0.9	2.16	0.34	26.56	0.29	0.55
					2	3.87	12.77	1.96	18.3%	0.9	1.91	0.30	13.70	0.16	0.30
					3	3.92	12.77	1.96	18.6%	0.9	2.29	0.36	20.46	0.22	0.41

Variant	Composition (Mass Fracs.)			Desired	12.7mm	Length	Diameter	Density	Porosity	Crack D.	Arc Len.	Alpha	Fmax	σ_tens	KIC
	Al	Fe2O3	PTFE	Porosity	Disc #	mm	mm	g	%	mm	mm		N	Mpa	Mpa*m^(1/2)
25Al/75PTFE-C	29.11%	0.00%	70.89%	10%	1	4.02	12.77	2.144	10.7%	0.91	2.54	0.40	43.53	0.43	0.81
					2	4.06	12.77	2.133	11.2%	0.91	2.54	0.40	35.81	0.35	0.66
					3	4.06	12.76	2.138	11.0%	0.91	2.54	0.40	42.71	0.42	0.79
					4	4.03	12.76	2.146	10.6%	0.91	2.54	0.40	45.73	0.45	0.85
				20%	1	3.94	12.78	1.935	19.4%	0.91	2.79	0.44	19.28	0.18	0.35
					2	3.96	12.78	1.911	20.4%	0.91	2.54	0.40	20.68	0.21	0.39
					3	4	12.78	1.912	20.4%	0.91	2.29	0.36	14.59	0.15	0.29
					4	3.93	12.78	1.926	19.8%	0.91	2.29	0.36	19.62	0.21	0.39

High Velocity Impact Tests - Specimen Specifics

Variant	Composition (Mass Fracs.)			Desired	6.35mm	Length	Diameter	Mass	Volume	Density	Porosity
	Al	Fe2O3	PTFE	Porosity	Cylinder #	mm	mm	g	cm3	g	%
100Al-F	100%	0%	0%	5%	1	6.22	6.33	0.501	0.196	2.559	5.8%
					2	6.33	6.32	0.513	0.199	2.583	4.9%
					3	6.32	6.33	0.507	0.199	2.549	6.1%

Vented Calorimetry Tests - Specimen Specifics

Variant	Composition (Mass Fracs.)			Desired	6.35mm	Length	Diameter	Mass	Volume	Density	Porosity
	Al	Fe2O3	PTFE	Porosity	Cylinder #	mm	mm	g	cm3	g	%
100Al-C	100%	0%	0%	5%	1	6.22	6.33	0.501	0.196	2.559	5.8%
					3	6.32	6.33	0.507	0.199	2.549	6.1%

Kolsky Compression Tests Specimen Specifics

Variant	Composition (Mass Fracs.)			Desired	6.35mm	Length	Diameter	Mass	Volume	Density	Porosity
	Al	Fe2O3	PTFE	Porosity	Cylinder #	mm	mm	g	cm3	g	%
100PTFE-F	100%	0%	0%	5%	1	6.39	6.33	0.512	0.201	2.546	6.3%
					2	6.27	6.33	0.508	0.197	2.575	5.2%
					3	6.28	6.33	0.505	0.198	2.555	5.9%
Variant	Composition (Mass Fracs.)			Desired	6.35mm	Length	Diameter	Mass	Volume	Density	Porosity
	Al	Fe2O3	PTFE	Porosity	Cylinder #	mm	mm	g	cm3	g	%
100PTFE-C	100%	0%	0%	5%	1	6.28	6.34	0.512	0.198	2.583	4.2%
					2	6.24	6.33	0.504	0.196	2.567	4.8%
					3	6.32	6.33	0.511	0.199	2.569	4.7%

Variant	Composition (Mass Fracs.)			Desired	6.35mm	Length	Diameter	Mass	Volume	Density	Porosity
	Al	Fe2O3	PTFE	Porosity	Cylinder #	mm	mm	g	cm3	g	%
100Al-F	0%	0%	100%	5%	1	5.85	6.3	0.398	0.182	2.183	4.4%
					2	6.12	6.3	0.414	0.191	2.170	5.0%
					3	6.15	6.3	0.416	0.192	2.170	5.0%
Variant	Composition (Mass Fracs.)			Desired	6.35mm	Length	Diameter	Mass	Volume	Density	Porosity
	Al	Fe2O3	PTFE	Porosity	Cylinder #	mm	mm	g	cm3	g	%
100Al-C	0%	0%	100%	5%	1	6.42	6.33	0.429	0.202	2.123	6.7%
					2	6.21	6.33	0.423	0.195	2.164	4.9%
					3	6.35	6.33	0.42	0.200	2.102	7.6%

Variant	Composition (Mass Fracs.)			Desired	6.35mm	Length	Diameter	Mass	Volume	Density	Porosity
	Al	Fe2O3	PTFE	Porosity	Cylinder #	mm	mm	g	cm3	g	%
25Al/75PTFE-F	100%	0%	0%	5%	1	6.39	6.33	0.512	0.201	2.546	6.3%
					2	6.27	6.33	0.508	0.197	2.575	5.2%
					3	6.28	6.33	0.505	0.198	2.555	5.9%
Variant	Composition (Mass Fracs.)			Desired	6.35mm	Length	Diameter	Mass	Volume	Density	Porosity
	Al	Fe2O3	PTFE	Porosity	Cylinder #	mm	mm	g	cm3	g	%
25Al/75PTFE-C	100%	0%	0%	5%	1	6.28	6.34	0.512	0.198	2.583	4.2%
					2	6.24	6.33	0.504	0.196	2.567	4.8%
					3	6.32	6.33	0.511	0.199	2.569	4.7%

APPENDIX C

SUPPLEMENTAL IMAGES OF RECOVERED FRAGMENTS

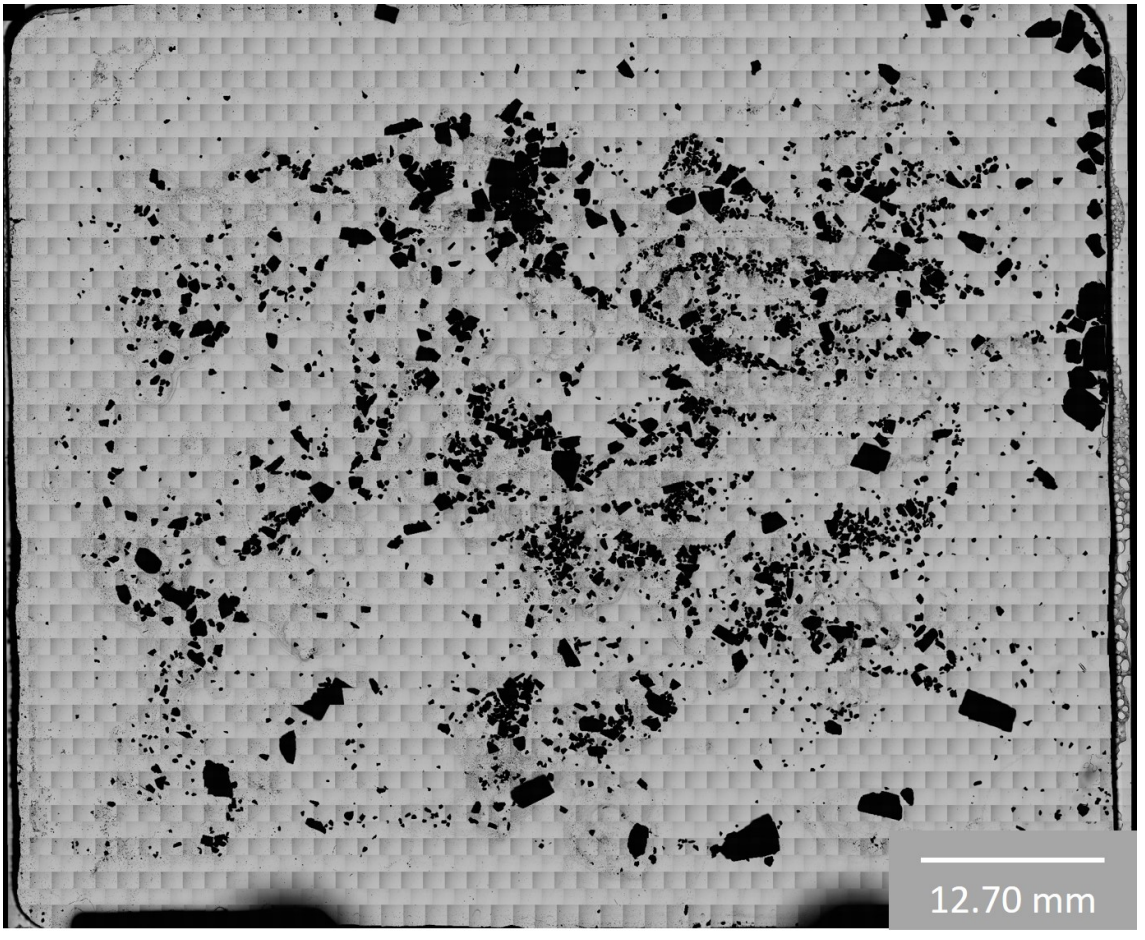

Figure C.1: Stitched microscope image of 100Al-5-F Specimen 1 fragments greater than 150 µm from Kolsky bar compression tests.

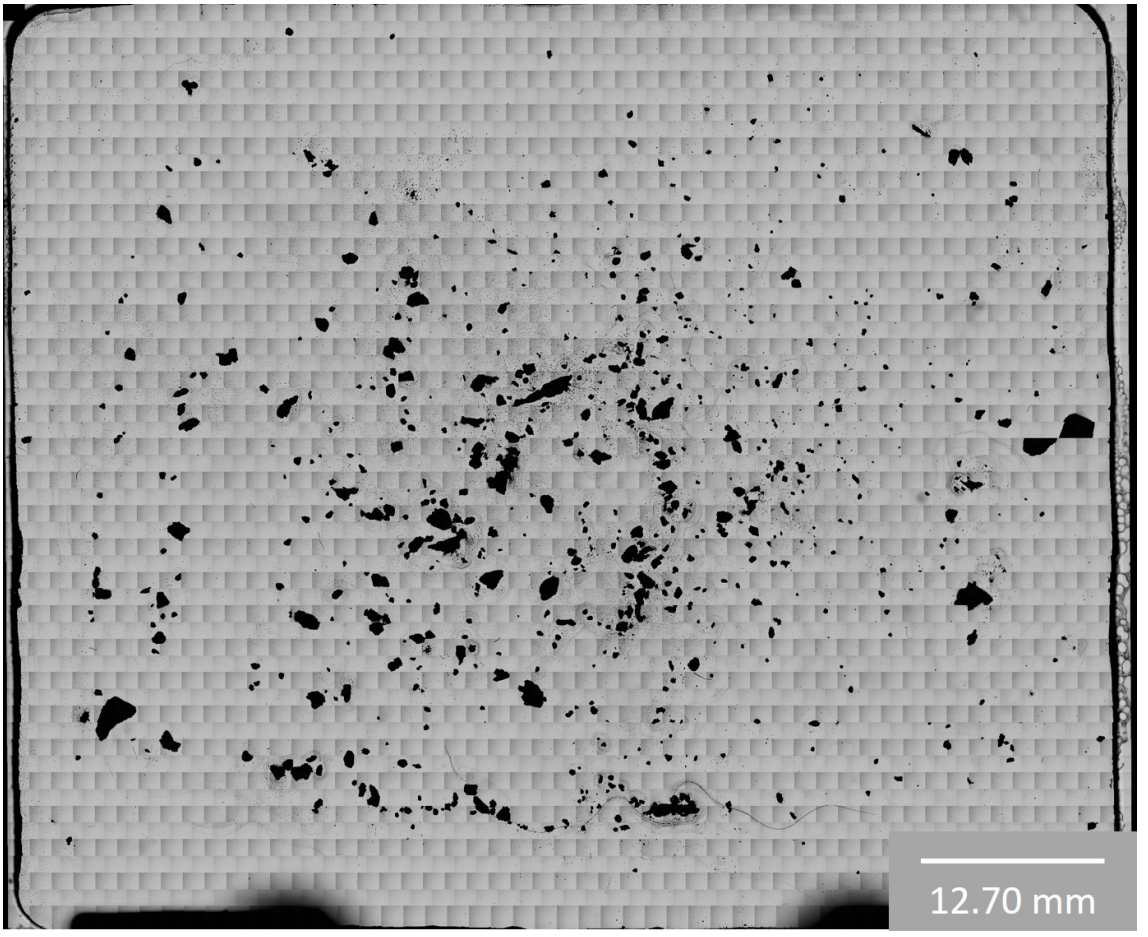

Figure C.2: Stitched microscope image of 100Al-5-C Specimen 1 fragments greater than 150 μm from Kolsky bar compression tests.

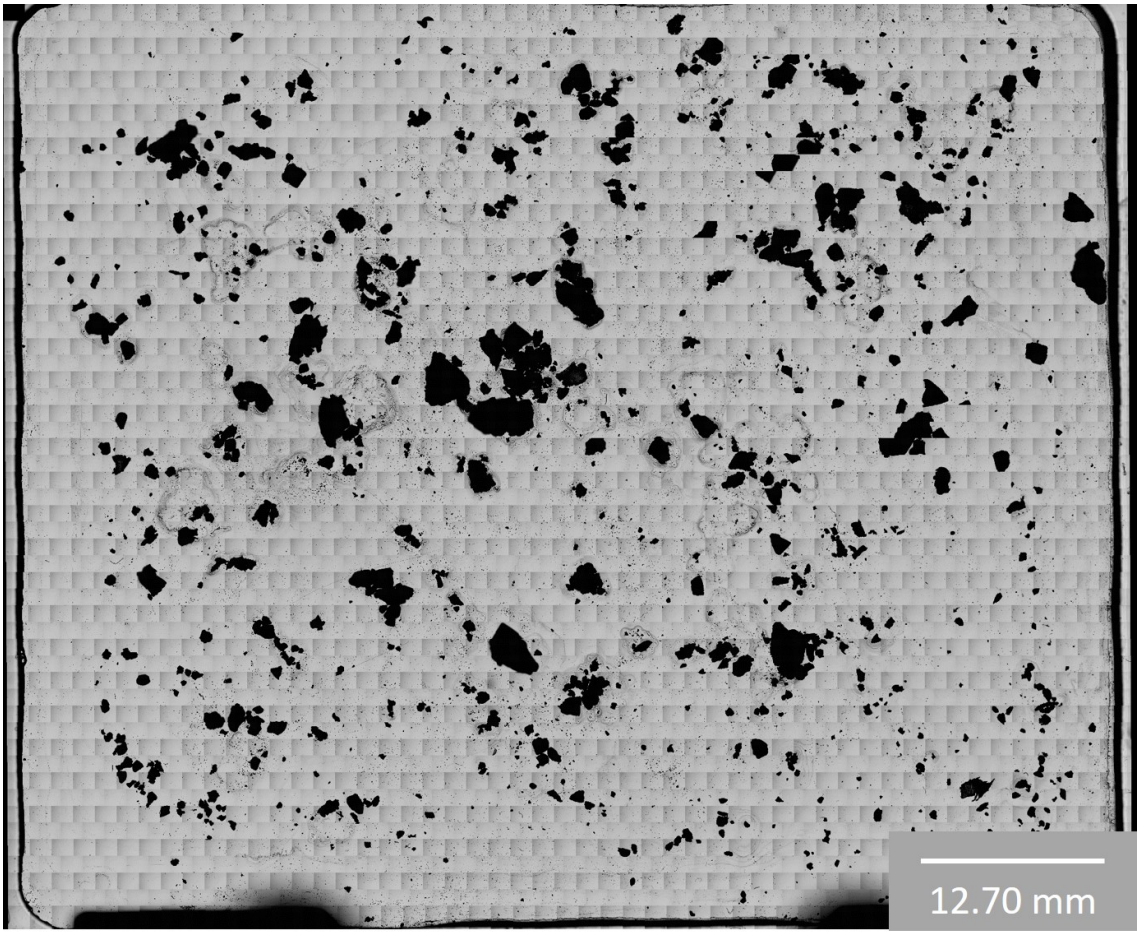

Figure C.3: Stitched microscope image of 100PTFE-5-C Specimen 1 fragments greater than 150 µm from Kolsky bar compression tests.

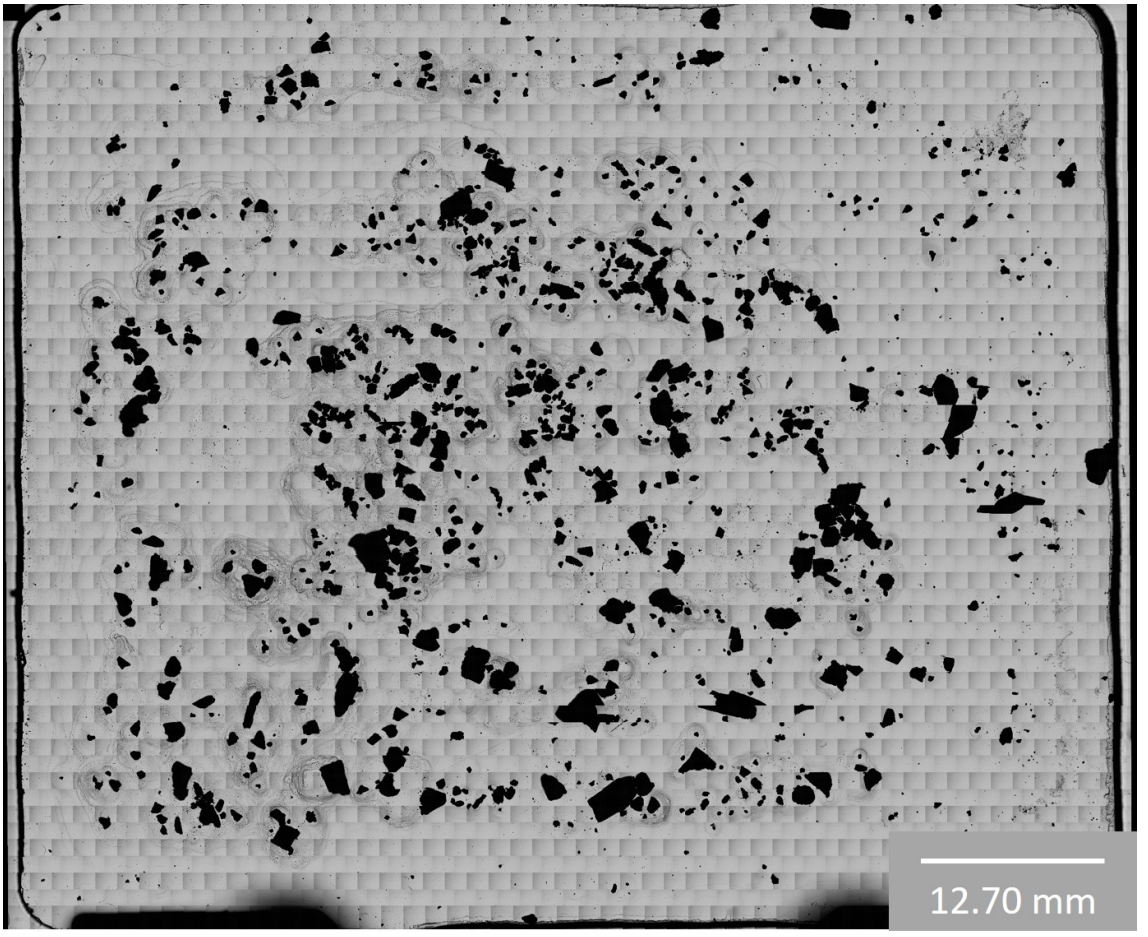

Figure C.4: Stitched microscope image of 25Al75PTFE-5-F Specimen 3 fragments greater than 150 µm from Kolsky bar compression tests.

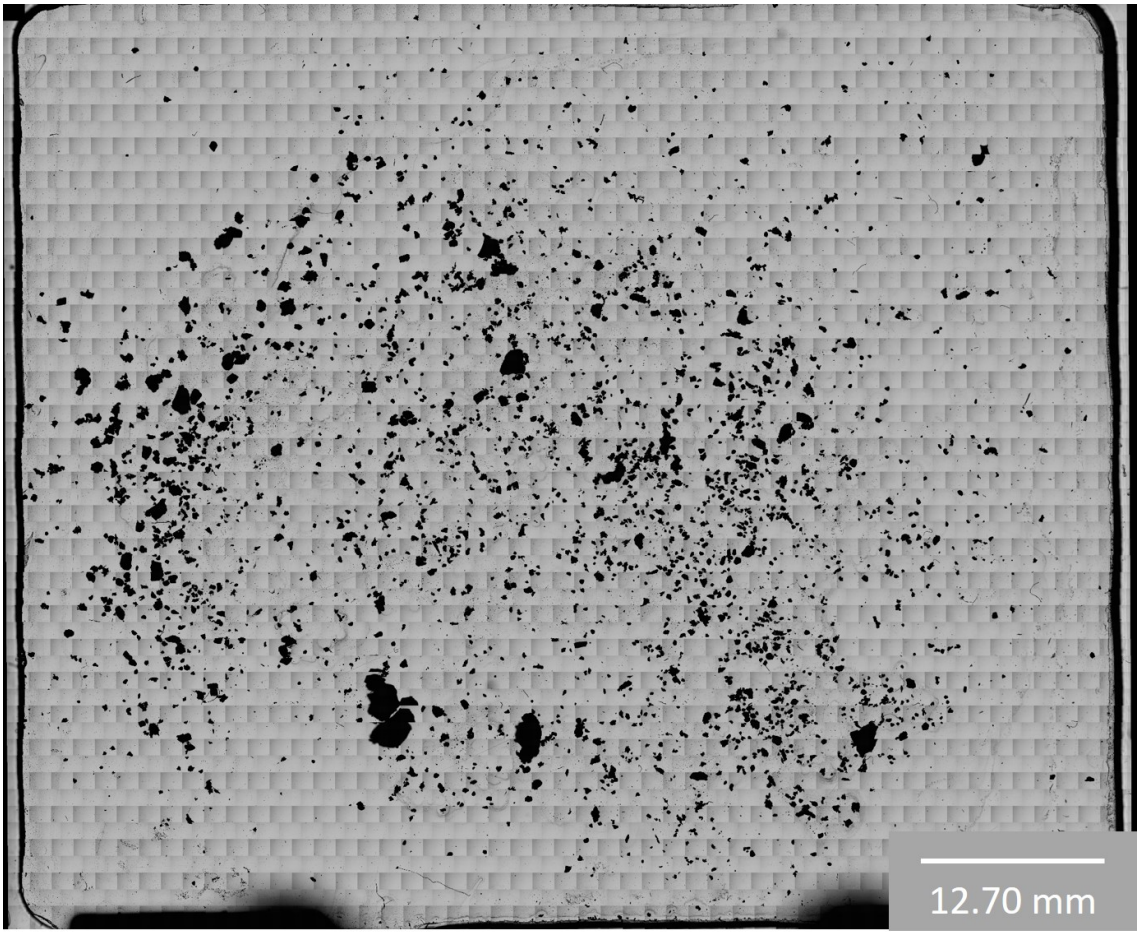

Figure C.5: Stitched microscope image of 100Al-5-F Specimen 1 fragments greater than 150 µm from high velocity impact tests.

APPENDIX D

THERMODYNAMIC DATA SET FOR EQUILIBRIUM SOLVER

```
<!--    Phase Compliant Data Set for the reaction of Al/PTFE. All data
    from
NIST Webbook/JANAF Tables and polynomial coefficients and temperature
    bounds verified.
Completed: 01/15/2023 by S. Youngblood   -->

<ctml>
  <validate reactions="yes" species="yes"/>

                <!--GAS PHASE SPECIES INITIATION-->
<!--    phase gas    -->
  <phase dim="3" id="Gas_Comps">
    <elementArray datasrc="elements.xml"> Al C F</elementArray>
    <speciesArray datasrc="#species_data"> AlF AlF2 AlF3 F F2 C2F4 CF
       CF2 CF3 CF4 C2F2</speciesArray>
    <reactionArray datasrc="#reaction_data"/>
    <state>
      <temperature units="K">298.0</temperature>
      <pressure units="Pa">101325.0</pressure>
    </state>
    <thermo model="IdealGas"/>
    <kinetics model="None"/>
    <transport model="None"/>
  </phase>
                <!--LIQUID PHASE SPECIES INITIATION-->
<!-- Al(L)   -->
  <phase dim="3" id="Al(L)">
    <elementArray datasrc="elements.xml"> Al </elementArray>
    <speciesArray datasrc="#species_data"> Al(L) </speciesArray>
    <state>
      <temperature units="K">298.0</temperature>
      <pressure units="Pa">101325.0</pressure>
    </state>
    <thermo model="StoichSubstance">
      <density units="g/cm3">2.375</density>
    </thermo>
    <transport model="None"/>
```

```
    <kinetics model="none"/>
  </phase>


                <!--SOLID PHASE SPECIES INITIATION-->

<!-- Al(s)   -->
  <phase dim="3" id="Al(s)">
    <elementArray datasrc="elements.xml"> Al </elementArray>
    <speciesArray datasrc="#species_data"> Al(s) </speciesArray>
    <state>
      <temperature units="K">298.0</temperature>
      <pressure units="Pa">101325.0</pressure>
    </state>
    <thermo model="StoichSubstance">
      <density units="g/cm3">2.70</density>
    </thermo>
    <transport model="None"/>
    <kinetics model="none"/>
  </phase>

<!-- AlF3(s)   -->
  <phase dim="3" id="AlF3(s)">
    <elementArray datasrc="elements.xml"> F Al </elementArray>
    <speciesArray datasrc="#species_data"> AlF3(s) </speciesArray>
    <state>
      <temperature units="K">298.0</temperature>
      <pressure units="Pa">101325.0</pressure>
    </state>
    <thermo model="StoichSubstance">
      <density units="g/cm3">3.10</density>
    </thermo>
    <transport model="None"/>
    <kinetics model="none"/>
  </phase>

<!-- Al4C3(s)   -->
  <phase dim="3" id="Al4C3(s)">
    <elementArray datasrc="elements.xml"> C Al </elementArray>
    <speciesArray datasrc="#species_data"> Al4C3(s) </speciesArray>
    <state>
      <temperature units="K">298.0</temperature>
      <pressure units="Pa">101325.0</pressure>
    </state>
    <thermo model="StoichSubstance">
      <density units="g/cm3">2.36</density>
    </thermo>
    <transport model="None"/>
    <kinetics model="none"/>
  </phase>
```

```
<!-- species C2F4n(s)    -->
    <phase dim="3" id="C2F4n(s)">
    <elementArray datasrc="elements.xml"> C F </elementArray>
    <speciesArray datasrc="#species_data"> C2F4n(s) </speciesArray>
    <state>
      <temperature units="K">298.0</temperature>
      <pressure units="Pa">101325.0</pressure>
    </state>
    <thermo model="StoichSubstance">
      <density units="g/cm3">2.2</density>
    </thermo>
    <transport model="None"/>
    <kinetics model="none"/>
  </phase>

<!-- species C(gr)    -->
  <phase dim="3" id="C(gr)">
    <elementArray datasrc="elements.xml"> C </elementArray>
    <speciesArray datasrc="#species_data"> C(gr) </speciesArray>
    <state>
      <temperature units="K">298.0</temperature>
      <pressure units="Pa">101325.0</pressure>
    </state>
    <thermo model="StoichSubstance">
      <density units="g/cm3">2.26</density>
    </thermo>
    <transport model="None"/>
    <kinetics model="none"/>
  </phase>


<!--     species definitions     -->
  <speciesData id="species_data">

                                      <!--GAS PHASE SPECIES DATA-->

    <!-- species Al    -->
    <!-- NIST Chemistry Webbook Polynomial, temperature bounds based on
        reported data in
     JANAF NIST 1998 tables database -->
    <species name="Al">
      <atomArray>Al:1 </atomArray>
      <thermo>
        <SHOMATE Tmax="2900.0" Tmin="2791.0" P0="100000.0">
           <floatArray name="coeffs" size="7">
             2.037692000E+01,   6.608170000E-01,  -3.136310000E-01,   4
                .510600000E-02,
             7.817300000E-02,   3.238575000E+02,   1.894808000E+02</
```

```
                floatArray>
          </SHOMATE>
          <SHOMATE Tmax="6000.0" Tmin="2900.0" P0="100000.0">
             <floatArray name="coeffs" size="7">
               2.037692000E+01,   6.608170000E-01,  -3.136310000E-01,   4
                  .510600000E-02,
               7.817300000E-02,   3.238575000E+02,   1.894808000E+02</
                  floatArray>
          </SHOMATE>
        </thermo>
      </species>

      <!-- species AlF   -->
      <!-- NIST Chemistry Webbook Polynomial, Temperature bounds based on
          DTA Data from
      Reillo2016 and experimental observations from Hildenbrand1981 in
         JANAF NIST 1998 tables-->
      <species name="AlF">
        <atomArray>Al:1 F:1 </atomArray>
        <thermo>
          <SHOMATE Tmax="2000.0" Tmin="835" P0="100000.0">
             <floatArray name="coeffs" size="7">
               3.511320000E+01,   2.296787000E+00,  -6.740090000E-01,   8
                  .227900000E-02,
               -0.385217000E+00,  -2.776862000E+02,   2.552098000E+02</
                  floatArray>
          </SHOMATE>
          <SHOMATE Tmax="6000.0" Tmin="2000.0" P0="100000.0">
             <floatArray name="coeffs" size="7">
               3.511320000E+01,   2.296787000E+00,  -6.740090000E-01,   8
                  .227900000E-02,
               -0.385217000E+00,  -2.776862000E+02,   2.552098000E+02</
                  floatArray>
          </SHOMATE>
        </thermo>
      </species>

  <!-- species AlF2   -->
      <!-- NIST Chemistry Webbook Polynomial, Temperature bounds based on
          DTA Data from
      Reillo2016 and experimental observations from Hildenbrand1981 in
         JANAF NIST 1998 tables-->
      <species name="AlF2">
        <atomArray>Al:1 F:2 </atomArray>
        <thermo>
          <SHOMATE Tmax="2000.0" Tmin="880" P0="100000.0">
             <floatArray name="coeffs" size="7">
               4.703067000E+01,   1.962409000E+01,  -1.235535000E+01,   2
                  .636130000E+00,
               -0.540506000E+00,  -7.111503000E+02,   3.127477000E+02</
```

```
                floatArray>
          </SHOMATE>
          <SHOMATE Tmax="6000.0" Tmin="2000.0" P0="100000.0">
             <floatArray name="coeffs" size="7">
               6.315999000E+01,   -3.003845000E+00,  0.592408000E+00,
                  -0.027109000E+00,
               -6.411562000E+00,  -7.249533000E+02,   3.273022000E+02</
                  floatArray>
          </SHOMATE>
        </thermo>
      </species>

<!-- species AlF3   -->
      <!-- NIST Chemistry Webbook Polynomial, Temperature bounds based on
          DTA Data from
      Reillo2016 and experimental observations from Blackburn1965 in
         JANAF NIST 1998 tables-->
      <species name="AlF3">
        <atomArray>Al:1 F:3 </atomArray>
        <thermo>
          <SHOMATE Tmax="2000.0" Tmin="880" P0="100000.0">
             <floatArray name="coeffs" size="7">
               8.306746000E+01,   0.033893000E+00,  -0.005659000E+00,
                  -0.000335000E+00,
               -3.326694000E+00,  -1.243401000E+03,   3.631469000E+02</
                  floatArray>
          </SHOMATE>
          <SHOMATE Tmax="6000.0" Tmin="2000.0" P0="100000.0">
             <floatArray name="coeffs" size="7">
               8.306746000E+01,   0.033893000E+00,  -0.005659000E+00,
                  -0.000335000E+00,
               -3.326694000E+00,  -1.243401000E+03,   3.631469000E+02</
                  floatArray>
          </SHOMATE>
        </thermo>
      </species>

<!-- species C2F4    -->
<!-- NIST Chemistry Webbook Polynomial, temperature bounds based on
     reported data in
       JANAF NIST 1998 database -->
      <species name="C2F4">
        <atomArray>C:2 F:4 </atomArray>
        <thermo>
          <NASA Tmax="1000.0" Tmin="300.0" P0="100000.0">
             <floatArray name="coeffs" size="7">
               3.616618300E+00,   2.648861800E-02,  -2.243326600E-05,   6
                  .228644500E-09,
               6.214924400E-13,  -8.127724200E+04,   8.523764070E+00</
                  floatArray>
```

```
        </NASA>
        <NASA Tmax="5000.0" Tmin="1000.0" P0="100000.0">
           <floatArray name="coeffs" size="7">
             3.616618300E+00,   2.648861800E-02,  -2.243326600E-05,   6
                .228644500E-09,
             6.214924400E-13,  -8.127724200E+04,   8.523764070E+00</
                floatArray>
        </NASA>
      </thermo>
    </species>

 <!-- species CF    -->
<!-- NIST Chemistry Webbook Polynomial, temperature bounds based on
    reported data in
      JANAF NIST 1998 database -->
    <species name="CF">
      <atomArray>C:1 F:1 </atomArray>
      <thermo>
        <NASA Tmax="1000.0" Tmin="300.0" P0="100000.0">
           <floatArray name="coeffs" size="7">
             3.465514300E+00,  -6.877980500E-04,   5.678476600E-06,  -6
                .458298200E-09,
             2.298824800E-12,   2.965559800E+04,   5.881354890E+00</
                floatArray>
        </NASA>
        <NASA Tmax="5000.0" Tmin="1000.0" P0="100000.0">
           <floatArray name="coeffs" size="7">
             3.686967900E+00,   9.114349100E-04,  -3.646385500E-07,   6
                .748285400E-11,
             -4.526959600E-15,   2.947812500E+04,   4.174510090E+00</
                floatArray>
        </NASA>
      </thermo>
    </species>

<!-- species CF2    -->
<!-- NIST Chemistry Webbook Polynomial, temperature bounds based on
    reported data in
      JANAF NIST 1998 database -->
    <species name="CF2">
      <atomArray>C:1 F:2 </atomArray>
      <thermo>
        <NASA Tmax="1000.0" Tmin="300.0" P0="100000.0">
           <floatArray name="coeffs" size="7">
             2.768882100E+00,   7.237296200E-03,  -1.602815200E-06,  -4
                .551237900E-09,
             2.664801100E-12,  -2.301578600E+04,   1.113769580E+01</
                floatArray>
        </NASA>
        <NASA Tmax="5000.0" Tmin="1000.0" P0="100000.0">
```

```
            <floatArray name="coeffs" size="7">
              5.226714200E+00,   2.083768000E-03,  -9.903727800E-07,   2
                 .126484800E-10,
              -1.583111400E-14,  -2.375584700E+04,  -1.910904230E+00</
                 floatArray>
          </NASA>
        </thermo>
      </species>

<!-- species CF3    -->
<!-- NIST Chemistry Webbook Polynomial, temperature bounds based on
    reported data in
     JANAF NIST 1998 database -->
      <species name="CF3">
        <atomArray>C:1 F:3 </atomArray>
        <thermo>
          <NASA Tmax="1000.0" Tmin="300.0" P0="100000.0">
             <floatArray name="coeffs" size="7">
               2.065016800E+00,   1.642415800E-02,  -1.083814600E-05,  -8
                  .531799700E-10,
               2.387807000E-12,  -5.781197600E+04,   1.570469300E+01</
                  floatArray>
          </NASA>
          <NASA Tmax="5000.0" Tmin="1000.0" P0="100000.0">
             <floatArray name="coeffs" size="7">
               7.201262200E+00,   3.066393500E-03,  -1.314418100E-06,   2
                  .499692500E-10,
               -1.755092800E-14,  -5.923863100E+04,  -1.094571000E+01</
                  floatArray>
          </NASA>
        </thermo>
      </species>

<!-- species CF4    -->
<!-- NIST Chemistry Webbook Polynomial, temperature bounds based on
    reported data in
     JANAF NIST 1998 database -->
      <species name="CF4">
        <atomArray>C:1 F:4 </atomArray>
        <thermo>
          <NASA Tmax="1000.0" Tmin="200.0" P0="100000.0">
             <floatArray name="coeffs" size="7">
               1.051439920E+00,   2.782464680E-02,  -2.465252600E-05,   6
                  .745483040E-09,
               9.189093160E-13,  -1.135740670E+05,   1.819008990E+01</
                  floatArray>
          </NASA>
          <NASA Tmax="6000.0" Tmin="1000.0" P0="100000.0">
             <floatArray name="coeffs" size="7">
               9.472153590E+00,   3.595252160E-03,  -1.403785020E-06,   2
```

```
                .391881880E-10,
             -1.485589060E-14,  -1.158163370E+05,  -2.497090910E+01</
                floatArray>
          </NASA>
        </thermo>
      </species>

<!-- species C2F2    -->
<!-- NIST Chemistry Webbook Polynomial, temperature bounds based on
    reported data in
     JANAF NIST 1998 database -->
      <species name="C2F2">
        <atomArray>C:2 F:2 </atomArray>
        <thermo>
          <NASA Tmax="1000.0" Tmin="300.0" P0="100000.0">
             <floatArray name="coeffs" size="7">
               3.534583700E+00,   1.444584500E-02,  -1.218969200E-05,   3
                  .604298500E-09,
               1.911895100E-13,   9.213356200E+02,   5.419465110E+00</
                  floatArray>
          </NASA>
          <NASA Tmax="5000.0" Tmin="1000.0" P0="100000.0">
             <floatArray name="coeffs" size="7">
               7.516458100E+00,   3.168646200E-03,  -1.331138500E-06,   2
                  .496004900E-10,
               -1.734207200E-14,  -1.610765500E+02,  -1.506806220E+01</
                  floatArray>
          </NASA>
        </thermo>
      </species>

      <!-- species F   -->
      <!-- NIST Chemistry Webbook Polynomial, temperature bounds based on
          studies of the
      dissociation of Fluorine ghas from Gilles1952 and Doescher1951 in
         JANAF NIST 1998 tables-->
      <species name="F">
        <atomArray> F:1 </atomArray>
        <thermo>
          <SHOMATE Tmax="2000.0" Tmin="815" P0="100000.0">
             <floatArray name="coeffs" size="7">
               3.144510000E+01,   8.413831000E+00,  -2.778850000E+00,   0
                  .218104000E+00,
               -0.211175000E+00,  -1.0432600000E+01,   2.372770000E+02</
                  floatArray>
          </SHOMATE>
          <SHOMATE Tmax="6000.0" Tmin="2000.0" P0="100000.0">
             <floatArray name="coeffs" size="7">
               3.144510000E+01,   8.413831000E+00,  -2.778850000E+00,   0
                  .218104000E+00,
```

```
          -0.211175000E+00,  -1.0432600000E+01,   2.372770000E+02</
             floatArray>
      </SHOMATE>
    </thermo>
</species>

<!-- species F2   -->
<!-- NIST Chemistry Webbook Polynomial, temperature bounds based on
     studies of the
dissociation of Fluorine ghas from Gilles1952 and Doescher1951 in
    JANAF NIST 1998 tables-->
<species name="F2">
  <atomArray> F:2 </atomArray>
  <thermo>
    <SHOMATE Tmax="2000.0" Tmin="298" P0="100000.0">
       <floatArray name="coeffs" size="7">
         2.197336000E+01,   8.413831000E+00,  -2.778850000E+00,   0
             .218104000E+00,
         -0.211175000E+00,  -1.0432600000E+01,   2.372770000E+02</
             floatArray>
    </SHOMATE>
    <SHOMATE Tmax="6000.0" Tmin="2000.0" P0="100000.0">
       <floatArray name="coeffs" size="7">
         3.144510000E+01,   -0.9581820000E+00,  0.251916000E+00,
             -0.021107000E+00,
         0.103471000E+00,  7.3225860000E+01,   1.862286000E+02</
             floatArray>
    </SHOMATE>
  </thermo>
</species>


                          <!--LIQUID PHASE SPECIES DATA-->

<!-- species Al(L)    -->
<!-- NIST Chemistry Webbook Polynomial, temperature bounds based on
     reported data in
 JANAF NIST 1998 tables database -->
<species name="Al(L)">
  <atomArray>Al:1 </atomArray>
  <thermo>
    <SHOMATE Tmax="1000.0" Tmin="933.0" P0="100000.0">
       <floatArray name="coeffs" size="7">
         3.175104000E+01,   3.935826000E-08,  -1.786515000E-08,   2
             .694171000E-09,
         5.480037000E-09,  -9.546840000E-01,   7.339949000E+01</
             floatArray>
    </SHOMATE>
    <SHOMATE Tmax="2791.0" Tmin="1000.0" P0="100000.0">
       <floatArray name="coeffs" size="7">
```

```
          3.175104000E+01,   3.935826000E-08,  -1.786515000E-08,   2
             .694171000E-09,
          5.480037000E-09,  -9.546840000E-01,   7.339949000E+01</
             floatArray>
      </SHOMATE>
    </thermo>
  </species>

                                <!--SOLIDS PHASE SPECIES DATA-->
<!-- species Al(s)    -->
<!-- NIST Chemistry Webbook Polynomial, temperature bounds based on
    reported data in
 JANAF NIST 1998 tables database -->
 <species name="Al(s)">
   <atomArray>Al:1 </atomArray>
   <thermo>
     <SHOMATE Tmax="400.0" Tmin="298.0" P0="100000.0">
        <floatArray name="coeffs" size="7">
          2.808920000E+01,  -5.414849000E+00,   8.560423000E+00,   3
             .427370000E+00,
          -2.773750000E-01,  -9.147187000E+00,   6.190981000E+01</
             floatArray>
     </SHOMATE>
     <SHOMATE Tmax="933.0" Tmin="400.0" P0="100000.0">
        <floatArray name="coeffs" size="7">
          2.808920000E+01,  -5.414849000E+00,   8.560423000E+00,   3
             .427370000E+00,
          -2.773750000E-01,  -9.147187000E+00,   6.190981000E+01</
             floatArray>
     </SHOMATE>
   </thermo>
 </species>

 <!-- species AlF3(s)    -->
 <!-- NIST Chemistry Webbook Polynomial, temperature bounds based on
     reported data in
  JANAF NIST 1998 tables database -->
 <species name="AlF3(s)">
   <atomArray>Al:1 F:3</atomArray>
   <thermo>
     <SHOMATE Tmax="728.0" Tmin="298.0" P0="100000.0">
        <floatArray name="coeffs" size="7">
          -2.717362000E+01,   5.942661000E+02,  -1.042272000E+03,
             6.624444000E+02,
          0.019262000E+00,  -1.520775000E+03,   -1.030055100E+02</
             floatArray>
     </SHOMATE>
     <SHOMATE Tmax="1550.0" Tmin="728.0" P0="100000.0">
        <floatArray name="coeffs" size="7">
          9.296722000E+01,   8.667826000E+00,  0.148503000E+00,   -0
```

```
                .006692000E+00,
              -0.942781000E+00,  -1.541369000E+03,   1.702754000E+02</
                 floatArray>
          </SHOMATE>
        </thermo>
      </species>

      <!-- species Al4C3(s)    -->
      <!-- NIST Chemistry Webbook Polynomial, temperature bounds based on
           reported data in
       JANAF NIST 1998 tables database -->
      <species name="Al4C3(s)">
        <atomArray>Al:4 C:3</atomArray>
        <thermo>
          <SHOMATE Tmax="1000" Tmin="298.0" P0="100000.0">
             <floatArray name="coeffs" size="7">
               1.461931000E+01,   4.963437000E+01,  -1.880758000E+01,   2
                  .593487000E+00,
               -3.812223000E+00,  -2.741792000E+02,   2.302171000E+02</
                  floatArray>
          </SHOMATE>
          <SHOMATE Tmax="2270.0" Tmin="1000.0" P0="100000.0">
             <floatArray name="coeffs" size="7">
               1.461931000E+01,   4.963437000E+01,  -1.880758000E+01,   2
                  .593487000E+00,
               -3.812223000E+00,  -2.741792000E+02,   2.302171000E+02</
                  floatArray>
          </SHOMATE>
        </thermo>
      </species>

   <!-- species C(gr)    -->
  <!-- NIST Chemistry Webbook Polynomial, temperature bounds based on
     reported data in
       JANAF NIST 1998 tables database -->
      <species name="C(gr)">
        <atomArray>C:1 </atomArray>
        <thermo>
          <NASA Tmax="1000.0" Tmin="200.0" P0="100000.0">
             <floatArray name="coeffs" size="7">
               -3.108720720E-01,   4.403536860E-03,   1.903941180E-06,
                  -6.385469660E-09,
               2.989642480E-12,  -1.086507940E+02,   1.113829530E+00</
                  floatArray>
          </NASA>
          <NASA Tmax="5000.0" Tmin="1000.0" P0="100000.0">
             <floatArray name="coeffs" size="7">
               1.455718290E+00,   1.717022160E-03,  -6.975627860E-07,   1
                  .352770320E-10,
               -9.675906520E-15,  -6.951388140E+02,  -8.525830330E+00</
```

```
                floatArray>
          </NASA>
        </thermo>
      </species>

      <!-- species C2F4n(s)    -->
<!-- Polynomial format of data from "The thermodynamic properties of
    polytetrafluoroethylene", Lau 1983. Temperature bounds from Lau
    1983-->
      <species name="C2F4n(s)">
        <atomArray> C:2 F:4 </atomArray>
        <thermo>
          <NASA Tmax="690.0" Tmin="200.0" P0="100000.0">
             <floatArray name="coeffs" size="7">
               7.17671433E-01,   2.08417705E-02,  -2.06929437E-05,   1
                  .24321147E-08,
               -2.56247884E-12,  -9.87957685E+04,  2.86322036E+00</
                  floatArray>
          </NASA>
          <NASA Tmax="700.0" Tmin="690.0" P0="100000.0">
             <floatArray name="coeffs" size="7">
                -4.67840526E-07,   -2.04575915E-04,  7.56546855E-05,   -1
                   .25480661E-07,
               6.21750437E-11,  9.95408741E+04,  4.84773489E+00</
                  floatArray>
          </NASA>
        </thermo>
      </species>



  </speciesData>
  <reactionData id="reaction_data"/>
</ctml>
```

APPENDIX E

PHASE COMPLIANT EQUILIBRIUM SOLVER

E.0.1 Solver Control

```
clc
clear all
close all
%% Created by: Stewart Youngblood. Written: 8/19/2019. Edited:
   10/15/2022
%
%Controller of interface script for Cantera for performing equilibrium
%calculations with multiphase reactants/products. Application is
   directed
%towards energy release calculations for thermites, intermetllics, and
%combustible metals.
%
%Notes:
%1) Energy out by mass or moles is by total mass of reactants/products

%INPUTS:
%1)Reac_LiqSol - Cell array of liquid/solid phase reactants
%2)moles_Reac - Cell array of number of moles of each liquid/solid
   phase
%               reactant. Order is the same as the order of
   constituents
%               in Reac_array
%3)Reac_gasphase - Cell array of gas phase reactants
%4)moles_Reacgas - Cell array of number of moles of each gas phase
   reactant
%                 reactant. Order is the same as the order of
   constituents
%                 in Reac_gasphase
%5)P_Eqpre - Pressure of reactant mixture pre-equlibrium (ATM)
%6)T_Eqpre - Temperature of reactant mixture pre-equlibrium (Kelvin)
%7)type - Equilibrate Type. Constant Enthalp only known good. Used for
%energy and flame temperature calculations. Available options are:
%                           'HP' - Enthalpy and Pressure Fixed
%                           'TP' - Temp. and Pressure Fixed
%                           'TV' - Temp. and Volume Fixed
```

```
%                           'SP' - Entropy and Pressure Fixed
%8)iter_all - Allowable number of iterations for finding solution to
   the
%constant Temperature/Pressure problem of Gibbs free energy
%9)report - Diagnostic output for Cantera Equilibrate function. Higher
%           integer values increase level of diagnostic outputs. Value
   of 3
%           provides full diagnostics of solver and execution history
%10)mechfilesource - Mechanism file to use for thermodata

%% INITIALIZATION/USER INPUT
%%%---USER SELECTION OF THERMODYNAMIC MECHANISM XML DATA FILE---%%%
%Mechanism File to use
mechfilesource = 'MultiPhasePHC_AlPTFE.xml';

%%%---REPORT AVAILABLE SPECIES---%%%
[GasAvail_array, LiqAvail_array, SolAvail_array,ThermoSum_array] =...
    CanteraXMLReader2(mechfilesource);

%%%---USER INPUT REACTANT SPECIES AND NUMBER OF MOLES---%%%
%Reaction Details
Reac_LiqSol = {'Al(s)','C2F4n(s)'}; %Fuel First
moles_Reac = {1.075,0.71}; % # of moles Fuel.
Reac_gasphase = {'C2F4'};
moles_Reacgas= {10^-10}; %MUST HAVE NONZERO VALUE (~10^-10) TO PREVENT
   CRASHING EQ> SOLVER

%Al/C2F4 Reaction-Stoic AFT~2300K
%Reac_LiqSol = {'Al(s)','C2F4n(s)'}; %Fuel First
%moles_Reac = {1.075,0.71}; % # of moles Fuel.
%Reac_gasphase = {'C2F4'};
%moles_Reacgas= {10^-10}; %MUST HAVE NONZERO VALUE (~10^-10) TO PREVENT
    CRASHING EQ> SOLVER


%%%---USER INPUT INITIAL STATE---%%%
P_Eqpre = 1; %ATM, Note: Pressure prior to equilibrate.
%           Cantera expects pascals but ATM is converted to pascals
T_Eqpre = 298; %K, Note: Temperature prior to equilibrate

GlobeEquil = 'NO'; %Returns Global Equilibrium State

%%%---USER INPUT EQUILIBRIUM TYPE---%%%
type = 'HP';
%'TP' - Temp. and Pressure Fixed
%'HP' - Enthalpy and Pressure Fixed
%'TV' - Temp. and Volume Fixed
%'SP' - Entropy and Pressure Fixed
%'UV' - Internal Energy Volume Fixed-> Cantera's multiphase gibbs
   solver
```

```
%does not support this option.

%%%---USER INPUT: ALLOWABLE ITERATIONS---%%%
iter_all = 1000;

%%%---USER INPUT: SOLUTION REPORTING---%%%
%Larger integer values increase reporting
report =0;

%Report Saving Location
Save_to = 'Report'; % Location to save report

%% MULTIPHASE REACTION SOLVER
[Reac_report,massprods_Report,moleprods_Report, massreacs_Report,...
    molereacs_Report] = UnivMultiphaseReac_Solver(...
    Reac_LiqSol,moles_Reac,Reac_gasphase,moles_Reacgas,P_Eqpre,...
    T_Eqpre,type,iter_all,report,mechfilesource,GlobeEquil);

%% REPORTING
%%---ORDER MASS/MOLE FRACTION ARRAY---%%%
%Rearrange Mass/Mole Fraction arrays to descending order and report
   only
%fractions >10^-4
[massfracprods_Ordered] = FracOrdering(massprods_Report);
[molefracprods_Ordered] = FracOrdering(moleprods_Report);

%%---RETURN MASS FRAC ARRAY AND REACTION TEMP/ENERGY RELEASE---%%
molefracprods_Ordered
massfracprods_Ordered
Reac_report
```

E.0.2 Solver

```
function [Reac_report,massprods_Report,moleprods_Report,
   massreacs_Report,...
    molereacs_Report,specs_cons,toler_it,reac_occur] = ...
    UnivMultiphaseReac_Solver(Reac_condphase,moles_Reaccond,...
    Reac_gasphase,moles_Reacgas,P_Eqpre, T_EqpreUser,type,iter_all,...
    report,mechfilesource,GlobeEquil)
%% Created by: Stewart Youngblood. Written: 8/19/2019. Edited:
   08/23/2022
%
%Interface for Cantera for performing equilibrium calculations with
%multiphase reactants/products. Function constructs multiphase mixtures
%that Cantera can calculate equilibrium for. Function also extracts
   mole
%and mass fractions of product components and calculates the adiabatic
%flame temperature and heat of reaction of the mix. Application is
   directed
```

```
%towards energy release calculations for thermites, intermetllics, and
%combustible metals.
%
%Script hgas be written to accept any XML data file. The script scans
%assigned files to extract available species for indexing
%
%OUTPUTS:
%1)Reac_report - Cell array reporting energy release in SI and imperial
%                units and Adiabatic Flame Temeprature of reaction
%2)massprods_Report - Cell array reporting total mass of products and
   mass
%                     fractions of constituents
%3)moleprods_Report - Cell array reporting total moles of products and
   mole
%                     fractions of constituents
%4)massreacs_Report - Cell array reporting total mass of reactants and
   mass
%                     fractions of constituents
%5)molereacs_Report - Cell array reporting total moles of reactants and
    mole
%                     fractions of constituents
%
%6)specs_cons - Considered species for reaction including gaseous and
%               condensed based on elements present in reactants and
%               species available in data file
%
%7)toler_it - Tolerance for HP equilibrium (H convergence interation)
%
%8)reac_occur - Report of if reaction took place
%
%9)Continuity Check - Compare individually calculated mass for
   reactants
%                     and products to validate calculations (Cantera
   works
%                     with moles). Error tolerance for good continuity
%                     check is 10^-4
%10)Equilibrium Check - Compare mix temperature post equilibrium to pre
%                       equilibrium temperature. If no change is
   observed
%                       (<10^-4), mix is considered not to have reacted
%
%INPUTS:
%1)Reac_LiqSol - Cell array of liquid/solid phase reactants
%2)moles_Reac - Cell array of number of moles of each liquid/solid
   phase
%               reactant. Order is the same as the order of
   constituents
%               in Reac_array
%3)Reac_gasphase - Cell array of gas phase reactants
%4)moles_Reacgas - Cell array of number of moles of each gas phase
```

```
   reactant
%                  reactant. Order is the same as the order of
   constituents
%                  in Reac_gasphase
%5)P_Eqpre - Pressure of reactant mixture pre-equlibrium (ATM)
%6)T_EqpreUser - Temperature of reactant mixture pre-equlibrium (Kelvin
   )
%7)type - Equilibrate Type. Constant Enthalp only known good. Used for
%energy and flame temperature calculations. Available options are:
%                           'HP' - Enthalpy and Pressure Fixed
%                           'TP' - Temp. and Pressure Fixed
%                           'TV' - Temp. and Volume Fixed
%                           'SP' - Entropy and Pressure Fixed
%8)iter_all - Allowable number of iterations for finding solution
%9)report - Diagnostic output for Cantera Equilibrate function. Higher
%          integer values increase level of diagnostic outputs. Value
   of 3
%          provides full diagnostics of solver and execution history
%10)mechfilesource - Mechanism file to use for thermodata
%
%11)GlobeEquil - Print Mix Condtion for Global Equilibrium
%
%KNOWN ISSUES
%1) Primary solid phase oxide of fuel (ie Al2O3, Fe2O3) present for
   high
% temperature reactions where solid phase of oxide can't be present can
% lead to equilibrate failure for fuel/O2 reaction mixs (TIED TO VCS
   Poly
% EXTRAPOLATION)
%2) Species present in the mechanism file that are not assigned mole
   values
% for fuel/O2 reactions lead to equilibrate failure (SUCK IT UP)
%3)There are still some random errors thrown when working around
% stochiometric. Trying different molar amounts for the same
   stoichiometry
% to correct (SOLVED)
%4) If a product species is included with an element not present in
% the reactants, solver will fail. Because indexing is based on
   presence of
% a single element present in the reactants, will also pick out the
% flourinated aluminum compounds. (SOLVED)
%5) Cantera equilibrium solver fails to work using specified Gibbs
   solver
%   due to species lacking polynomials at different temps

%Major Modifications to solver script:
%07/27/2020: 1) Function added to allow script to create gas object
   that is
%               constructed of species that are elementally appropriate
%               (GAME CHANGER)
```

```
%08/10/2020: 1) Adaptive enthalpy convergence tolerance adjustment
   added to
%               UnivMultiphaseReac_Solver.m file to improve solution
%               finding and reduce oscillation of results around phase
%               transitions
%08/11/2020: 1) Functionality added for range evaulation of bimodal
%               compositions
%            2) Thermo results and product species reported out in
   .xlsx
%09/02/2020: 1) Functionality added to use python module to specify '
   gibbs'
%              solver for Cantera equilibrium function
%05/20/2021: 1) CanteraXMLReader2 implemented that returns polynomial
%              temperature bounds of species for phase compliancy
%10/13/2021: 1) Snip small mole fractions <10^-6 for stability
%            2) Change from length function to size function at line
   599
%               for cases when only one gas phase species
%07/13/2022: 1)Phase compliancy routine updated to maintain elemental
   mass
%               conservation and energy conservation

%% BUILD MECHANISM FILE
%%%---AVAILABLE SPECIES---%%%
%Open XML file to extract available species and temperature bounds of
%polynomials
[GasAvail_array, LiqAvail_array, SolAvail_array,ThermoSum_array] =...
    CanteraXMLReader2(mechfilesource);

%%%---SPECIES INDEXING---%%%
%Remove phase designation to allow proper indexing
Reac_LiqSolEval = eraseBetween(Reac_condphase,'(',')','Boundaries','
   inclusive');
Reac_gasphaseEval = eraseBetween(Reac_gasphase,'(',')','Boundaries','
   inclusive');

%Identify elements in reactant species array for later indexing of
   product
%species.
Reac_EleList_cond = regexp(Reac_LiqSolEval,['[','A':'Z',']['','a':'z','
   ]?'],'match');
Reac_EleList_gas = regexp(Reac_gasphaseEval,['[','A':'Z',']['','a':'z','
   ]?'],'match');

%Combine elements from gas phase and condensed pahse arrays and remove
%duplicate elements
Reac_EleList = unique(horzcat(Reac_EleList_cond{1,:},Reac_EleList_gas
   {1,:}));

%Index considered gas species based on elemental availability
```

```
%Must handled single element molecules differently
Gas_idx = zeros(numel(GasAvail_array),1);
for n=1:numel(GasAvail_array)
    Gasspecsing_eval = eraseBetween(GasAvail_array{n},'(',')','
       Boundaries','inclusive');
    species_elem = regexp(Gasspecsing_eval,['[','A':'Z',']['','a':'z','
       ]?'],'match');

    out_singhold = 0;
    for k = 1:numel(species_elem)
        for j = 1:numel(Reac_EleList)
            out_hold = regexp(species_elem{k},Reac_EleList(j));
            if strlength(species_elem{k})== strlength(Reac_EleList{j})
                %Addition issue, need to redseign so purely adding
                   doubles to
                %doubles
                if ~isempty(out_hold{1})
                    out_singhold = out_singhold + out_hold{1};
                end
            end
        end
    end
    %For single-element species, a single match for element present in
    %reactants mean species should be considered
    if numel(species_elem)<2 && sum(out_singhold)~=0
        Gas_idx(n) = 1;
        % For multi-element species, all elements in the species must
        % be matched to the elements present in the reactants to be
        % considered
    elseif out_singhold == numel(species_elem)
        Gas_idx(n) = 1;
    end
end

%Index considered liquid species based on elemental availability
%Must handled single element molecules differently
Liq_idx = zeros(numel(LiqAvail_array),1);
for n=1:numel(LiqAvail_array)
    Liqspecsing_eval = eraseBetween(LiqAvail_array{n},'(',')','
       Boundaries','inclusive');
    species_elem = regexp(Liqspecsing_eval,['[','A':'Z',']['','a':'z','
       ]?'],'match');

    out_singhold = 0;
    for k = 1:numel(species_elem)
        for j = 1:numel(Reac_EleList)
            out_hold = regexp(species_elem{k},Reac_EleList(j));
            if strlength(species_elem{k})== strlength(Reac_EleList{j})
                %Addition issue, need to redseign so purely adding
                   doubles to
```

```
                %doubles
                if ~isempty(out_hold{1})
                    out_singhold = out_singhold + out_hold{1};
                end
            end
        end
    end
    %For single-element species, a single match for element present in
    %reactants mean species should be considered
    if numel(species_elem)<2 && sum(out_singhold)~=0
        Liq_idx(n) = 1;
        % For multi-element species, all elements in the species must
        % be matched to the elements present in the reactants to be
        % considered
    elseif out_singhold == numel(species_elem)
        Liq_idx(n) = 1;
    end
end

%Index considered solid species based on elemental availability
%Must handled single element molecules differently
Sol_idx = zeros(numel(SolAvail_array),1);
for n=1:numel(SolAvail_array)
    Solspecsing_eval = eraseBetween(SolAvail_array{n},'(',')','
       Boundaries','inclusive');
    species_elem = regexp(Solspecsing_eval,['[','A':'Z',']['','a':'z','
       ]?'],'match');

    out_singhold = 0;
    for k = 1:numel(species_elem)
        for j = 1:numel(Reac_EleList)
            out_hold = regexp(species_elem{k},Reac_EleList(j));
            if strlength(species_elem{k})== strlength(Reac_EleList{j})
                %Addition issue, need to redseign so purely adding
                   doubles to
                %doubles
                if ~isempty(out_hold{1})
                    out_singhold = out_singhold + out_hold{1};
                end
            end
        end
    end
    %For single-element species, a single match for element present in
    %reactants mean species should be considered
    if numel(species_elem)<2 && sum(out_singhold)~=0
        Sol_idx(n) = 1;
        % For multi-element species, all elements in the species must
        % be matched to the elements present in the reactants to be
        % considered
    elseif out_singhold == numel(species_elem)
```

```
        Sol_idx(n) = 1;
    end
end


%Reconstruct arrays to include only components with elements in
   specified
%reactants
GasAvail_array(Gas_idx~=1) = {''};
GasAvail_array = GasAvail_array(~cellfun('isempty',GasAvail_array));

LiqAvail_array(Liq_idx~=1) = {''};
LiqAvail_array = LiqAvail_array(~cellfun('isempty',LiqAvail_array));

SolAvail_array(Sol_idx~=1) = {''};
SolAvail_array = SolAvail_array(~cellfun('isempty',SolAvail_array));

%Assemble Liquid/Solid Array
CondAvail_array = cat(1,SolAvail_array,LiqAvail_array);

%Initialize Species Lists for use
GasUse_array = GasAvail_array;
CondUse_array = CondAvail_array;

%% SAVE SPECIES CONSIDERED TO REPORT VARIABLE
specs_cons = cat(1,GasUse_array,CondUse_array);

%% CALCULATIONS: REACTANTS
%%---CREATE PHASE OBJECTS---%%
%Gas object created by writing .cti file telling cantera what species
   to
%consider. Liquid and solid phase objects created simply by loading
%specified condensed phase species into individual objects

%Create .CTI file to tell Cantera what species to add from XML
% specified by mechfilesource

%Format allow elements and species arrays and XML data  file name for
   CTI
ele_allow = string(strjoin(Reac_EleList,' '));
gasspecs_allow = string(strjoin(GasUse_array,' '));
mechfilesource_write = erase(mechfilesource,'.xml');

%Creat .CTI file defining gas object state and species for Cantera to
%create. This file is called 'GasIndexControl.cti' and is opened from
   the
%current folder in the Matlab path
fid = fopen('GasIndexControl.cti', 'wt');
if fid ~= -1
    fprintf(fid,'ideal_gas(name = "Gas_Comps",\n');
```

```
    fprintf(fid,strjoin(['elements = " ',  ele_allow,' ",\n']));
    fprintf(fid,strjoin(['species = """',mechfilesource_write,':',...
        gasspecs_allow,'""",\n']));
    fprintf(fid,'reactions = "all",\n');
    fprintf(fid,'initial_state = state(temperature = 298,\n');
    fprintf(fid,'pressure = 101325))');
    fclose(fid);
else
    warningMessage = sprintf(['Make sure GasIndexControl.cti file is '
        ...
        'in path']);
    uiwait(warndlg(warningMessage));
    return
end

%Create gas object based on indexed species and specified XML data file
%Note: GasIndexControl.cti exists in the current folder in the Matlab
   path.
%Cantera must be told where this file is. However, Cantera will look in
%'C:\Program Files\Cantera\data' for the XML data file specified in
%GasIndexControl.cti to extract information to build the ideal gas
   mixture
%object file.
gascontfileloc = fileparts(which('GasIndexControl.cti'));
mix_gas = IdealGasMix(fullfile(gascontfileloc,'GasIndexControl.cti'));

%Gas Phase Reactant Component Indexing
nsp1 = nSpecies(mix_gas); %Get number of species in mix for creating
   array
X_gas = zeros(nsp1,1);    % Mole fraction array with zeros

for k = 1:length(Reac_gasphase)
    igas = speciesIndex(mix_gas,Reac_gasphase{1,k}); %Get Index for
       species
    % Calculate mole fraction for indexed component
    X_gas(igas) = [moles_Reacgas{1,k}]/sum([moles_Reacgas{:}]);
end
%Set Mole Fractions of Gas Mixture
set(mix_gas,'X', X_gas);

%Create cell array containing liquid/solid phase component objects
Mix_SolLiq = cell(length(CondUse_array),3);
for i = 1:length(CondUse_array)
    Mix_SolLiq{i,1} = CondUse_array{i}; %Insert names for object
       indexing
    Mix_SolLiq{i,2} = Solution(mechfilesource,CondUse_array{i}); %
       Create object for substance
    Mix_SolLiq{i,3} = 0; %Set moles for each object to zero
end
```

```
%Set mole amounts for liquid/solid phase components as reactants
for i = 1:length(Reac_condphase)
    Index = find(contains(CondUse_array,Reac_condphase{i}));
    Mix_SolLiq{Index,3} = moles_Reaccond{i};
end
%%---CALCULATE REACTANT HEAT OF FORMATIONS---%%
%Combine phased mixtures into single mixture
%   Note that the objects representing each phase compute only the
%   intensive state of the phase - they do not store any information
%   on the amount of this phase. Mixture objects, on the other hand,
%   represent the full extensive state.
%
%   Mixture objects are 'lightweight' in the sense that they do not
%   store parameters needed to compute thermodynamic or kinetic
%   properties of the phases. These are contained in the
%   ('heavyweight') phase objects. Multiple mixture objects may be
%   constructed using the same set of phase objects. Each one stores
%   its own state information locally, and synchronizes the phase
%   objects whenever it requires phase properties.

%Create mix for making enthalpy of formation calculations of the
   reactants
mixReacSTP_moles = cell(length(CondUse_array)+1,2);
for i =1:(length(CondUse_array)+1)
    if i ==1
        set(mix_gas,'T',298,'P',101325);
        mixReacSTP_moles{i,1}= mix_gas;
        mixReacSTP_moles{i,2}= sum([moles_Reacgas{:}]);
    else
        set(Mix_SolLiq{i-1,2},'T',298,'P',101325);
        mixReacSTP_moles{i,1}= Mix_SolLiq{i-1,2};
        mixReacSTP_moles{i,2}= Mix_SolLiq{i-1,3};
    end
end

%Form Mix for Enthalpy of Formation Calculations
%Seperate mix required due to equilibrate solver issues
mix_form = Mixture(mixReacSTP_moles);

%Calculate heat of formation of reactants at STP
hform_reacs = 0;
for j = 1:length(mixReacSTP_moles)
    hform_reacs = hform_reacs + enthalpy_mole(mixReacSTP_moles{j,1})*
       mixReacSTP_moles{j,2}/(1000*1000);

end


%Create mix for making enthalpy caluclations of reactants
mixReac_moles = cell(length(CondUse_array)+1,2);
```

```
for i =1:(length(CondUse_array)+1)
    if i ==1
        set(mix_gas,'T',T_EqpreUser,'P',101325);
        mixReac_moles{i,1}= mix_gas;
        mixReac_moles{i,2}= sum([moles_Reacgas{:}]);
    else
        set(Mix_SolLiq{i-1,2},'T',T_EqpreUser,'P',101325);
        mixReac_moles{i,1}= Mix_SolLiq{i-1,2};
        mixReac_moles{i,2}= Mix_SolLiq{i-1,3};
    end
end

%Form Mix for Enthalpy of Formation Calculations
%Seperate mix required due to equilibrate solver issues
mix_form = Mixture(mixReac_moles);

%Calculate the enthalpy of the reactants at user specified temp
h_reac = 0;
for j = 1:length(mixReac_moles)
    h_reac = h_reac + enthalpy_mole(mixReac_moles{j,1})*mixReac_moles{j
       ,2}/1000;

end

%%%---TOTAL MASS AND MOLE FRACTIONS OF REACTANTS---%%%
%Calculate mole and mass fractions of total system
reac_molefracs = cell(length(mixReac_moles),1);
reac_massfracs = cell(length(mixReac_moles),1);
reac_mass = 0;
for i =1:length(mixReac_moles)
    %Calculate total mole fraction of mixture
    reac_molefracs{i,1} = moleFractions(mixReac_moles{i,1}).*...
        mixReac_moles{i,2}/sum([mixReac_moles{:,2}]);

    %Calculate total mass of mixture (g)
    reac_mass = reac_mass + meanMolecularWeight(mixReac_moles{i,1})*
       mixReac_moles{i,2};
end

%Calculate total mass fraction of mixture
for i =1:length(mixReac_moles)
    reac_massfracs{i,1} = (reac_molefracs{i,1}.*...
        molecularWeights(mixReac_moles{i,1}).*sum([mixReac_moles{:,2}])
           )/reac_mass;
end

%Assemble Labeled Mole Fraction Array for Reporting
%Assemble Gas Phase Species
molefrac_reacs_label = cell((length(mixReac_moles)+length(speciesNames(
   mixReac_moles{1,1}))-1),2);
```

```
gas_compname = speciesNames(mixReac_moles{1,1});
gas_molfrac = reac_molefracs{1,1};
for i =1:length(speciesNames(mixReac_moles{1,1}))
    molefrac_reacs_label{i,1} = gas_compname{1,i};
    molefrac_reacs_label{i,2} = gas_molfrac(i);
end

%Assemble liquid/solidphase species
start = length(speciesNames(mixReac_moles{1,1}))+1;
liqsol_compname = cell(1,length(2:length(mixReac_moles)));
liqsol_molfrac = cell(length(2:length(reac_molefracs)),1);

for j = 1:length(liqsol_compname)
    liqsol_compname{1,j} = char(speciesNames(mixReac_moles{j+1,1}));
    liqsol_molfrac{j} = reac_molefracs{j+1,1};
end

for i =start:length(molefrac_reacs_label)
    molefrac_reacs_label{i,1} = liqsol_compname{1,i-length(gas_molfrac)
       };
    molefrac_reacs_label{i,2} = liqsol_molfrac{i-length(gas_molfrac)};
end

%Create Report for Reactant Mole Fractions
molereacs_Report = cat(1,cat(2,{'Total Moles'}, sum([moles_Reacgas{:},
   moles_Reaccond{:}])),...
    molefrac_reacs_label,...
    cat(2,{'Frac Sum (%)'},...
    num2cell(100*sum(cat(1,reac_molefracs{1,1},reac_molefracs{2:length(
       reac_molefracs),1})))));

%Assemble Labeled Mass Fraction Array for Reporting
%Assemble Gas Phase Species
massfrac_reacs_label = cell((length(mixReac_moles)+length(speciesNames(
   mixReac_moles{1,1}))-1),2);
gas_compname = speciesNames(mixReac_moles{1,1});
gas_massfrac = reac_massfracs{1,1};
for i =1:length(speciesNames(mixReac_moles{1,1}))
    massfrac_reacs_label{i,1} = gas_compname{1,i};
    massfrac_reacs_label{i,2} = gas_massfrac(i);
end

%Assemble liquid/solidphase species
start = length(speciesNames(mixReac_moles{1,1}))+1;
liqsol_compname = cell(1,length(2:length(mixReac_moles)));
liqsol_massfrac = cell(length(2:length(reac_massfracs)),1);

for j = 1:length(liqsol_compname)
    liqsol_compname{1,j} = char(speciesNames(mixReac_moles{j+1,1}));
    liqsol_massfrac{j} = reac_massfracs{j+1,1};
```

```
end

for i =start:length(massfrac_reacs_label)
    massfrac_reacs_label{i,1} = liqsol_compname{1,i-length(gas_massfrac
        )};
    massfrac_reacs_label{i,2} = liqsol_massfrac{i-length(gas_massfrac)
        };
end

%Create Report for Reactant Mass Fractions
massreacs_Report = cat(1,cat(2,{'Total Mass (g)'}, num2cell(reac_mass))
    ,...
    massfrac_reacs_label,...
    cat(2,{'Frac Sum (%)'},...
    num2cell(100*sum(cat(1,reac_massfracs{1,1},reac_massfracs{2:length(
        reac_massfracs),1})))));



%%---EQUILIBRIUM ROUTINE START---%%
%Phase check count variable initialization
PHcheck = 20;
PHfinal = 1; %If 20 iteration can not find phase compliant mix, will
    use the lowest enthalpy error condition which is triggered by
%Initiate equilibrium routine
T_Eqpre = T_EqpreUser;
h_pCOE = 0;
COEErrormin = 1000; %Minimum COE error calculated
COEmin_Reac_condphase = 0;
mixmade = 'No';
while PHcheck > 0 || PHfinal > 0
    %If max iterations met, set system to run with best PHC system
    if PHcheck == 0
        PHfinal =0;
    end

    %%---CREATE PHASE OBJECTS---%%
    %Gas object created by writing .cti file telling cantera what
        species to
    %consider. Liquid and solid phase objects created simply by loading
    %specified condensed phase species into individual objects

    %Create .CTI file to tell Cantera what species to add from XML
    % specified by mechfilesource

    %Format allow elements and species arrays and XML data  file name
        for CTI
    ele_allow = string(strjoin(Reac_EleList,' '));
    gasspecs_allow = string(strjoin(GasUse_array,' '));
    mechfilesource_write = erase(mechfilesource,'.xml');
```

```
%Creat .CTI file defining gas object state and species for Cantera
   to
%create. This file is called 'GasIndexControl.cti' and is opened
   from the
%current folder in the Matlab path
fid = fopen('GasIndexControl.cti', 'wt');
if fid ~= -1
    fprintf(fid,'ideal_gas(name = "Gas_Comps",\n');
    fprintf(fid,strjoin(['elements = " ',  ele_allow,' ",\n']));
    fprintf(fid,strjoin(['species = """',mechfilesource_write,':',
       ...
        gasspecs_allow,'""",\n']));
    fprintf(fid,'reactions = "all",\n');
    fprintf(fid,'initial_state = state(temperature = 298,\n');
    fprintf(fid,'pressure = 101325))');
    fclose(fid);
else
    warningMessage = sprintf(['Make sure GasIndexControl.cti file
       is '...
        'in path']);
    uiwait(warndlg(warningMessage));
    return
end

%Create gas object based on indexed species and specified XML data
   file
%Note: GasIndexControl.cti exists in the current folder in the
   Matlab path.
%Cantera must be told where this file is. However, Cantera will
   look in
%'C:\Program Files\Cantera\data' for the XML data file specified in
%GasIndexControl.cti to extract information to build the ideal gas
   mixture
%object file.
gascontfileloc = fileparts(which('GasIndexControl.cti'));
mix_gas = IdealGasMix(fullfile(gascontfileloc,'GasIndexControl.cti'
   ));

%Gas Phase Reactant Component Indexing
nsp1 = nSpecies(mix_gas); %Get number of species in mix for
   creating array
X_gas = zeros(nsp1,1);    % Mole fraction array with zeros

for k = 1:length(Reac_gasphase)
    igas = speciesIndex(mix_gas,Reac_gasphase{1,k}); %Get Index for
        species
    % Calculate mole fraction for indexed component
    X_gas(igas) = [moles_Reacgas{1,k}]/sum([moles_Reacgas{:}]);
end
```

```
%Set Mole Fractions of Gas Mixture
set(mix_gas,'X', X_gas);

%Create cell array containing liquid/solid phase component objects
Mix_SolLiq = cell(length(CondUse_array),3);
for i = 1:length(CondUse_array)
    Mix_SolLiq{i,1} = CondUse_array{i}; %Insert names for object
        indexing
    Mix_SolLiq{i,2} = Solution(mechfilesource,CondUse_array{i}); %
        Create object for substance
    Mix_SolLiq{i,3} = 0; %Set moles for each object to zero
end

%Set mole amounts for liquid/solid phase components as reactants
for i = 1:length(Reac_condphase)
    Index = find(contains(CondUse_array,Reac_condphase{i}));
    Mix_SolLiq{Index,3} = moles_Reaccond{i};
end


%% EQUILIBRATE REACTANTS
%%%---ASSEMBLE MIXTURE FOR EQUILIBRATION---%%%
%Must set P and T of component objects before making mix to prevent
    crashing
%equilibrate...no fucking idea why.
mixEQ_moles = cell(length(CondUse_array)+1,2);
for i =1:(length(CondUse_array)+1)
    if i ==1
        set(mix_gas,'T',T_Eqpre,'P',P_Eqpre*101325);
        mixEQ_moles{i,1}= mix_gas;
        mixEQ_moles{i,2}= sum([moles_Reacgas{:}]);
    else
        set(Mix_SolLiq{i-1,2},'T',T_Eqpre,'P',P_Eqpre*101325);
        mixEQ_moles{i,1}= Mix_SolLiq{i-1,2};
        mixEQ_moles{i,2}= Mix_SolLiq{i-1,3};
    end
end

%Form Mix for Equilibrium Calculations
mix_EQ = Mixture(mixEQ_moles);

%%%---PHASE COMPLIANCY ENERGY CONSERVATION---%%%
%If equilibrating for phase compliancy, need to adjust temperature
    of
%components until enthalpy of new mix aligns with enthalpy of
    product
%state before sending back to equilibrate
%Uses iterative method to adjust T
if PHfinal>0
    COEError=0;
```

```
if h_pCOE~=0
    %Initialize variables
    Ttest= T_Eqpre-1; %First guess is the temperature of the
       mix prior to
    %PHC enforcment
    tolerCOE = 1;%Within 1 percent of enthalpy
    h_pTest = 0;
    itcnt = 1000;
    while abs(100*(h_pCOE - h_pTest)/h_pCOE)>tolerCOE
        %Recreate mix with new temperature guess
        %Reinitilaize variables
        mixEQ_molesTest = mixEQ_moles;
        mix_gasTest = mix_gas;

        for i =1:(length(CondUse_array)+1)
            if i ==1
                set(mix_gasTest,'T',Ttest,'P',P_Eqpre*101325);
                mixEQ_molesTest{i,1}= mix_gasTest;
                mixEQ_molesTest{i,2}= sum([moles_Reacgas{:}]);
            else
                set(Mix_SolLiq{i-1,2},'T',Ttest,'P',P_Eqpre
                   *101325);
                mixEQ_molesTest{i,1}= Mix_SolLiq{i-1,2};
                mixEQ_molesTest{i,2}= Mix_SolLiq{i-1,3};
            end
        end
        %Let mix equilibrate using the Cantera Function
        mix_EQ = Mixture(mixEQ_molesTest);
        equilibrate(mix_EQ, 'TP', 1.0, iter_all, 200, report);

        %Determine enthalpy of mixture
        h_pTest= 0;
        for j = 1:length(mixEQ_molesTest)
            h_pTest = h_pTest + enthalpy_mole(mixEQ_molesTest{j
               ,1})*mixEQ_molesTest{j,2};%KJ/MOL
        end

        %Report Difference
        COEError = 100*(h_pCOE - h_pTest)/h_pCOE;
        Ttest

        %Check to see if tolerance met. Break if it does,
           update guess
        %if it doesn't
        if abs(100*(h_pCOE - h_pTest)/h_pCOE)<tolerCOE
            fprintf('
               <**************************************************>
                \n')
            fprintf(' \n')
            fprintf('Energy conserved on phase compliant mix\n'
```

```
            )
            fprintf(' \n')
            break
        else
            %Update temperature guess bounds
            if h_pTest > h_pCOE
                Ttest = Ttest-1;
            else
                Ttest = Ttest+1;
            end
        end
        %Count iteration times
        itcnt = itcnt-1;

        %If temperature converges but contant enthalpy
           enforcement
        %fails after itcnt attempts, go ahead and break out and
            try
        %temperature guess anyways
        if itcnt<=0

            fprintf('
               <*****************************************************>
                \n')
            fprintf(' \n')
            fprintf('Failed to obtain enthalpy convergence,
               convergence error %%: \n')
            100*(h_pCOE - h_pTest)/h_pCOE
            fprintf('Attempting to use converged temperature
               value \n')
            fprintf(' \n')
            break
        end
    end
    %If temperature changes to require enthalpy convergence,
       update TEqpre
    if Ttest~=T_Eqpre
        T_Eqpre = Ttest;
    end
    %Save lowest convergence error and state, if PHC
       equilibrium checks
    %iterate out, use lowest error state
    %%%HOWEVER, I NEED TO CONSIDER HOW TO DEAL WITH MULTIPLE
    %%%MINIMUM STATES UNDER PRESSURE (HIGH PRESSURE DRIVES DOWN
        GAS
    %%%FORMATION)
    %%%The issue is by varying the pressure, we obtain multiple
    %%%solution states- Need to identify the best one
    %%%FOR AL/FE2O3 Stoich, believe most condensed species
       state, but T is too high force non
```

```
        %%%phase compliance
        if length(Reac_condphase)>=length(COEmin_Reac_condphase)
            COEErrormin = COEError;
            COEmin_Reac_gasphase =  Reac_gasphase;
            COEmin_moles_Reacgas = moles_Reacgas;
            COEmin_Reac_condphase =  Reac_condphase;
            COEmin_moles_Reaccond =  moles_Reaccond;
            COEmin_T = T_Eqpre;

        end

    end
end

%%%---CREATE EQUILIBRIUM VARIABLES FOR PYTHON SOLVER SCRIPT---%%%
%Data files
gascontfileloc = fileparts(which('GasIndexControl.cti')); %Loc. gas
    file
cti_gas = fullfile(gascontfileloc,'GasIndexControl.cti'); %Gas data
    file
cti_cond = mechfilesource; %Condensed data file
spec_c = CondUse_array'; %Considered condensed species
moles_c = Mix_SolLiq(:,3)'; %Moles of condensed species
moles_g = sum([moles_Reacgas{:}]); %Total moles of gas phase
   species
molfrac_g = X_gas';%Mole fractions of gas phase

%%%---INITIALIZE PYTHON---%%%
%Create python module to communicate with Cantera's equilibrate
   function
%Check to make sure python is loaded
if strcmp(pyversion,'')
    pyversion C:\Python37\python.exe
end
%Create equilibrium python module
Equil = py.importlib.import_module('PyEquil');
Equil = py.importlib.reload(Equil);

%Initialization variables
solver = 'vcs'; %vcs or gibbs only options for multiphase
toler_it = 1.0e-9; %Error tolerance in iterations to find solution
max_steps = iter_all; %Number of steps in finding equilibrium at
   specified T,P
max_iter = 200; %Number of steps iterations in finding equil. for
   HP or UV
estimate_equil = 1; %Whether solver should estimate initial
   condition.
%0 means no estimation
log_level = report; %Requested output during solution finding
   process
```

```
pysol = [];

%NOTE:
%Implement error catch in case equlibrium calculation fails and
   increase
%error tolerance until solution is found. 1000 attempts are tried
%This is a more robust solution method than attempting to
   equilibrate once
%with the most restrictive error tolerance imposed. DAMN CANTERA
   GREMLINS!

% Equilibrium success variable
equilgood = 'false';

%Number of equilibrium attempts to be made
equilcnt = 100;
m = 0;
%Convergence error tolerance step size
dtoler_itlarge = 0.001;

while strcmp(equilgood,'false')
    %Reset success variable
    equilgood = 'true';
    %Update iteration count
    m = m +1;

    try
        %Report attempted tolerance every one hundred iterations
        if rem(m,100)==0
            fprintf('
               <*****************************************************>
                \n')
            fprintf(' \n')
            fprintf('100x Cantera Equilibrate Failure, Increasing
               convergence error tolerance \n')
            fprintf(' \n')
            fprintf(['Cantera Equilibrate Start, ',...
                'Convergence ', num2str(toler_it),' error tolerance
                    \n'])
            fprintf(' \n')
        end
        %Python Module for Equilibration
        if log_level==0
            %Suppress output from solver
            [T,pysol] = evalc(['Equil.HP(T_Eqpre,P_Eqpre*101325,
               solver,',...
                'toler_it,max_steps,max_iter,estimate_equil,
                   log_level,',...
                'spec_c,moles_c,moles_g,num2cell(molfrac_g),',...
                'cti_gas,cti_cond)']);
```

```
        else
            %Allow equilibrium solver to report to console
            pysol = Equil.HP(T_Eqpre,P_Eqpre*101325,solver,toler_it
                ,...
                max_steps,max_iter,estimate_equil,log_level,spec_c,
                    ...
                moles_c,moles_g,num2cell(molfrac_g),cti_gas,
                    cti_cond);
        end
        %Cantera Module for Equilibration
        %equilibrate(mix_EQ, type, toler_it, iter_all, 200, report)
            ;
        %equilibrate(mix_EQ, type, 1.0e-4, iter_all, 200, report);
    catch
        if m==equilcnt
            %If max iteration limit met, report input reaction
                conditions
            %may be wrong and to recheck input
            fprintf('
                <**************************************************>
                 \n')
            fprintf(' \n')
            fprintf([num2str(m),'X Cantera Equilibrate Failure,
                Check Input \n'])
            fprintf(' \n')

        else
            equilgood = 'false';
            %If max iteration limit not met, adjust convergence
                error
            %tolerance
            %Adjust tolerance
            if toler_it < dtoler_itlarge
                %For tight error tolerance, increase tolerance by
                    order of magnitude
                toler_it = toler_it *10;
            else
                %Once attempted tolerance reaches dtoler_itlarge,
                    increase by
                %prescribed tolerance step dtoler_itlarge
                %This criteria is based on intuition and experience
                     in
                %solution hunting.
                toler_it = toler_it + dtoler_itlarge;
            end

        end
    end
end
```

```
%%%---REFORM PYTHON DATA INTO MATLAB/CANTERA MIXTURE---%%%
%If solution found by python module, reconstruct mix_eq, else using
    OG
%mix_eq
if ~isempty(pysol)
    %Extract information from solution returned by python
    Tp = pysol{1}; %Temperature of products
    Pp = pysol{2}; %Pressure of products
    specs_p = cellstr(string(cell(pysol{3}))); %List of Product
       Species
    Np = cell(pysol{4}); % Moles of products

    %Create array of species and moles
    Mixp_raw = [specs_p',Np'];

    %Identify condensed species
    Ind_c = strfind(Mixp_raw(:,1),'('); %Index by paranthesis
    tf1 = cellfun('isempty',Ind_c); %Index empty cells
    Ind_c(tf1) = {0}; %Add zero to empty cells
    Ind_c = cell2mat(Ind_c);
    Ind_c(Ind_c(:)>1) = 1;
    Ind_c = logical(Ind_c); %Convert array to logical array
    Prods_condphase = [Mixp_raw(Ind_c,1),Mixp_raw(Ind_c,2)];

    %Identify gas species
    Ind_g = ~Ind_c;
    Prods_gasphase = [Mixp_raw(Ind_g,1),Mixp_raw(Ind_g,2)];

    %Convert gas moles to indexed mole fractions
    %First Reset Gas mole fraction variable, X_gasP, to be empty
       array
    X_gasP=[];
    for k = 1:size(Prods_gasphase,1)
        igas = speciesIndex(mix_gas,Prods_gasphase{k,1}); %Get
           Index for species
        % Calculate mole fraction for indexed component
        %Check if no gas phase present
        if sum([Prods_gasphase{:,2}])== 0
            X_gasP(igas) = 1E-9;
        else
            %Snip mole fractions that are <10^-6 for stability
            %                 if Prods_gasphase{k,2}<10^-6
            %                     Prods_gasphase{k,2} = 0;
            %                 end
            X_gasP(igas) = [Prods_gasphase{k,2}]/sum([
               Prods_gasphase{:,2}]);
        end
    end
    %Create new condensed phase cell array for product species
       reported by Python
```

```
    Mix_SolLiqP = cell(length(Prods_condphase(:,1)),3);
    for i = 1:length(CondUse_array)
        Mix_SolLiqP{i,1} = Prods_condphase{i,1}; %Insert names for
            object indexing
        Mix_SolLiqP{i,2} = Solution(mechfilesource,Prods_condphase{
            i,1}); %Create object for substance
        Mix_SolLiqP{i,3} = Prods_condphase{i,2}; %Set moles for
            each object
        set(Mix_SolLiq{i,2},'T',Tp,'P',Pp);
    end

        %Set temperature, pressure, and mole fractions of product
            gas mixture
        set(mix_gas,'T',Tp,'P',Pp,'X', X_gasP);

        %Set cell array for constructing mixture
        mixprods_moles = cell(length(Prods_condphase(:,1))+1,2);
        for i =1:(length(CondUse_array)+1)
            if i ==1
                mixprods_moles{i,1}= mix_gas;
                mixprods_moles{i,2}= sum(cat(3,Prods_gasphase{:,2})
                    );
            else
                set(Mix_SolLiqP{i-1,2},'T',Tp,'P',Pp);
                mixprods_moles{i,1}= Mix_SolLiqP{i-1,2};
                mixprods_moles{i,2}= Mix_SolLiqP{i-1,3};
            end
        end

    %Create Mixture of products
    mix_EQ = Mixture(mixprods_moles);

else
    %Determine moles of products in reactedmix
    mixprods_moles = cell(length(CondUse_array)+1,2);
    for i =1:(length(CondUse_array)+1)
        if i ==1
            mixprods_moles{i,1}= mix_gas;
            mixprods_moles{i,2}= phaseMoles(mix_EQ,i);
        else
            mixprods_moles{i,1}= Mix_SolLiq{i-1,2};
            mixprods_moles{i,2}= phaseMoles(mix_EQ,i);
        end
    end
end
%% CALCULATIONS: PRODUCTS
%%%---TOTAL MASS AND MOLE FRACTIONS OF PRODUCTS---%%%

%%%---OG CODE HERE DOWN---%%%
%Calculate mole and mass fractions of total system
```

```
prods_molefracs = cell(length(mixprods_moles),1);
prods_massfracs = cell(length(mixprods_moles),1);
prods_mass = 0;
for i =1:length(mixprods_moles)
    %Calculate total mole fraction of mixture
    prods_molefracs{i,1} = moleFractions(mixprods_moles{i,1}).*...
        mixprods_moles{i,2}/sum([mixprods_moles{:,2}]);

    %Calculate total mass of mixture (g)
    prods_mass = prods_mass + meanMolecularWeight(mixprods_moles{i
       ,1}).*mixprods_moles{i,2};
end

%Calculate total mass fraction of mixture
for i =1:length(mixprods_moles)
    prods_massfracs{i,1} = (prods_molefracs{i,1}.*...
        molecularWeights(mixprods_moles{i,1}).*sum([mixprods_moles
           {:,2}]))/prods_mass;
end

%Assemble Labeled Mole Fraction Array for Reporting
%Assemble Gas Phase Species
molefrac_prods_label = cell((length(mixprods_moles)+length(
   speciesNames(mixprods_moles{1,1}))-1),2);
gas_compname = speciesNames(mixprods_moles{1,1});
gas_molfrac = prods_molefracs{1,1};
for i =1:length(speciesNames(mixprods_moles{1,1}))
    molefrac_prods_label{i,1} = gas_compname{1,i};
    molefrac_prods_label{i,2} = gas_molfrac(i);
end

%Assemble liquid/solidphase species
start = length(speciesNames(mixprods_moles{1,1}))+1;
liqsol_compname = cell(1,length(2:length(mixprods_moles)));
liqsol_molfrac = cell(length(2:length(prods_molefracs)),1);

for j = 1:length(liqsol_compname)
    liqsol_compname{1,j} = char(speciesNames(mixprods_moles{j+1,1})
       );
    liqsol_molfrac{j} = prods_molefracs{j+1,1};
end

for i =start:length(molefrac_prods_label)
    molefrac_prods_label{i,1} = liqsol_compname{1,i-length(
       gas_molfrac)};
    molefrac_prods_label{i,2} = liqsol_molfrac{i-length(gas_molfrac
       )};
end

%Create Report for Reactant Mole Fractions
```

```
moleprods_Report = cat(1,cat(2,{'Total Moles'}, sum([mixprods_moles
    {:,2}])),...
    molefrac_prods_label,...
    cat(2,{'Frac Sum (%)'},...
    num2cell(100*sum(cat(1,prods_molefracs{1,1},prods_molefracs{2:
        length(prods_molefracs),1})))));

%Assemble Labeled Mass Fraction Array for Reporting
%Assemble Gas Phase Species
massfrac_prods_label = cell((length(mixprods_moles)+length(
    speciesNames(mixprods_moles{1,1}))-1),2);
gas_compname = speciesNames(mixprods_moles{1,1});
gas_massfrac = prods_massfracs{1,1};
for i =1:length(speciesNames(mixprods_moles{1,1}))
    massfrac_prods_label{i,1} = gas_compname{1,i};
    massfrac_prods_label{i,2} = gas_massfrac(i);
end

%Assemble liquid/solidphase species
start = length(speciesNames(mixReac_moles{1,1}))+1;
liqsol_compname = cell(1,length(2:length(mixprods_moles)));
liqsol_massfrac = cell(length(2:length(prods_massfracs)),1);

for j = 1:length(liqsol_compname)
    liqsol_compname{1,j} = char(speciesNames(mixprods_moles{j+1,1})
        );
    liqsol_massfrac{j} = prods_massfracs{j+1,1};
end

for i =start:length(massfrac_prods_label)
    massfrac_prods_label{i,1} = liqsol_compname{1,i-length(
        gas_massfrac)};
    massfrac_prods_label{i,2} = liqsol_massfrac{i-length(
        gas_massfrac)};
end

%Create Report for Reactant Mass Fractions
massprods_Report = cat(1,cat(2,{'Total Mass (g)'}, num2cell(
    prods_mass)),...
    massfrac_prods_label,...
    cat(2,{'Frac Sum (%)'},...
    num2cell(100*sum(cat(1,prods_massfracs{1,1},prods_massfracs{2:
        length(prods_massfracs),1})))));

%%%---ADIABATIC FLAME TEMPERATURE---%%%
%Temperature of entire mix
T = temperature(mix_EQ);

%%%---ENTHALPY OF MIXTURE---%%%
%Save enthalpy of products for conservation of energy enforcement
```

```
h_pCOE = 0;
for j = 1:length(mixprods_moles)
    h_pCOE = h_pCOE + enthalpy_mole(mixprods_moles{j,1})*
        mixprods_moles{j,2};%KJ/MOL
end

%%%---ERROR CHECKS---%%%
%Initialize phase compliancy confirmation variable
PHcomp = 'No';

% Continuity Check
if abs(prods_mass-reac_mass)<10^-4
    fprintf('
        <**************************************************> \
        n')
    fprintf(' \n')
    fprintf('Continuity Check GOOD(Total error <10^-4) \n')
    fprintf(' \n')
else
    fprintf('
        <**************************************************> \
        n')
    fprintf(' \n')
    fprintf('!! WARNING: Continuity Check BAD (Total error >10^-4)
        !! \n')
    fprintf(' \n')
end

%Reaction/Temperature Validity Check
if abs(T)>6000
    fprintf('
        <**************************************************> \
        n')
    fprintf(' \n')
    fprintf('!! WARNING:FALSE EQUILIBRIUM LIKELY (T>6000K) !! \n')
    fprintf('!! ENDING SOLVER ROUTINE !! \n')
    fprintf(' \n')
    PHcomp='Yes';
end

%Reaction Occurance Check
if abs(T-T_Eqpre)<1
    fprintf('
        <**************************************************> \
        n')
    fprintf(' \n')
    fprintf('!! WARNING: No Combustion Reaction Occured (ABS(T-
        T_Eqpre)<1K) !! \n')
    fprintf(' \n')
    reac_occur = 'No';
```

```
else
    fprintf('
       <**************************************************> \
       n')
    fprintf(' \n')
    fprintf('Combustion Reaction Occured, Equilibrium Determined
       Pending Cantera Solver Report \n')
    fprintf(' \n')
    reac_occur = 'Yes';
end

%%---PHASE COMPLIANCY ENFORCEMENT---%%
if PHfinal >0
    %Save list of species originally considered
    GasTried_array = GasUse_array;
    CondTried_array = CondUse_array;

    %Determine number of moles for elements present in species
    %Create storage array for mole count by species
    SpecElem_moles = cell([(length(GasTried_array)+ length(
       CondTried_array)),length(Reac_EleList)+1]);
    SpecElem_moles = cat(1,cat(2,{'Species'},Reac_EleList),
       SpecElem_moles);
    %Create storage array for moles by element only
    Elem_moles = cell(1,length(Reac_EleList));
    Elem_moles = cat(1,Reac_EleList,Elem_moles);
    Elem_moles(2,:)={0};

    %Sweep through species to determine moles of atoms present
    for i=1:length(Reac_EleList)
        for j=1:length(mixprods_moles)
            if j==1 %We will index the gas phase slightly
               differently
                %Pull gas object out for indexing
                gasforAtoms = mixprods_moles{1,1};
                for g = 1:1:nSpecies(mixprods_moles{1,1})
                    %Get number of moles of element present in
                       species
                    try
                        cntAtom = nAtoms(gasforAtoms,g,Reac_EleList
                           {i});
                    catch
                        cntAtom =0;
                    end
                    %Save species and elemental amount
                    SpecElem_moles{g+1,1} = char(speciesName(
                       gasforAtoms,g));
                    SpecElem_moles{g+1,i+1} = cntAtom*
                       moleprods_Report{g+1,2};
```

```
            end
        else
            %Get number of moles of element present in species
            try
                cntAtom = nAtoms(mixprods_moles{j,1},name(
                    mixprods_moles{j,1}),Reac_EleList{i});
            catch
                cntAtom =0;
            end
            %Save species and elemental amount
            SpecElem_moles{j+g,1} = name(mixprods_moles{j,1});
            SpecElem_moles{j+g,i+1} = cntAtom*moleprods_Report{
                j+g,2};

        end
    end
end


%Reinitialize considered species variables and include
    reactants
%regardless of phase compliancy
%GasUse_array =  Reac_gasphase';
%CondUse_array = Reac_Cond';
GasUse_array =  {};
CondUse_array = {};


%Determine species that are phase compliant for the product
%temperature and assemble new phase compliant mixture
%Loosen bounds so if riding a phase transition don't over
    constrain
tolerT_low = 10;
tolerT_high = 10;

for i = 1:length(ThermoSum_array)
    %Extract temperature boundaries of species
    Tmin = str2double(ThermoSum_array{i,3});
    Tmax = str2double(ThermoSum_array{i,4});

    %Determine if species could potentially exist at the
        calcualted
    %temperature
    if (Tmin < T+tolerT_low) && (Tmax > T-tolerT_high)
        %Determine if species is available for consideration
        if any(strcmp(GasAvail_array,ThermoSum_array{i,1}))
            %If species passes both checks, add to species
                compilant
            %gas species array if doesn't exist
            if ~any(strcmp(GasUse_array,ThermoSum_array{i,1}))
```

```
                GasUse_array = cat(1, GasUse_array ,
                    ThermoSum_array{i,1});
            end
        elseif any(strcmp(CondAvail_array,ThermoSum_array{i,1})
            )
            %If species passes both checks, add to species
                complaint
            %condensed species array if doesn't exist
            if ~any(strcmp(CondUse_array,ThermoSum_array{i,1}))
                CondUse_array = cat(1, CondUse_array ,
                    ThermoSum_array{i,1});
            end
        end
    else
        %If species not phase compliant, but had non zero moles
            in
        %the prior equilibrium solution, save amount of moles
            of
        %elements to be redistributed
        ind = find(strcmp(SpecElem_moles(:,1),ThermoSum_array{i
            ,1}));

        if ~isempty(ind)%
            for k=1:length(Reac_EleList)
                %Multiply moles of elements by moles present in
                    mix
                Elem_moles{2,k} = Elem_moles{2,k}+
                    SpecElem_moles{ind,k+1};
            end
        end
    end
end

%%%BUILD NEW REACTANTS SET (SPECIES AND MOLES)
%Reinitialize reaction species variables
Reac_gasphase ={};
moles_Reacgas = {};
Reac_condphase = {};
moles_Reaccond = {};

%Remove any species that are not phase compliant
for j=1:length(mixprods_moles)
    if j==1 %We will index the gas phase slightly differently
        %Pull gas object out for indexing
        for g = 1:1:nSpecies(mixprods_moles{1,1})
            %Gas Product Molar Amounts
            %Reac_gasphase Stores names of gas species.
            %moles_Reacgas stores moles or each species
            %Check to see if species from prior equilibrium is
                allowed
```

```
            %by PHC, if so add it and molar amounts
            if any(strcmp(GasUse_array,char(speciesName(
               mixprods_moles{1,1},g))))
                Reac_gasphase = cat(2,Reac_gasphase,speciesName
                   (mixprods_moles{1,1},g));
                moles_Reacgas = cat(2, moles_Reacgas,
                   mixprods_moles{1,2}*moleFraction(
                   mixprods_moles{1,1},speciesName(
                   mixprods_moles{1,1},g)));
            end
        end
        %Condensed Product Molar Amounts
        %Reac_gasphase Stores names of gas species.
        %moles_Reacgas stores moles or each species
        %Check to see if species from prior equilibrium is
           allowed
        %by PHC, if so add it and molar amounts
    elseif any(strcmp(CondUse_array,char(speciesName(
       mixprods_moles{j,1},1))))
        Reac_condphase = cat(2,Reac_condphase,speciesName(
           mixprods_moles{j,1},1));
        moles_Reaccond = cat(2,moles_Reaccond,mixprods_moles{j
           ,2});
    end
end
%Add any species back in that may have dropped out but are now
   phase
%compliant
for n=1:length(GasUse_array)
    if ~ismember(GasUse_array(n),Reac_gasphase)
        Reac_gasphase = cat(2,Reac_gasphase,GasUse_array(n));
        moles_Reacgas = cat(2, moles_Reacgas, 0);
    end
end

for n=1:length(CondUse_array)
    if ~ismember(CondUse_array(n),Reac_condphase)
        Reac_condphase = cat(2,Reac_condphase,CondUse_array(n))
           ;
        moles_Reaccond = cat(2, moles_Reaccond, 0);
    end
end


%%%REDISTRIBUTE ELEMENTS OF REMOVE SPECIES TO ENSURE CONTINUITY
    MET
%Increase molar amount of single element species to ensure
   continuity
%maintained
%Elem_moles contains molar amount of elements that need to be
```

```
    %redistributed

    for i = 1:length(Elem_moles(1,:))

        %Check to see if any elements remain, if they do need to
        %redistribtue in the condense phase first(Solid then liquid
            )
        if sum([Elem_moles{2,:}],'all')~=0
            %Check Liquid Elements

            elSol_check = strcat(Elem_moles{1,i},'(s)');
            eldist_idx =strcmp(Reac_condphase,elSol_check);
            eldist_idx = find(eldist_idx~=0,1,'first');
            if eldist_idx~=0
                moles_Reaccond{eldist_idx} = moles_Reaccond{
                    eldist_idx}+Elem_moles{2,i};

            else
                elLiq_check = strcat(Elem_moles{1,i},'(L)');
                eldist_idx =strcmp(Reac_condphase,elLiq_check);
                eldist_idx = find(eldist_idx~=0,1,'first');
                if eldist_idx~=0
                    moles_Reaccond{eldist_idx} = moles_Reaccond{
                        eldist_idx}+Elem_moles{2,i};
                end
            end
        end

        %Check Gas phase next. Don't want to do gas phase first as
            elements
        %intuitively distribtute to condensed phase and then gas
            phase
        eldist_idx =strcmp(Reac_gasphase,Elem_moles{1,i});
        eldist_idx = find(eldist_idx~=0,1,'first');
        if eldist_idx~=0
            moles_Reacgas{eldist_idx} = moles_Reacgas{eldist_idx}+
                Elem_moles{2,i};
        end

    end
end

%%% REPORT SPECIES and MOLES CONSIDERED AT TEMP
Reac_gasphase
moles_Reacgas
Reac_condphase
moles_Reaccond
T
```

```
%Check to see if no species meet phase compliancy
%Check solid species and if neither solid and gas species meet
   phase
%compliancy, break out of the solver
if strcmp(PHcomp,'No')
    if isempty(CondUse_array)&& isempty(GasUse_array)
        error('CANNOT DETERMINE A PHASE COMPLIANT MIX');
    end

    %Check gas species
    if isempty(GasUse_array)
        GasUse_array =  Reac_gasphase';
    end
end

%Check if phase compliant mixture matches equilibrated mixture
if length(GasUse_array)==length(GasTried_array)
    if length(CondUse_array) ==length(CondTried_array)
        PHcomp = 'Yes';
    end
end

%Set gas mixture equilibrium temperature to start at AFT of
   previous
%reaction unless PH comp and want GLobal Equil
T_Eqpre = T;


%%---EQUILIBRIUM ROUTINE END---%%
%Report on phase compliancy of mixture
if strcmp(PHcomp, 'Yes')
    %If mixture is phase compliant, report to console and break
       equilibrium
    %routine loop
    PHcheck = 0;
    fprintf('
       <**************************************************> \
       n')
    fprintf(' \n')
    fprintf('Product Mixture IS Phase Compliant\n')
    fprintf(' \n')

    %Reset T_Eqpre Variable to initial starting state variable
    T_Eqpre = T_EqpreUser;

elseif PHcheck == 1
    %If max number of checks performed, report not phase compliant
       and
    %break equilibrium routine loop
    PHcheck = 0;
```

```
        fprintf('
            <*****************************************************> \
            n')
        fprintf(' \n')
        fprintf('PHC Check Max Iterations Met. Will Use PHCSystem With
            Lowest Enthalpy Convergence Error.!!\n')
        fprintf(' \n')

        %Use best PHC System
        COEError = COEErrormin;
        Reac_gasphase = COEmin_Reac_gasphase;
        moles_Reacgas = COEmin_moles_Reacgas ;
        Reac_condphase = COEmin_Reac_condphase;
        moles_Reaccond= COEmin_moles_Reaccond;
        T = COEmin_T;
        GasUse_array = Reac_gasphase';
        CondUse_array = Reac_condphase';
    else
        %If mix not phase compliant, but max number of checks not yet
            performed
        %Reduce remaining check out
        PHcheck = PHcheck - 1;
        fprintf('
            <*****************************************************> \
            n')
        fprintf(' \n')
        fprintf('Removing Out Of Phase Species And Resending For
            Equilibrium\n')
        fprintf(' \n')
    end

end

%%---CALCUALTE GLOBAL EQUILIBRIUM STATE---%
if strcmp(GlobeEquil,'YES')
    %Rebuild mix and Equilibrate at PreEq temp
 mixEQ_moles = cell(length(CondUse_array)+1,2);
    for i =1:(length(CondUse_array)+1)
        if i ==1
            set(mix_gas,'T',T_Eqpre,'P',P_Eqpre*101325);
            mixEQ_moles{i,1}= mix_gas;
            mixEQ_moles{i,2}= sum([moles_Reacgas{:}]);
        else
            set(Mix_SolLiq{i-1,2},'T',T_Eqpre,'P',P_Eqpre*101325);
            mixEQ_moles{i,1}= Mix_SolLiq{i-1,2};
            mixEQ_moles{i,2}= Mix_SolLiq{i-1,3};
        end
    end

    %Form Mix for Equilibrium Calculations
```

```
    mix_EQ = Mixture(mixEQ_moles);
    equilibrate(mix_EQ, 'TP', 1.0, iter_all, 200, report);

    %Extract info
    %Determine moles of products in reactedmix
    mixprods_moles = cell(length(CondUse_array)+1,2);
    for i =1:(length(CondUse_array)+1)
        if i ==1
            mixprods_moles{i,1}= mix_gas;
            mixprods_moles{i,2}= phaseMoles(mix_EQ,i);
        else
            mixprods_moles{i,1}= Mix_SolLiq{i-1,2};
            mixprods_moles{i,2}= phaseMoles(mix_EQ,i);
        end
    end

    %Print product mixture
    %mixprods_moles

end

%%---CALCULATE PRODUCT HEAT OF FORMATIONS---%%
%Calculate enthalpy of products at adiabatic flame temperature (final
%reaction temperature)
h_prods = 0;
for j = 1:length(mixprods_moles)
    h_prods = h_prods + enthalpy_mole(mixprods_moles{j,1})*
       mixprods_moles{j,2}/(1000*1000);%KJ/MOL
end

%Create mix for making enthalpy of formation calcs at STP for products
mixReac_moles = cell(length(CondUse_array)+1,2);
for i =1:(length(CondUse_array)+1)
    if i ==1
        set(mix_gas,'T',298,'P',101325);
        mixSTP_prods_moles{i,1}= mix_gas;
        mixSTP_prods_moles{i,2}= phaseMoles(mix_EQ,i);
    else
        set(Mix_SolLiq{i-1,2},'T',298,'P',101325);mixprods_moles{i,1}=
           Mix_SolLiq{i-1,2};
        mixSTP_prods_moles{i,1}= Mix_SolLiq{i-1,2};
        mixSTP_prods_moles{i,2}= phaseMoles(mix_EQ,i);
    end
end

%Calculate heat of formation of products at STP
hform_prods = 0;
for j = 1:length(mixSTP_prods_moles(:,1))
    hform_prods = hform_prods + enthalpy_mole(mixSTP_prods_moles{j,1})*
       mixSTP_prods_moles{j,2}/(1000*1000);%KJ/MOL
```

```
end

%%%---HEAT OF REACTION---%
%Heat of reaction in SI and 'Merica Units
deltah_si = (hform_prods-hform_reacs)/(prods_mass); %kj/g, implied sign
    is negtive (-q)
deltah= (hform_prods-hform_reacs); %kj/mol
%deltah_imp = 2.326*deltah_si; %BTU/lb
deltah_mm = 0.239006*deltah; %kcal/mol
deltah_mg = 0.239006*deltah_si; %kcal/g

%Construct AFT and Heat of Reaction Report
Reac_report = cat(1,cat(2,{'Energy Release, SI'},num2cell(deltah_si),{'
   KJ/g'}),...
    cat(2,{'Energy Release, SI'},num2cell(deltah),{'KJ'}),...
    cat(2,{'Energy Release'},num2cell(deltah_mg),{'kcal/g'}),...
    cat(2,{'Energy Release'},num2cell(deltah_mm),{'kcal'}),...
    cat(2,{'Adiabatic Flame Temp.'},num2cell(T),{'K'}));

%REPORT FINAL SOLVER ERRORS
if abs(COEError)>0
    fprintf('<*****************************************************>
       \n')
    fprintf(' \n')
    fprintf('Conservation of Energy Convergence Error %%:\n')
    COEError
    fprintf(' \n')
end
if ~isempty(toler_it)
    fprintf('<*****************************************************>
       \n')
    fprintf('<*****************************************************>
       \n')
    fprintf(' \n')
    fprintf('Cantera Enthalpy Convergence Error %%: \n')
    toler_it*100
    fprintf(' \n')
end

fprintf('<*****************************************************> \n')
fprintf(' \n')
fprintf('Continuity error %%:) \n')
100*(prods_mass-reac_mass)/reac_mass
fprintf(' \n')
fprintf('<*****************************************************> \n')
end
```

E.0.3 Thermodynamic File Reader

```
function [GasAvail_array, LiqAvail_array, SolAvail_array,
    ThermoSum_array] =...
     CanteraXMLReader2(mechfilesource)

%% Created by: Stewart Youngblood. Written: 7/24/2019. Edited:
    06/22/2021
%
%Reads thermodynamic mechanism XML data file sent to Cantera and
    reports
%avialable species by phase (gas, liquid, solid)
%
%Script has beeen written to accept any XML data file assuming file has
%already been validated using XMl valdiation tool suite. No error
    catches
%are employed so code will fail if error thrown in this function
%
%%OUTPUTS:
%1)GasAvail_array - Cell array of gas species in the XML file
%2)LiquidAvail_array - Cell array of liquid species in the XML file
%3)Solid Avail_array - Cell array of solid species in the XML file
%4) ThermoSum_array - Cell array of polynomial temperature bounds

%INPUT:
%1)mechfilesource - String with XML file name of thermodynamic
    mechanism
%file in C:\Program Files\Cantera\data

%Major Modifications to solver script:
%06/22/2021: 1) Indexing functionality added to extract minimum and
    maximum
%               temperature bounds of polynomial data
%            2) Indexing modified to determine

%% PROCESSOR
%Open XML file to extract available species
%Get file extension
inFileLoc = fullfile('C:\Program Files\Cantera\data',mechfilesource);
%Read and parse XML file into structured array
XMLobject = xml2struct(inFileLoc);

%Get number of indvidual species present in file
%1st phase: gas phase, all gas species listed here
Gas_spectot = length(split(XMLobject.ctml.phase{1,1}.speciesArray.Text)
    )-1;
%Subsequent phases: solid or liquid, indidvidual species
Cond_spectot = length(XMLobject.ctml.phase);

%Create Arrays for containing species
gas_spec = cell(Gas_spectot-1,1); %Gas Species Array
liquid_spec = cell(Cond_spectot-1,1); %liquid Species Array
```

```
solid_spec = cell(Cond_spectot-1,1); %Solid Species Array

%%%---AVAILABLE SPECIES LISTING---%%%
%Cycle through XML array to obtain species name and build species list
for i=1:Cond_spectot
    if i==1
        %Get gas species from XML array
        gasarray= split(XMLobject.ctml.phase{1,i}.speciesArray.Text);
        %Input into gas species array
        for j=1:(length(gasarray)-1)
            gas_spec{j}=gasarray{j+1};
        end

    else %Identify Condensed phase species
        condensed= split(XMLobject.ctml.phase{1,i}.speciesArray.Text);
        %Determine if condensed phase is liquid
        liq_tf = contains(condensed{2,1},'(L)');
        if liq_tf ==1
            liquid_spec{i} = condensed{2,1};
        else
            %If not liquid, add to solid phase list
            solid_spec{i} = condensed{2,1};
        end
    end
end

%Index empty cells in liquid and solid arrays for removal
in_l = cellfun(@isempty, liquid_spec) == 0;
in_s = cellfun(@isempty, solid_spec) == 0;

%Array of available gas/liquid/solid phase components in mechanism file
GasAvail_array = gas_spec;
LiqAvail_array = liquid_spec(in_l);
SolAvail_array = solid_spec(in_s);

%%%---THERMO DATA LISTING---%%%
%Determine number of species with data for indexing
spectot = length(XMLobject.ctml.speciesData.species);

%Create Arrays for containing species
%Order is: Species, Poly Type, Min Poly Temp, Max Poly Temp
ThermoSum_array = cell(spectot-1,4); %Thermo data summary array

%Load data into array
for i=1:spectot
    %Load species name
    ThermoSum_array{i,1} = XMLobject.ctml.speciesData.species{1,i}
       .Attributes.name;
    %Load polynomial data type
    ThermoSum_array{i,2} = char(fieldnames(
```

```
        XMLobject.ctml.speciesData.species{1,i}.thermo));
    polytype = ThermoSum_array{i,2};

    %Load polynomial temperature bounds based on polynomial type (NASA
        and
    %Shomate types)
    switch polytype
        case 'NASA'
        %Load minimum polynomial temperature range
        ThermoSum_array{i,3} =  XMLobject.ctml.speciesData.species{1,i}
            .thermo.NASA{1,1}.Attributes.Tmin;
        %Load maximum polynomial temperature range
        ThermoSum_array{i,4} =  XMLobject.ctml.speciesData.species{1,i}
            .thermo.NASA{1,2}.Attributes.Tmax;

        case 'SHOMATE'
        %Load minimum polynomial temperature range
        ThermoSum_array{i,3} =  XMLobject.ctml.speciesData.species{1,i}
            .thermo.SHOMATE{1,1}.Attributes.Tmin;
        %Load maximum polynomial temperature range
        ThermoSum_array{i,4} =  XMLobject.ctml.speciesData.species{1,i}
            .thermo.SHOMATE{1,2}.Attributes.Tmax;
    end


end
```

E.0.4 Python Interface Script for Cantera

```
"""
Multiphase equilibrium interface for Cantera that allows the
equilibrium solver type to be specified. Default is Gibbs.
"""
#PyEquil.py
import cantera as ct
import numpy as np
import sys
import csv

def HP(T,P,solv,rt,m_s,m_i,e_e,log_l,spec_c,N_c,N_g,X_g,cti_g,cti_c):
    ###############################################################################

    # INPUTS:
    # 1) T - Temperature of reactants, pre-equilibrium
    # 2) P - Pressure of reactants, pre-equilibrium
    # 3) solv (solver) - equilibrium solver to be used. vcs and gibbs
        are only options
    # 4) rt (rtol) - relative error tolerance for HP or UV iterations
    # 5) m_s (max_steps) - Number of steps in finding equilibrium at
```

```
    specified T,P
# 6) m_i (max_iter) - Number of steps iterations in finding equil.
    for HP or UV
# 7) e_e (est_equil) - Whether solver should estimate initial
    condition. 0 means no estimation
# 8) log_l (log_level) - Requested output during solution finding
    process
# 9) spec_c - Name of condensed species to consider
# 10) N_c - Moles of condensed species
# 11) N_g - Number of moles of gas phase
# 12) X_g - Mole fractions of gas phase
# 13) cti_g - Thermo file for gas phases
# 14) cti_c - Thermo file for condensed phases

# OUTPUTS:
# 1) Tp - Temperature of products
# 2) Pp - Pressure of products
# 3) specs_p - list of mixture product species (same as what was
    initialized but ordered)
# 4) N_p - Moles of gas and condensed phase products

# Create phases
gas = ct.Solution(cti_g)
condensed = ct.import_phases(cti_c,spec_c)

# Set gas mole ratios
gas.X = X_g

#Create Mixture
mix_phases = [gas] + condensed
mix = ct.Mixture(mix_phases)

#Set Mixture State
mix.T = T #Mix temp before equilibration
mix.P = P #Mix pressure before equilibration

#Set moles for phases
gasspec_moles = [N_g*x for x in X_g]
phase_moles = gasspec_moles + list(N_c)
mix.species_moles = phase_moles

################################################################################

# equilibrate the mixture at constant HP
mix.equilibrate('HP', solver=solv, rtol=rt, max_steps=m_s,max_iter=
    m_i,estimate_equil=e_e,log_level=log_l)

# MIXTURE VARIABLES
Tp = mix.T
Pp = mix.P
```

```
specs_p = list(mix.species_names)
N_p = list(mix.species_moles)

# RETURN VARIABLES
#print([Tp,Pp,specs_p,N_p])
return([Tp,Pp,specs_p,N_p])
```

APPENDIX F

PERMISSIONS

Figures 3.12, 3.14, and 3.15 are reprints from the journal article "In situ measurement of the fragmentation behavior of Al/PTFE reactive materials subjected to explosive loading, Part 1: Fragment size measurements" authored by Stewart H. Youngblood, Sean Palmer, David A. Avalos Violante, Jamie Kimberley, Michael J. Hargather and published in Pyrotechnics, Explosives, and Propellants in 2022. No permissions are needed.

FUNDAMENTAL STUDY OF FRAGMENTATION BEHAVIOR AND ENERGY RELEASE OF REACTIVE MATERIALS

by

Stewart H. Youngblood